Bioinspired Copper Complexes for Incorporation into UiO-67

Dissertation for the degree of Philosophiae Doctor

Isabelle Gerz

Department of Chemistry

Faculty of Mathematics and Natural Sciences

University of Oslo

2022

Acknowledgements

I want to thank the students I worked with for their curiosity, their enthusiasm and their hard work. Among them, I want to thank especially Rafael Cortez Sgroi Pupo and Sander Johannes Thorbjørnsen Guttorm, who have contributed to the project in a dedicated way. Thank you for relentlessly searching and finding solutions, both in the laboratory and in the literature. I am super proud of you.

I also want to thank all my colleagues in and outside of the UiO catalysis section that I have worked and/or procrastinated with. I would like to thank all the members of the CUBE project, you have taught me a lot. It is inspiring to see the same challenge from the perspectives of different fields. A special thanks to Sergio Jannuzzi and Serena DeBeer from the MPI for Chemical Energy Conversion in Mülheim for the good collaboration. I want to thank Chiara Negri for the good collaboration on the UV/Vis experiments. You showed me a whole new world. I want to thank Erlend S. Aunan for the good collaborations, discussions and help with the MOF-related research. Your calm wisdom is impressive, be it during teaching, beam time or CUBE meetings. I want to also thank Kaiqi Xu and Ole Golten for their help and explanations.

I want to thank Karoline Kvande and Julie Héron for their friendship and the shared joys and suffering of having a project with copper in the lead role. I would like to thank Inga Schmidtke for mini-vacations, crystal structures and talks about God and the world. I want to thank Knut Hylland for the good collaboration and all the advice I have gotten throughout the years. Thank you for reading all my manuscripts and my thesis and never ceasing to propose further experiments and additional literature. I am also very grateful that you happened to develop many impeccable procedures during your thesis work; they were a solid basis to build upon. I would also thank Reidar Lund's group from the depth of my heart for making me feel welcome on the second floor. I would like to thank Frode Rise and Dirk Petersen for the support and advice concerning the NMR experiments. Your enthusiasm is contagious and this thesis would be non-existent without the work conducted in your labs.

I would like to thank Unni Olsbye for all the support and advice. I highly appreciate that you take the time to dive into the strange world of homogeneous catalysts. I want to thank my supervisors Mats Tilset and Mohamed Amedjkouh for always having an open door for discussions and for giving me a lot of freedom in my work. Thank you for the advice, support and trust you showed me.

I would like to thank my friends, near and far, for their support and my sincerest apologies for all the times I did not have time. I would like to thank Verena, Gunn, Gijs, Knut and my flatmates for the best memories of my time in Oslo. Thank you, Saskia, for being there, no matter what, no matter when. Thank you Sophie for reading my thesis. Lastly, I want to thank my mother, my father, my amazing lillebror Leonard (who proofread this thesis) and the rest of my family. Thank you for always offering me a place to rest my heart, head and soul throughout the years.

Abstract

In this thesis, copper complexes bearing bidentate, tridentate, and tetradentate *N*-ligands were synthesised and characterised. The ligands' design draws inspiration from the histidine copper brace, a structural motif found in enzymes. The compounds were investigated, among other techniques, with nuclear magnetic resonance (NMR) spectroscopy and UV/Vis spectroscopy. A combination of Variable Temperature (VT) ^{1}H NMR, Diffusion Ordered Spectroscopy (DOSY) and ^{1}H-^{15}N Heteronuclear Multiple-Bond Correlation (HMBC) allowed to study the aggregation behaviour of the compounds. Pyridine and imidazole bearing N,N,N,N-copper(I) complexes both formed dimers, yet these dimers are of different constitution. ^{15}N NMR coordination shifts were obtained for several copper(I) complexes, highlighting the interplay between imine and heterocycle. In UV/Vis experiments, the aggregation behaviour of a bispyridine copper(I) complex in solution led to deviation from the linear correlation between concentration and absorption given by the Lambert-Beer law. While exploring the synthetic scope of the protocol for the tetradentate ligands, the formation of dibenzo[d,f]-1,2-dihydro-[1,3]diazepines was observed. The formation of this side product was influenced by a delicate interplay of the substituents on the employed aldehyde and Lewis acidic reagents present in the reaction mixture. Additionally to the aforementioned copper complexes, two pentacoordinated salen-type copper(II) complexes were synthesised. Their ligands differ only by a nitro-substitution *para* to the oxygen binding copper, yet this had a strong effect on the coordination geometry around copper as seen by single crystal X-ray diffraction. The oxidation of a tetracoordinated bisimidazole copper(I) complex in acetonitrile solution upon air exposure was studied by UV/Vis spectroscopy. The majority of copper complexes were synthesised with the aim to incorporate them into metal organic frameworks. The incorporation was successfully shown for two of the complexes. Preliminary studies of the oxidation of the complexes and their catalytic performance suggest that the herein presented complexes are promising catalyst candidates for aliphatic C–H oxidation.

This thesis is based on the following articles:

<u>First author contributions:</u>

Paper I
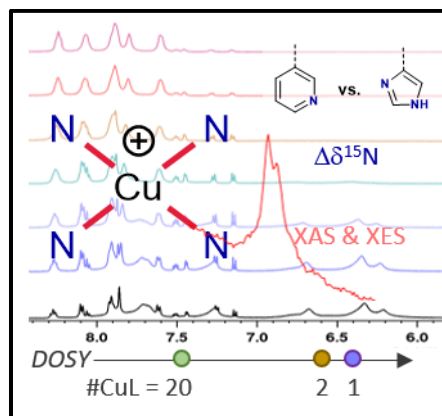
Structural Elucidation, Aggregation, and Dynamic Behaviour of N,N,N,N-Copper(I) Schiff Base Complexes in Solid and in Solution: a Combined NMR, X-ray Spectroscopic and Crystallographic Investigation
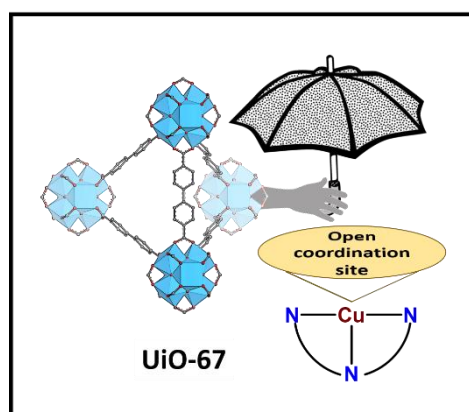
Isabelle Gerz, Sergio Augusto Venturinelli Jannuzzi, Knut T. Hylland, Chiara Negri, David S. Wragg, Sigurd Øien-Ødegaard, Mats Tilset, Unni Olsbye, Serena DeBeer, Mohamed Amedjkouh

Abstract: A series of Cu(I) complexes of bidentate or tetradentate Schiff base ligands bearing either 1-*H*-imidazole or pyridine moieties were synthesized. The complexes were studied by a combination of NMR and X-Ray spectroscopic techniques. The differences between the imidazole- and pyridine-based ligands were examined by ^{1}H, ^{13}C and ^{15}N NMR spectroscopy. The magnitude of the $^{15}N_{imine}$ coordination shifts was found to be strongly affected by the nature of the heterocycle in complexes. These trends showed good correlation with the obtained Cu-N_{imine} bond lengths from single-crystal X-ray diffraction measurements. Variable-temperature NMR experiments, in combination with Diffusion Ordered SpectroscopY (DOSY) revealed that one of the complexes underwent a temperature-dependent interconversion between a monomer, a dimer and a higher aggregate. The complexes bearing tetradentate imidazole ligands were further studied using Cu K-edge XAS and VtC XES, where DFT-assisted assignment of spectral features suggested that these complexes may form polynuclear oligomers in solid state. Additionally, the Cu(II) analogue of one of the complexes was incorporated into a Metal-Organic Framework (MOF) as a way to obtain discrete, mononuclear complexes in the solid state.

Paper II

Enabling a Bioinspired N,N,N- Copper Coordination through Spatial Control in UiO-67: Synthesis and Reactivity towards H$_2$O and O$_2$

Isabelle Gerz, Erlend S. Aunan, Knut T. Hylland, Ning Cao, David S. Wragg, Ainara Nova, Mohamed Amedjkouh

Manuscript under preparation

Abstract: Two molecular copper(I) complexes were synthesized. Their ligands are inspired by the histidine copper brace found in monooxygenases. The ligands contain an imidazole, a pyridine and either a secondary amine or an imine functionality. The molecular copper complexes did not show the characteristic T-shaped threefold coordination found in the enzyme. Instead, ML$_2$ complexes were obtained with either four- or twofold coordination by two ligands per copper centre. The reactivity of the molecular, amine-bearing copper(I) complexes in air was investigated, showing oxidation under ambient conditions. Its ligand was immobilised in the metal organic framework (MOF) UiO-67. The MOF was metalated with Cu(BF$_4$)$_2$·6H$_2$O, affording an incorporated copper(II) complex. A temperature dependent colour change, monitored by UV/Vis, was observed for the MOF but not for the corresponding molecular copper(II) complex. The possible dehydration was supported by DFT calculations. The bond distances of the computational, MOF incorporated structures were in good agreement to those of the active site in lytic polysaccharide monooxygenase (LPMO).

Paper III
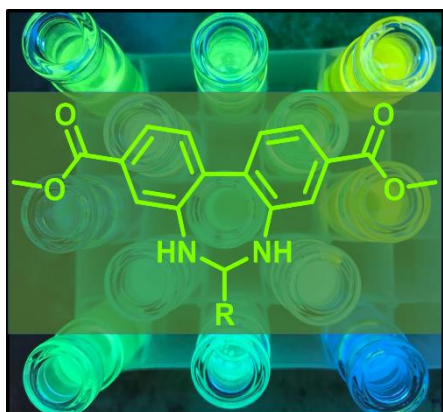
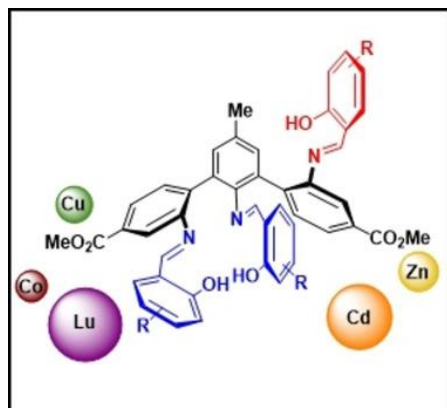*Synthesis and Luminescence of Dibenzo[d,f]-1,2-dihydro-[1,3]diazepines*

Isabelle Gerz, Rafael Cortez Sgroi Pupo, David S. Wragg, Ainara Nova, Mohamed Amedjkouh

Manuscript under preparation

Abstract: A series of 2-substituted dibenzo[*d,f*]-1,2-dihydro-[1,3]diazepines was synthesised from a 2,2'-diaminobiphenyl and different aldehydes. The product formation and selectivity were found to be highly dependent on the aldehyde. Addition of a Lewis acid (Zn^{2+}, Cu^+) to the reaction mixture influenced conversion of starting material and selectivity for the diazepine. Additionally, the photophysical properties of the compounds in solution were explored by UV/Vis spectroscopy and DFT computations. The diazepine motif extended the absorption into the visible light range for most substituents. We found the fluorescent emission to be solvatochromic, a property not previously reported for dibenzo[*d,f*]-1,2-dihydro-[1,3]diazepines.

Other contributions:

Paper IV

The Reactivity of Multidentate Schiff Base Ligands Derived from Bi- and Terphenyl Polyamines towards M(II) (M=Ni, Cu, Zn, Cd) and M(III) (M=Co, Y, Lu)

Knut Tormodssønn Hylland, Isabelle Gerz, David S. Wragg, Sigurd Øien-Ødegaard, Mats Tilset

Abstract: Multidentate Schiff base ligands derived from a selection of biphenyl- and terphenyl polyamines were synthesized, and their reactivity towards divalent (Ni, Cu, Zn, Cd) and trivalent (Co, Y, Lu) metals was studied by single-crystal X-ray diffraction analysis, NMR spectroscopy, and UV/Vis spectroscopy for the Cu(II) complexes. Large variations in the resulting complexes were observed based on the relative position of the amine substituents in the parent triamines, as well as the electronic properties of the Schiff base ligand itself. Most notably, Schiff base ligands derived from a *m*-terphenyl-2,2',2''-triamine were found to coordinate in a tetradentate, pentadentate or hexadentate fashion, depending on the size and the valency of the corresponding metal center.

List of Oral Communications and Posters Presented at National and International Conferences

NKS Landsmøte, October **2018**, Norsk Kjemisk Selskap, *poster*

MR2020, January **2020**, Norwegian Society for Magnetic Resonance, *oral communication*

OKV35, January **2020**, Norsk Kjemisk Selskap, *poster*

ISHHC19, June **2022**, International Symposium on the Relations between Heterogeneous and Homogeneous Catalytic Phenomena, *oral communication*

x

List of Abbreviations

AA	Ascorbic acid
bpdc	Biphenyl-4,4'-dicarboxylic acid
CFT	Covalent Triazine-based Framework
CN	Coordination number
d	Doublet
DFT	Density functional theory
DMF	N,N-dimethylformamide
DMSO	Dimethyl sulfoxide
DOSY	Diffusion Ordered Spectroscopy
EPR	Electron paramagnetic resonance
Equiv.	Equivalent(s)
ESI	Electrospray ionization
Et	Ethyl
EXSY	Exchange spectroscopy
GC	Gas chromatography
HMBC	Heteronuclear multiple-bond correlation
HRMS	High resolution mass spectrometry
HSAB	Hard soft acid base
HSQC	Heteronuclear single-quantum correlations
L	Ligand
LPMO	Lytic Polysaccharide Monooxygenase
m	Multiplet
M	Metal
Me	Methyl
MIL	Matériaux de l'Institut Lavoisier
MLCT	Metal to ligand charge transfer
mp	Melting point

MP-AES	Microwave Plasma Atomic Emission Spectroscopy
MOF	Metal organic framework
MS	Mass spectrometry
m/z	Mass-to-charge ratio
NMR	Nuclear Magnetic Resonance
NOESY	Nuclear Overhauser effect spectroscopy
OAc	Acetate
OTf	Triflate
PMLS	Pre-made linker synthesis
pMMO	Particular Methane Monooxygenase
PSLE	Post-synthetic linker exchange
PSLM	Post-synthetic linker modification
q	Quartet
RT	Room temperature
s	Singlet
SBU	Secondary building unit
SI	Supporting Information
t	Triplet
TGA	Thermogravimetric analysis
THF	Tetrahydrofuran
TON	Turnover number
UV/Vis	Ultraviolet-visible spectroscopy
VT	Variable temperature
XES	X-Ray emission spectroscopy
XRD	X-Ray diffraction

Table of Contents

Scientific Aim

The work summarised in this thesis aimed at producing copper complexes that carry aspects of the LPMO (lytic polysaccharide monooxygenase) enzyme's active site, both in terms of structure and reactivity. The enzyme's active site displays a tricoordinate geometry around copper, stemming from two histidine moieties. Alike the histidine copper brace, the complexes should activate oxygen and C–H bonds. The molecular complexes and the functionalised metal organic framework are intended as catalysts for alkane oxidation.

However, the goal was not to replicate the enzymatic active site, but to transfer its key properties into a synthetic material. A range of denticities was explored for the ligands, as well as different functional groups to provide the N-coordination of copper. This results in synthetic procedures of varying degrees of complexity. Special emphasis was set on the possibility of integrating the molecular complexes into the metal organic framework UiO-67. Ligands with and without the (protected) carboxyl group necessary for UiO-67 formation were included to investigate their influence on the complexes' properties.

Copper(I) was chosen for its diamagnetic nature, enabling studies with nuclear magnetic resonance (NMR). NMR spectroscopy allows not only to verify the constitution of the ligand, but also offers a wealth of experiments that offer insight into the solution behaviour of the complexes. The copper(I) complexes could also be assessed for their air sensitivity. The build-up of a copper(II) species from copper(I) complexes exposed to air could be monitored by UV/Vis spectroscopy. In addition, some copper(II) complexes were synthesised, either as references or in the case of the pentadentate ligands as the sole synthetic goal.

Introduction
Coordination compounds

A coordination complex (or as IUPAC's Gold Book encourages to call it, coordination entity)[1] consists of a coordination centre and one or more ligands. The central atom is usually a positively charged metal ion surrounded by neutral or anionic ligands. Chelating ligands can form multiple bonds to the metal atom (herein: copper). A chelating ligand's denticity denotes how many bonds it can form towards the central atom. The rich chemistry related to coordination compounds has resulted in the development of many concepts dedicated to rationalising their structures, properties and reactivity, and while they without doubt are fundamental to the understanding of such compounds, adequate descriptions of those concepts exceed the scope of this introduction. Therefore, only two concepts are explained in this chapter, geometry indices and open coordination sites, as they are central to later discussions in this thesis.

The most common oxidation states for copper in coordination compounds are +I and +II. Cu(I) has a closed d-shell (d^{10}) and is therefore diamagnetic. Copper(I) coordination compounds

most commonly are two-coordinated linear, three-coordinated trigonal planar or four-coordinate tetrahedral (Figure 1). Cu(II) has a d^9 configuration and is paramagnetic. Transitions in the open d-shell give rise to the blue and green colours commonly associated with cupric compounds.[2] Copper(II) prefers higher coordination numbers (CN) than copper(I) (CN = 4, 5, 6). When tetracoordinated, copper(II) is commonly found in a square planar coordination environment (Figure 1). In terms of the HSAB (hard soft acid base) principle,[3] copper(II) is harder than the soft acid copper(I).[2]
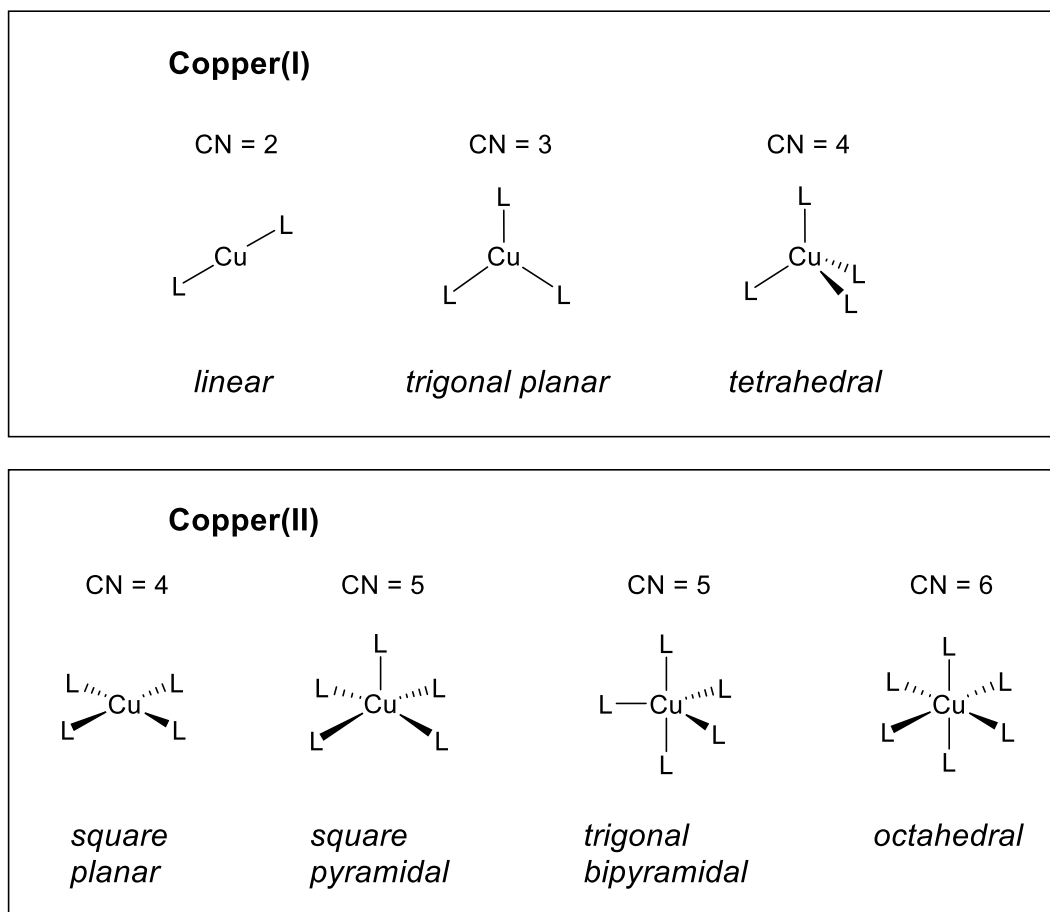
Figure 1. Typical coordination numbers and geometries for copper.[2]

Geometry Indices

One central aspect when discussing coordination compounds is the geometry around the central metal atom. While a linear structure is easily described through two bond lengths and an angle, higher coordination numbers are more demanding. Discussing the relative position of the ligating atoms quickly becomes a stew of angles, making comparisons between structures difficult. Addison *et al.* introduced τ '*as a general descriptor of five-co-ordinate centric molecules*' in 1984 (see equation 2).[4] More than 20 years later, Yang *et al.* introduced a similar descriptor for four-coordinate compounds,[5] creating the current notations τ_5 and τ_4. While they are now used across different fields, it is noteworthy that both descriptors were

first presented on copper compounds. Both coordination numbers (CN = 4, 5) have two ideal geometries (see Figure 2).
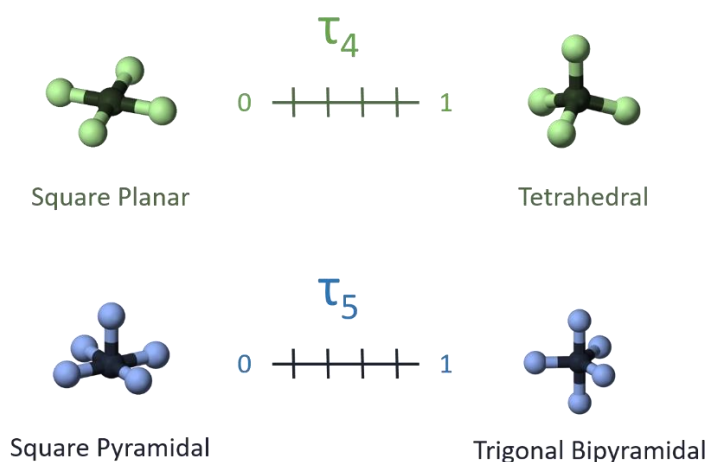
$$\tau_4$$

0 ├──┼──┼──┼──┤ 1

Square Planar   Tetrahedral

$$\tau_5$$

0 ├──┼──┼──┼──┤ 1

Square Pyramidal   Trigonal Bipyramidal

Figure 2. Visual representation of the geometry indices τ_4 and τ_5.

The descriptors are defined in a way that the geometry index can range from 0 to 1 (see equations below). Each end of the scale represents one of the ideal geometries for that coordination number (see Figure 2). The biggest (β) and second biggest (α) angles between bonds to the coordination centre are utilised to determine the corresponding geometry index.

$$\tau_4 = \frac{360° - (\alpha + \beta)}{360° - 2\theta} \qquad 1$$

$$\tau_5 = \frac{\beta - \alpha}{60°} \qquad 2$$

For example, τ_4 becomes unity, when both angles approach the tetrahedral angle Θ ($\approx$ 109.), see equation 1.

Open Coordination Sites

Open coordination sites are crucial to enable catalysis by coordination compounds. Without them, substrates and potential co-substrates would be unable to interact with the metal atom that catalyses the breaking and formation of bonds.[6,7] The importance of low coordination numbers and/or labile ligands for catalytic activity has been discussed for bioinspired complexes in general,[8] and bioinspired multicopper cores in specific.[9] Naturally, an open coordination site attracts ligands other than the substrate, e.g. counter ions and solvent molecules. Solvents[10] and anions[11] impact the catalytic performance in many ways, for example by coordination to the catalytic site. If the coordination is too strong and outcompetes substrate binding, the catalyst is deactivated. Another effect related to coordinatively unsaturated metal centres that can interfere with catalytic processes is the formation of dimers.[12–14] Therefore, the introduction of non-coordinating ions and bulky substituents close to the coordination centre are common strategies to enable an open coordination site.[7,12,15]

Copper–Catalysed C–H activation

Both copper(I)[16,17] and copper(II)[18] compounds have been extensively researched for C–H activation. Copper activates C–H bonds in all hybridizations (sp^3, sp^2, sp)[16,19] and thereby forms C–C, C–N, C–O, and C–S bonds.[17,19] Copper catalysts are also employed in the synthesis of heterocycles.[17] Therefore, it is beyond the scope of this introduction to go through the various ways copper activates C–H bonds. Instead, a common methodology to evaluate catalytic oxidation of aliphatic C–H bonds by homogeneous systems will be presented. Many of the transformations described above have been researched extensively for more expensive metals than copper, and research into copper is often argued for with its lower cost and greater abundancy.[17,19]

Homogeneous Testing of Aliphatic C–H Oxidation

A widely employed model compound for catalytic testing for C–H oxidation in homogeneous, liquid phase is cyclohexane. For one, cyclohexane is a liquid, allowing for a homogeneous phase if the solubility in the solvent is not exceeded. Secondly, all hydrogen atoms are equivalent, meaning that the obtained product is the same independent of which C–H bond is oxidised. The analysis is therefore not complicated by e.g. lack of stereoselectivity, as it would be the case for *n*-hexane, where three different constitutional isomers can be obtained by the introduction of one alcohol group.
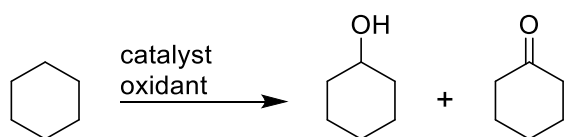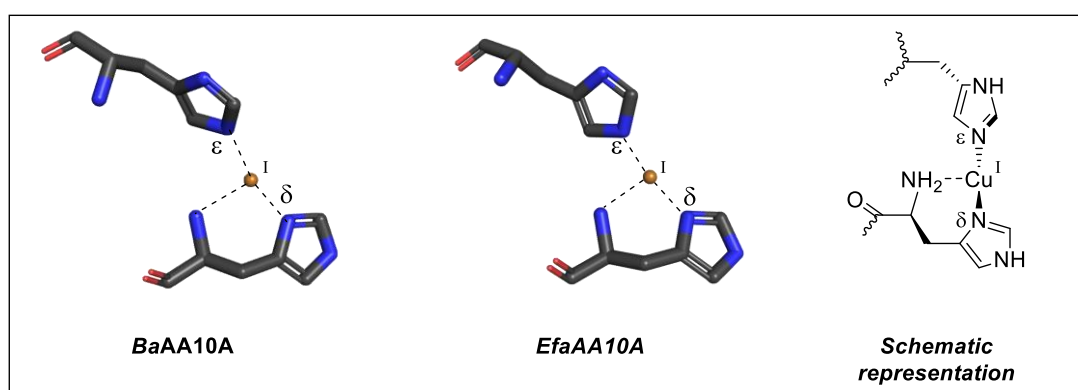

Scheme 1. Cyclohexane oxidation yields either cyclohexanol or cyclohexanone.

Kirillov *et al*. have reported cyclohexane oxidation by multinuclear copper complexes, with increased conversion compared to the industrial process,[9] which is cobalt-catalysed.[20] Garcia-Bosch and Siegler showed that commercial, nitrogen-based tetradentate ligands improve the efficiency of alcohol formation.[21] In the context of biomimetic complexes, Fukatsu *et al*. reported high selectivity for the alcohol, but with low conversion (catalyst shown in Figure 3).[22] All the aforementioned studies were conducted in acetonitrile, which is immiscible with cyclohexane. Thereby, the systems are biphasic, and not actually homogeneous. Another drawback of cyclohexane oxidation as a model for aliphatic C–H oxidation is the potential formation of products other than the alcohol and the ketone. When hydrogen peroxide is the oxidant, the oxidation often proceeds through the corresponding cyclohexyl peroxide, which is unstable, and decomposes to cyclohexanone over time.[23] It can be converted to the alcohol by treatment with PPh$_3$, a procedure developed by Shul'pin.[24] Additional products, such as adipic acid,[20,25] are often not detected in GC, which is the preferred method of analysis in these studies. Nevertheless, cyclohexane oxidation is both, an interesting model for C–H activation and a valid target for catalytic processes, as the current liquid-phase industrial process is run at 6 % conversion.[20,26]

Inspiration from Nature

The field of biomimetic chemistry is concerned with taking lessons from biological systems into chemistry. A central goal is to recreate enzymatic active sites without the extensive peptide structure around them.[27] When it comes to tuning the selectivity of oxidations, oxygenases can serve as blueprints for catalysts.[28] Monooxygenases are, as specified by their name, a class of enzymes that can add a single hydroxyl group to their substrate. Two prominent examples of this class utilise copper as a cofactor: the particulate methane monooxygenase (pMMO) and the lytic polysaccharide monooxygenase (LPMO). They both feature a structural motif known as histidine brace, coordinating a copper atom.[29–33] Small model complexes are of bilateral interest: If the model behaves analogously in spectroscopy and catalysis, a better understanding of the active sites of LPMOs and pMMOs is attainable. Reproducing the feat of activating C–H bonds under mild conditions would advance industrial processes, making them more energy-efficient.[34,35] Approaches from this biomimetic angle have resulted in a variety of *N*-coordinated copper complexes that combine aliphatic amines, amides or imines with heterocycles in the ligand (examples in Figure 1).[21–23,36–38] The most commonly employed heterocycles are pyridines and imidazoles.[37]

LPMO Histidine Brace:

*Ba*AA10A   *Efa*AA10A   *Schematic representation*

Mimetic Complexes:

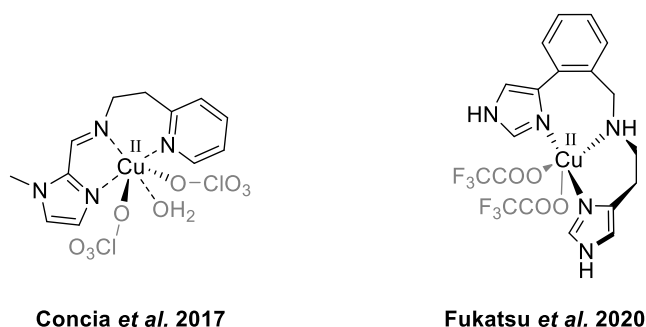Concia *et al.* 2017   Fukatsu *et al.* 2020

Figure 3. The histidine brace motif: The top row shows the histidine copper brace in two photoreduced fungal LPMOs: BaAA10A (PDB-code: 2YOX; AA10 enzymes were previously referred to as CBM33), reported by Hemsworth et al., EfaAA10A (PDB-code: 4ALT), reported by Gudmundsson et al., and their schematic representation.[30,39] Below, two mimics of the active site.[22,36]

While small molecule mimics can contribute to developing catalytic systems with similarities to the enzymatic system, there are limitations to the mimicry. Enzymes are very large molecules. This allows to impacting the catalytic process in ways that are hard to recreate in a molecule that is orders of magnitude smaller.[40] Even mutations distal to the active site can have a pronounced effect on the reactivity, attributable to either a change in availability and predominance of conformers or changes in molecular interaction patterns reaching into the enzyme.[41]

Heterogenization

While molecular complexes offer the opportunity to fine-tune the steric and electronic properties of the metal by rational design of the ligand, their application as catalysts can suffer from a series of drawbacks. Especially catalysts for selective C–H oxidation of small gaseous substrates such as methane have a hard stance in a homogeneous setting. For one, the substrate is less soluble in solution than the product. Supposing a reversible mechanism, this favours the back reaction over product formation. Additionally, there are many more easily activated C–H bonds present, be it from the solvent or another catalyst molecule. Thereby, substrate selectivity can cause the catalyst to degrade.[14,42,43] Lastly, homogeneous catalysts are more challenging to use in continuous stream processes and are often run in batches.[44] The catalyst needs to be separated from the product and solvent after reaction, which can be a cumbersome and expensive process.[44] Heterogeneous catalysts however are less readily tunable and can suffer from diffusion problems.[44]

This formulates the challenge to transform a homogeneous system into a heterogeneous system without losing the well-defined environment around the metal atom that is typical for homogeneous systems. As Thomas outlined in his book 'Design and Application of Single-Site Heterogeneous Catalysts',[45] the characteristics of a single-site heterogeneous catalyst encompass active sites that are identical throughout the material, spatially separated from each other (as to avoid 'cross-talk') and readily accessible due to the equal distribution in a porous solid. Heterogenization of metal complexes has been performed on a series of supports, such as silica, polymers, zeolites, metal organic frameworks (MOFs) and many other materials.[45–50]
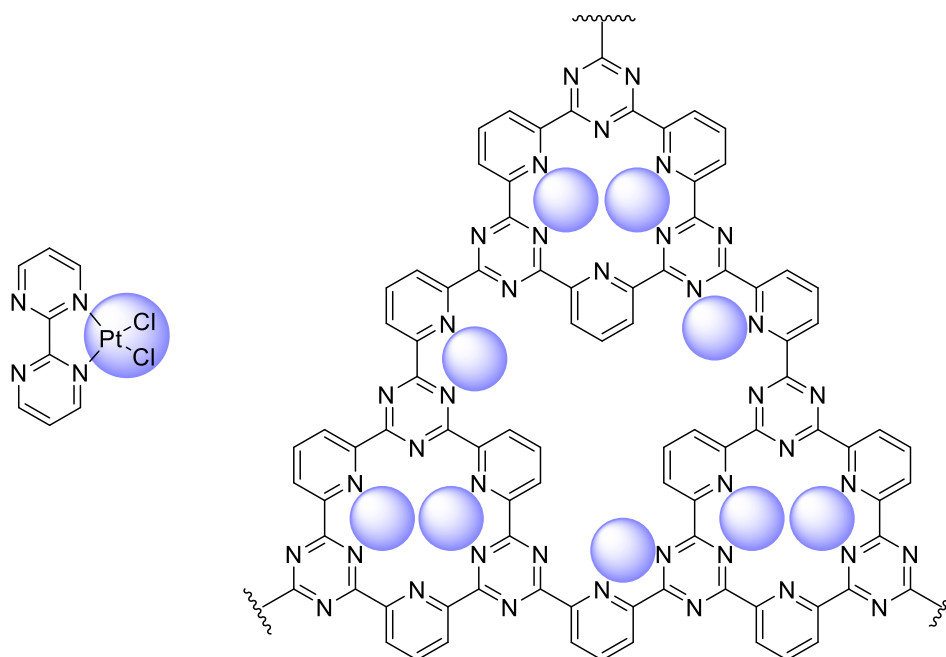
Figure 4. The molecular platinum catalyst developed by Periana *et al*.[51] (left) and its incorporation into a covalent triazine-based framework (CTF) by Palkovits *et al*.[52] (right). In the CTF, the bipyridine ligated $PtCl_2$ is represented as blue sphere for simplicity.

In the context of C–H activating molecular complexes, a successful example of the heterogenization of a molecular catalyst is the platinum complex developed by the group of Periana (Figure 4, left side).[51] The complex was incorporated into a covalent triazine-based framework (CFT) by Palkovits and co-workers (Figure 4, right side). The dipyrimidine ligand is not preserved, but exchanged for C–C-bridged, alternating triazole and pyridine rings. The resulting heterogeneous catalyst performs with comparable TON to the original Periana catalyst.[52]

MOF Incorporation

Metal organic frameworks (MOFs) are, as the name suggests, organic-inorganic hybrid materials. MOFs can be seen as periodic coordination compounds, where ligands with two or more binding moieties form a 3-dimensional network by coordinating metal ions or clusters. Therefore, the ligands are referred to as linkers in this context. The well-defined, repeating units create a crystalline structure. The materials' microporosity and tunability makes MOFs suitable for heterogeneous catalysis.[53] Due to the vast number of MOFs reported and the exponential increase in reports,[54] this subchapter will focus on the UiO-MOFs,[55] an isoreticular group of Zr-cluster MOFs that owe their name to their development at the University of Oslo (*Universitetet i Oslo* in Norwegian). The linkers of the UiO system are aromatic diacids (see Figure 5).
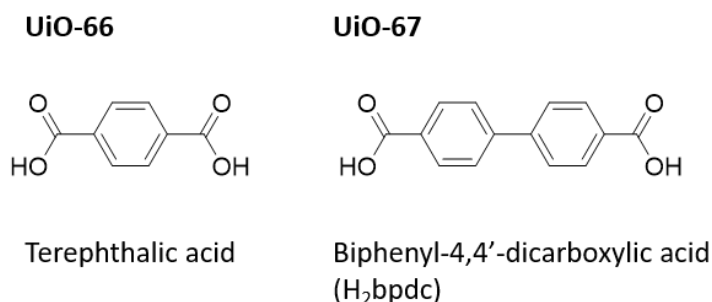
UiO-66

UiO-67

Terephthalic acid

Biphenyl-4,4'-dicarboxylic acid
(H$_2$bpdc)

Figure 5. Linkers for UiO-66 and UiO-67.

Additional functionality can be introduced either at the node or by derivatization of the linker.[56] In order to add functionality to the node, an open coordination site stemming either from missing linker defectivity or from the morphology of the MOF is required. These accessible metal sites in the cluster can be functionalized with a new ligand, or be (co)catalysts in their own right. [57–61] Recently, monooxygenase-like single-sites in metal organic frameworks as catalysts for C–H activation have been reported (Figure 6). A histidine-functionalised MOF 808 was reported by Baek *et al*.[62] Feng *et al.* chose a different approach – by placing two copper atoms inside of the secondary building unit (SBU) of MIL-125(Ti) the monooxygenase-inspired catalytic site is constructed.[63] However, both catalysts represent (and mimic) oxygen-bridged dicopper sites. In contrast, the histidine copper brace is a monocopper site.

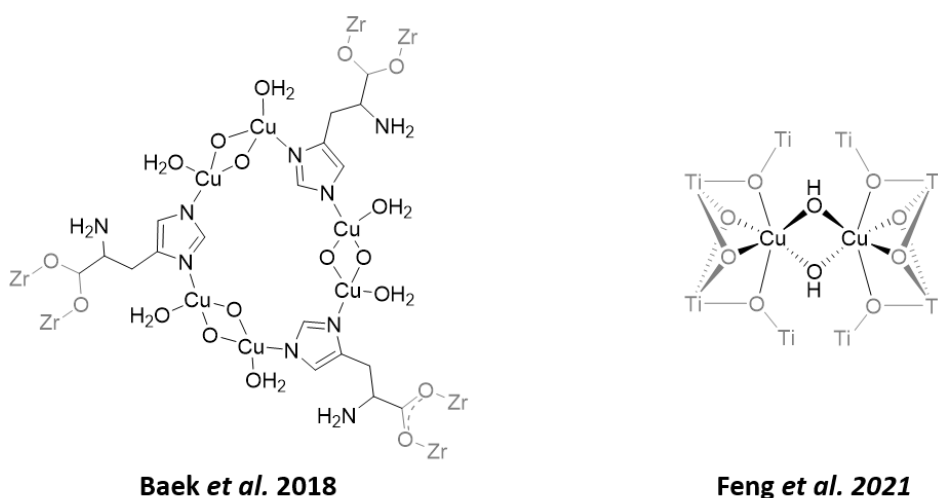**Baek *et al.* 2018**

Feng *et al.* 2021

Figure 6. Monooxygenase-like single-sites reported in literature. To the left: Histidine coordinating to the cluster of MOF 808 coordinating three dicopper sites inspired by the enzyme pMMO.[62] To the right: Functionalised (SBU) of MIL-125(Ti) to create a Cu$^{II}_2$(μ_2-OH)$_2$ site resembling the active centre of a tyrosinase.[63]

Another strategy of functionalization is to have a linker that bears additional moieties to those required for its structural function. The 'unusual' linker can be introduced directly when the MOF is synthesised (**p**re-**m**ade **l**inker **s**ynthesis, PMLS) or in a post-synthetic manner (**p**ost-**s**ynthetic **l**inker **m**odification, PSLM or **p**ost-**s**ynthetic **l**inker **e**xchange, PSLE; see Figure 7).
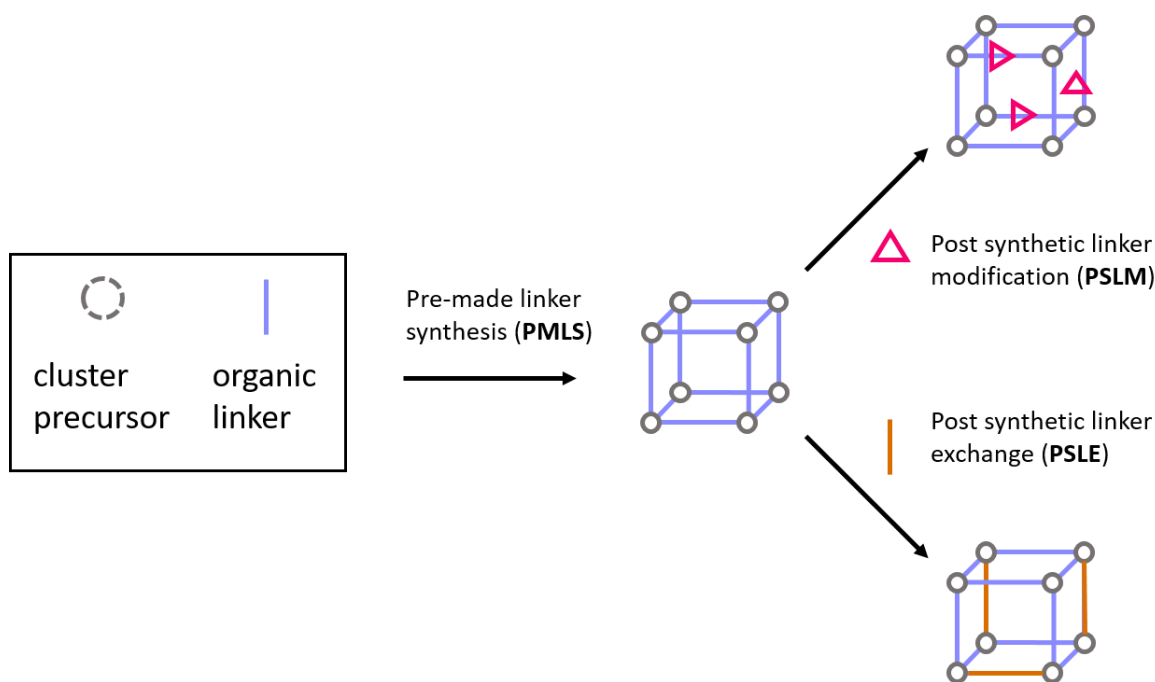
Figure 7. Synthetic strategies to incorporate a linker into a metal organic framework (MOF).

The choice of method depends on the compatibility of materials and protocols. On one side, it is advisable to install acid-sensitive groups in a post-synthetic manner, as HCl is a byproduct of the UiO-MOF synthesis from ZrCl$_4$.[55] On the other side, synthesis steps involving harsh reagents, e.g. strong aqueous bases, must be conducted on the linker prior to its incorporation, as the framework would be destroyed.[64,65] Two examples of post-synthetic linker functionalization are shown in Scheme 2. On the left side, a Schiff base is formed from an amine-functionalized linker and an aldehyde.[66,67] On the right side, a bipyridine linker is metalated, yielding the corresponding coordination compound.[68]
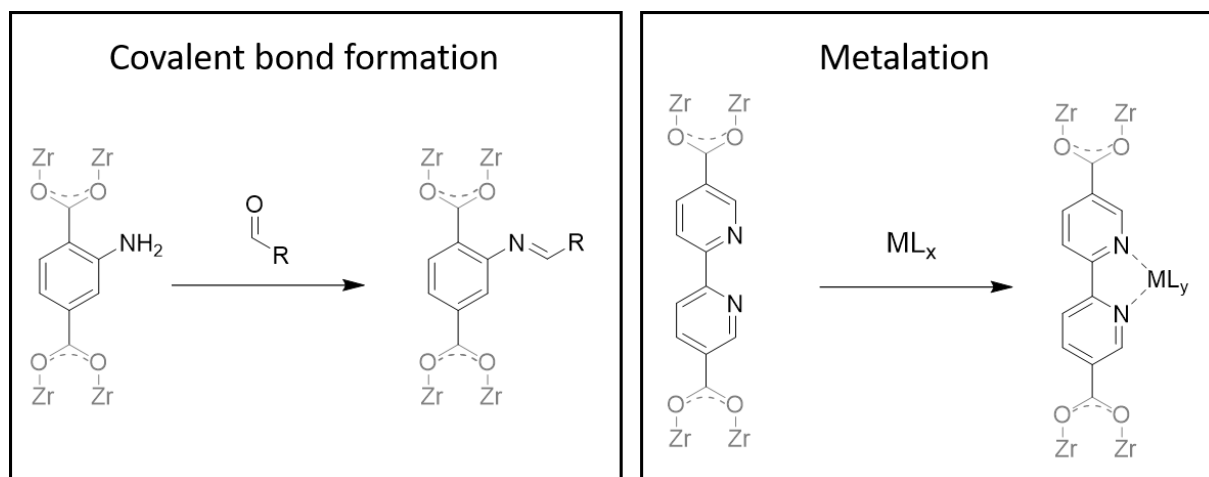
Scheme 2. Examples of post-synthetic linker modification (PSLM) in Zr-MOFs.[66–69]

The incorporation of additional functionality alters the stability of the MOF. Substituting the biphenyl linker for mono- and diamino biphenyl linkers in UiO-67 was reported to result in a faster loss of crystallinity over time compared to the parent MOF. However, mixed linker MOFs

with both, functionalized and unfunctionalized linkers allowed to combine functionality and stability.[70,71]

Synthesis and Characterization of Compounds
Overarching Ligand Design Elements

In this thesis, the underlying strategy was to develop histidine copper brace-inspired complexes that are suitable for incorporation into the metal organic framework UiO-67 (Figure 8). Many ligand backbones presented in this thesis are either biphenyls or phenylpyridines bearing linearly arranged dimethyl esters as substituents. The ester group increases solubility and protects the acid group during synthesis. Before incorporation, the ester is readily removed to yield the corresponding diacid.
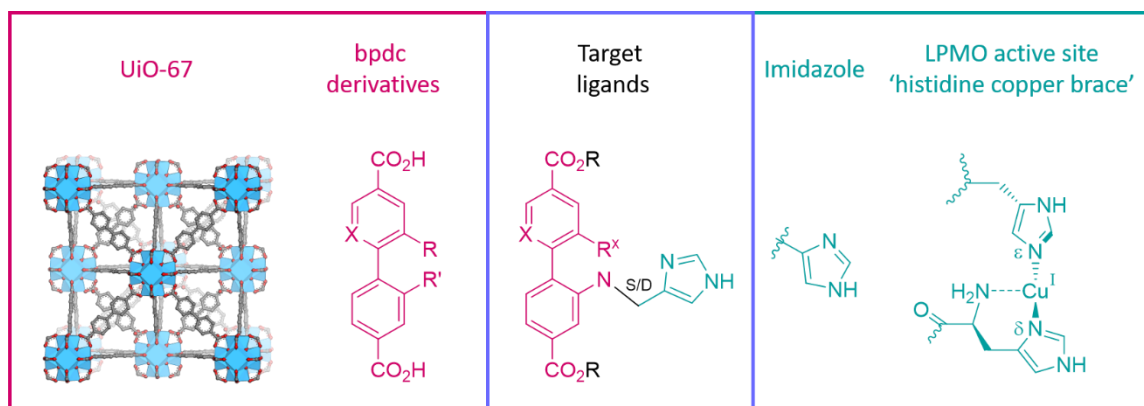

Figure 8. Design elements for the copper complexes are taken from the histidine copper brace in LPMO and the bpdc (biphenyl-4,4'-dicarboxylic) acid linker in UiO-67.[39,55]

Imidazoles are an obvious choice of motif for the ligand as histidine itself is a 4-imidazole derivate. The nitrogen atom in pyridine has similar properties to the sp^2-hybridised nitrogen in imidazole. Being a six-membered ring, pyridine can easily replace one or both phenyl rings in the bpdc linker, which was shown previously in our group for phenylpyridines and bipyridines.[68,72–74] Consequently, imidazole and pyridine are the two heterocyclic motifs employed in this work, in line with the bioinspired literature complexes discussed in the introduction. In the histidine copper brace, the third ligating nitrogen stems from a primary amine. Imines or secondary amines were chosen as additional copper ligating moieties in the complexes, as they allow connecting the heterocycle to the backbone. Only the pentadentate ligands (salen-type ligands, which are neither copper-histidine brace inspired, nor suitable linkers for UiO-67) discussed in the last subchapter bear primary amines.

The incorporation of some of these complexes into the framework will be discussed in the corresponding chapter. The following subchapters discuss the synthesis of molecular *N*-ligated copper complexes. The chapters are structured according to the intended denticity of the ligands, even when the actual denticity towards copper was different.

Schiff Base Synthesis

One and a half centuries have passed since the discovery of Schiff bases,[75] a class of imines, but they still represent a very active field of research.[76–78] Schiff bases are privileged ligands in homogeneous catalysis and are easily accessed through condensation of an amine and an aldehyde.[79] The imine bond can be functionalized on both sides, doubling as coordinating and bridging moiety in multidentate ligands. Some Schiff bases form spontaneously upon mixing of the reactants, while others require activation, for example through acid catalysis or by driving the equilibrium towards the product through removal of the byproduct water.
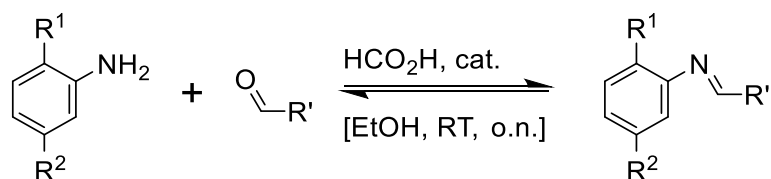
Scheme 3. General reaction scheme for the synthesis of Schiff base ligands in this thesis (R' = imidazole or pyridine).

Acid facilitates the imine formation through protonation of the aldehyde, but can also catalyse the hydrolysis of the product. Most ligands in this thesis were obtainable through the formic acid-catalysed route shown in Scheme 3, yet the one-pot synthesis, with imine formation and metalation in one step, was preferred (see below). The Lewis acidic copper ion can stabilise the Schiff base in multidentate ligands against hydrolysis. The free ligands in this work were synthesised after the procedure reported by Hylland et al.[80] (Scheme 3) and will be presented together with their complexes. Paper III focuses on the synthetic aspect of the reaction of aldehydes with diamines, highlighting that the outcome of the reaction is highly dependent on the reaction conditions and the nature of the aldehyde.

Copper Complexes of Bidentate Ligands

In Paper I, three bidentate ligands and their copper(I) complexes were investigated. The synthesis of the free imidazole ligands **4** and **6** suffered from poor yields (33-40 %, Figure 9). Better yields were obtained from the one-pot syntheses with CuOTf yielding the corresponding CuL_2 complexes **3** and **5** (68-76 %, Figure 9).
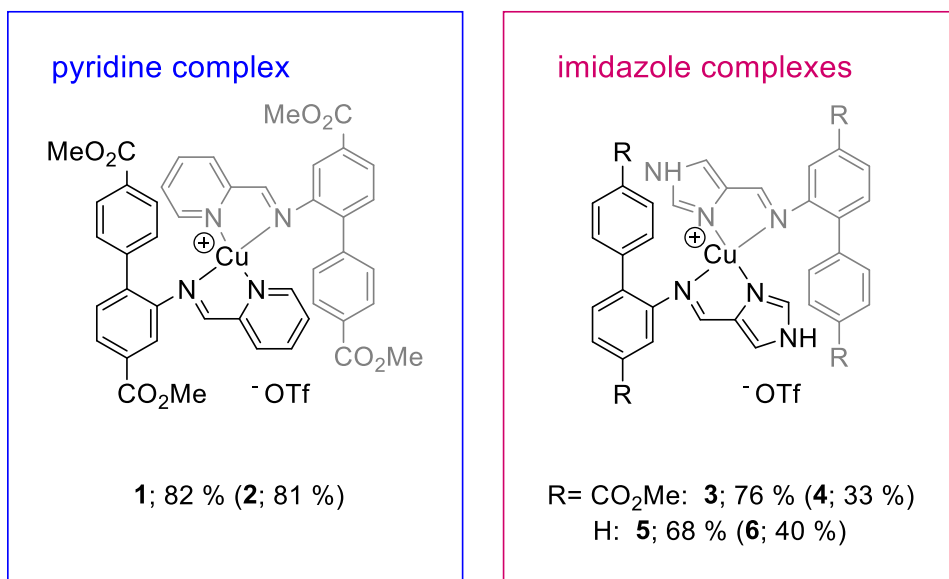
12

Figure 9. CuL$_2$ complexes bearing bidentate ligands reported in Paper I. The yields for the free ligands are given in parentheses.

The full characterization of both free ligands and their copper complexes, including SC-XRD structures of **1** and **3**, can be found in the SI of Paper I. Both single crystal XRD structures were found to have intermediate geometries between tetrahedral and square planar ($\tau_4' = 0.50$ for **1** and $\tau_4' = 0.60$ for **3**). This highlights once more that metals with d^{10} configuration form geometries far from the ideal tetrahedral geometry when the ligand demands it.[80,81] For all three complexes in Figure 9 ^{15}N NMR coordination shifts were determined, and they will be discussed with the tetradentate ligands bearing the same heterocycles.

In d_6-DMSO, the ^{1}H NMR resonances of the imidazole-bearing complexes **3** and **5** were broadened. In contrast, the ^{1}H NMR resonances of pyridine-bearing complex **1** gave rise to sharp resonances. However, multiple species were observed (Paper I). A variable temperature (VT) ^{1}H NMR experiment of **1** in CD$_3$CN (Figure 3 in Paper I) could not unambiguously identify the underlying process(es). The free ligand **2** was not observed in the ^{1}H NMR spectrum of **1** (Figure 10). Nevertheless, it is possible that the CuL$_2$ complexes are in equilibrium with their free ligand and a CuL complex. The ligand reassociation likely happens too fast after dissociation for the free ligand to be observable on the NMR timescale.

An ^{1}H NMR spectrum of a solution containing both, complex **1** and complex **3**, was measured (Figure 10, bottom spectrum). The ^{1}H NMR spectrum of the mixture showed resonances that could not be attributed to either species or their free ligands (reference spectra in Figure 10).
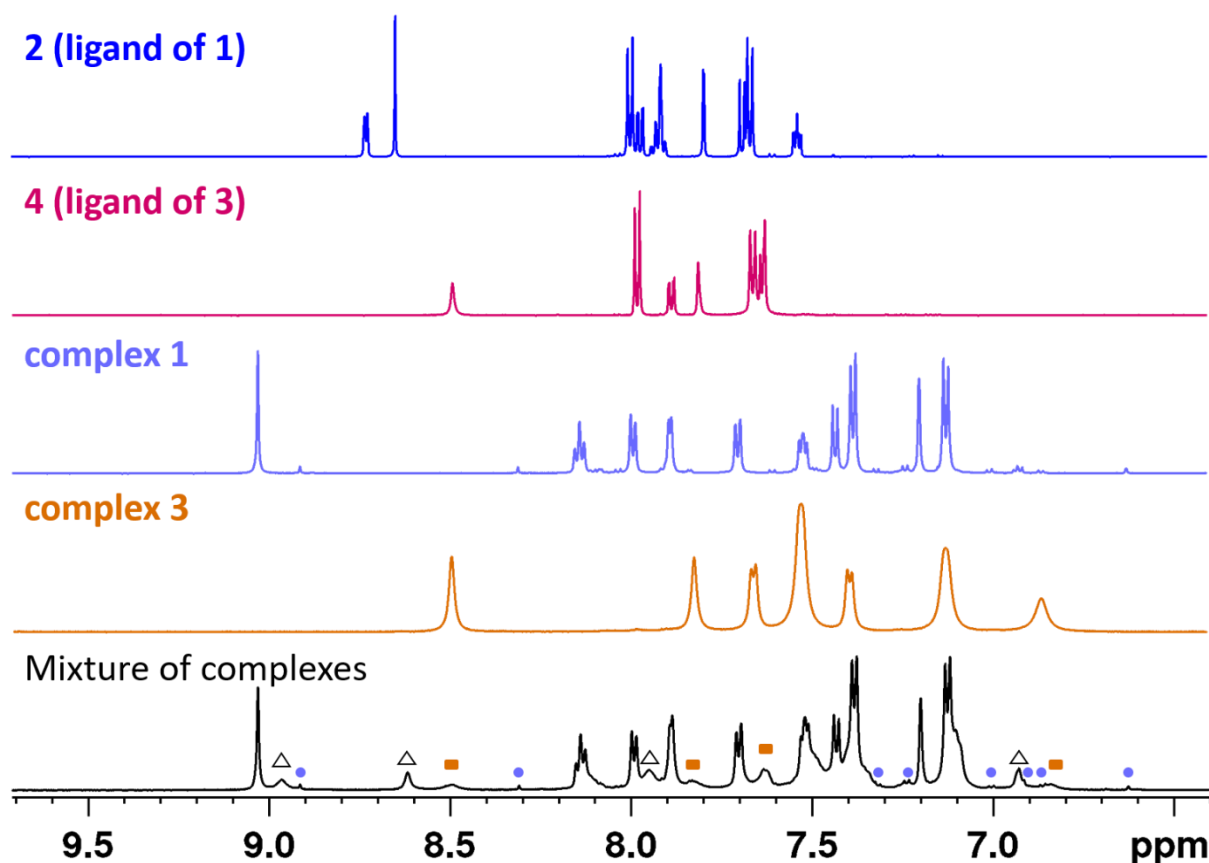
Figure 10. Overlay of the ^{1}H NMR spectra (d_6-DMSO, 600 MHz) of complexes **1** and **3**, their ligands **2** and **4**, and a mixture of both complexes (bottom spectrum). The mixture does not only contain peaks belonging to the minor (purple circles) and major species of **1** and broadened resonances of **3** (orange squares), but also an additional species (triangles). No resonances belonging to the free ligands were observed.

The mixture's EXSY spectrum shows exchange peaks between the complexes and the new species (Figure 39 in the Appendix). This suggests that the mixture is in a state of dynamic equilibrium. The spectrum of the mixture did not change from the first measurement to the last measurement (time span: 5 min to 1 d). The new resonances might stem from the heteroleptic complex, which is formed *via* the dissociation of one ligand from an CuL$_2$ complex (see Scheme 4). The inverse process, the formation of homoleptic complexes from heteroleptic complexes, is a major concern for copper photosensitizers.[82–84]
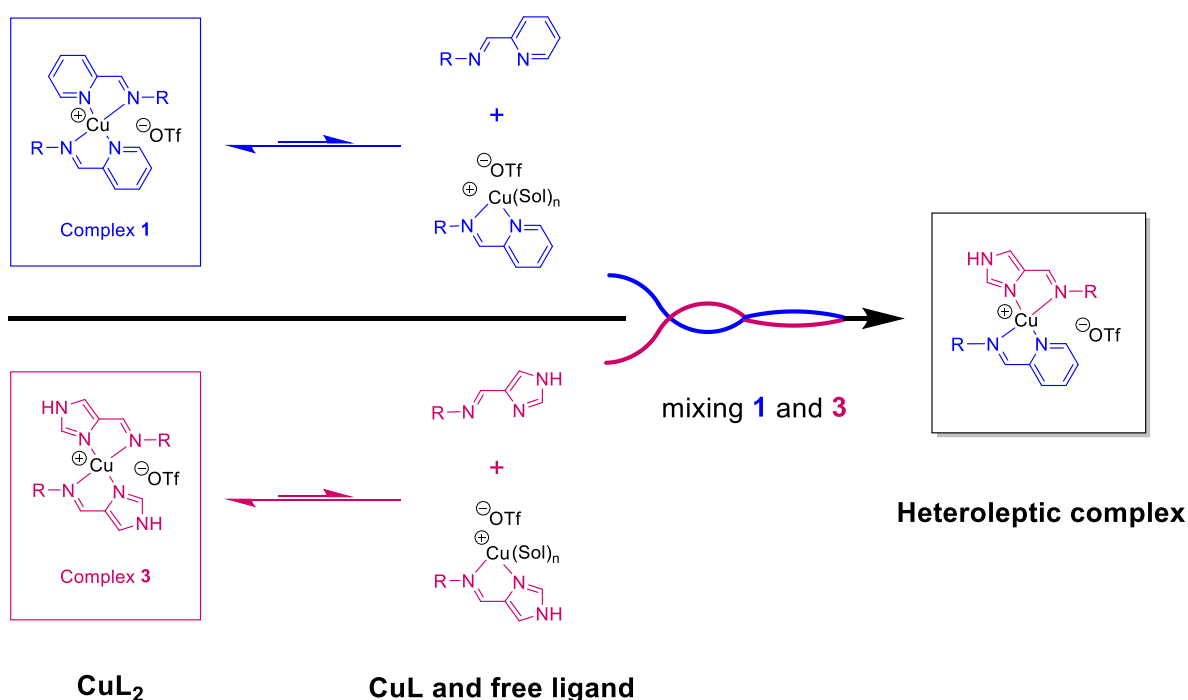
Scheme 4. Possible reaction scheme giving rise to the additional species (heteroleptic complex) in the mixture of complex **1** and **3**.

While the homo- and heteroleptic complexes were sufficiently stable to be observed on an NMR timescale, neither the free ligand nor the CuL complex was observed. Absence of the free ligand in the spectrum of the mixture rules out the possibility of the additional species being the CuL complex, as they would necessarily occur together. The heteroleptic complex may either possess a CuL_2 structure (see Scheme 4), as found in single crystal XRD for **1** and **3**, or a dimeric Cu_2L_4 structure (Figure 11). The dimerisation of **1** also offers a potential explanation for the observation of an additional, minor species in the ^1H NMR spectrum of **1** (see Figure 10). An attempt to confirm the dimeric nature of the minor species with a DOSY experiment (see Appendix, Figure 49) suggested that the minor species was larger than the major species. However, the minor species could not unambiguously be identified as the dimer by molecular weight estimation.
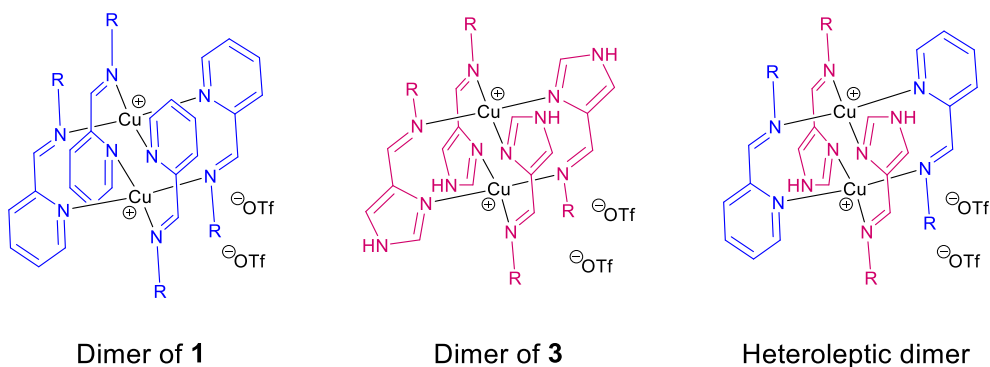

Figure 11. Proposed dimeric structures for **1**, **3**, and a possible heteroleptic dimer formed upon mixing of **1** and **3**. The relative orientation of the ligands in each complex is arbitrary.

Copper Complexes of Tridentate Ligands

The copper-histidine brace depicted in Figure 8 shows a κ^3-*N,N,N*-ligation. Tridentate ligands are therefore thought to be better mimics than e.g. bi- and tetradentate ligands. The complexes are more thoroughly discussed in Paper II, and this section aims solely at summarising the synthetic approach.

Given the successful incorporation of phenylpyridine complexes of ruthenium and gold into UiO-MOFs in our group,[68,74] the synthesis of an imidazole-bearing copper complex starting from a methyl ester protected (2-aminophenyl)pyridine **7** was attempted. Knut Hylland reported the (2-nitrophenyl)pyridine starting material as part of his work on 2-aminobiphenyls,[80] and performed the reduction to **7**. The synthetic procedure for the reduction can be found in Paper II. The one-pot synthesis yielded CuL$_2$ complex **8** (see Scheme 5), the pyridine analogue of complex **1**, instead of the intended tricoordinate CuL complex.
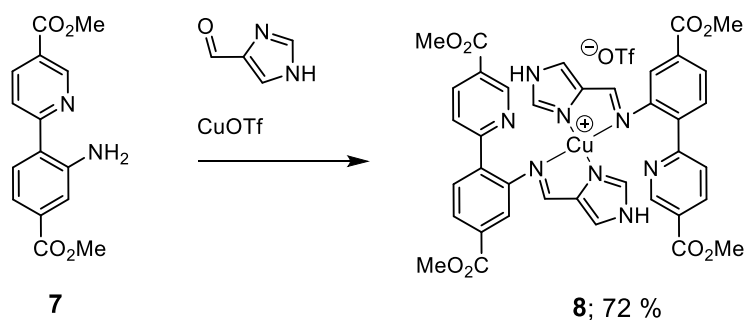
Scheme 5. One-pot synthesis of **8**.

In order to further improve the similarity between the ligand and the copper histidine brace, the imine was reduced to the corresponding amine. The reductive amination to obtain the secondary amine **9** proved to be challenging. As the ligand of **8** was not isolatable with the procedure employed for the bidentate and tetradentate ligands in Paper I, it is plausible that the formation of the imine is not favourable in the absence of a metal ion. Therefore, an indirect approach *via* a zinc complex was chosen. A zinc analogue of **8** was synthesised and reduced with NaBH$_4$ to yield the corresponding amine as a free ligand (see Paper II). Zinc can be handled under ambient conditions and the complex is diamagnetic, facilitating NMR analysis. Furthermore, zinc is not expected to react with NaBH$_4$,[85] unlike the redox-active copper.[86] Ligand **9** was obtained in fair yields, and was metalated with CuOTf to form **10** (Scheme 6). A linear coordination of copper by two ligands through the imidazole moiety was found for **10**.
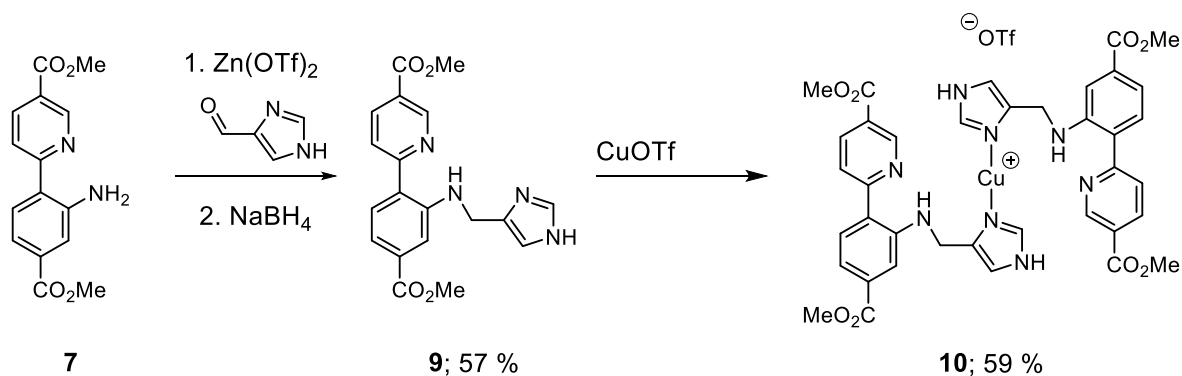
Scheme 6. The synthesis of **9** proceeds through the reduction of Zn^{2+} analogue of **8**. The metalation of **9** yields the CuL_2 complex **10**.

Neither molecular complex, **8** nor **10**, showed the tricoordinate copper coordination the ligand was designed for. From these results it seems that the formation of CuL_2 complexes is more favourable. The formation of CuL_2 complexes has been found to depend on synthesis conditions in literature.[87,88] While it may be possible to control the outcome of the synthesis by careful choice of solvent, it is rather likely that the CuL_2 complex forms under the typical testing conditions for homogeneous cyclohexane oxidation., as the testing is performed in acetonitrile. Paper II exemplifies that heterogenization may offer a solution to the recurring problem of ML_2 formation.

Copper Complexes of Tetradentate Ligands

In addition to the five copper complexes of bi- and tridentate ligands discussed above, copper complexes of tetradentate ligands were synthesised (Figure 12), of which four are presented in Paper I. The complexes were synthesised from the respective biphenyl diamine, the respective aldehyde and copper(I) triflate. The one-pot approach pursued in the paper was especially favourable for complex **14**, as its free ligand synthesis gave a 23 % yield. While the free ligand synthesis was more successful for **12** and **19**, the ligands required purification by recrystallization, while the one-pot synthesis yielded products of high purity (**11** and **18**) after filtration alone. Metalation of the Schiff base ligands (conducted for **12** and **15**) yielded compounds with identical ^{1}H NMR spectra as the complexes obtained via the one-pot synthesis.

pyridine complexes

R= CO$_2$Me: **11**; 74 % (**12**; 82 %)
H: **13**; 97 %

imidazole complexes

R= CO$_2$Me: **14**; 80 % (**15**; 23 %)
copper(II) analogue: **16**; 96 %
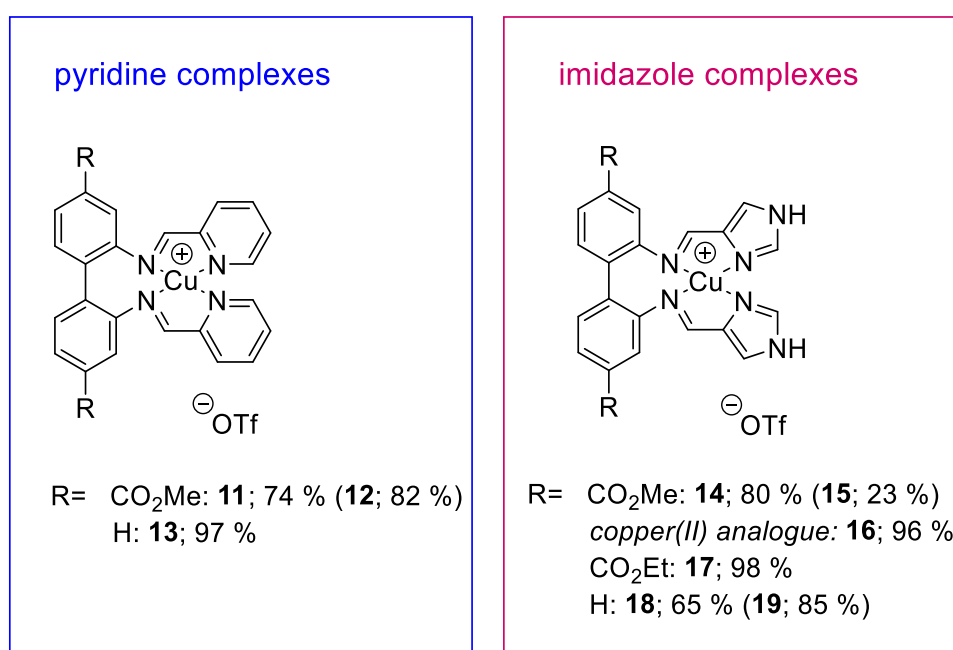CO$_2$Et: **17**; 98 %
H: **18**; 65 % (**19**; 85 %)

Figure 12. Copper complexes of tetradentate ligands. When obtained, the yields for the synthesis of the ligand alone are given in parentheses for comparison.

Pyridine Complexes

Pyridine-bearing compound **11**'s elemental analysis was consistent with the structure shown in Figure 12 and MS showed a single peak corresponding to the molecular cation (Figure 50 in the Appendix), yet its ^{1}H NMR spectrum in d_6-DMSO shows three species (Figure 13, bottom spectrum). The observation of this non-trivial behaviour in NMR stimulated the aggregation studies central to Paper I. A combination of the VT ^{1}H NMR experiment (Figure 13) displayed below and a DOSY experiment (Paper I, Figure 5) identified the following equilibrium to be in effect for **11**:

$$\text{Monomer} \quad \rightleftharpoons \quad \text{Dimer} \ \rightleftharpoons \quad \text{Higher Aggregates}$$

No species was detected that corresponds to an oligomer with a low number of complexes other than two, as it was reported for other copper systems.[89,90]
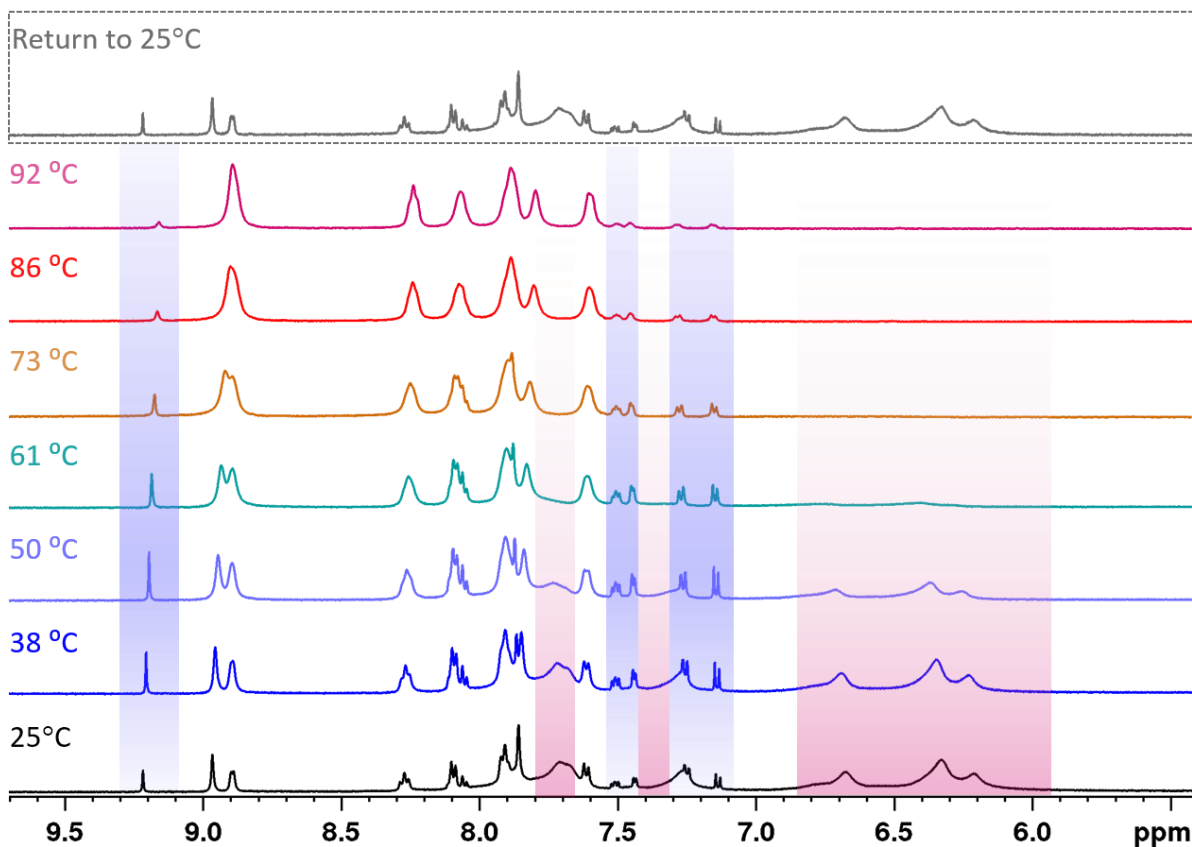
Figure 13. VT ^{1}H NMR of **11** (500 MHz, d_6-DMSO).

The monomeric and dimeric species of **11** could be further studied by ^{15}N NMR. The ^{1}H-^{15}N HMBC of **11** showed crosspeaks for the monomer and the dimer (Figure 14).
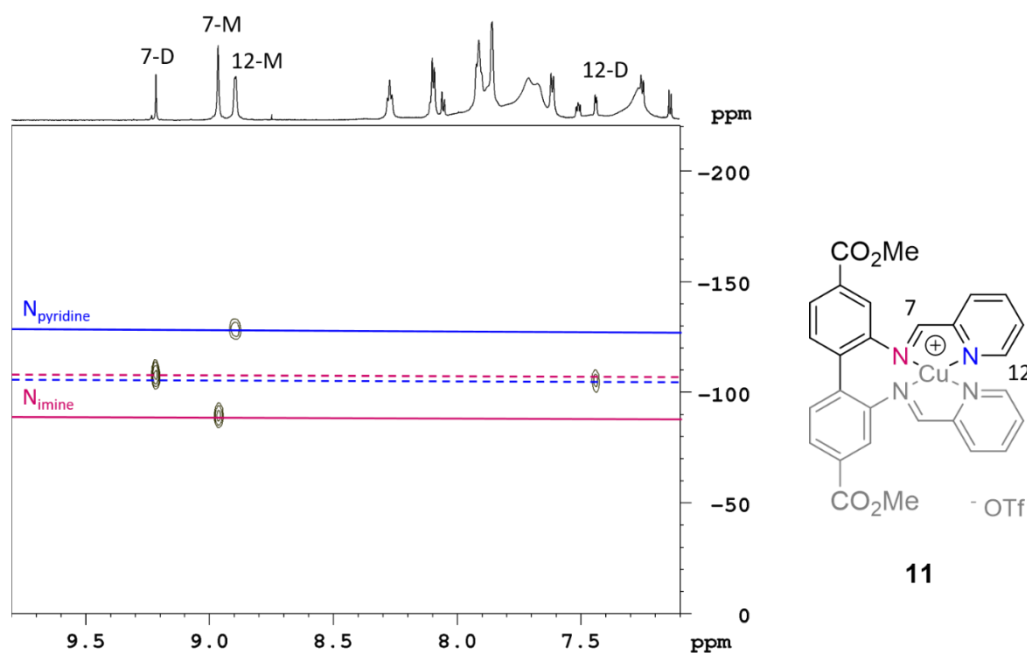

Figure 14. ^{1}H-^{15}N HMBC (800 MHz, d_6-DMSO) of **11**. Solid lines designate the ^{15}N shifts belonging to the monomer, while dotted lines designate the ^{15}N shifts of the dimer.

Following equation 3, coordination shifts could be obtained (Table 1) from the ^{15}N NMR shifts of the free ligands and the respective complexes.

$$\Delta\delta = \delta[complex] - \delta[free\ ligand] \qquad\qquad 3$$

In the monomer, the coordination shift was greater for N_{py} than for N_{imine}, suggesting a stronger ligation to the heterocycle than to the imine. The coordination shifts and the ^{15}N shifts themselves were in good agreement with those found for the CuL$_2$ complex of the bidentate analogue **1**. The dimer of **11** had distinctly different ^{15}N NMR resonances. The coordination shifts' magnitudes for N_{py} and N_{imine} are inverted, indicating a stronger interaction between N_{imine} and copper.

Table 1. ^{15}N NMR shifts (d_6-DMSO, *vs*. MeNO$_2$) and coordination shifts of pyridine complexes **11** and **1** in ppm.

Compound	$\delta^{15}N_{imine}$ [$\Delta\delta^{15}N_{imine}$]	$\delta^{15}N_{pyridine}$ [$\Delta\delta^{15}N_{pyridine}$]
Monomer of **11**	−89.6 [−41.7]	−128.6 [−67.0]
Dimer of **11**	−107.7 [−59.8]	−105.3 [−43.7]
1 (CuL$_2$ complex of the bidentate ligand)	−94.1 [−46.2]	−126.7 [−64.5]

In addition to the ^{15}N NMR analysis presented in Paper I, the dimerisation process can be studied through the ^{1}H NMR shifts. They were strongly affected, allowing a comprehensive analysis of the aggregation dynamics (VT NMR, DOSY) discussed above. A new method of visualisation for chemical shift changes was developed to facilitate the discussion. The $\Delta\delta$ is colour coded and each proton (transferable to other nuclei) is marked accordingly. Thereby, the reader can assess at a glance the magnitude of shift changes and identify which parts of the molecule respond strongest. The change in δ^1H upon metalation is visualised in Figure 15.
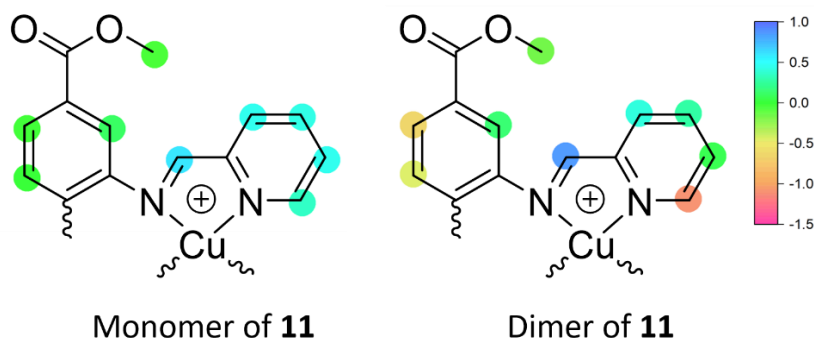

Monomer of **11**   Dimer of **11**

Figure 15. Change in δ^1H between upon copper metalation of **12**, yielding complex **11**. The shift values can be found in the Appendix, Table 5.

The $\Delta\delta$ is calculated from the chemical shifts of the monomer and dimer of **11** and the free ligand **12** following equation 3. For the monomer, the biphenyl backbone is barely affected by the copper metalation, while the imine and pyridine shifts are shifted downfield.

The change upon dimerisation (Figure 16, left side) is maybe even clearer if the shift difference between monomer and dimer is plotted instead (δ(monomer) $-$ δ(dimer), Figure 16, left). The largest $\Delta\delta$ was found for the proton adjacent to the pyridine-nitrogen (α-C**H** or H12 in Figure 14) with -1.46 ppm. This is in line with the findings for the carbon shifts, where the largest, albeit small with respect to the ^{13}C NMR chemical shift range, $\Delta\delta$ was found for the α-**C**H with $\Delta\delta= 2.4$ ppm. The second area affected by the dimerisation is the biphenyl backbone, where the protons in *para* and *meta* position to the imine are shifted upfield.
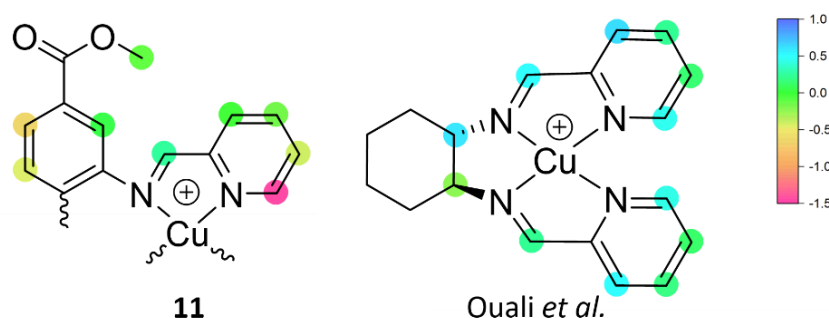

Figure 16. Left: Change in ^{1}H δ between monomer and dimer in compound **11**. The shift values can be found in the Appendix, Table 5. Right: Change in ^{1}H δ between monomer and dimer of the literature compound reported by Ouali *et al.*[13] The structure of the monomer represents the relative configuration.

Ouali *et al.*[13] have reported ^{1}H NMR data for both, dimer and monomer, of a related structure with a cyclohexyl backbone (Figure 16, right). The ligand is racemic and the dimer is formed by combination of an (*R,R*)- and an (*S,S*)-trans-cyclohexane complex. The dimer is reported with two sets of resonances, where significant differences are observed close to the stereogenic centre. Interestingly, the majority of the resonances of their dimeric structure are shifted downfield. The ^{1}H $\Delta\delta$ (monomer vs. dimer) for the α-C**H** is not larger than for other protons in the molecule. The α-C**H** resonance of related dimeric structures differing in the type of backbone can be found in Table 2. In addition to Ouali *et al.*,[13] ^{1}H NMR shifts of related structures have been reported by Amendola *et al.*,[91] Hamblin *et al.*,[92] and van Stein *et al.*[93] NMR shifts are solvent-dependent, and so is the aggregation behaviour, as seen for VT ^{1}H NMR of **11** in d_6-DMSO (Figure 13) and CD$_3$CN (Figure S61, Paper I) and literature examples, e.g. Hylland *et al.*[94] and Ouali *et al.*[13]). In order to obtain the chemical shift assignments for a species in a certain solvent, it has to be soluble and observable on an NMR timescale. Therefore, it is not possible to measure all compounds in the same solvent, as comparability would dictate. In favour of the comparison of ^{1}H NMR data in different solvents stands however that Ouali *et al.* measured the monomer in both, CD$_3$CN and CD$_2$Cl$_2$ and found similar chemical shifts.[13] Furthermore, the chemical shift range is much larger than e.g. the shift

difference for α-C**H** due to methylation of the pyridine-nitrogen ($|\Delta\delta|$ = 0.59 ppm in D_2O),[95] which arguably presents a bigger change to the local environment than a change in solvent.

Table 2. Chemical shifts of the proton adjacent to the pyridine-nitrogen (α-C**H)** in dimeric structures of copper pyridine Schiff base complexes.

backbone	solvent	δ α-C**H**
binaphthyl[92]	CD_3CN	5.60 ppm
dimethyl biphenyl-4,4'-dicarboxylate (**11**)	d_6-DMSO	7.44 ppm
cis-cyclohexane[93]	CD_3OD	8.11 ppm
trans-cyclohexane[13]	CD_2Cl_2	8.49 ppm, 8.46 ppm
ethane[91]	CD_3CN	8.42 ppm

The α-C**H** resonance in the dimers with the ethane and cyclohexane backbones show little deviation from typical α-CH chemical shifts in pyridines, and for the *trans*-cyclohexane also little difference to the monomer (see discussion of Figure 16). Contrary to that, the α-C**H** in the dimers with binaphthyl and biphenyl backbone are strongly shifted upfield. The binaphthyl variant's α-C**H** is located at 5.60 ppm, meaning it even left the region associated with aromatic protons. These shifts suggest a correlation between the nature of the backbone and the chemical shift of the α-C**H**. A possible cause may be the backbone forcing the α-C**H** into a position where it experiences a ring current.

*Aggregation of **11** studied by UV/Vis*

As a solid and in solution, complex **11** is intensely green coloured. Green is often associated with copper(II) complexes, where the colour stems from d-d transitions. Due to the d^{10} configuration, copper(I) complexes do not produce a d-d band. Copper(I) complexes owe their colour, if they have one, to the ligand itself or charge transfer bands between metal and ligand. The free ligand of **11**, compound **12**, was found to be pale yellow, nearly colourless. The UV/Vis spectrum of complex **11** shows two bands in the visible region, one at 450 nm and one at 620 nm (left side of Figure 17).
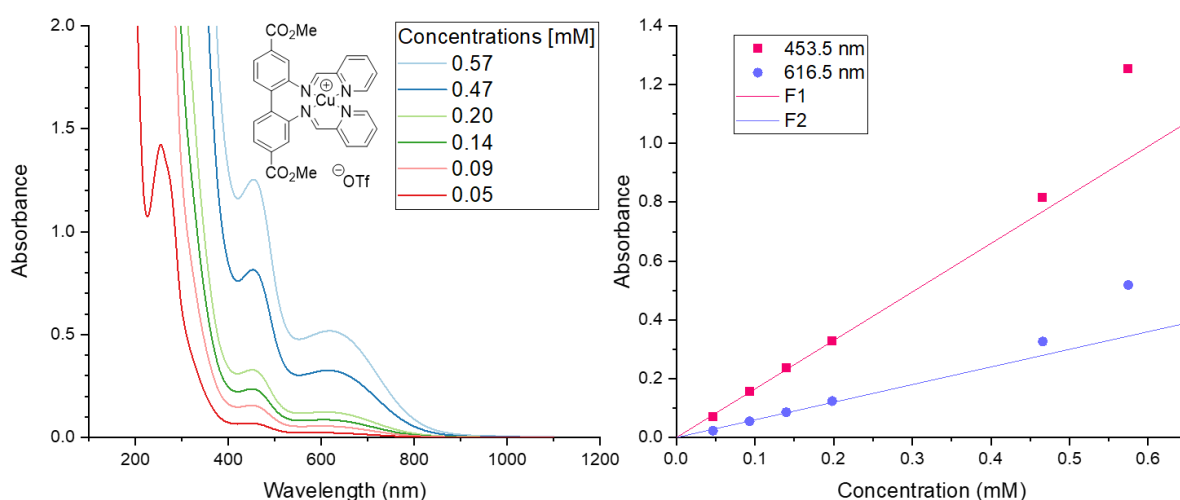

Figure 17. Left: UV/Vis spectra of **11** at different concentrations. Right: absorbance at the two maxima *vs.* the concentration. Linear functions are added to emphasise the deviation from linearity at higher concentrations.

Interestingly, both bands in the visible region do not follow the regime dictated by the Lambert-Beer law at higher concentrations, despite reasonable absorbance values (right side of Figure 17). In combination with the intensity of the band, a copper(II) impurity causing the green colour can be ruled out. An impurity's band would follow the linear regime and bands stemming from d-d transition are less intense. Based on literature data on a dimeric diimine bipyridine copper complex exhibiting bands at 452 nm and 600 nm[96] and the NMR studies discussed above, it can be suggested that the concentration dependency may be due to aggregation behaviour. For porphyrins, deviations from the Lambert-Beer law have been associated with aggregation.[97,98] Given that the concentration is ca. 40 times lower in the highest concentrated UV/Vis sample than in the NMR samples used in the VT ^{1}H NMR in Figure 13, it is likely that only a small fraction of the sample is present as a dimer. While the extinction coefficient is not accessible for an interconverting species of unknown prevalence, it is likely that the absorption is rather strong.

*Compound **13***

Another tetradentate pyridine copper complex was synthesised in addition to those discussed in Paper I during the thesis work (Figure 12). Complex **13** is an analogue of **11**, not bearing ester groups. Compound **13** shows two species in ^{1}H NMR in d_6-DMSO (see Figure 18). At room temperature, the aggregation for **13** is less pronounced than for **11** (for comparison, see Figure 13). A paramagnetic iron(II) chloride complex of the same ligand was reported by Vedder *et al.*[99] Interestingly, their catalytic testing of the iron complex hinted toward polynuclear species, but the ^{1}H NMR spectra (in CDCl$_3$) presented in that publication show only one species. The difference between their findings and the ones presented herein might be attributable to either the solvent, iron as the metal or chlorides as (coordinating) counter ions.
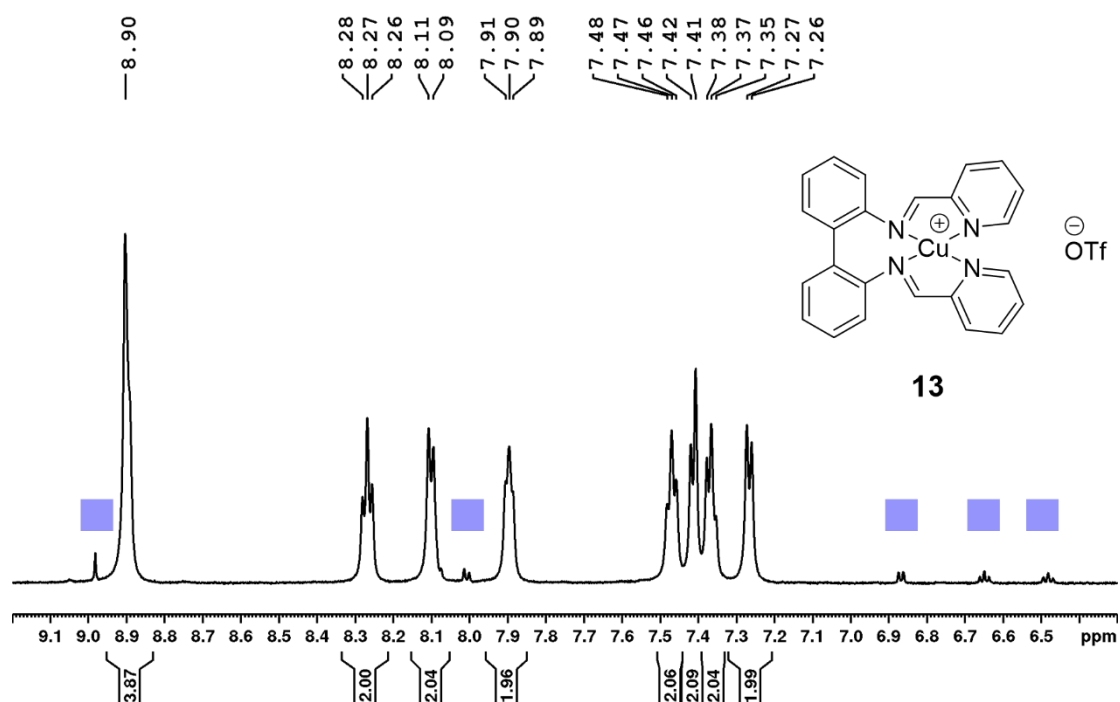

Figure 18. Aromatic region of the ^{1}H NMR spectrum of **13** (600 MHz, d_6-DMSO). The minor species (blue squares) has comparable chemical shifts to the ones observed for the ester substituted derivate **11**.

A DOSY experiment was conducted on **13** (see Figure 19). The minor species diffuses slower than the major one, similarly to the observations for **11** in Paper I. The diffusion coefficients ($4.21 \cdot 10^{-10}$ m/s^2 and $3.17 \cdot 10^{-10}$ m/s^2) were analysed using the Stoke-Einstein-Gierer-Wirtz model developed by Evans *et al.*[100,101] and the calculated M$_w$ are consistent with the a monomeric and a dimeric species (M$_w$exp: [major]= 429 g/mol, [minor]= 794 g/mol; M$_w$calc: [CuL$^+$]= 426 g/mol, [Cu$_2$L$_2$$^{2+}$]= 852 g/mol).
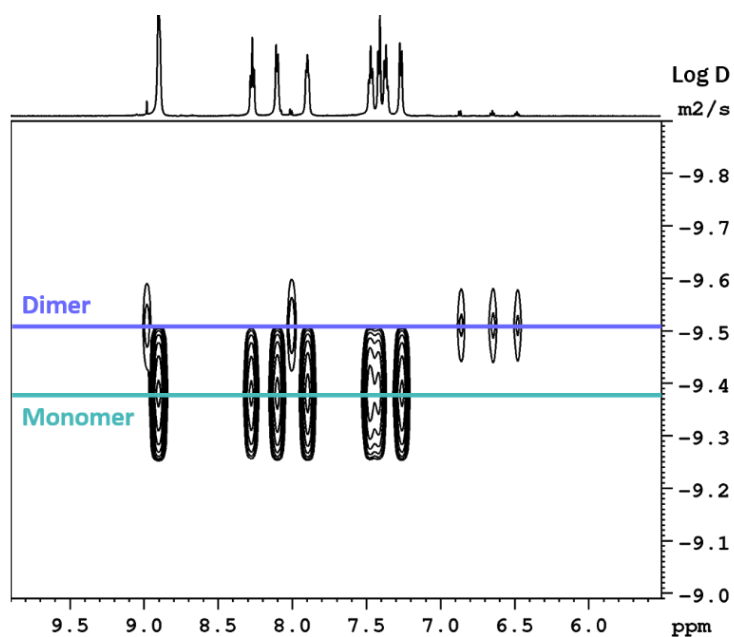
24

Figure 19. DOSY spectrum of compound **13** (600 MHz, d_6-DMSO).

As discussed above for the UV/Vis study of **11**, the degree of aggregation is expected to be concentration dependent. Therefore, a series of ^{1}H NMR experiments with varying concentrations was conducted on compound **13**.
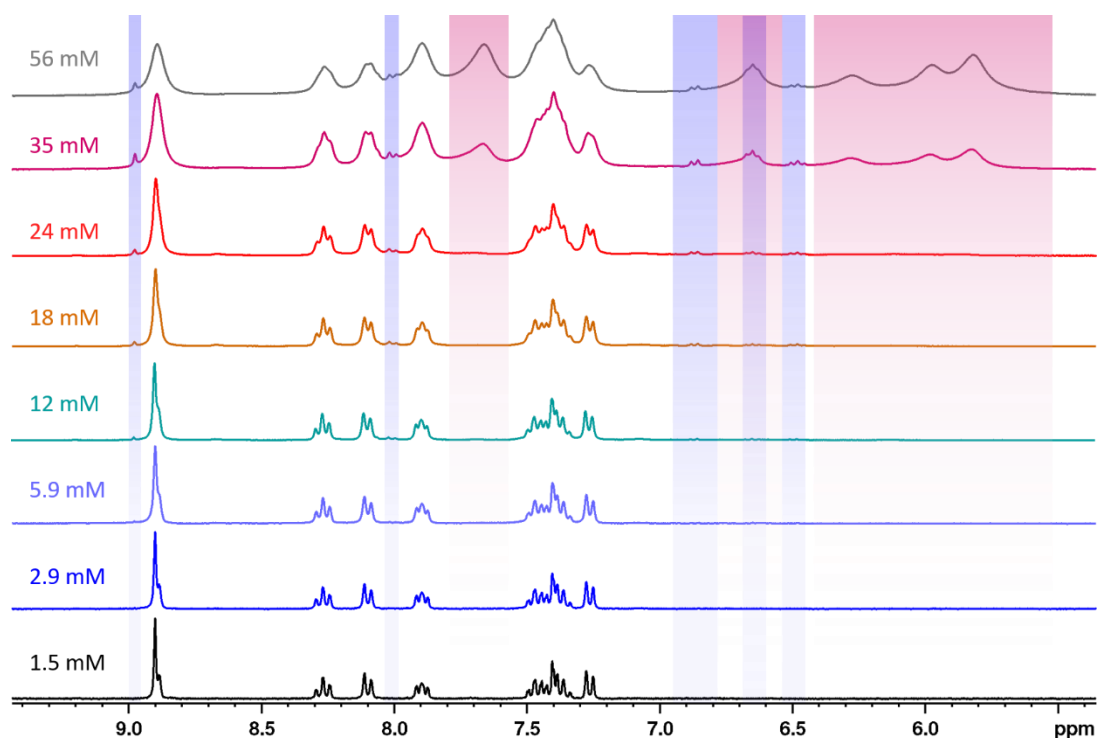

Figure 20. Concentration dependence of the ^{1}H NMR spectrum of compound **13** (d_6-DMSO, 300 MHz, all spectra are recorded at ambient temperature).

The ^{1}H NMR spectrum of **13** in d_6-DMSO was recorded for a range of concentrations (Figure 20). Peaks that are attributable to higher aggregates were observed only at high concentrations. At low concentrations, only the monomer could be detected. The chemical

shifts and peak shape of the agglomerate strongly resemble those of **11**. In combination with the little effect of the dimerisation on the methyl resonance (Figure 16), the methyl ester substitution seems to affect the degree of aggregation, but not the type of species formed.

The VT ^{1}H NMR of complex **11** (Figure 13) showed that the decrease of the higher aggregate was concomitant with an increase in the dimeric species. This suggests that the formation of higher aggregate might proceed through a propagating mechanism in the dimeric species. Based on the ligand exchange experiment with the bidentate complexes, it is possible to speculate that a copper centre coordinated with just one imine-pyridine pair is involved. Such a complex is unstable and another imine-pyridine pair would quickly coordinate. This creates another unstable copper site (Figure 21), if it stems from another dimer. The aggregation would therefore quickly proceed towards a large molecule, without stabilising intermediate oligomers.
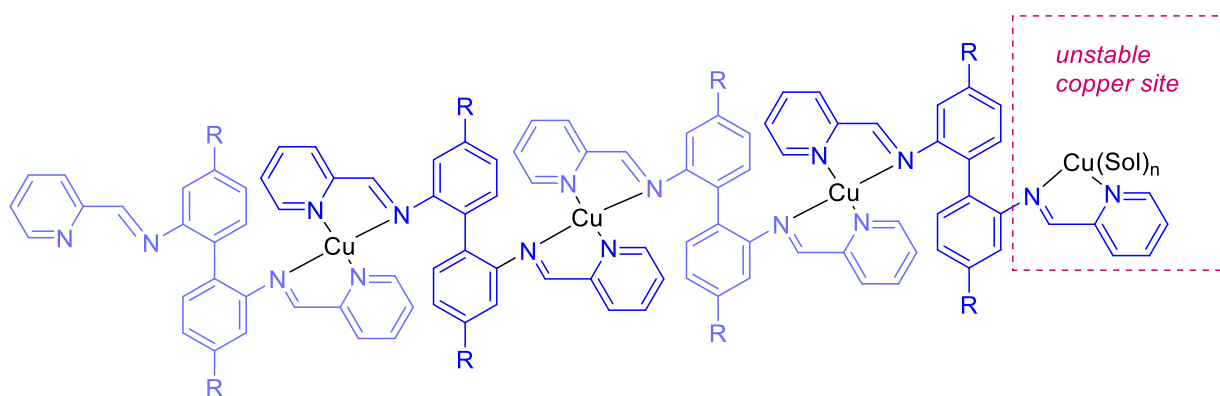

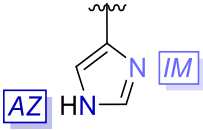Figure 21. Proposed intermediate of the formation of higher aggregates.

The formation of oligomeric and polymeric structures of imine pyridine copper complexes is well-documented.[96,102,103] The nuclearity of the formed species varies from ligand to ligand. A polymeric structure similar to the one resulting from the proposed mechanism in Figure 21 was reported by Tuna *et al*. for copper complexes of pyridine substituted bishydrazones.[102] Such supramolecular assemblies have also been studied for copper(II) complexes of imine imidazole ligands.[104–106] In the next subchapter, the copper(I) complexes of the imidazole analogues of the tetradentate ligands discussed above are investigated.

Imidazole Complexes

In addition to the tetradentate pyridine complexes, four tetradentate imidazole copper complexes were synthesised (structures in Figure 12). Complexes **14** and **18** take a central role in Paper I, and are the imidazole analogues of the pyridine complexes **11** and **13**. Complex **16** is the copper(II) analogue of complex **14**, which was synthesised as a reference for UV/Vis spectroscopy of the oxidation of **14** (see corresponding chapter). Additionally, **16** was incorporated in UiO-67, which will be discussed in the respective chapter. Lastly, **17** is the ethyl ester analogue of **14**. The synthesis and motivation for **17** will be discussed at the end of this subchapter. Only **14** and **18** were subjected to extensive NMR studies and will be discussed in this subchapter in comparison to their pyridine analogues.

The ^{1}H NMR spectrum of **14** in d_6-DMSO showed sharp resonances, while those in the spectrum of **18** were too broadened to display fine structure. ^{15}N NMR shifts of complexes for **14** and **18**, as well as of the CuL$_2$ complexes **3** and **5** were collected in either d_6-DMSO or CD$_3$CN (Table 3). With the exception of **18**, the ^{15}N NMR shifts of the free ligands could be obtained in the same solvent, yielding the coordination shifts. To the best of the author's knowledge, these represent the first instance of copper-imidazole coordination shifts.

Table 3. ^{15}N NMR shifts (*vs*. MeNO$_2$) of imidazole complexes **3**, **5**, **14** and **18** in ppm. All data was collected in d_6-DMSO, apart from **18**, which was measured in CD$_3$CN. Coordination shifts, if obtained, are given in brackets.

Compound	$\delta^{15}N_{imine}$ [$\Delta\delta^{15}N_{imine}$]	$\delta^{15}N_{IM}$ [$\Delta\delta^{15}N_{IM}$]	$\delta^{15}N_{AZ}$ [$\Delta\delta^{15}N_{AZ}$]
3	−86.0 [−16.1]	−171.7 [−55.2]	−205.6
5	−86.1 [−21.1]	−170.0 [−52.8]	−206.1 [+3.5]
14	−83.2 [−13.7]	−173.4 [−57.3]	−203.7 [+7.1]
18	−79.1	−170.5	−211.4

$\Delta\delta^{15}N_{imine}$ for the imidazole copper complexes were in the range of −13.7 to −21.1 ppm; significantly smaller than those observed for the pyridine complexes (−41.7 ppm for the monomer of **11**). The $\Delta\delta^{15}N_{IM}$ ranged from −52.8 to −57.3 ppm, an intermediate value between the $\Delta\delta^{15}N_{pyr}$ of the monomer and dimer of **11**.

In CD$_3$CN, the imidazole complexes **14** and **18** display temperature-dependent aggregation. At room temperature, the ^{1}H NMR spectrum of complex **14** in CD$_3$CN showed a second species (Figure 22), whereas there was only a single species in the ^{1}H NMR spectrum of **14** in d_6-DMSO, showing that the aggregation is solvent-dependent.
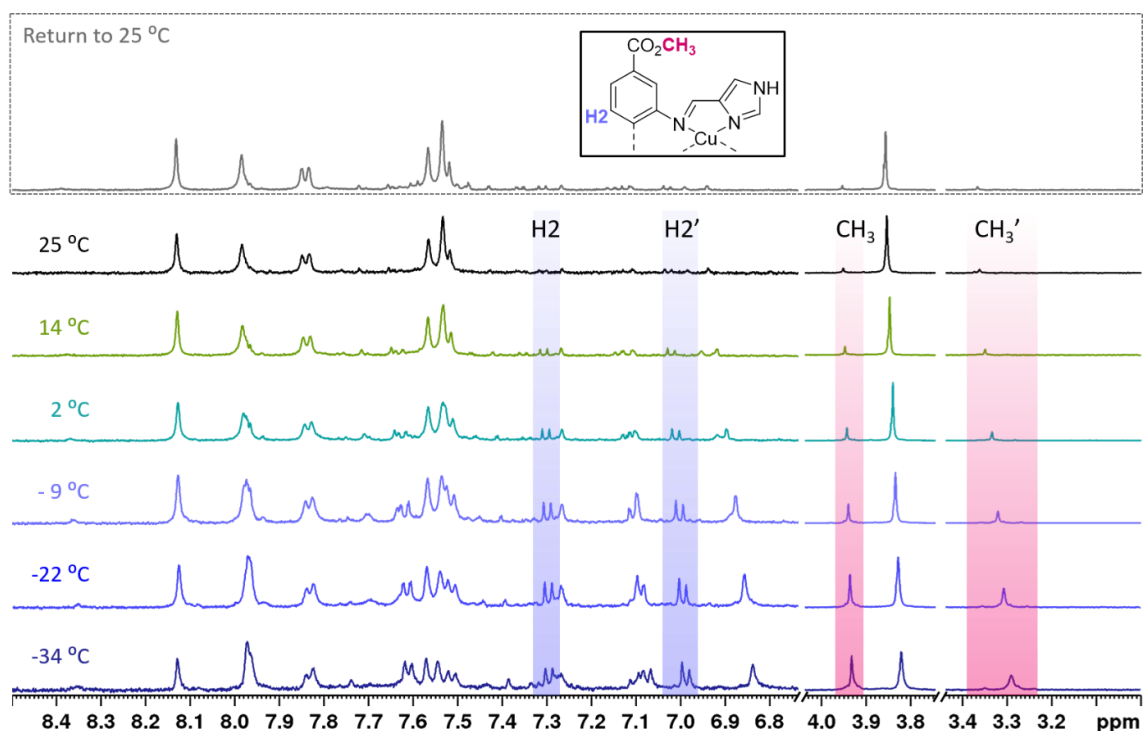
Figure 22. Selected regions of the VT ^{1}H NMR of **14** (500 MHz, CD$_3$CN).

The aggregation is different to that observed for the pyridine complexes of tetradentate ligands. The minor species has two sets of resonances, as highlighted in Figure 22 for the resonances of the methyl group and one of the phenyl ring protons. For a more detailed discussion, see Paper I.

The minor species was only observable in the VT ^{1}H NMR at temperatures $\leq$ 2 °C for **18** (Figure 23). It is unclear how exactly the ester groups influence aggregation. For the two pairs of CuL complexes presented herein (pyridine and imidazole complexes), the methyl ester substituted analogue shows a higher degree of aggregation. The DFT-assisted X-ray emission spectroscopy (XES) studies on complexes **14** and **18** conducted by Sergio Jannuzzi (Paper I) further supported the subtle, but significant influence of the methyl ester group. Both complexes showed a pair of very similar K$\beta_{2,5}$ peaks. They differed in the intensity of the second K$\beta_{2,5}$ peak, which was lower for **18** than **14**. The decrease in intensity was linked to a more open seesaw like conformation (for more details, see Paper I).
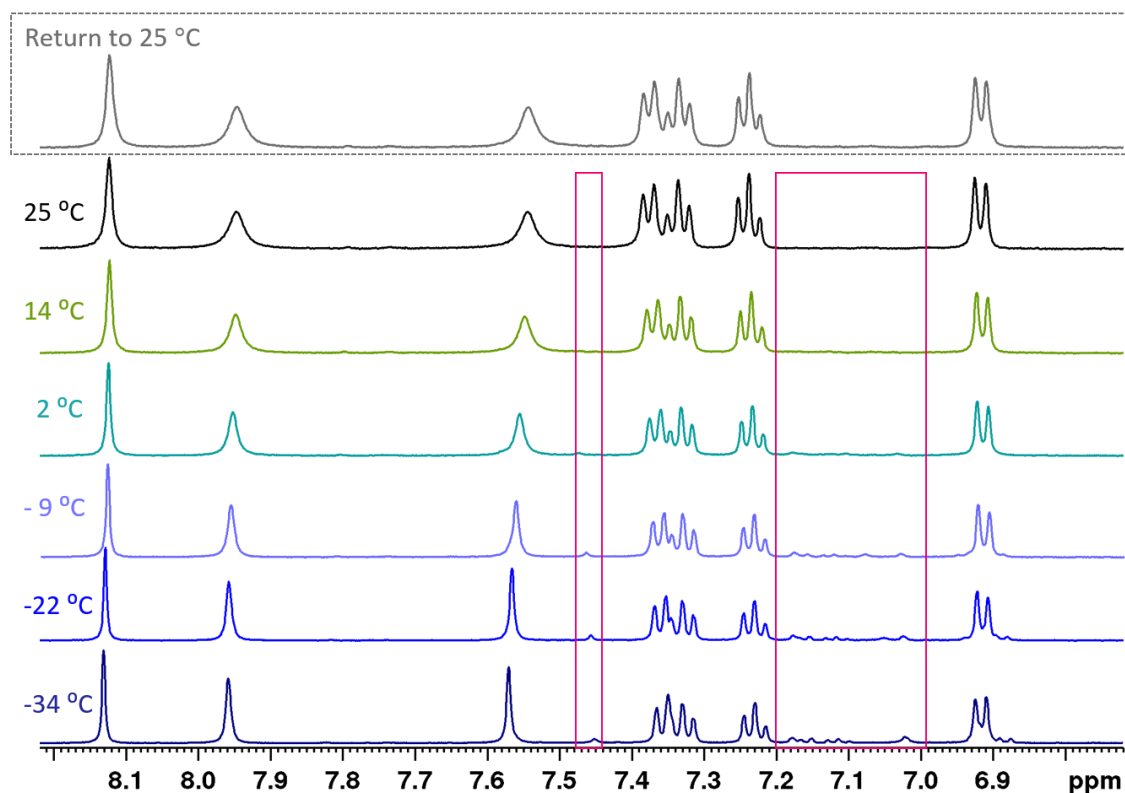
28

Figure 23. Aromatic region of the VT ^{1}H NMR of **18** (500 MHz, CD$_3$CN).

Some of the NMR methods applied to study the aggregation behaviour of **11**, DOSY and ^{15}N coordination shifts, could not be applied to **14** or **18**. The intensity of the minor species in **14** is too low at ambient temperature to obtain ^{15}N coordination shifts. Lowering the temperature would require constant monitoring of the experiment, which is challenging for multiple day measurements. A DOSY experiment of **14** in CD$_3$CN shows that the minor species diffuses slower (Figure 51 in the Appendix). However, a qualitative analysis, as presented for **11** and **13** is hampered by the lower viscosity of CD$_3$CN compared to d_6-DMSO[107] and the low intensity of the minor species. Nevertheless, it was possible to assign the resonances of the minor species of **18** based on an EXSY spectrum (Figure 24) collected at –34 °C. The chemical shifts of the resonances of both species of **18** in CD$_3$CN at -34 °C can be found in the Appendix (Table 7).

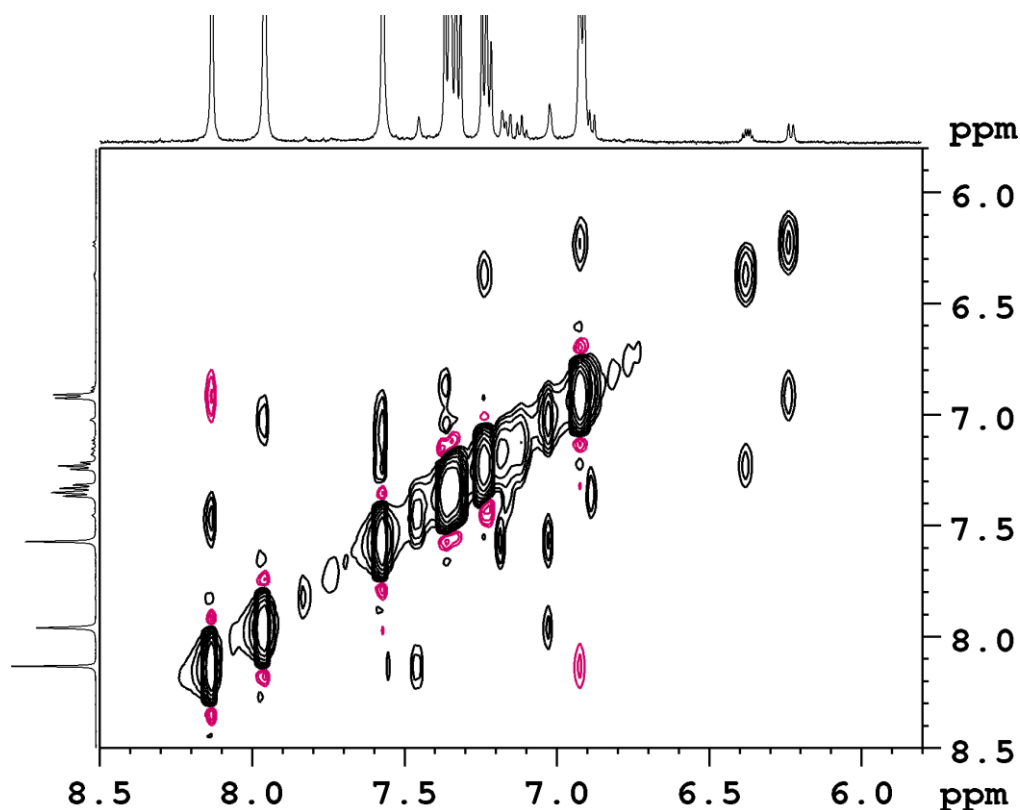Figure 24. Aromatic region of the NOESY/EXSY of **18** at −34 °C (500 MHz, CD$_3$CN). EXSY peaks are in the same phase as the diagonal. Full spectrum in the Appendix (Figure 52).

Analogously to the analysis performed for pyridine complexes above, it is possible to map the chemical shift change upon presumed dimerisation for **18** (Figure 25). It visualises that the difference in dimerisation extends further than the breakage of the magnetic inequivalence. While the dimerisation of **11** had only a pronounced effect on the backbone and the α-C**H**, the dimerisation of **18** affects the ^{1}H shifts of the whole molecule.
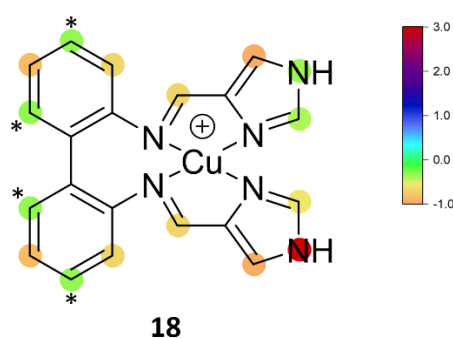

18

Figure 25. Change in chemical shift between monomer and presumed dimer of the protons in compound **18**. The shift values can be found in the Appendix, Table 7. Due to overlap, two of the phenyl protons are shown as average (marked with a star).

In the biphenyl backbone there is a stronger change in the *para* and *ortho* positions than in the *meta* positions relative to the imine. This hints towards an electronic effect induced by the imine rather than a change due to intermolecular interactions of the protons themselves, as

speculated for the pyridine complexes. While all other protons are shifted upfield, one of the imidazole N**H** protons is shifted 3.03 ppm downfield.

Ethyl ester analogue of 14

One of the limitations that were encountered with compound **14** (denominated **1** in Paper I) is its limited solubility in solvents other than DMSO. While the copper(II) analogue **16** (denominated **1b** in Paper I) readily dissolves in acetonitrile, the copper(I) compounds solubility in acetonitrile is strongly limited. The NMR sample of **14** was saturated already at low concentrations (ca. 0.5 mg in 0.5 mL MeCN). This motivated the synthesis of an analogue with a longer aliphatic chain. The ethyl ester analogue **17** was readily obtained from diethyl 2,2'-diaminobiphenyl-4,4'-dicarboxylate (compound gifted by Knut Hylland, the procedure can be found in reference 80) following the general procedure for the tetradentate complexes. The product was obtained in 98 % yield, foreshadowing poor solubility in acetonitrile. The change from methyl to ethyl group had very little effect on the NMR shifts of the compound. The synthesis procedure, elemental analysis, HRMS and ^{1}H and ^{13}C NMR spectra can be found in the Appendix.

Secondary amine analogue of 15

The comparison of complexes **8** and **10** showed a significant difference between imine and amine in the coordination to copper. Ligand **20** was obtained by direct reductive amination of dimethyl 2,2'-diaminobiphenyl-4,4'-dicarboxylate with 1*H*-imidazole-4-carbaldehyde. The procedure and characterisation of **20** (HRMS, ^{1}H and ^{13}C NMR spectroscopy) can be found in the Appendix.
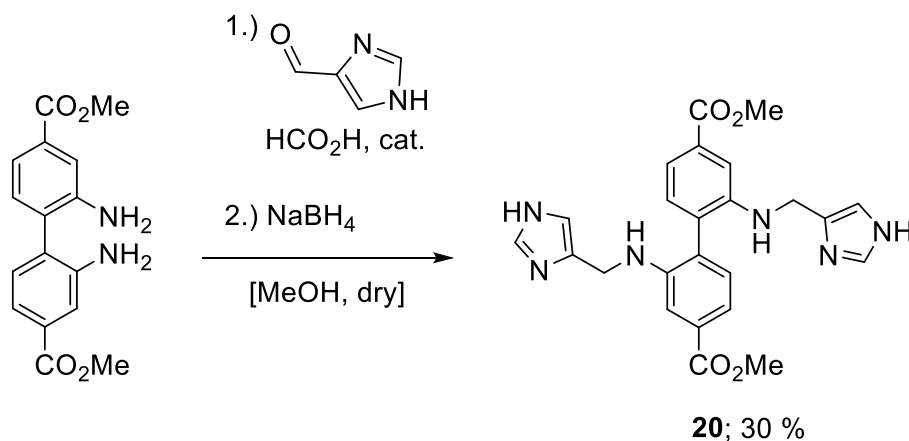
Scheme 7. Synthesis of **20** through reduction of the *in situ* generated **15**.

A Janus-Faced Reaction

Instead of the Schiff base formation discussed at the beginning of this chapter, the condensation of an aldehyde and a diamine can result in the formation of a diazepine. When 6-bromo-2-pyridinecarbaldehyde and 2-thiazolecarbaldehyde were employed in the one-pot synthesis route reported in Paper I, the dibenzo[*d,f*]-1,2-dihydro-[1,3]diazepines depicted in Figure 26 were formed instead of the targeted copper complexes.
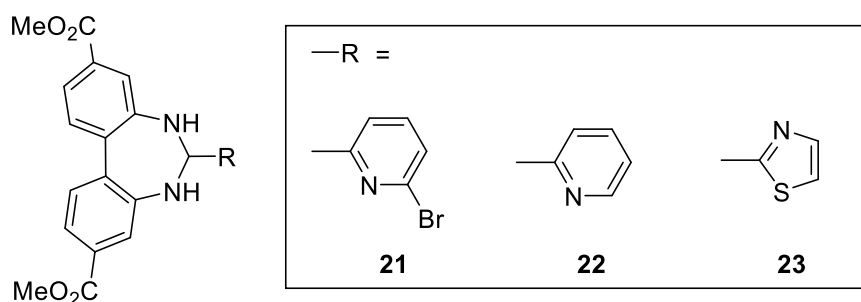

Figure 26: Dibenzo[*d,f*]-1,2-dihydro-[1,3]diazepines that formed while attempting to obtain the diimine complex.

This type of cyclisation is a well-established reaction.[108] While limiting the scope of the one-pot synthesis presented above, it creates intriguing compounds in their own rights, which, along with other, similar compounds, are discussed in Paper III. The work in Paper III was performed in collaboration with Rafael Cortez Sgroi Pupo, who at the time of writing is a Master student in our group and is co-supervised by this thesis author.

The selectivity for benzodiazepine *vs*. diamine was affected by the presence of a Lewis acid. Some aldehydes formed different products depending on the reagent used for the condensation (Scheme 8). When a commercial supplier erroneously delivered ScOTf$_3$ instead of CuOTf, some of the syntheses reported in Paper I yielded the diazepine instead. Furthermore, the addition of Zn(OAc)$_2$·2H$_2$O could either promote or inhibit the formation of dibenzodiazepines, depending on the aldehyde in question (see Paper II). These results may hint at the involvement in multiple reaction steps, but further research is necessary to elucidate the role of the metal salt.
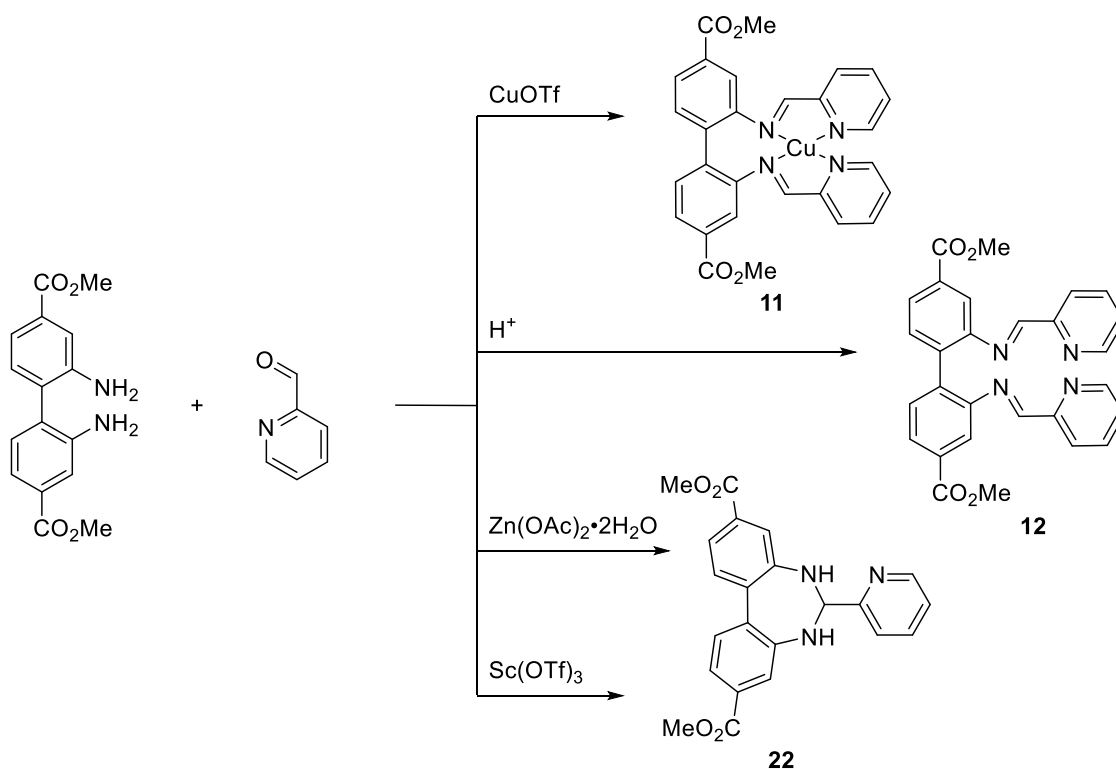
Scheme 8. Different reaction outcomes for the condensation of 2-pyridinealdehyde with dimethyl 2,2'-diaminobiphenyl-4,4'-dicarboxylate.

The reaction of dimethyl 2,2'-diaminobiphenyl-4,4'-dicarboxylate with two equivalents of 2-thiazolecarbaldehyde and one equivalent of CuI was found to give compound **23** by MS (Scheme 9).
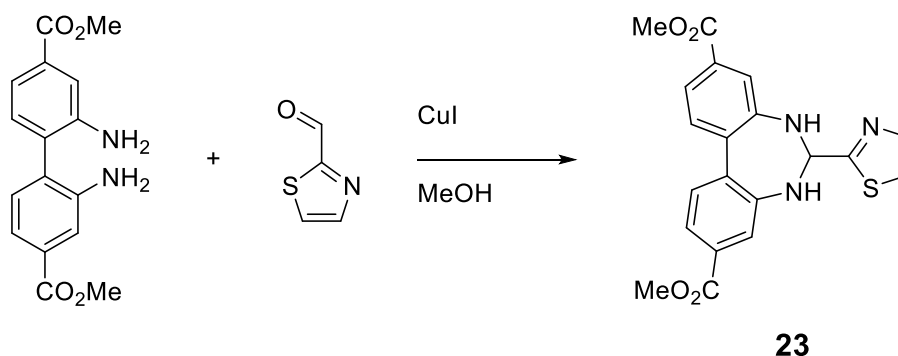
Scheme 9. Synthesis of **23**.

Recrystallization of the crude product from acetonitrile yielded single crystals suitable for single crystal X-Ray diffraction. The structure was found to be copper complex **24** (Figure 27). Compound **23** acts as a ligand for copper by coordination through the thiazole nitrogen. The tetrahedral coordination environment around copper is completed by two acetonitrile molecules and two bridging iodides, creating a dimeric structure. When the reaction was instead performed with Zn(OAc)$_2$·2H$_2$O, ^{1}H NMR and elemental analysis showed that the salt was not retained by the diazepine (see Paper II).
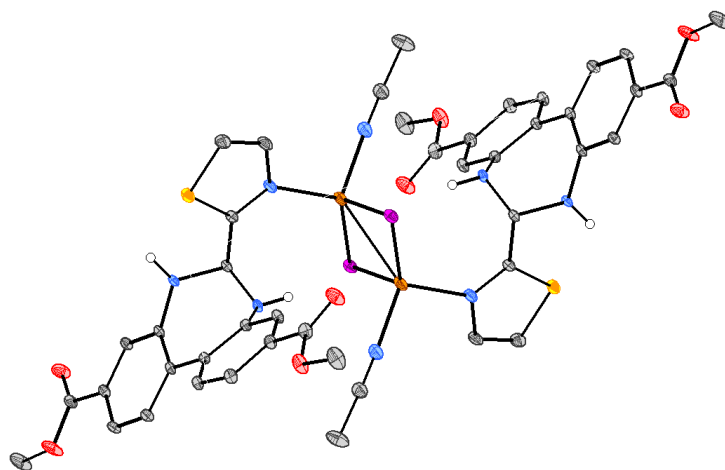
Figure 27. Single Crystal XRD structure of compound **24**. The hydrogen atoms (with exception of the NH) and the non-coordinating acetonitrile are removed for clarity. The Cu–Cu distance is 2.8281(4) Å.

Comparison to literature structures

In addition to the structure of **24**, a crystal structure of **21** was obtained (Figure 28).
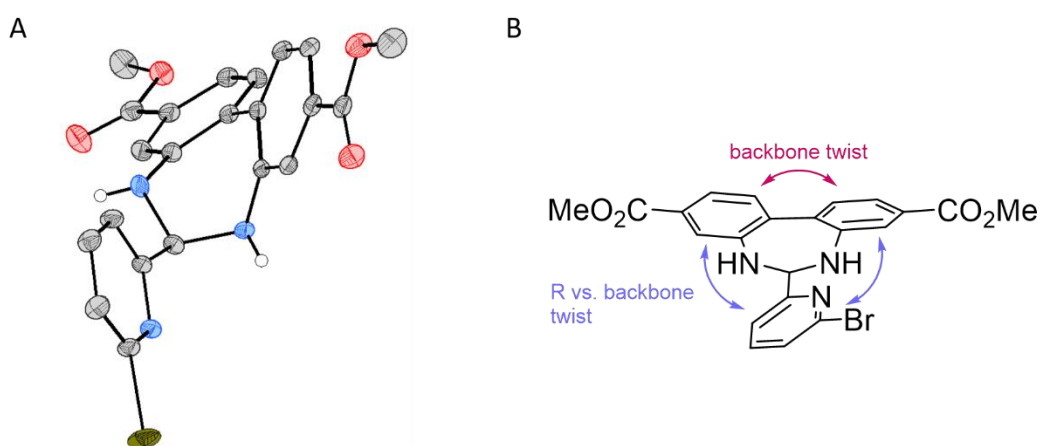
Figure 28. A: Single Crystal XRD structure of compound **21**. The hydrogen atoms (with exception of the NH) are removed for clarity. B: Angles between aromatic rings discussed below.

The angles between the planes of the three aromatic rings in the structures were compared to those reported by Tomar *et al.*[109] Their structures are fully unsaturated dibenzo-[*d,f*][1,3]-diazepines, which are structurally different to the dibenzo[*d,f*]-1,2-dihydro-[1,3]-diazepines investigated in this work (Figure 29).
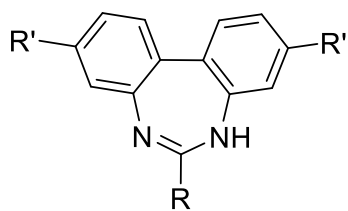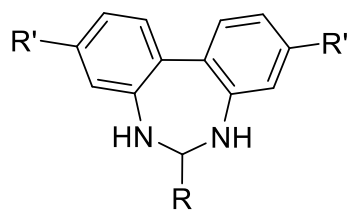
dibenzo[*d*,*f*][1,3]diazepine   dibenzo[*d*,*f*]-1,2-dihydro-[1,3]diazepine

Figure 29. Dibenzo[*d,f*][1,3]-diazepines are reported in literature either in the fully unsaturated form[109–111] (left) or the dihydro analogue[111,112] (right), depending on the conditions during synthesis and work-up.

Unsubstituted biphenyls are planar in solid state, but have a torsion angle of 44° in gas phase, resulting from many-atom interactions.[113] The torsion angle is increasing with the size of substituent on *diortho*-substituted biphenyls.[114] The imine-type nitrogen in the fully unsaturated structures allows to extend the aromatic system from the backbone towards the aromatic ring attached to the benzodiazepine. This is not possible in the dihydro analogue due to the lack of bridging sp^2-hybridised atoms. This distinction is reflected in the angles between the three aromatic rings (two substituted phenyl rings and the rest R attached *via* the benzodiazepine (Table 4). The structures found in this thesis work have a backbone twist of 29° and 40°. All structures reported by Tomar *et al.* also fall within this regime. Therefore, the biphenyl backbone twist seems to originate from steric restraints between the 2- and the 2'-substituents, independently of the saturation of the diazepine. In contrast, the angles between the aromatic substituent and the phenyl rings strongly differ between the two systems. For the dihydro diazepines studied in this thesis work, the aromatic ring is closer to an orthogonal than a planar relation to the backbone (angles between 53−82°). Meanwhile, the angles in Tomar *et al.*'s structures indicate an aromatic system spanning from one backbone phenyl ring to the substituent R (which is also a phenyl ring in their structures). The smaller angle (2−12°) is always found towards the ring in the biphenyl that is bridged through the imine-type nitrogen. It is natural that the other angle resembles the backbone twist with small deviations owed to an additional bend.

Table 4. Angles between the planes created by the aromatic rings in benzodiazepines. The angle between the phenyl rings in the backbone is denoted 'backbone twist'. The angles between the aromatic rest R (see Figure 26) and the phenyl rings in the backbone are given in increasing order.

Structure (CCDC number for literature structures)	Backbone twist	R *vs.* backbone
21	40°	53°/ 76°
24	29°	67°/ 82°
927528*	31°	2°/ 32°
927529*	34°	4°/ 31°
927530*	36°	12°/ 26°
927531*	38°	9°/ 30°

* Tomar *et al., reference 109*

Concluding Remarks

Concluding, a synthesis route for tetracoordinated Schiff base complexes was developed. It yielded the targeted imidazole- and pyridine-bearing copper complexes. The resulting complexes showed aggregation behaviour, which was studied by NMR and UV/Vis. The synthetic route has limited scope due to the formation of dibenzodiazepines as a side product.

Copper Complexes of Pentadentate Ligands

Paper IV describes the synthesis of a series of Schiff Base metal complexes, where the metal has the oxidation state +II or +III. The contribution of this thesis' author to Paper IV is limited to the copper complexes, and was performed in collaboration with the main author, Knut Hylland. Two salen-type copper complexes were synthesised and characterised. They are not closely related to the other Schiff base copper complexes presented in this work. For one, they were not inspired by the histidine copper brace and do not bear imidazoles. The study also focuses on copper(II), as pentacoordination is less common for copper(I).[2] Lastly, the ligand backbone is larger and bent, making it less suitable for incorporation into UiO-67 or similarly structured MOFs. Nevertheless, this chapter highlights aspects of copper Schiff base complex chemistry that are of interest for the scientific question that this thesis aims to answer. Copper-salen complexes have been employed as biomimics for a series of enzymes that catalyse interconversion of H_2O_2, H_2O and O_2.[76] H_2O_2 has been identified as crucial to LPMO activity,[115] making it of interest to have moieties generating it from O_2.

The nitrosubstituted ligand (see Scheme 10, called **1b** in the Paper IV)) has the potential to be hexadentate with three imine nitrogens and three phenolic oxygens. The reactivity of this ligand towards different metal salts were investigated (see Paper IV for details). The hexadentate ligation was only observed for the large Lu(III) cation. Zn(II) and Cd(II) had hydrolysed one of the imine bonds to generate pentacoordinated complexes. The ligand's metalation with $Cu(OAc)_2$ however yielded a mixture of the hydrolysed pentacoordinate copper complex (**25**) and a copper complex where the remaining imine is intact, but presumably not coordinated (**26**) (see Scheme 10).
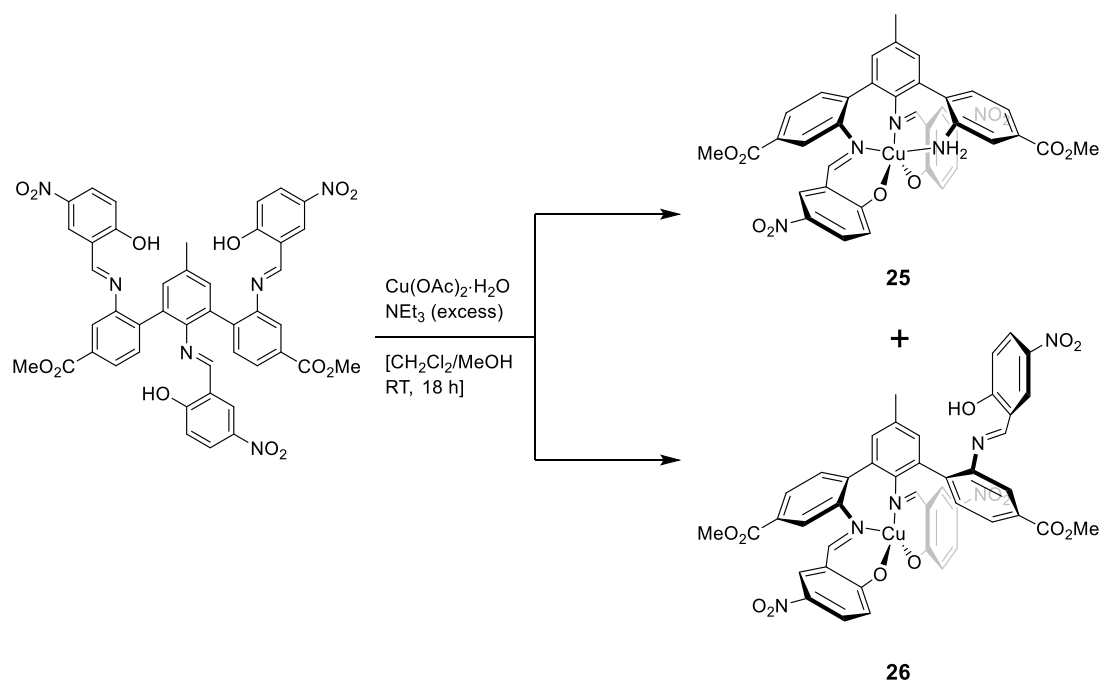
Scheme 10. Product mixture obtained from the metalation of the potentially hexadentate Schiff-Base ligand.

Crystallisation attempts were fruitless with respect to bulk purification. However, a crystal of **25** suitable for single crystal XRD (Figure 30, the structure will be discussed below) was obtained.
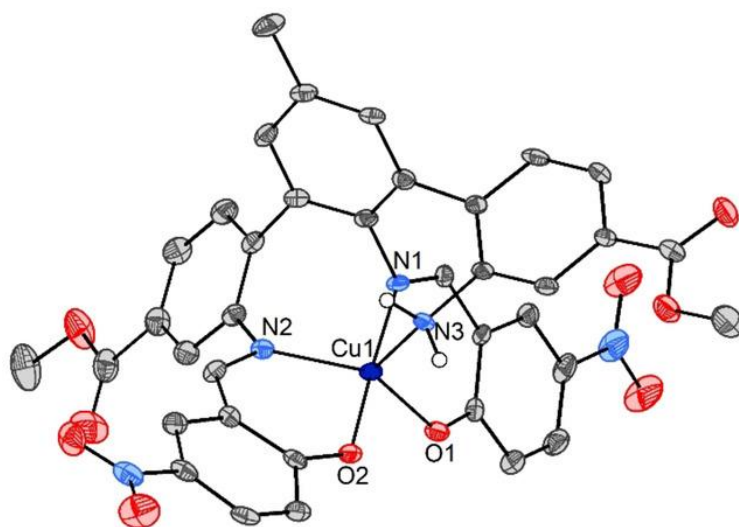

Figure 30. Single crystal XRD structure of **25**. Coordination bond lengths [Å]: Cu1–N1, 1.933(3); Cu1–N2, 2.041(3); Cu1–N3, 2.299(3); Cu1–O1, 1.986(2); Cu1–O2, 1.903(2).

This result was encouraging for potential applications, as amino groups have been identified as a key feature in transition metal complex catalysed CO_2 conversion.[116] The synthetic value of a procedure that yields a mixture is rather limited, therefore an alternative synthesis route was sought out. Earlier in this chapter, the one-pot approach was crucial for the synthesis of **8** (see section about tridentate ligands) and improved the yield of complex **14** significantly (see section about tetradentate ligands), likely due to the stabilisation of the imine. In the hope that the presence of copper would favour the formation of the diimine over the triimine, the synthetic procedure was adapted to the salen-type ligand (Scheme 11).
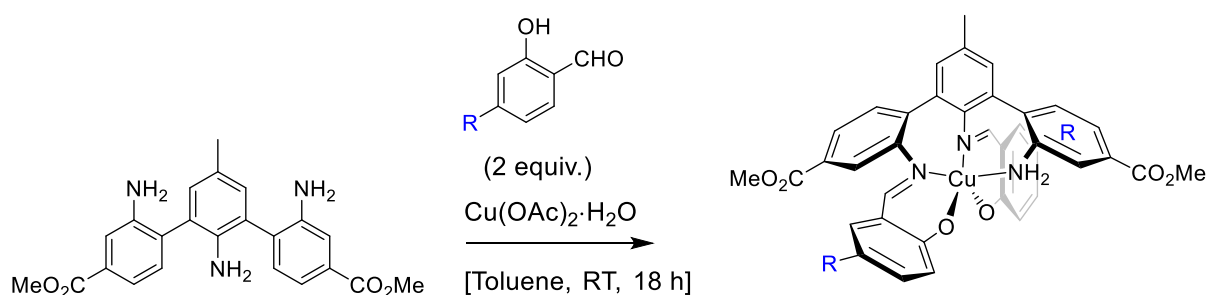
25: R = NO_2; 84 %
27: R = H; 71 %

Scheme 11. One-pot route that selectively yields amino-coordinated products **25** and **27**.

The approach proved successful, and only the pentacoordinated complex **25** was obtained. The potential redox catalyst application created an incentive to synthesise an analogue without nitro groups, as nitro groups can be redox-active themselves.[117] The procedure was

therefore extended to the unsubstituted salicylaldehyde, and the desired product was obtained. The slightly lower yield can be attributed to the work-up, a filtration. Complex **27** shows moderate solubility in toluene, while **25** is poorly soluble in toluene. Both copper complexes were analysed by UV/Vis, elemental analysis and HRMS, confirming identity and bulk purity. Recrystallisation of **27** from ethanol gave single crystals suitable for single crystal X-Ray diffraction (Figure 31).
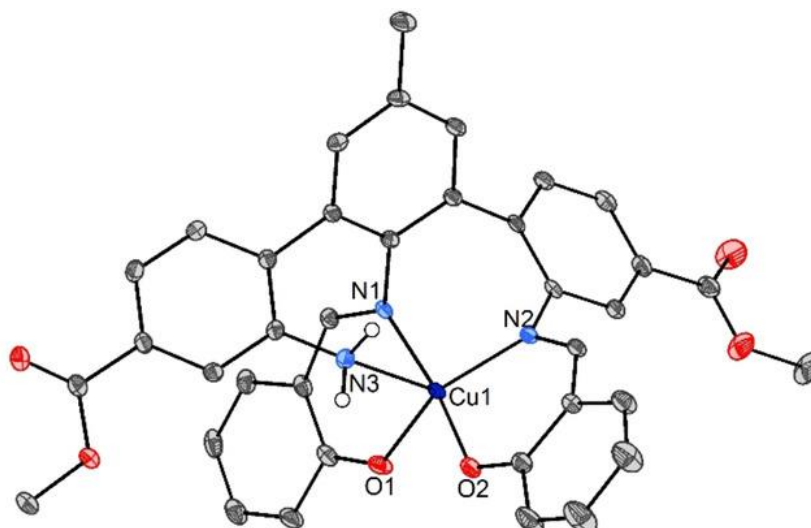

Figure 31. Single crystal XRD structure of **27**. Coordination bond lengths [Å]: Cu1–N1, 1.9618(15); Cu1–N2, 1.9818(14); Cu1–N3, 2.4795(15); Cu1–O1, 1.9154(13); Cu1–O2, 1.9205(13).

The change in substitution pattern on the phenol had a pronounced effect on the coordination to copper. The whole geometry is affected, best seen through the structures' τ_5 values (see Figure 32). For the nitro-substituted **25**, a distorted trigonal bipyramidal geometry was found (τ_5= 0.70). Intriguingly, the analogous Zn(II) complex (also reported in Paper IV) was found to have a distorted square pyramidal geometry (τ_5= 0.33). The unsubstituted **27** was found to have a geometry closer to square pyramidal (τ_5= 0.25). The Cu–N_{amino} bond lengths are 2.30 Å (**25**) and 2.48 Å (**27**), substantially longer than typical Cu(II)–NH_2 bond distances (ca. 2.0 Å).[118] The nitro-substituted zinc(II) complex had a Zn–N_{amino} bond length of 2.18 Å. The comparison of the bond lengths is difficult, due to the different geometries. Despite the similar geometry indices of **27** and the Zn-complex, they are different structures: the amine is found in the apical position in the copper complex, while it occupies a basal position in the zinc complex.

25   **27**

$\tau_5 = 0.70$ $\tau_5 = 0.25$
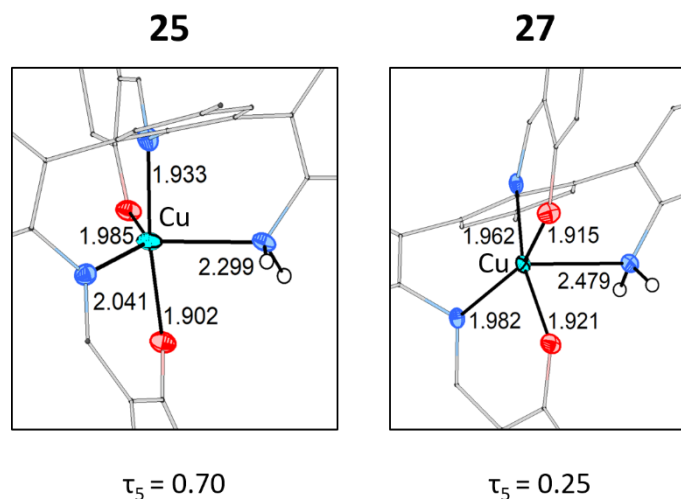
Figure 32. Comparison of the coordination geometry in the nitro-substituted and the unsubstituted pentacoordinate complex.

In addition to the crystallographic investigation of the coordination centre, UV/Vis spectra of the copper complexes were recorded. The d-d transition of **25** and **27** resemble each other strongly, in intensity, peak shape and energy (the d-d transition of the nitro-substituted **25** is blueshifted by 10 nm, see inlet in Figure 33).

Figure 33. UV/Vis spectrum of **25** and **27**.

Contrary to that, the spectra of the complexes differ in the MLCT (metal to ligand charge transfer) region. The band is much more intense for the nitro-substituted complex and shifted to higher energies (blue shift of 34 nm).

40

Incorporation of Copper Complexes into the Metal Organic Framework UiO-67
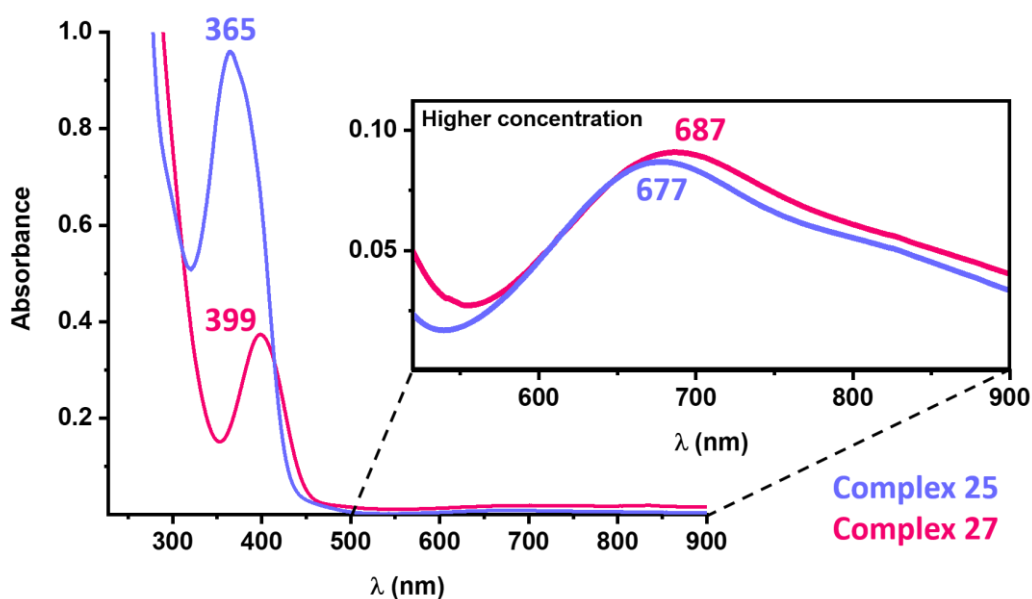
Incorporation of Complex 16

The majority of ligands discussed in this thesis bears ester groups on the biphenyl backbone. Therefore, they are functionalized analogues of bpdc (biphenyl-4,4-dicarboxylic acid), the linker in UiO-67,[55] a Zr-MOF developed at the University of Oslo. The ester moieties have two functions, they improve solubility and protect the acid functionality from unwanted reactivity during synthesis.

In a previous PhD project at the catalysis section at UiO, a synthesis of diamino functionalized UiO-67 was developed.[119] Starting from this material, the incorporation of the tetracoordinated copper(II) complex **16** is only a matter of adapting the synthetic protocol utilised in the one-pot synthesis of the molecular complex (Scheme 12). The synthesis is sensitive to the anion, as an attempt with CuCl$_2$ (instead of Cu(OTf)$_2$) as the copper source resulted in the formation of CuCl$_2$ crystals depositing on the MOF structure. As discussed in Paper I, the PSLM strategy is favourable for compounds with imine functionality, as the rather harsh, acidic conditions during MOF synthesis would most likely hydrolyse the imine bond during PMLS. Exchanging the linker after MOF synthesis with the copper complex is likely to result in copper complex incorporation. However, there is a risk that the aggregation behaviour that was the central aspect in Paper I might interfere with obtaining a well-defined single-site heterogeneous catalyst.
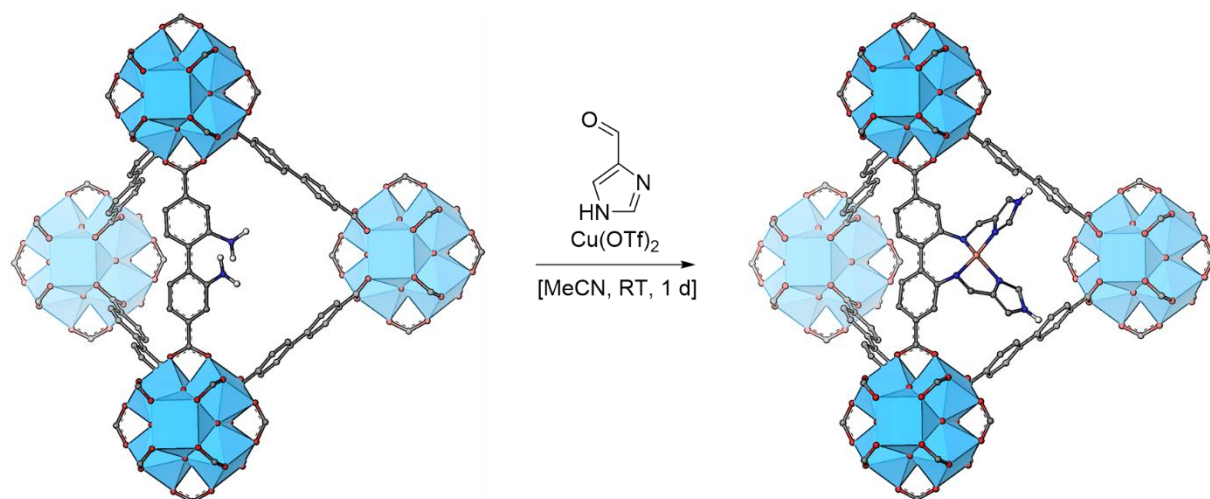
Scheme 12. Post-synthetic linker modification of UiO-67-(NH$_2$)$_2$-10%, resulting in the incorporation of **16** into a metal organic framework. The triflate anions are retained (fluorine detected by elemental mapping of the MOF), but omitted for clarity. The schematic illustrations in Materials Studio are a kind gift from Erlend Aunan.

It remains a challenge to unambiguously characterise the structures inside the MOF, but in this case the experimental data strongly suggests that the structure on the right side of Scheme 12 is indeed representative of the cation incorporated into the MOF. The UV/Vis data shows a broad d-d transition band at 670 nm for both, MOF and molecular material, giving

rise to a green colour (see Figure 13 in Paper I). 1H-imidazole-4-carbaldehyde forms a blue complex with Cu(OTf)$_2$, which is removed during the washing steps in the synthesis. Therefore, the UV/Vis data corroborates the formation of the Schiff base complex inside the metal organic framework. Further support for the suggested structure stems from ^{1}H NMR of the digested sample. The complex is not detected, but its hydrolysis products, bpdc linker, diamine linker and aldehyde. The ratio between bpdc linker and diamine linker is in very good agreement with the Zr:Cu ratio found by elemental analysis, suggesting that the copper incorporation is proportional to the diamine functionalisation (see SI of Paper I).

Attempted Covalent PSLM of UiO-67 with Incorporated 7

In light of the encouraging results obtained for the incorporation of the Schiff base complex in Paper I, a similar approach was tempted for the Schiff base complex **8** discussed in Paper II. The first step was to synthesise the diacid *via* hydrolysis of the ester **7** (Scheme 13). The diacid **28** was analysed by ^{1}H and ^{13}C NMR spectroscopy, as well as HRMS (the procedure and the characterisation can be found in the Appendix).
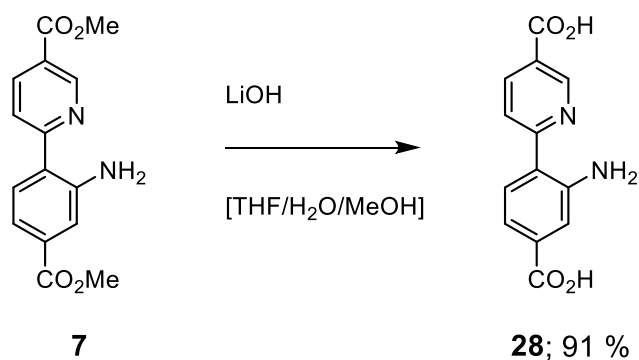
Scheme 13. Hydrolysis of the amine **7** to diacid **28**.

A MOF with a fraction of **28** as linker was synthesised by Erlend Aunan. The characterisation of UiO-67-**28** by TGA and ^{1}H NMR spectroscopy (of the digested MOF) suggested a ratio of linker **28** to the [Zr$_6$O$_4$(OH)$_4$] cluster of 1:1.2. Post-synthetic linker modification of UiO-67-**28** with an adaptation of the procedure developed in Paper I was attempted (Scheme 14).
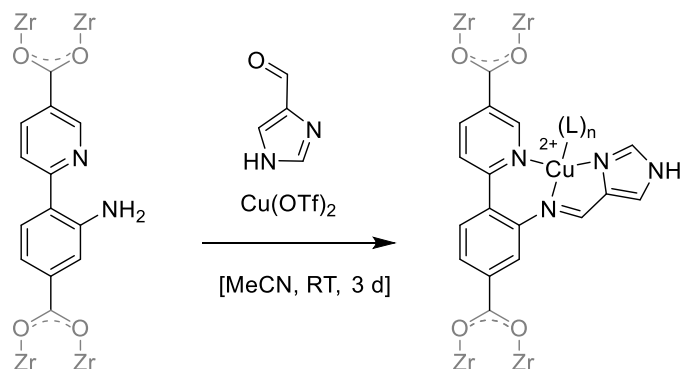
Scheme 14. Attempted PSLM of UiO-**28**.

The reaction time was extended to three days, analogously to the reaction time for the synthesis of the molecular complex **8**. MP-AES was performed by Erlend Aunan and showed a very low copper loading (Cu/Zr$_6$ = 0.075 $\pm$ 0.003). This is much lower than expected from the amount of incorporated **28**. Therefore, it can be concluded that an imine copper complex has either only formed in trace amounts or failed to form. It is reasonable to speculate that the pyridine deactivates the amine for the Schiff base formation compared to the phenyl ring. The free ligand of **8** was not obtained through common protocols for Schiff base formation, and the reaction time for copper complex **8** was significantly longer than for complex **1** (the biphenyl analogue). Another issue might be masking of the amine functionality through formylation of the amine during synthesis of UiO-67-**28**. Formylation can arise from decomposing DMF during synthesis of amino-functionalized MOFs.[120] Nevertheless, the approach may be valid for more reactive aldehydes than 1*H*-imidazole-4-carbaldehyde.

Incorporation of 9

The incorporation of the tridentate ligand **9** into UiO-67 and metalation of the incorporated ligand are discussed in Paper II. The MOF synthesis, modification and characterisation were performed by Erlend Aunan and can be found in Paper II and its SI. The ligand's multi-step synthesis is not achievable inside a framework. Therefore, the free acid **29** was synthesised from **9**. The synthetic procedure is adapted from that reported by Ko *et al.* for 2,2' diaminobiphenyl 4,4'dicarboxylic acid, the linker for UiO-67-(NH$_2$)$_2$.[71] The free base could not be obtained, presumably due to the four nitrogen moieties, which are expected to cover a range of pK$_a$s and pK$_b$s, favouring zwitterions. Instead, the chloride salt was obtained, as evidenced by elemental analysis and the ^{1}H NMR spectrum that features two imidazole protons (SI of Paper II). As the salt is well soluble in water, the procedure had to be modified, as to wash the product with acetone instead of water.
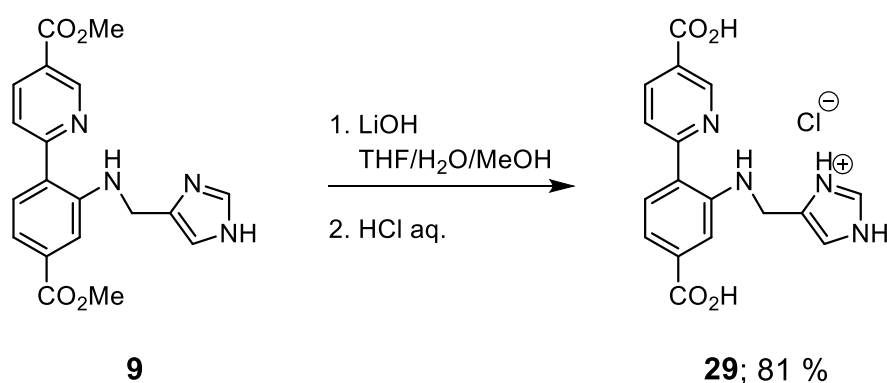
Scheme 15. Ester hydrolysis of **9** yields the corresponding diacid **29**, a suitable linker for the UiO-67 metal organic framework.

In Paper II, the reversible change in hydration of UiO-67-**29** is discussed. The temperature-induced dehydration was not observed for the molecular complexes. Given a suitable order of synthetic steps (synthesis of the ligand, ligand incorporation and lastly, metalation), the incorporation into a framework offers access to coordination environments that are inaccessible for molecular complexes.

Reactivity of Molecular Complexes
UV/Vis Studies of the Oxidation of Complexes in Solution upon Exposure to Air

Preliminary UV/Vis experiments on the oxidation on air of the complexes from Paper I in acetonitrile were performed in collaboration with Chiara Negri. The complexes' UV/Vis spectra were monitored over time. Only the tetradentate imidazole complexes **14** and **18** oxidised upon exposure to air. Complex **18** oxidised more rapidly but monitoring and quantification of its oxidation were hampered by poor solubility and the formation of insoluble components over time. Therefore, the discussion will focus on the oxidation behaviour of **14**, where concentrations up to 1.5 mM were attainable.

Due to the intensity difference between MLCT and d-d bands, the spectra had to be recorded at two different concentrations to obtain information on both. As the concentration-dependence (see below) was of interest, the dilute solution was prepared from the concentrated one immediately before the measurement. All samples were measured in parallel and stored together in order to obtain as comparable conditions as possible.
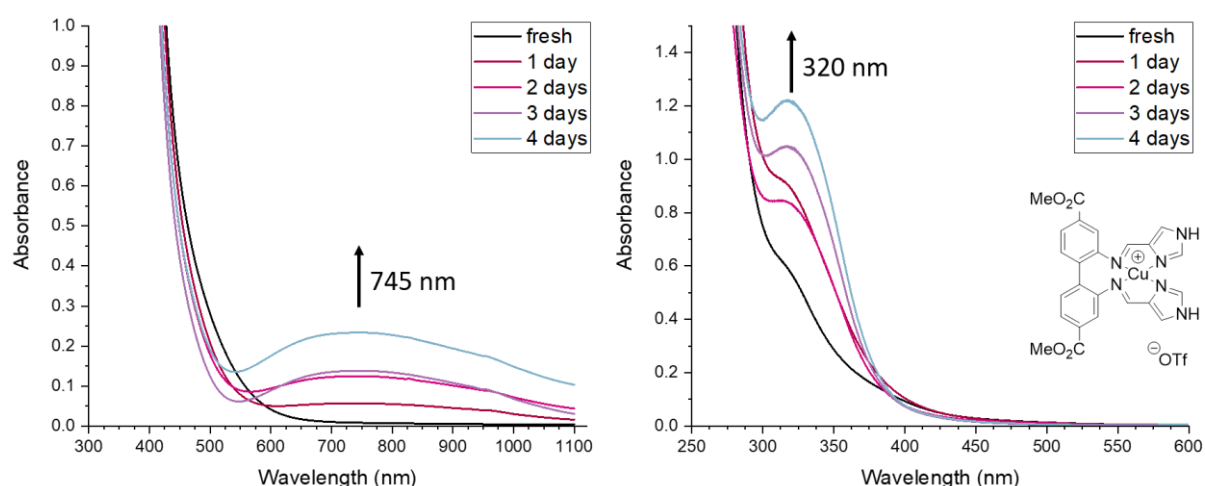

Figure 34. UV/Vis spectra of the oxidation on air of compound **14** in a 1.5 mM acetonitrile solution over time. Left: Evolution of the d-d band over time. Right. Dilution 1:30.

The change in oxidation state from copper(I) to copper(II) can be followed through the build-up of a band originating from the d-d transition that is only possible in the cupric d^9 configuration. The maximum of the d-d band (λ_{d-d}) is found at 745 nm (Figure 34, left side). This represents a red-shift compared to the d-d band of complex **16**, which is synthesised directly from copper(II) triflate (λ_{d-d} = 670 nm, Figure 13 in Paper I). The shift may indicate the presence of an additional ligand.[121]

Additionally, a shoulder appeared around 320 nm (Figure 34, right side). The intensity of the shoulder does not consistently in- or decrease over time. Overall, the shoulder seems to

increase over time but its intensity is lower on day two than on day three. As it becomes more defined with each day, it is likely that the shoulder's absolute intensity is the result of overlap with other, more intense bands in the UV region that also changed over time.

Intriguingly, the progression of the oxidation did not seem to follow a clear regime over time. Little difference is observed between two and three days in Figure 35, while the time intervals between 24 h to 48 h and from 72 h to 96 h see a strong increase in absorbance at λ_{d-d}. These findings need further investigation and repetition, but as the behaviour is observed in five different, independent samples that were measured in parallel, it seems not to be an experimental error (the UV/Vis spectra of **14** at other concentrations can be found in the Appendix). Therefore, it can be speculated that an external stimulus, which was not constant over time, is necessary for oxidation. A possible stimulus could be light.[122,123]
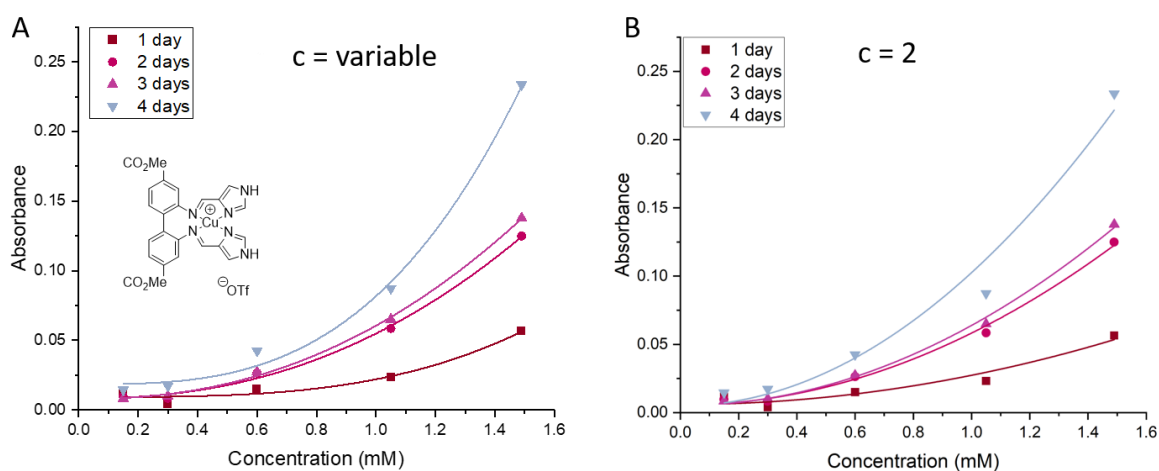

Figure 35. Evolution of the absorbance at the d-d band as a function of the concentration of complex **14** at different time intervals after air exposure (symbols: experimental data, lines: least square fits following equation 5). A: fitted with variable reaction order c, for fit parameters see Table 8 in the Appendix. B: fitted with reaction order c of 2, for fit parameters see Table 9.

Under the assumption that processes other than oxidation are negligible, each copper(I) complex forms one copper(II) complex (equation 4). Thereby, the d-d transition should be a sensitive tool to detect the kinetics of the oxidation. If the oxidation were to take place between a single complex and an oxygen molecule, the absorption at λ_{d-d} linearly depends on the starting concentration. However, the absorption at λ_{d-d} increases more than linearly with the concentration of **14**. Fitting of the absorbance at λ_{d-d} across the samples of different concentrations after the same time interval t with equation 5 gave values of c ≥ 2 (Figure 35A, the fitting parameters are listed in Table 8 in the Appendix). The amount of copper(II) formed in a given time interval is equal to the amount of copper(I) consumed in the same time interval. The rate of copper(II) formation should be proportional to the concentration of copper(I) to the power of the reaction order c with respect to copper(I), yielding equation 6.[124]

$$c * \text{Cu}^{\text{I}} + n * \text{O}_2 \rightarrow c * \text{Cu}^{\text{II}} \qquad\qquad 4$$

$$y = a + bx^c \qquad\qquad 5$$

$$\frac{[\text{Cu}^{\text{II}}]}{dt} = -\frac{[\text{Cu}^{\text{I}}]}{dt} = k[\text{Cu}^{\text{I}}]^c \qquad\qquad 6$$

$$Absorbance(\lambda_{d-d}) * E = k * [Cu^I]^c \qquad\qquad 7$$

The absorbance at $\lambda_{d\text{-}d}$ is proportional to the concentration of copper(II). Equation 6 can thus be rewritten to equation 7, with the constant E containing both, the molar extinction coefficient of the d-d transition and the time interval.

While this data is preliminary and the irregularities in the time-dependency merit further investigation, it seems likely that a dinuclear copper complex is involved in the reaction with oxygen. The data was fitted again with *c* fixed to two (Figure 35B) to validate a reaction order of two. The resulting fits are reasonable, supporting the hypothesis. The worse fit quality compared to the fit with variable *c* is expected, as two instead of three parameters were employed.

In literature, CuL_2 complexes with bulk around the coordination centre have been associated with inertia towards oxygen.[125] No oxidation was observed for the tetracoordinated CuL_2 complexes **3** and **5** (see Appendix Figure 57 and Figure 58). In contrast, solutions of **10** oxidise readily in air (see Paper II). Unlike the encumbered 4-fold coordination found in **3** and **5**, **10** shows a linear coordination environment around copper. Therefore, it is likely that copper is more accessible to O_2 in this CuL_2 complex.

Catalytic Testing of Compounds 10, 14, and 16 for Cyclohexane Oxidation with H₂O₂

The compounds synthesised in the thesis work presented herein are intended as catalysts for aliphatic C–H bond oxidation. Initial tests with **14** as catalysts for cyclohexane oxidation were done following the protocol established by Kirillov *et al*.[9] (see Introduction). Two pitfalls were encountered with the procedure that had to be overcome. For one, the work-up procedure did not yield two phases, as MeCN (reaction solvent) and Et₂O (extraction solvent) are miscible. However, the procedure requires phase separation for the subsequent analysis. The work-up was revised and a suitable work-up was found by Sander Guttorm, who did his bachelor thesis in the spring semester of 2021 in our group. The Bachelor thesis was co-supervised by this thesis author.

His criteria for evaluating the work-up were that the copper compound had to be separated from the reaction mixture without altering the analyte ratio (analysed by GC-MS). A liquid-liquid extraction failed due to the different partitions of the different analytes. After screening a series of systems for solid phase extraction, he found the following method to be suitable:
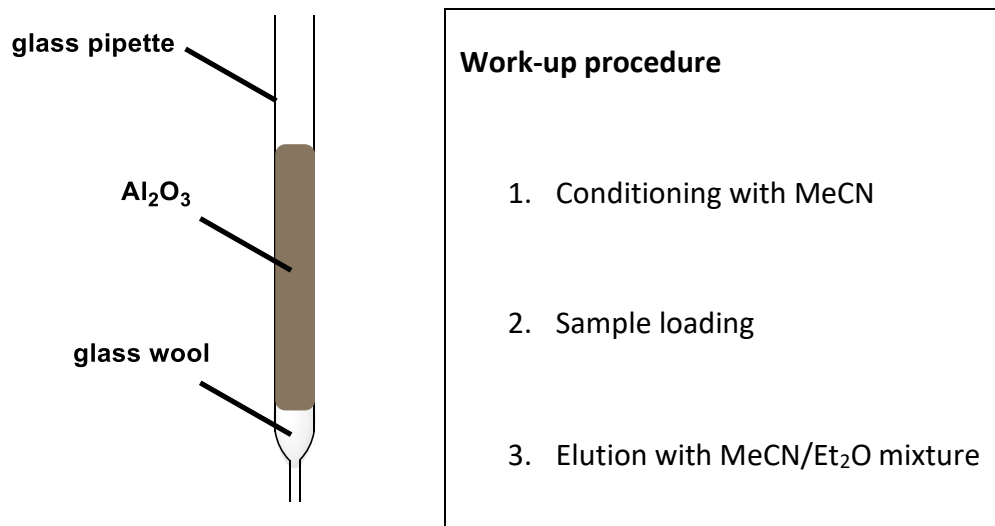
Figure 36. Solid phase extraction to work up the homogeneous catalytic testing reaction mixture for GC-MS analysis, as developed by Sander Guttorm.

The second adaptation was made to the procedure after realising that the TON of the compound and the salt alone were very similar. Kirillov *et al*. use HNO_3 as a cocatalyst. Compound **14** bears two imine groups that are likely to be hydrolysed in the presence of an acid. Therefore, the catalytic testing was performed without the addition of acid as a co-catalyst.

All tests with the adjusted protocol were preliminary and demand further validation with replicas. Nevertheless, the preliminary testing shows a significantly higher conversion for the copper(I) complexes, **10** and **14**, than for the copper(I) salt they are synthesised from. In contrast, the activity of copper(II) complex **16** resembles that of its parent salt, cupric triflate.
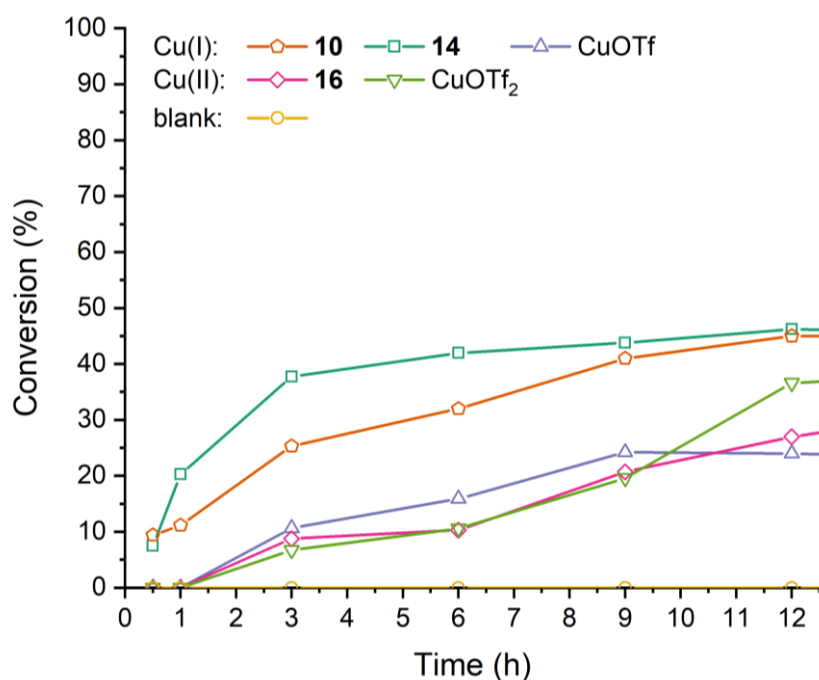

Figure 37. Preliminary catalytic testing of complexes **10**, **14**, and **16**.

Reactivity towards Ascorbic Acid

LPMO's active site is reduced from copper(II) to copper(I) by ascorbic acid (AA) to generate the active catalyst.[29,126] The reduction of complex **16** with AA was studied with ^{1}H NMR (Figure 38).
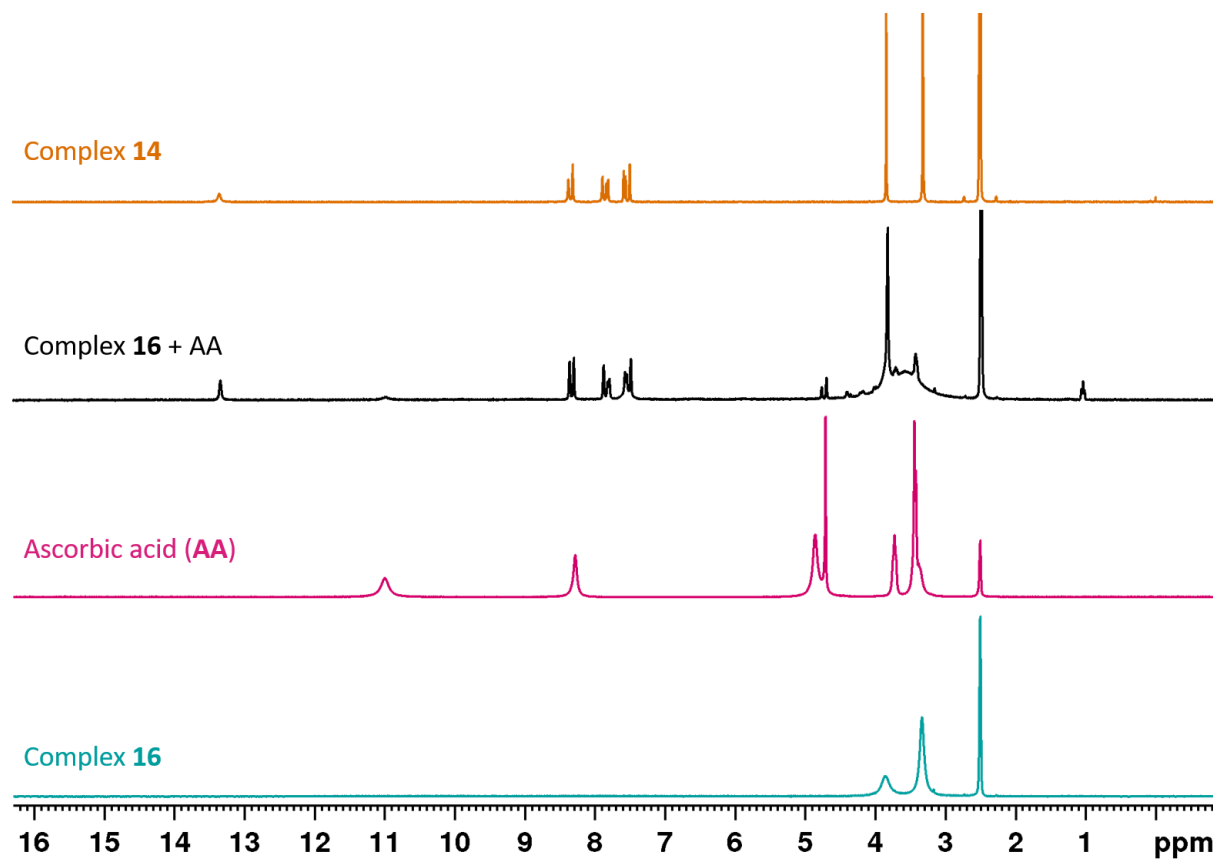

Figure 38. Reduction of complex **16** with ascorbic acid (300 MHz, d_6-DMSO).

Due to the paramagnetic nature of copper(II), the ^{1}H NMR spectrum of complex **16** has extremely broadened resonances. With the exception of the methyl group, the resonances have merged completely into the baseline. When a small excess of AA was added, resonances identical to those of complex **14** appeared in ^{1}H NMR spectrum. The experiment corroborates that **16** is the copper(II) analogue of complex **14** and that reduction can be achieved with the same reductant as for LPMO. However, catalytic testing of **16** in the presence of ascorbic acid showed no cyclohexane conversion.

Conclusion

In this doctoral thesis work, a series of novel copper compounds was synthesised. Different advantageous aspects of one-pot syntheses were underlined in the work: For one, one-pot syntheses of some Schiff base gave the desired product in good yields, where the free ligand was either not at all isolable or only in poor yields (Paper I and Paper II). Additionally, it allowed to selectively synthesising one product, where the metalation of the ligand gave two different complexes (Paper IV). The scope of the synthesis of diimine copper complexes from dimethyl 2,2'-diaminobiphenyl-4,4'-dicarboxylate was limited by the formation of dibenzo[*d,f*]-1,2-dihydro-[1,3]-diazepines. The influence of the aldehyde and the metal salt on the reaction outcome was investigated (Paper III).

The focus was set on copper(I) complexes, allowing extensive NMR studies. VT ^{1}H NMR revealed that the tetradentate complexes dimerised in solution. For pyridine-bearing tetradentate complexes, resonances of three species could be linked to a monomer, a dimer, and a higher aggregate through DOSY experiments. While tetradentate complexes with both imidazole and pyridine engage in dimerisation, their respective dimers are fundamentally different. The difference between their coordination to copper was further studied by ^{15}N NMR coordination shifts, revealing that the imine coordination shift is dependent on the adjacent heterocycle. Preliminary testing of three of the imidazole copper complexes for C-H oxidation showed higher conversion than for the respective salt. This suggests that the presented ligands have a beneficial effect on the catalytic performance of the copper catalyst.

As discussed in the introduction, heterogenization of the complexes is an important step towards applicability of the catalyst. Beyond the general motivations discussed in the introduction, the complexes herein have shown to be prone to aggregation and CuL_2 formation, possible pitfalls of rational ligand design. The incorporation into metal organic frameworks was achieved for one of the compounds within this thesis and for another one by a co-worker.

Outlook

Synthesis of Compounds

Future work should aim at incorporating more compounds into UiO-67. For isolable ligands, the diacid has to be synthesised from the ester. Thereafter, the ligand can be incorporated in UiO-67 and subsequently metalated. In Figure 39, the synthetic steps are outlined for the incorporation of compound **20**.
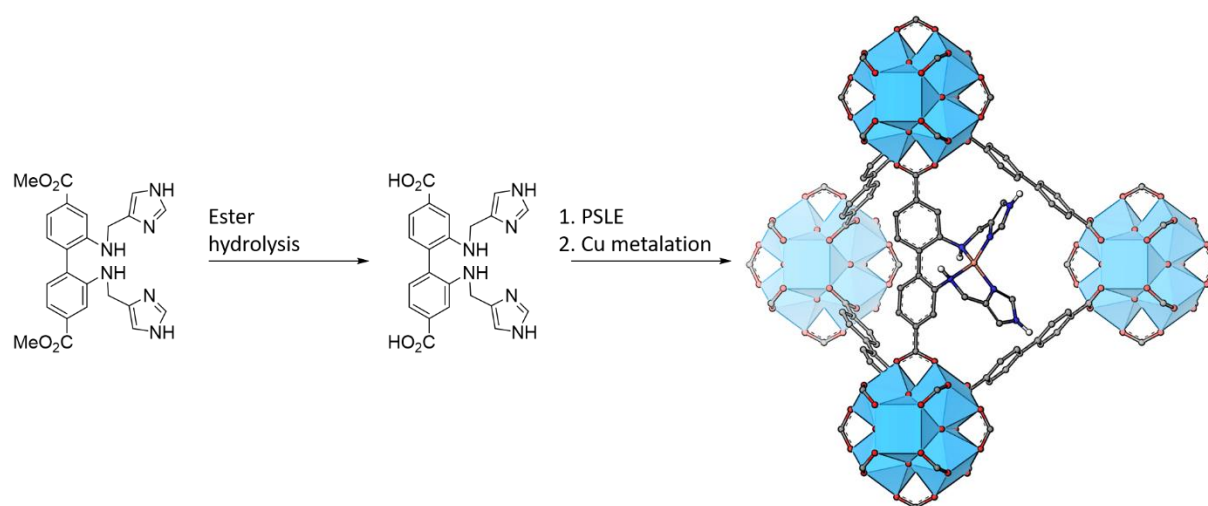

Figure 39. Synthetic plan for the incorporation of compound **20** into UiO-67. Material studio model of the incorporated copper complex produced by Erlend Aunan.

Furthermore, additional ligands should be synthesised. The impact of the heterocycle and imine vs. secondary amine has been synthetically explored in this thesis. Additional synthetic work has to be conducted to introduce primary amines in combination with imidazole moieties to enhance the biomimetic approach.

Spectroscopy

This project was focused on NMR and UV/Vis studies of the copper(I) complexes. It would be beneficial to evaluate the UV/Vis spectra with DFT to gain mechanistic insight and identify the oxygen species. For copper(II) complexes, either as-synthesised or after oxidation of copper(I) compounds, EPR could give insights into the structure around copper.

In order to further investigate the copper coordination inside of a MOF, spectroscopic methods other than NMR are better suited. The informative value of digestion NMR is strongly limited by the harsh conditions in common protocols (either strong acids or strong bases).[127] Copper(I) species are likely to oxidise, while imines may hydrolyse. Therefore, methods that operate on the intact MOF are preferable. While studies of solid-state $^{63}Cu/^{65}Cu$ NMR are reported, they are limited to highly symmetric compounds.[128] Other nuclei might however give indirect insight into the coordination mode in solid state.[129,130] X-ray absorption and emission spectroscopy are element-specific techniques that are well-suited to investigate the structure and reactivity of metals after incorporation.

Catalytic testing

Future work will focus on the application of the synthesised copper compounds in catalytic applications, e.g. C–H activation. Despite the improvements for the homogeneous testing procedure made in this thesis and a related Bachelor thesis, fundamental challenges to the homogeneous testing remain. The development of a robust, standardized procedure for homogeneous cyclohexane oxidation would be beneficial far beyond this project and ensure comparability between catalysts. In addition to the homogeneous testing of molecular complexes, the MOF incorporated copper complexes could be tested for the oxidation of gaseous hydrocarbons. In analogy to the enzyme,[131] a copper(II) MOF might require a reductant to initiate the catalytic cycle. The UV/Vis studies of **14** supported a mechanism involving two copper complexes. It remains therefore to be seen if spatially separated mononuclear copper(I) sites in the MOF are capable of activating molecular oxygen. The pentacoordinated Cu(II) salen-type complexes are interesting candidates for catalytic applications other than C–H oxidation, e.g. CO_2 reduction (see the corresponding chapter).

Sources

(1)   Chemistry (IUPAC), T. I. U. of P. and A. *IUPAC - coordination entity (C01330)*. https://goldbook.iupac.org/terms/view/C01330 (accessed 2022-01-08). https://doi.org/10.1351/goldbook.C01330.

(2)   Conry, R. R. Copper: Inorganic & Coordination Chemistry Based in Part on the Article Copper: Inorganic & Coordination Chemistry by Rebecca R. Conry & Kenneth D. Karlin Which Appeared in the Encyclopedia of Inorganic Chemistry, First Edition. In *Encyclopedia of Inorganic Chemistry*; John Wiley & Sons, Ltd, 2006. https://doi.org/10.1002/0470862106.ia052.

(3)   Pearson, R. G. Hard and Soft Acids and Bases. *J. Am. Chem. Soc.* **1963**, *85* (22), 3533–3539. https://doi.org/10.1021/ja00905a001.

(4)   Addison, A. W.; Rao, T. N.; Reedijk, J.; Rijn, J. van; Verschoor, G. C. Synthesis, Structure, and Spectroscopic Properties of Copper(II) Compounds Containing Nitrogen–Sulphur Donor Ligands; the Crystal and Molecular Structure of Aqua[1,7-Bis(N-Methylbenzimidazol-2'-Yl)-2,6-Dithiaheptane]Copper(II) Perchlorate. *J. Chem. Soc., Dalton Trans.* **1984**, No. 7, 1349–1356. https://doi.org/10.1039/DT9840001349.

(5)   Yang, L.; Powell, D. R.; Houser, R. P. Structural Variation in Copper(I) Complexes with Pyridylmethylamide Ligands: Structural Analysis with a New Four-Coordinate Geometry Index, T4. *Dalton Trans.* **2007**, No. 9, 955–964. https://doi.org/10.1039/B617136B.

(6)   Graf, E.; Mahoney, J. R.; Bryant, R. G.; Eaton, J. W. Iron-Catalyzed Hydroxyl Radical Formation. Stringent Requirement for Free Iron Coordination Site. *J. Biol. Chem.* **1984**, *259* (6), 3620–3624. https://doi.org/10.1016/S0021-9258(17)43139-5.

(7)   Riddlestone, I. M.; Kraft, A.; Schaefer, J.; Krossing, I. Taming the Cationic Beast: Novel Developments in the Synthesis and Application of Weakly Coordinating Anions. *Angew. Chem. Int. Ed.* **2018**, *57* (43), 13982–14024. https://doi.org/10.1002/anie.201710782.

(8)   Vicens, L.; Olivo, G.; Costas, M. Rational Design of Bioinspired Catalysts for Selective Oxidations. *ACS Catal.* **2020**, *10* (15), 8611–8631. https://doi.org/10.1021/acscatal.0c02073.

(9)   Kirillov, A. M.; Kopylovich, M. N.; Kirillova, M. V.; Haukka, M.; Silva, M. F. C. G. da; Pombeiro, A. J. L. Multinuclear Copper Triethanolamine Complexes as Selective Catalysts for the Peroxidative Oxidation of Alkanes under Mild Conditions. *Angew. Chem. Int. Ed.* **2005**, *44* (28), 4345–4349. https://doi.org/10.1002/anie.200500585.

(10)   J. Dyson, P.; G. Jessop, P. Solvent Effects in Catalysis: Rational Improvements of Catalysts via Manipulation of Solvent Interactions. *Catal. Sci. Technol.* **2016**, *6* (10), 3302–3316. https://doi.org/10.1039/C5CY02197A.

(11)   Macchioni, A. Ion Pairing in Transition-Metal Organometallic Chemistry. *Chem. Rev.* **2005**, *105* (6), 2039–2074. https://doi.org/10.1021/cr0300439.

(12)   Borovik, A. S.; Zinn, P. J.; Zart, M. K. Chapter 6: Dioxygen Binding and Activation: Reactive Intermediates. In *Activation of Small Molecules: Organometallic and Bioinorganic Perspectives*; Tolman, W. B., Ed.; Wiley-VCH: Weinheim, 2006; pp 187–234.

(13)   Ouali, A.; Taillefer, M.; Spindler, J.-F.; Jutand, A. Precatalysts Involved in Copper-Catalyzed Arylations of Nucleophiles. *Organometallics* **2007**, *26* (1), 65–74. https://doi.org/10.1021/om060706n.

(14) Grau, M.; Kyriacou, A.; Martinez, F. C.; Wispelaere, I. M. de; White, A. J. P.; Britovsek, G. J. P. Unraveling the Origins of Catalyst Degradation in Non-Heme Iron-Based Alkane Oxidation. *Dalton Trans.* **2014**, *43* (45), 17108–17119. https://doi.org/10.1039/C4DT02067G.

(15) Strauss, S. H. The Search for Larger and More Weakly Coordinating Anions. *Chem. Rev.* **1993**, *93* (3), 927–942. https://doi.org/10.1021/cr00019a005.

(16) Chinchilla, R.; Nájera, C. The Sonogashira Reaction: A Booming Methodology in Synthetic Organic Chemistry. *Chem. Rev.* **2007**, *107* (3), 874–922. https://doi.org/10.1021/cr050992x.

(17) Guo, X.-X.; Gu, D.-W.; Wu, Z.; Zhang, W. Copper-Catalyzed C–H Functionalization Reactions: Efficient Synthesis of Heterocycles. *Chem. Rev.* **2015**, *115* (3), 1622–1651. https://doi.org/10.1021/cr500410y.

(18) Li, Z.-K.; Jia, X.-S.; Yin, L. Recent Advances in Copper(II)-Mediated or -Catalyzed C–H Functionalization. *Synthesis* **2018**, *50* (21), 4165–4188. https://doi.org/10.1055/s-0037-1609932.

(19) Aneeja, T.; Neetha, M.; Afsina, C. M. A.; Anilkumar, G. Progress and Prospects in Copper-Catalyzed C–H Functionalization. *RSC Adv.* **2020**, *10* (57), 34429–34458. https://doi.org/10.1039/D0RA06518H.

(20) Musser, M. T. Cyclohexanol and Cyclohexanone. In *Ullmann's Encyclopedia of Industrial Chemistry*; John Wiley & Sons, Ltd, 2011. https://doi.org/10.1002/14356007.a08_217.pub2.

(21) Garcia-Bosch, I.; Siegler, M. A. Copper-Catalyzed Oxidation of Alkanes with H2O2 under a Fenton-like Regime. *Angew. Chem. Int. Ed.* **2016**, *55* (41), 12873–12876. https://doi.org/10.1002/anie.201607216.

(22) Fukatsu, A.; Morimoto, Y.; Sugimoto, H.; Itoh, S. Modelling a 'Histidine Brace' Motif in Mononuclear Copper Monooxygenases. *Chem. Commun.* **2020**, *56* (38), 5123–5126. https://doi.org/10.1039/D0CC01392G.

(23) Garcia-Bosch, I. Copper-Catalyzed Oxidation of Alkanes under Mild Conditions. *Synlett* **2017**, *28* (11), 1237–1243. https://doi.org/10.1055/s-0036-1590202.

(24) Shul'pin, G. B. Metal-Catalyzed Hydrocarbon Oxygenations in Solutions: The Dramatic Role of Additives: A Review. *J. Mol. Catal. A: Chem.* **2002**, *189* (1), 39–66. https://doi.org/10.1016/S1381-1169(02)00196-6.

(25) Schuchardt, U.; Cardoso, D.; Sercheli, R.; Pereira, R.; da Cruz, R. S.; Guerreiro, M. C.; Mandelli, D.; Spinacé, E. V.; Pires, E. L. Cyclohexane Oxidation Continues to Be a Challenge. *Appl. Catal. A: Gen.* **2001**, *211* (1), 1–17. https://doi.org/10.1016/S0926-860X(01)00472-0.

(26) Abutaleb, A.; Ali, M. A. A Comprehensive and Updated Review of Studies on the Oxidation of Cyclohexane to Produce Ketone-Alcohol (KA) Oil. *Rev. Chem. Eng.* **2021**. https://doi.org/10.1515/revce-2020-0059.

(27) Breslow, R. Biomimetic Chemistry: A Frontier at the Chemistry/Biology Interface. *Chem. Biol.* **1998**, *5* (2), R27–R28. https://doi.org/10.1016/S1074-5521(98)90138-7.

(28) Engelmann, X.; Monte-Pérez, I.; Ray, K. Oxidation Reactions with Bioinspired Mononuclear Non-Heme Metal–Oxo Complexes. *Angew. Chem. Int. Ed.* **2016**, *55* (27), 7632–7649. https://doi.org/10.1002/anie.201600507.

(29) Quinlan, R. J.; Sweeney, M. D.; Leggio, L. L.; Otten, H.; Poulsen, J.-C. N.; Johansen, K. S.; Krogh, K. B. R. M.; Jørgensen, C. I.; Tovborg, M.; Anthonsen, A.; Tryfona, T.; Walter, C. P.; Dupree, P.; Xu, F.; Davies, G. J.; Walton, P. H. Insights into the Oxidative

Degradation of Cellulose by a Copper Metalloenzyme That Exploits Biomass Components. *PNAS* **2011**, *108* (37), 15079–15084. https://doi.org/10.1073/pnas.1105776108.

(30) Hemsworth, G. R.; Taylor, E. J.; Kim, R. Q.; Gregory, R. C.; Lewis, S. J.; Turkenburg, J. P.; Parkin, A.; Davies, G. J.; Walton, P. H. The Copper Active Site of CBM33 Polysaccharide Oxygenases. *J. Am. Chem. Soc.* **2013**, *135* (16), 6069–6077. https://doi.org/10.1021/ja402106e.

(31) Aachmann, F. L.; Sørlie, M.; Skjåk-Bræk, G.; Eijsink, V. G. H.; Vaaje-Kolstad, G. NMR Structure of a Lytic Polysaccharide Monooxygenase Provides Insight into Copper Binding, Protein Dynamics, and Substrate Interactions. *PNAS* **2012**, *109* (46), 18779–18784. https://doi.org/10.1073/pnas.1208822109.

(32) Cao, L.; Caldararu, O.; Rosenzweig, A. C.; Ryde, U. Quantum Refinement Does Not Support Dinuclear Copper Sites in Crystal Structures of Particulate Methane Monooxygenase. *Angew. Chem. Int. Ed.* **2018**, *57* (1), 162–166. https://doi.org/10.1002/anie.201708977.

(33) Ross, M. O.; MacMillan, F.; Wang, J.; Nisthal, A.; Lawton, T. J.; Olafson, B. D.; Mayo, S. L.; Rosenzweig, A. C.; Hoffman, B. M. Particulate Methane Monooxygenase Contains Only Mononuclear Copper Centers. *Science* **2019**, *364* (6440), 566–570. https://doi.org/10.1126/science.aav2572.

(34) *Activation of Small Molecules: Organometallic and Bioinorganic Perspectives*; Tolman, W. B., Ed.; Wiley-VCH: Weinheim, 2006.

(35) Ciano, L.; Davies, G. J.; Tolman, W. B.; Walton, P. H. Bracing Copper for the Catalytic Oxidation of C–H Bonds. *Nat. Catal.* **2018**, *1* (8), 571–577. https://doi.org/10.1038/s41929-018-0110-9.

(36) Concia, A. L.; Beccia, M. R.; Orio, M.; Ferre, F. T.; Scarpellini, M.; Biaso, F.; Guigliarelli, B.; Réglier, M.; Simaan, A. J. Copper Complexes as Bioinspired Models for Lytic Polysaccharide Monooxygenases. *Inorg. Chem.* **2017**, *56* (3), 1023–1026. https://doi.org/10.1021/acs.inorgchem.6b02165.

(37) Elwell, C. E.; Gagnon, N. L.; Neisen, B. D.; Dhar, D.; Spaeth, A. D.; Yee, G. M.; Tolman, W. B. Copper–Oxygen Complexes Revisited: Structures, Spectroscopy, and Reactivity. *Chem. Rev.* **2017**, *117* (3), 2059–2107. https://doi.org/10.1021/acs.chemrev.6b00636.

(38) C. Bete, S.; Würtele, C.; Otte, M. A Bio-Inspired Imidazole-Functionalised Copper Cage Complex. *Chem. Commun.* **2019**, *55* (30), 4427–4430. https://doi.org/10.1039/C9CC00437H.

(39) Gudmundsson, M.; Kim, S.; Wu, M.; Ishida, T.; Momeni, M. H.; Vaaje-Kolstad, G.; Lundberg, D.; Royant, A.; Ståhlberg, J.; Eijsink, V. G. H.; Beckham, G. T.; Sandgren, M. Structural and Electronic Snapshots during the Transition from a Cu(II) to Cu(I) Metal Center of a Lytic Polysaccharide Monooxygenase by X-Ray Photoreduction. *J. Biol. Chem.* **2014**, *289* (27), 18782–18792. https://doi.org/10.1074/jbc.M114.563494.

(40) Torrelo, G.; Hollmann, F.; Hanefeld, U. Biocatalysis. In *Catalysis: An Integrated Textbook for Students*; Hanefeld, U., Lefferts, L., Eds.; Wiley-VCH: Weinheim, 2018; pp 127–189.

(41) Lee, J.; Goodey, N. M. Catalytic Contributions from Remote Regions of Enzyme Structure. *Chem. Rev.* **2011**, *111* (12), 7595–7624. https://doi.org/10.1021/cr100042n.

(42) Crabtree, R. H. The Stability of Organometallic Ligands in Oxidation Catalysis. *J. Organomet. Chem.* **2014**, *751*, 174–180. https://doi.org/10.1016/j.jorganchem.2013.07.061.

(43)   van Leeuwen, P. W. N. M. Decomposition Pathways of Homogeneous Catalysts. *Appl. Catal. A: Gen.* **2001**, *212* (1), 61–81. https://doi.org/10.1016/S0926-860X(00)00844-9.

(44)   Lefferts, L.; Hanefeld, U.; Bitter, H. Introduction. In *Catalysis: An Integrated Textbook for Students*; Hanefeld, U., Lefferts, L., Eds.; Wiley-VCH: Weinheim, 2018; pp 1–14.

(45)   Thomas, S. J. M. *Design and Applications of Single-Site Heterogeneous Catalysts: Contributions to Green Chemistry, Clean Technology and Sustainability*; Imperial College Press, 2012. https://doi.org/10.1142/p857.

(46)   Mitchell, S.; Vorobyeva, E.; Pérez-Ramírez, J. The Multifaceted Reactivity of Single-Atom Heterogeneous Catalysts. *Angew. Chem. Int. Ed.* **2018**, *57* (47), 15316–15329. https://doi.org/10.1002/anie.201806936.

(47)   De Vos, D. E.; Dams, M.; Sels, B. F.; Jacobs, P. A. Ordered Mesoporous and Microporous Molecular Sieves Functionalized with Transition Metal Complexes as Catalysts for Selective Organic Transformations. *Chem. Rev.* **2002**, *102* (10), 3615–3640. https://doi.org/10.1021/cr010368u.

(48)   Pomogailo, A. D. Catalysis by Heterogenized Metal Polymers: Advances and Prospects. *Kinet. Catal.* **2004**, *45* (1), 61–104. https://doi.org/10.1023/B:KICA.0000016109.46262.ce.

(49)   Baleizão, C.; Garcia, H. Chiral Salen Complexes: An Overview to Recoverable and Reusable Homogeneous and Heterogeneous Catalysts. *Chem. Rev.* **2006**, *106* (9), 3987–4043. https://doi.org/10.1021/cr050973n.

(50)   Wei, Y.-S.; Zhang, M.; Zou, R.; Xu, Q. Metal–Organic Framework-Based Catalysts with Single Metal Sites. *Chem. Rev.* **2020**, *120* (21), 12089–12174. https://doi.org/10.1021/acs.chemrev.9b00757.

(51)   Periana, R. A.; Taube, D. J.; Gamble, S.; Taube, H.; Satoh, T.; Fujii, H. Platinum Catalysts for the High-Yield Oxidation of Methane to a Methanol Derivative. *Science* **1998**, *280* (5363), 560–564. https://doi.org/10.1126/science.280.5363.560.

(52)   Palkovits, R.; Antonietti, M.; Kuhn, P.; Thomas, A.; Schüth, F. Solid Catalysts for the Selective Low-Temperature Oxidation of Methane to Methanol. *Angew. Chem. Int. Ed.* **2009**, *48* (37), 6909–6912. https://doi.org/10.1002/anie.200902009.

(53)   Pascanu, V.; González Miera, G.; Inge, A. K.; Martín-Matute, B. Metal–Organic Frameworks as Catalysts for Organic Synthesis: A Critical Perspective. *J. Am. Chem. Soc.* **2019**, *141* (18), 7223–7234. https://doi.org/10.1021/jacs.9b00733.

(54)   Zhang, X.; Chen, Z.; Liu, X.; L. Hanna, S.; Wang, X.; Taheri-Ledari, R.; Maleki, A.; Li, P.; K. Farha, O. A Historical Overview of the Activation and Porosity of Metal–Organic Frameworks. *Chem. Soc. Rev.* **2020**, *49* (20), 7406–7427. https://doi.org/10.1039/D0CS00997K.

(55)   Cavka, J. H.; Jakobsen, S.; Olsbye, U.; Guillou, N.; Lamberti, C.; Bordiga, S.; Lillerud, K. P. A New Zirconium Inorganic Building Brick Forming Metal Organic Frameworks with Exceptional Stability. *J. Am. Chem. Soc.* **2008**, *130* (42), 13850–13851. https://doi.org/10.1021/ja8057953.

(56)   Wang, Z.; Cohen, S. M. Postsynthetic Modification of Metal–Organic Frameworks. *Chem. Soc. Rev.* **2009**, *38* (5), 1315–1329. https://doi.org/10.1039/B802258P.

(57)   Xiang, W.; Ren, J.; Chen, S.; Shen, C.; Chen, Y.; Zhang, M.; Liu, C. The Metal–Organic Framework UiO-66 with Missing-Linker Defects: A Highly Active Catalyst for Carbon Dioxide Cycloaddition. *Appl. Energy* **2020**, *277*, 115560. https://doi.org/10.1016/j.apenergy.2020.115560.

(58)   N. Hall, J.; Bollini, P. Structure, Characterization, and Catalytic Properties of Open-Metal Sites in Metal Organic Frameworks. *React. Chem. Eng.* **2019**, *4* (2), 207–222. https://doi.org/10.1039/C8RE00228B.

(59)   Liu, Y.; Klet, R. C.; Hupp, J. T.; Farha, O. Probing the Correlations between the Defects in Metal–Organic Frameworks and Their Catalytic Activity by an Epoxide Ring-Opening Reaction. *Chem. Commun.* **2016**, *52* (50), 7806–7809. https://doi.org/10.1039/C6CC03727E.

(60)   Gutterød, E. S.; Lazzarini, A.; Fjermestad, T.; Kaur, G.; Manzoli, M.; Bordiga, S.; Svelle, S.; Lillerud, K. P.; Skúlason, E.; Øien-Ødegaard, S.; Nova, A.; Olsbye, U. Hydrogenation of CO2 to Methanol by Pt Nanoparticles Encapsulated in UiO-67: Deciphering the Role of the Metal–Organic Framework. *J. Am. Chem. Soc.* **2020**, *142* (2), 999–1009. https://doi.org/10.1021/jacs.9b10873.

(61)   Lyu, H.; Chen, O. I.-F.; Hanikel, N.; Hossain, M. I.; Flaig, R. W.; Pei, X.; Amin, A.; Doherty, M. D.; Impastato, R. K.; Glover, T. G.; Moore, D. R.; Yaghi, O. M. Carbon Dioxide Capture Chemistry of Amino Acid Functionalized Metal–Organic Frameworks in Humid Flue Gas. *J. Am. Chem. Soc.* **2022**, *144* (5), 2387–2396. https://doi.org/10.1021/jacs.1c13368.

(62)   Baek, J.; Rungtaweevoranit, B.; Pei, X.; Park, M.; Fakra, S. C.; Liu, Y.-S.; Matheu, R.; Alshmimri, S. A.; Alshehri, S.; Trickett, C. A.; Somorjai, G. A.; Yaghi, O. M. Bioinspired Metal–Organic Framework Catalysts for Selective Methane Oxidation to Methanol. *J. Am. Chem. Soc.* **2018**, *140* (51), 18208–18216. https://doi.org/10.1021/jacs.8b11525.

(63)   Feng, X.; Song, Y.; Chen, J. S.; Xu, Z.; Dunn, S. J.; Lin, W. Rational Construction of an Artificial Binuclear Copper Monooxygenase in a Metal–Organic Framework. *J. Am. Chem. Soc.* **2021**, *143* (2), 1107–1118. https://doi.org/10.1021/jacs.0c11920.

(64)   Kandiah, M.; Nilsen, M. H.; Usseglio, S.; Jakobsen, S.; Olsbye, U.; Tilset, M.; Larabi, C.; Quadrelli, E. A.; Bonino, F.; Lillerud, K. P. Synthesis and Stability of Tagged UiO-66 Zr-MOFs. *Chem. Mater.* **2010**, *22* (24), 6632–6640. https://doi.org/10.1021/cm102601v.

(65)   Leus, K.; Bogaerts, T.; De Decker, J.; Depauw, H.; Hendrickx, K.; Vrielinck, H.; Van Speybroeck, V.; Van Der Voort, P. Systematic Study of the Chemical and Hydrothermal Stability of Selected "Stable" Metal Organic Frameworks. *Micropor. Mesopor. Mat.* **2016**, *226*, 110–116. https://doi.org/10.1016/j.micromeso.2015.11.055.

(66)   Ingleson, M. J.; Barrio, J. P.; Guilbaud, J.-B.; Khimyak, Y. Z.; Rosseinsky, M. J. Framework Functionalisation Triggers Metal Complex Binding. *Chem. Commun.* **2008**, No. 23, 2680–2682. https://doi.org/10.1039/B718367D.

(67)   Servalli, M.; Ranocchiari, M.; Bokhoven, J. A. V. Fast and High Yield Post-Synthetic Modification of Metal–Organic Frameworks by Vapor Diffusion. *Chem. Commun.* **2012**, *48* (13), 1904–1906. https://doi.org/10.1039/C2CC17461H.

(68)   Thoresen, E. M.; Øien-Ødegaard, S.; Kaur, G.; Tilset, M.; Lillerud, K. P.; Amedjkouh, M. Strongly Visible Light-Absorbing Metal–Organic Frameworks Functionalized by Cyclometalated Ruthenium(II) Complexes. *RSC Adv.* **2020**, *10* (15), 9052–9062. https://doi.org/10.1039/C9RA06984D.

(69)   Marshall, R. J.; Forgan, R. S. Postsynthetic Modification of Zirconium Metal-Organic Frameworks. *Eur. J. Inorg. Chem.* **2016**, No. 27, 4310–4331. https://doi.org/10.1002/ejic.201600394.

(70)   Rasero-Almansa, A. M.; Corma, A.; Iglesias, M.; Sánchez, F. Zirconium Materials from Mixed Dicarboxylate Linkers: Enhancing the Stability for Catalytic Applications. *ChemCatChem* **2014**, *6* (12), 3426–3433. https://doi.org/10.1002/cctc.201402546.

(71) Ko, N.; Hong, J.; Sung, S.; Cordova, K. E.; Park, H. J.; Yang, J. K.; Kim, J. A Significant Enhancement of Water Vapour Uptake at Low Pressure by Amine-Functionalization of UiO-67. *Dalton Trans.* **2015**, *44* (5), 2047–2051. https://doi.org/10.1039/C4DT02582B.

(72) Øien, S.; Agostini, G.; Svelle, S.; Borfecchia, E.; Lomachenko, K. A.; Mino, L.; Gallo, E.; Bordiga, S.; Olsbye, U.; Lillerud, K. P.; Lamberti, C. Probing Reactive Platinum Sites in UiO-67 Zirconium Metal–Organic Frameworks. *Chem. Mater.* **2015**, *27* (3), 1042–1056. https://doi.org/10.1021/cm504362j.

(73) Braglia, L.; Borfecchia, E.; A. Lomachenko, K.; L. Bugaev, A.; A. Guda, A.; V. Soldatov, A.; L. Bleken, B. T.; Øien-Ødegaard, S.; Olsbye, U.; P. Lillerud, K.; Bordiga, S.; Agostini, G.; Manzoli, M.; Lamberti, C. Tuning Pt and Cu Sites Population inside Functionalized UiO-67 MOF by Controlling Activation Conditions. *Faraday Discuss.* **2017**, *201* (0), 265–286. https://doi.org/10.1039/C7FD00024C.

(74) Levchenko, V. A.; Siah, H.-S. M.; Øien-Ødegaard, S.; Kaur, G.; Fiksdahl, A.; Tilset, M. Catalytic Studies of Cyclometalated Gold(III) Complexes and Their Related UiO-67 MOF. *Mol. Catal.* **2020**, *492*, 111009. https://doi.org/10.1016/j.mcat.2020.111009.

(75) Schiff, H. *Untersuchungen über metallhaltige Anilinderivate und über die Bildung des Anilinroths*; Springer, 1864.

(76) Erxleben, A. Transition Metal Salen Complexes in Bioinorganic and Medicinal Chemistry. *Inorg. Chim. Acta* **2018**, *472*, 40–57. https://doi.org/10.1016/j.ica.2017.06.060.

(77) Hameed, A.; al-Rashida, M.; Uroos, M.; Abid Ali, S.; Khan, K. M. Schiff Bases in Medicinal Chemistry: A Patent Review (2010-2015). *Expert Opin Ther Pat* **2017**, *27* (1), 63–79. https://doi.org/10.1080/13543776.2017.1252752.

(78) da Silva, C. M.; da Silva, D. L.; Modolo, L. V.; Alves, R. B.; de Resende, M. A.; Martins, C. V. B.; de Fátima, Â. Schiff Bases: A Short Review of Their Antimicrobial Activities. *J. Adv. Res.* **2011**, *2* (1), 1–8. https://doi.org/10.1016/j.jare.2010.05.004.

(79) Cozzi, P. G. Metal–Salen Schiff Base Complexes in Catalysis: Practical Aspects. *Chem. Soc. Rev.* **2004**, *33* (7), 410–421. https://doi.org/10.1039/B307853C.

(80) Hylland, K. T.; Øien-Ødegaard, S.; Tilset, M. The Suzuki–Miyaura Cross-Coupling as the Key Step in the Synthesis of 2-Aminobiphenyls and 2,2'-Diaminobiphenyls: Application in the Synthesis of Schiff Base Complexes of Zn. *Eur. J. Org. Chem.* **2020**, No. 27, 4208–4226. https://doi.org/10.1002/ejoc.202000599.

(81) Doerrer, L. H.; Lippard, S. J. Zinc and Cadmium Tropocoronand Complexes: Effect of Metal Ion Radius on Macrocyclic Ligand Twist and Fold. *Inorg. Chem.* **1997**, *36* (12), 2554–2563. https://doi.org/10.1021/ic970033o.

(82) Leandri, V.; Pizzichetti, A. R. P.; Xu, B.; Franchi, D.; Zhang, W.; Benesperi, I.; Freitag, M.; Sun, L.; Kloo, L.; Gardner, J. M. Exploring the Optical and Electrochemical Properties of Homoleptic versus Heteroleptic Diimine Copper(I) Complexes. *Inorg. Chem.* **2019**, *58* (18), 12167–12177. https://doi.org/10.1021/acs.inorgchem.9b01487.

(83) Lennox, A. J. J.; Fischer, S.; Jurrat, M.; Luo, S.-P.; Rockstroh, N.; Junge, H.; Ludwig, R.; Beller, M. Copper-Based Photosensitisers in Water Reduction: A More Efficient In Situ Formed System and Improved Mechanistic Understanding. *Chem. Eur. J.* **2016**, *22* (4), 1233–1238. https://doi.org/10.1002/chem.201503812.

(84) Zhang, Y.; Heberle, M.; Wächtler, M.; Karnahl, M.; Dietzek, B. Determination of Side Products in the Photocatalytic Generation of Hydrogen with Copper Photosensitizers by Resonance Raman Spectroelectrochemistry. *RSC Adv.* **2016**, *6* (107), 105801–105805. https://doi.org/10.1039/C6RA21469J.

(85) Asato, E.; Furutachi, H.; Kawahashi, T.; Mikuriya, M. Polynuclear Zinc(II) Complexes of Phenol–Imine and –Amine Macrocycles. *J. Chem. Soc., Dalton Trans.* **1995**, No. 23, 3897–3904. https://doi.org/10.1039/DT9950003897.

(86) Mandal, S. K.; Nag, K. Synthesis of Some Macrocyclic Compounds Containing 2,6-Bis(N-Alkylamino)Phenol Units. *J. Org. Chem.* **1986**, *51* (20), 3900–3902. https://doi.org/10.1021/jo00370a029.

(87) Trammell, R.; See, Y. Y.; Herrmann, A. T.; Xie, N.; Díaz, D. E.; Siegler, Maxime. A.; Baran, P. S.; Garcia-Bosch, I. Decoding the Mechanism of Intramolecular Cu-Directed Hydroxylation of Sp3 C–H Bonds. *J. Org. Chem.* **2017**, *82* (15), 7887–7904. https://doi.org/10.1021/acs.joc.7b01069.

(88) Specht, P.; Petrillo, A.; Becker, J.; Schindler, S. Aerobic C–H Hydroxylation by Copper Imine Complexes: The Clip-and-Cleave Concept – Versatility and Limits. *Eur. J. Inorg. Chem.* **2021**, No. 20, 1961–1970. https://doi.org/10.1002/ejic.202100185.

(89) Nierengarten, H.; Rojo, J.; Leize, E.; Lehn, J.-M.; Dorsselaer, A. V. High Molecular Weight CuII Coordination Polymers and Their Characterisation by Electrospray Mass Spectrometry (ESMS). *Eur. J. Inorg. Chem.* **2002**, No. 3, 573–579. https://doi.org/10.1002/1099-0682(200203)2002:3<573::AID-EJIC573>3.0.CO;2-R.

(90) Sung, S.; Braddock, D. C.; Armstrong, A.; Brennan, C.; Sale, D.; White, A. J. P.; Davies, R. P. Synthesis, Characterisation and Reactivity of Copper(I) Amide Complexes and Studies on Their Role in the Modified Ullmann Amination Reaction. *Chem. Eur. J.* **2015**, *21* (19), 7179–7192. https://doi.org/10.1002/chem.201405699.

(91) Amendola, V.; Fabbrizzi, L.; Gianelli, L.; Maggi, C.; Mangano, C.; Pallavicini, P.; Zema, M. Electrochemical Assembling/Disassembling of Helicates with Hysteresis. *Inorg. Chem.* **2001**, *40* (14), 3579–3587. https://doi.org/10.1021/ic001155a.

(92) Hamblin, J.; Childs, L. J.; Alcock, N. W.; Hannon, M. J. Directed One-Pot Syntheses of Enantiopure Dinuclear Silver(I) and Copper(I) Metallo-Supramolecular Double Helicates. *J. Chem. Soc., Dalton Trans.* **2002**, No. 2, 164–169. https://doi.org/10.1039/B106987J.

(93) Van Stein, G. C.; Van Koten, G.; Vrieze, K.; Brevard, C. Proton and INEPT Nitrogen-15 and Silver-109 NMR Studies of the Structural and Dynamic Features in Solution of Some Silver(I) and Copper(I) Complexes with Polydentate N4-Donor Ligands, (RS)-1,2-(6-R-Py-2-CH:N)2Cy and 1,2-(6-R-Py-2-CH:N)2ethane (Cy = Cyclohexane, R = H or Me). *Inorg. Chem.* **1984**, *23* (25), 4269–4278. https://doi.org/10.1021/ic00193a034.

(94) Hylland, K. T.; Øien-Ødegaard, S.; Heyn, R. H.; Tilset, M. Zinc Schiff Base Complexes Derived from 2,2'-Diaminobiphenyls: Solution Behavior and Reactivity towards Nitrogen Bases. *Eur. J. Inorg. Chem.* **2020**, No. 38, 3627–3643. https://doi.org/10.1002/ejic.202000589.

(95) Katcka, M.; Urbanski, T. NMR Spectra of Pyridine, Picolines and Hydrochlorides and of Their Hydrochlorides and Methiodides. *Bull. Pol. Acad. Sci. Chem.* **1968**, *16*, 347–350.

(96) El-ghayoury, A.; Douce, L.; Skoulios, A.; Ziessel, R. Cation-Induced Macroscopic Ordering of Non-Mesomorphic Modules—A New Application for Metallohelicates. *Angew. Chem. Int. Ed.* **1998**, *37* (16), 2205–2208. https://doi.org/10.1002/(SICI)1521-3773(19980904)37:16<2205::AID-ANIE2205>3.0.CO;2-R.

(97) Pasternack, R. F.; Huber, P. R.; Boyd, P.; Engasser, G.; Francesconi, L.; Gibbs, E.; Fasella, P.; Cerio Venturo, G.; Hinds, L. deC. Aggregation of Meso-Substituted Water-Soluble Porphyrins. *J. Am. Chem. Soc.* **1972**, *94* (13), 4511–4517. https://doi.org/10.1021/ja00768a016.

(98) Kano, K.; Fukuda, K.; Wakami, H.; Nishiyabu, R.; Pasternack, R. F. Factors Influencing Self-Aggregation Tendencies of Cationic Porphyrins in Aqueous Solution. *J. Am. Chem. Soc.* **2000**, *122* (31), 7494–7502. https://doi.org/10.1021/ja000738g.

(99) Vedder, C.; Schaper, F.; Brintzinger, H.-H.; Kettunen, M.; Babik, S.; Fink, G. Chiral Iron(II) and Cobalt(II) Complexes with Biphenyl-Bridged Bis(Pyridylimine) Ligands – Syntheses, Structures and Reactivities. *Eur. J. Inorg. Chem.* **2005**, No. 6, 1071–1080. https://doi.org/10.1002/ejic.200400912.

(100) Evans, R.; Deng, Z.; Rogerson, A. K.; McLachlan, A. S.; Richards, J. J.; Nilsson, M.; Morris, G. A. Quantitative Interpretation of Diffusion-Ordered NMR Spectra: Can We Rationalize Small Molecule Diffusion Coefficients? *Angew. Chem. Int. Ed.* **2013**, *52* (11), 3199–3202. https://doi.org/10.1002/anie.201207403.

(101) Evans, R.; Dal Poggetto, G.; Nilsson, M.; Morris, G. A. Improving the Interpretation of Small Molecule Diffusion Coefficients. *Anal. Chem.* **2018**, *90* (6), 3987–3994. https://doi.org/10.1021/acs.analchem.7b05032.

(102) Tuna, F.; Hamblin, J.; Jackson, A.; Clarkson, G.; Alcock, N. W.; Hannon, M. J. Metallo-Supramolecular Libraries: Triangles, Polymers and Double-Helicates Assembled by Copper(I) Coordination to Directly Linked Bis-Pyridylimine Ligands. *Dalton Trans.* **2003**, No. 11, 2141–2148. https://doi.org/10.1039/B211005A.

(103) Childs, L. J.; Alcock, N. W.; Hannon, M. J. Assembly of Nano-Scale Circular Supramolecular Arrays through π–π Aggregation of Arc-Shaped Helicate Units. *Angew. Chem. Int. Ed.* **2001**, *40* (6), 1079–1081. https://doi.org/10.1002/1521-3773(20010316)40:6<1079::AID-ANIE10790>3.0.CO;2-Q.

(104) Alves, W. A.; Cerchiaro, G.; Paduan-Filho, A.; Tomazela, D. M.; Eberlin, M. N.; Da Costa Ferreira, A. M. Infinite Zig-Zag and Cyclic-Tetranuclear Isomeric Imidazolate-Bridged Polynuclear Copper(II) Complexes: Magnetic Properties, Catalytic Activity and Electrospray Mass and Tandem Mass Spectrometry Characterization. *Inorg. Chim. Acta* **2005**, *358* (13), 3581–3591. https://doi.org/10.1016/j.ica.2005.06.006.

(105) Mimura, M.; Matsuo, T.; Nakashima, T.; Matsumoto, N. Zigzag-Chain and Cyclic-Tetrameric Compounds Derived by Deprotonation of Mononuclear Copper(II) Complexes with N,N′-Bis(2-Substituted-Imidazol-4-Ylmethyl-Idene)-1,4-Diaminobutane (2-Substituent = H, Me): Synthesis, Characterization, Structure, Substituent Effect, and Interconvertibility. *Inorg. Chem.* **1998**, *37* (14), 3553–3560. https://doi.org/10.1021/ic971609c.

(106) Sunatsuki, Y.; Motoda, Y.; Matsumoto, N. Copper(II) Complexes with Multidentate Schiff-Base Ligands Containing Imidazole Groups: Ligand-Complex or Self-Complementary Molecule? *Coord. Chem. Rev.* **2002**, *226* (1), 199–209. https://doi.org/10.1016/S0010-8545(01)00417-9.

(107) Claridge, T. D. W. *High-Resolution NMR Techniques in Organic Chemistry*; Elsevier, 2016.

(108) Weiss, R.; Chledowski, L. Bildung zyklischer Verbindungen aus aromatischen Diaminen mittels Chloral. *Monatsh. Chem.* **1934**, *65*, 357–366. https://doi.org/10.1007/BF01522074.

(109) Tomar, M.; Lucas, N. T.; Müllen, K.; Jacob, J. Facile Synthesis and Coupling of 3,9-Dibromo-6-Aryl-5H-Dibenzo[d,f][1,3]Diazepine Derivatives. *Tetrahedron Lett.* **2013**, *54* (44), 5883–5885. https://doi.org/10.1016/j.tetlet.2013.08.107.

(110) Ried, W.; Sinharay, A. Über heterocyclische Siebenringsysteme, XIV. Weitere Ringschlußreaktionen mit o.o'-Diamino-biphenyl. *Chem. Ber.* **1965**, *98* (11), 3523–3531. https://doi.org/10.1002/cber.19650981113.

(111) Gumbau-Brisa, R.; Hayward, J. J.; Wallis, J. D.; Rawson, J. M.; Pilkington, M. Structural Insights into the Coordination Chemistry and Reactivity of a 3,3'-Bis-Imine-2,2'-Bipyridine Ligand. *CrystEngComm* **2016**, *18* (11), 1892–1903. https://doi.org/10.1039/C5CE02349A.

(112) Montanaro, S.; Wright, I. A.; Batsanov, A. S.; Bryce, M. R. Synthesis of Tetracyclic 2,3-Dihydro-1,3-Diazepines from a Dinitrodibenzothiophene Derivative. *J. Org. Chem.* **2018**, *83* (19), 12320–12326. https://doi.org/10.1021/acs.joc.8b02029.

(113) Laplaza, R.; Boto, R. A.; Contreras-García, J.; Montero-Campillo, M. M. Steric Clash in Real Space: Biphenyl Revisited. *Phys. Chem. Chem. Phys.* **2020**, *22* (37), 21251–21256. https://doi.org/10.1039/D0CP03359F.

(114) Leroux, F. Atropisomerism, Biphenyls, and Fluorine: A Comparison of Rotational Barriers and Twist Angles. *ChemBioChem* **2004**, *5* (5), 644–649. https://doi.org/10.1002/cbic.200300906.

(115) Müller, G.; Chylenski, P.; Bissaro, B.; Eijsink, V. G. H.; Horn, S. J. The Impact of Hydrogen Peroxide Supply on LPMO Activity and Overall Saccharification Efficiency of a Commercial Cellulase Cocktail. *Biotechnol. Biofuels* **2018**, *11* (1), 209. https://doi.org/10.1186/s13068-018-1199-4.

(116) Jakobsen, J. B.; Rønne, M. H.; Daasbjerg, K.; Skrydstrup, T. Are Amines the Holy Grail for Facilitating CO2 Reduction? *Angew. Chem. Int. Ed.* **2021**, *60* (17), 9174–9179. https://doi.org/10.1002/anie.202014255.

(117) Wirtanen, T.; Rodrigo, E.; Waldvogel, S. R. Recent Advances in the Electrochemical Reduction of Substrates Involving N−O Bonds. *Adv. Synth. Catal.* **2020**, *362* (11), 2088–2101. https://doi.org/10.1002/adsc.202000349.

(118) Orpen, A. . G.; Brammer, L.; Allen, F. H.; Kennard, O.; Watson, D. G.; Taylor, R. Appendix A: Typical Interatomic Distances in Organic Compounds and Organometallic Compounds and Coordination Complexes of the d- and f-Block Metals. In *Structure Correlation*; John Wiley & Sons, Ltd, 1994; pp 752–858. https://doi.org/10.1002/9783527616091.app1.

(119) Kaur, G. Optimization of UiO-67 Type Metal-Organic Frameworks for Catalysis. PhD Thesis, Oslo University, 2020.

(120) Zwoliński, K. M.; Nowak, P.; Chmielewski, M. J. Towards Multifunctional MOFs – Transforming a Side Reaction into a Post-Synthetic Protection/Deprotection Method. *Chem. Commun.* **2015**, *51* (49), 10030–10033. https://doi.org/10.1039/C5CC03469H.

(121) Horikoshi, R.; Funasako, Y.; Yajima, T.; Mochida, T.; Kobayashi, Y.; Kageyama, H. Copper(II) Solvatochromic Complexes [Cu(Acac)(N^N)(Ligand)]BPh4 with Various Axial Ligands. Correlation between Coordination Geometries and d–d Transition Energies (Acac=acetylacetonato, N^N=1,10-Phenanthoroline, 2,2'-Bipyridyl). *Polyhedron* **2013**, *50* (1), 66–74. https://doi.org/10.1016/j.poly.2012.09.063.

(122) Sýkora, J.; Brandšteterová, E.; Jabconová, A. Photoredox Reactivity of Copper Complexes and Photooxidation of Organic Substrates. In *Photosensitive Metal—Organic Systems*; Advances in Chemistry; American Chemical Society, 1993; Vol. 238, pp 377–397. https://doi.org/10.1021/ba-1993-0238.ch019.

(123) Ferraudi, G.; Muralidharan, S. Photochemical Properties of Copper Complexes. *Coord. Chem. Rev.* **1981**, *36* (1), 45–88. https://doi.org/10.1016/S0010-8545(00)80505-6.

(124) Wedler, G. *Lehrbuch Der Physikalischen Chemie*, 5th ed.; Wiley-VCH: Weinheim, 2004.

(125) Lerch, M.; Weitzer, M.; Stumpf, T.-D. J.; Laurini, L.; Hoffmann, A.; Becker, J.; Miska, A.; Göttlich, R.; Herres-Pawlis, S.; Schindler, S. Kinetic Investigation of the Reaction of Dioxygen with the Copper(I) Complex [Cu(PimiPr2)(CH3CN)]CF3SO3 PimiPr2 = Tris[2-(1,4-Diisopropylimidazolyl)]Phosphine. *Eur. J. Inorg. Chem.* **2020**, No. 33, 3143–3150. https://doi.org/10.1002/ejic.202000462.

(126) Kracher, D.; Andlar, M.; Furtmüller, P. G.; Ludwig, R. Active-Site Copper Reduction Promotes Substrate Binding of Fungal Lytic Polysaccharide Monooxygenase and Reduces Stability. *J. Biol. Chem.* **2018**, *293* (5), 1676–1687. https://doi.org/10.1074/jbc.RA117.000109.

(127) Garibay, S. J.; Wang, Z.; Cohen, S. M. Evaluation of Heterogeneous Metal−Organic Framework Organocatalysts Prepared by Postsynthetic Modification. *Inorg. Chem.* **2010**, *49* (17), 8086–8091. https://doi.org/10.1021/ic1011549.

(128) Gschwind, R. M. Organocuprates and Diamagnetic Copper Complexes: Structures and NMR Spectroscopic Structure Elucidation in Solution. *Chem. Rev.* **2008**, *108* (8), 3029–3053. https://doi.org/10.1021/cr800286r.

(129) Klug, C. A.; Swift, M. W.; Miller, J. B.; Lyons, J. L.; Albert, A.; Laskoski, M.; Hangarter, C. M. High Resolution Solid State NMR in Paramagnetic Metal-Organic Frameworks. *Solid State Nucl. Magn. Reson.* **2022**, *120*, 101811. https://doi.org/10.1016/j.ssnmr.2022.101811.

(130) He, C.; Li, S.; Xiao, Y.; Xu, J.; Deng, F. Application of Solid-State NMR Techniques for Structural Characterization of Metal-Organic Frameworks. *Solid State Nucl. Magn. Reson.* **2022**, *117*, 101772. https://doi.org/10.1016/j.ssnmr.2022.101772.

(131) Stepnov, A. A.; Forsberg, Z.; Sørlie, M.; Nguyen, G.-S.; Wentzel, A.; Røhr, Å. K.; Eijsink, V. G. H. Unraveling the Roles of the Reductant and Free Copper Ions in LPMO Kinetics. *Biotechnol. Biofuels* **2021**, *14* (1), 28. https://doi.org/10.1186/s13068-021-01879-0.

Appendix A

Synthetic Procedures and Characterization of Compounds not Included in Manuscripts

The general considerations given in the SI of Paper I apply.

Compound 13

A mixture of biphenyl-2,2′-diamine (0.540 mmol, 100 mg), CuOTf (0.540 mmol, 115 mg, 1 equiv.) and picolinaldehyde (1.08 mmol, 116 mg, 2 equiv.) were stirred in MeCN (2 mL) overnight. Et$_2$O was added and the solid was collected through filtration and washed (2x 1 mL Et$_2$O). Residual solvent was left to evaporate over night to yield **13** as a dark green solid (0.524 mmol, 301 mg, 97 %).
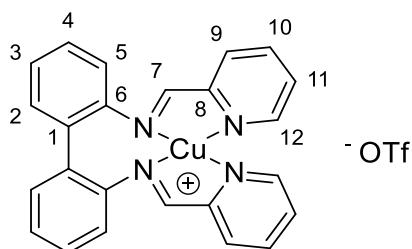
^{1}H NMR for the major species (600 MHz, d_6-DMSO): δ[ppm] *Overlap* (4 H) of 8.90 (H7) and 8.89 (H12), 8.27 (2H, m, H10), 8.10 (2H, d, $^3J_{H,H}$ = 7.4 Hz, H11), 7.90 (2H, m, H9), 7.47 (2H, m, H4), 7.41 (2H, d, $^3J_{H,H}$ = 7.5 Hz, H2), 7.37 (2H, m, H3), 7.27 (2H, d, $^3J_{H,H}$ = 7.4 Hz, H5). ^{13}C NMR (150 MHz, d_6-DMSO): δ[ppm] 161.4 (C7), 150.3 (C12), 150.2 (C8), 146.1 (C6), 138.9 (C10), 132.8 (C2), 129.6 (C1), 129.4 (C9), 129.0 (C4), 128.8 (C11), 126.3 (C3), 120.7 (m*, $^1J_{C,F}$ = 322 Hz, **C**F$_3$), 120.1 (C5). HRMS *m/z* [^{63}CuL$^+$] (C$_{24}$H$_{18}$CuN$_4^+$): Calcd: 425.0822 Found: 425.0822. Anal. Calcd: C, 55.22; H, 3.16; N, 9.74 Found: C, 52.20; H, 3.14; N, 9.73.

* d visible, expected q
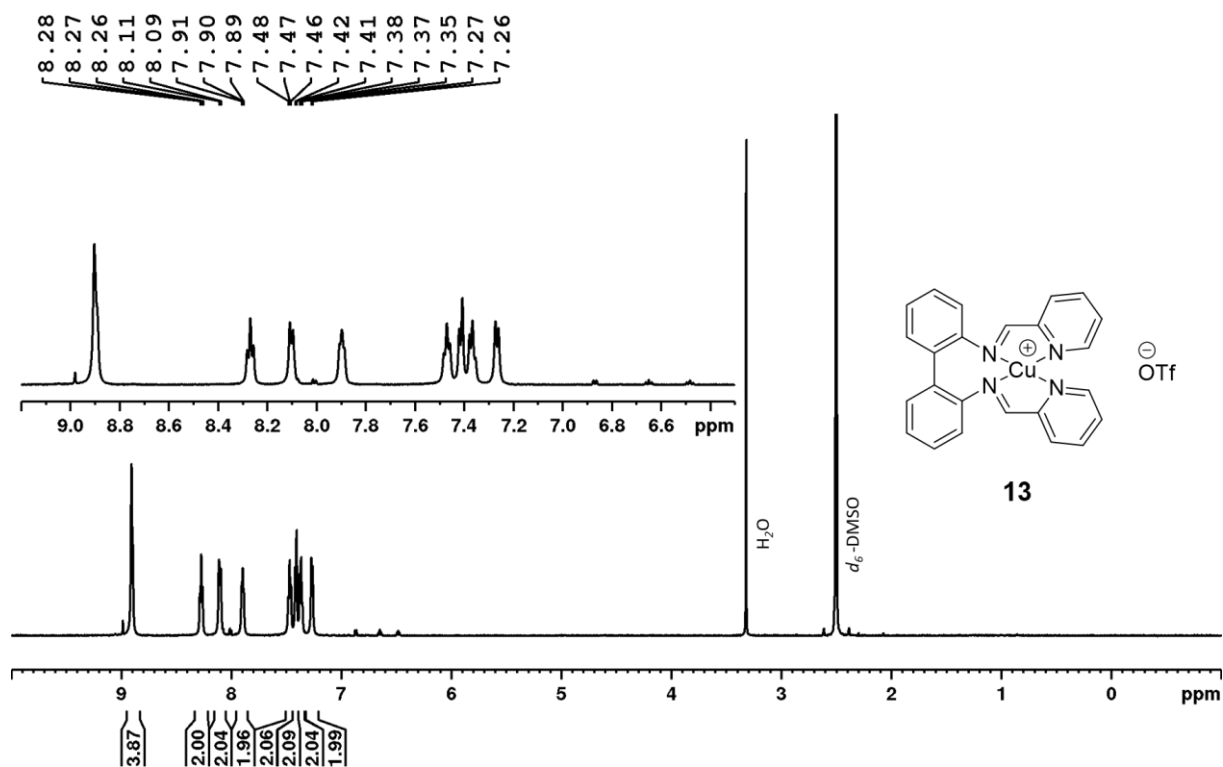
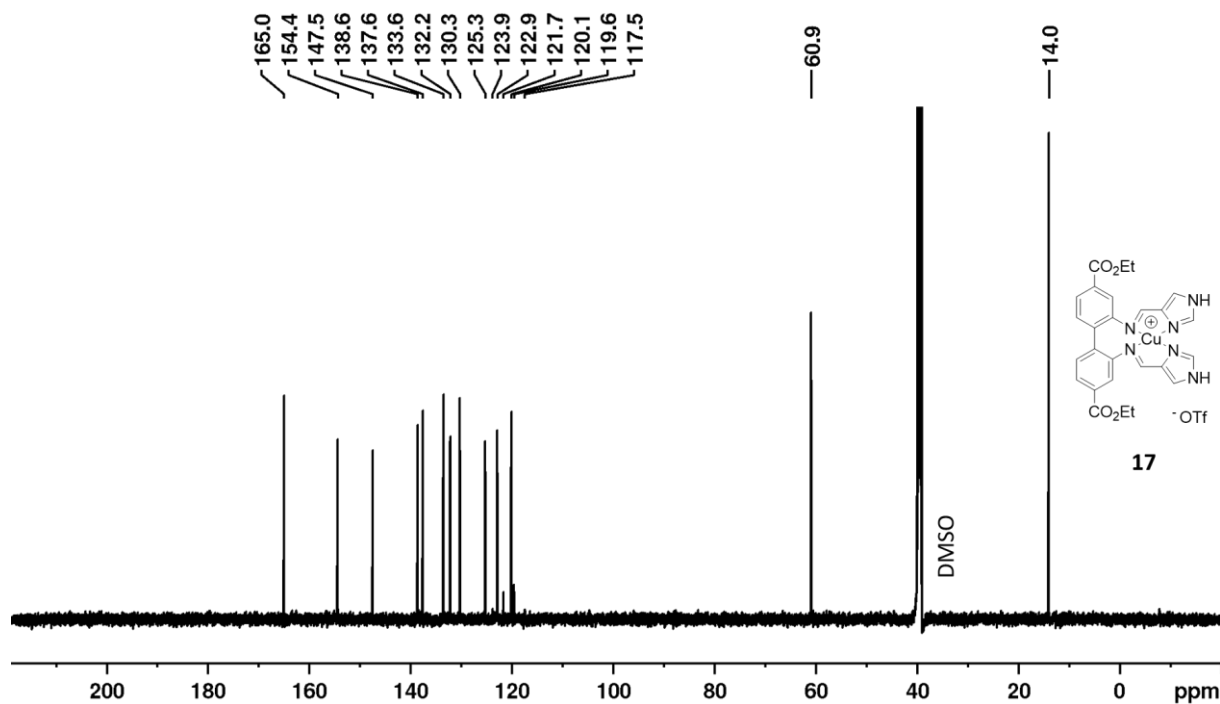Figure 40. ^{1}H NMR spectrum (600 MHz, d_6-DMSO) of **13.**
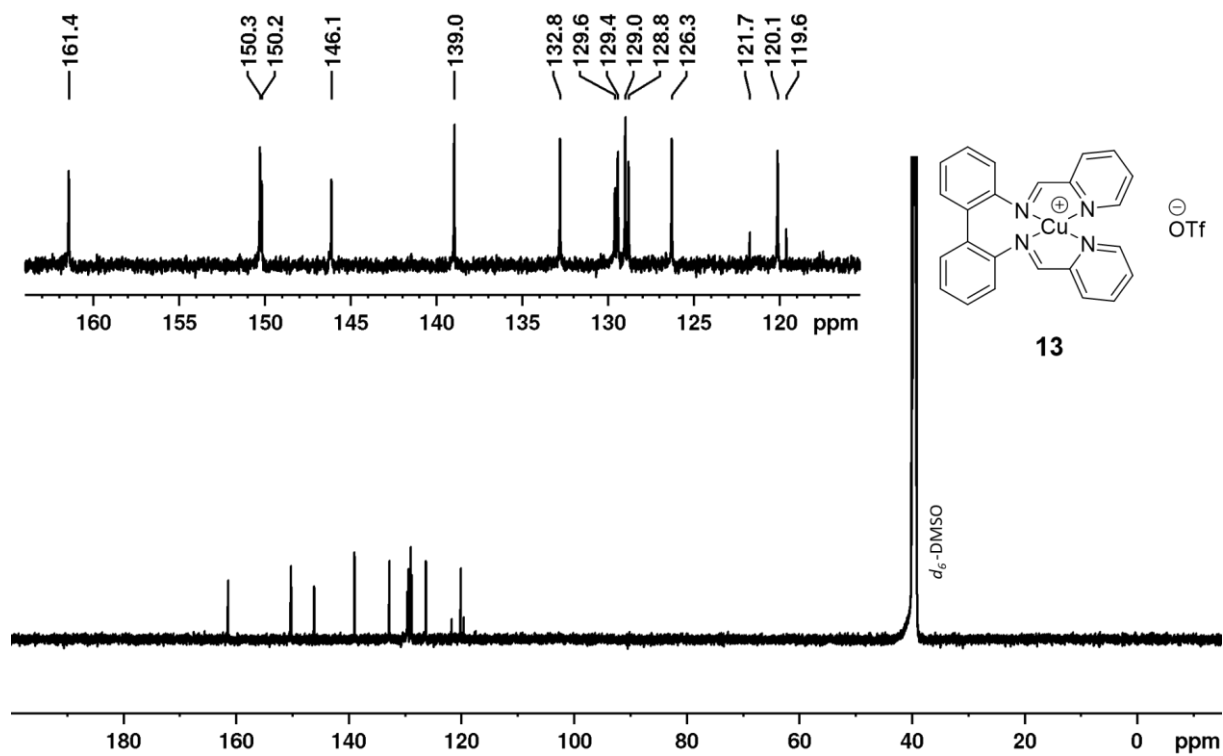
Figure 41. ^{13}C NMR spectrum (150 MHz, d_6-DMSO) of **13.**

Compound 17

A mixture of diethyl 2,2′-diaminobiphenyl-4,4′-dicarboxylate (0.610 mmol, 200 mg), CuOTf·4MeCN (0.610 mmol, 230 mg, 1 equiv.) and 1*H*-imidazole-4-carbaldehyde (1.20 mmol, 118 mg, 2 equiv.) were stirred in acetonitrile (2 mL) overnight. The solid was collected through filtration and washed with diethyl ether (4 mL). Residual solvent was left to evaporate overnight to yield **17** as an ochre solid (0.597 mmol, 416 mg, 98 %).
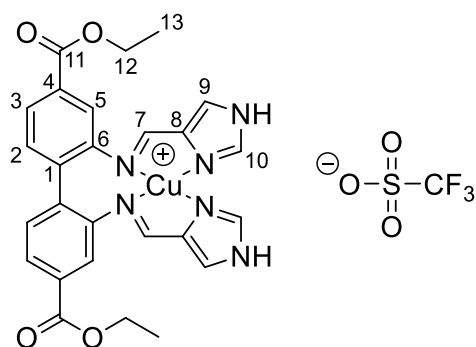
^{1}H NMR (d_6-DMSO, 600 MHz): δ[ppm] 13.33 (2H, s, N**H**), 8.37 (2H, s, H10), 8.31 (2H, s, H7), 7.88 (2H, s, H9), 7.81 (2H, dd, $^3J_{H,H}$ = 8.0 Hz, $^4J_{H,H}$ = 1.7 Hz, H3), 7.56 (2H, d, $^3J_{H,H}$ = 8.0 Hz, H2), 7.49 (2H, d, $^4J_{H,H}$ = 1.6 Hz, H5), 4.30 (4H, q, $^3J_{H,H}$ = 7.1 Hz, H12), 1.30 (6H, t, $^3J_{H,H}$ = 7.1 Hz, H13).

^{13}C NMR (d_6-DMSO, 150 MHz): δ[ppm] 165.0 (C11), 154.4 (C7), 147.5 (C6), 138.6 (C10), 137.6 (C8), 133.6 (C1), 132.2 (C2), 130.3 (C4), 125.3 (C3), 122.9 (C9), 120.7 (q,$^1J_{C-F}$ = 321 Hz, **C**F$_3$) 120.1 (C5), 60.9 (C12), 14.0 (C13). ESI-MS: *m/z* 547.115 (100 %, [^{63}CuL]$^+$), 549.113 (47 %, [^{65}CuL]$^+$). HRMS *m/z* [^{63}CuL$^+$] (C$_{26}$H$_{24}$CuN$_6$O$_4^+$): Calcd: 547.1150 Found: 547.1146. Anal. Calcd: C, 46.52; H, 3.47; N, 12.06 Found: C, 46.04; H, 3.41; N, 11.88.
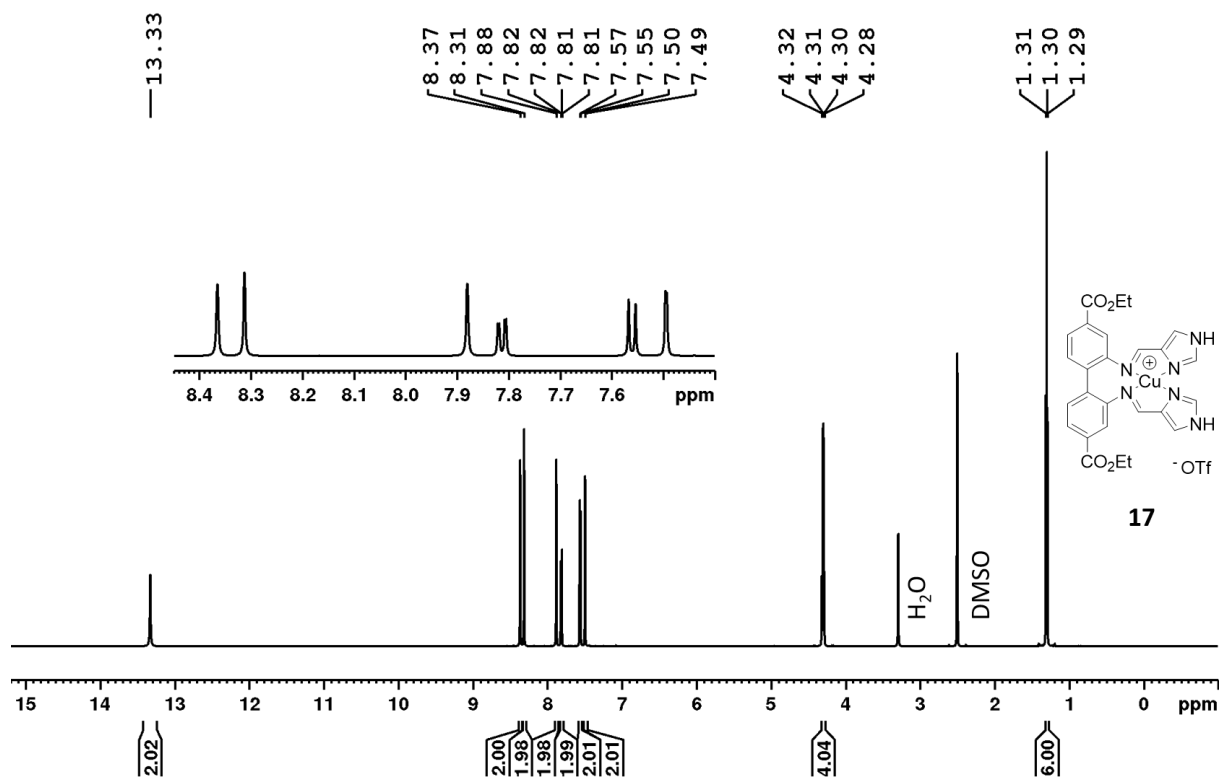
Figure 42. ^{1}H NMR spectrum (600 MHz, d_6-DMSO) of **17.**

Figure 43. ^{13}C NMR spectrum (150 MHz, d_6-DMSO) of **17.**

Compound 20

A mixture of dimethyl 2,2′-diaminobiphenyl-4,4′-dicarboxylate (2.60 mmol, 780 mg), 1*H*-imidazole-4-carbaldehyde (5.20 mmol, 500 mg, 2 equiv.) and five drops of formic acid were stirred in dry methanol overnight. The reaction mixture was cooled with an ice bath. NaBH$_4$ (26.0 mmol, 980 mg, 10 equiv.) was added portionwise over the course of ten minutes. The ice bath was removed and the reaction was stirred at ambient temperature for two more hours. The reaction was diluted in NaHCO$_3$ (aq., sat., 50 mL). The aqueous phase was extracted with CH$_2$Cl$_2$ (2x 100 mL). The combined organic phase was dried over Na$_2$SO$_4$. The solvent was removed under reduced pressure. After recrystallization from acetonitrile, a pale brown solid was obtained (354 mg, 0.779 mmol, 30 %).
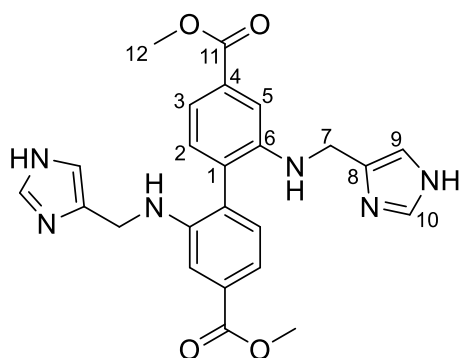
Mp.147-149 °C. ^{1}H NMR (*d$_6$*-DMSO, 600 MHz): δ[ppm] 12.04 (2H, *br*, s, imidazole N**H**), 7.58 (2H, s, H10), 7.31 (2H, d, $^4J_{H,H}$ = 1.6 Hz, H5), 7.30 (2H, dd, $^3J_{H,H}$ = 7.7 Hz, $^4J_{H,H}$ = 1.6 Hz, H3), 7.11 (2H, d, $^3J_{H,H}$ = 7.7 Hz, H2), 6.92 (2H, s, H9), 4.99 (2H, t, $^3J_{H,H}$ = 5.25 Hz, sec. amine N**H**) 4.23 (4H, m, H7), 3.83 (6H, s, H12). ^{13}C NMR (*d$_6$*-DMSO, 150 MHz): δ[ppm] 166.5 (C11), 145.3 (C6), 135.1 (C10), 130.8 (C2), 130.1 (C4), 128.1 (C1) 117.3 (C3), 111.0 (C5), 51.9 (C12), 40.3* (C7) C9 missing. *detected by HSQC, overlapping with solvent signal. HRMS *m/z* [M+H$^+$] (C$_{24}$H$_{25}$N$_6$O$_4{}^+$): Calcd: 461.1932 Found: 461.1931.
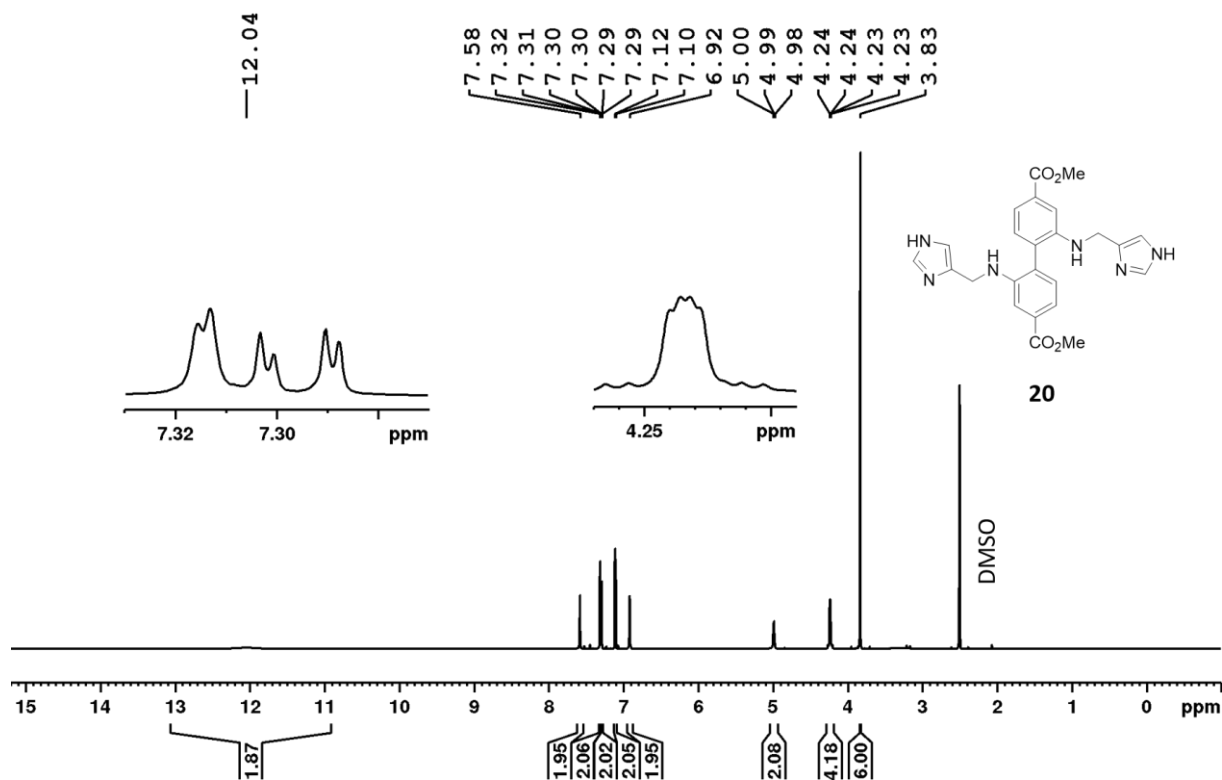
Figure 44. ^{1}H NMR spectrum (600 MHz, d_6-DMSO) of **20**.
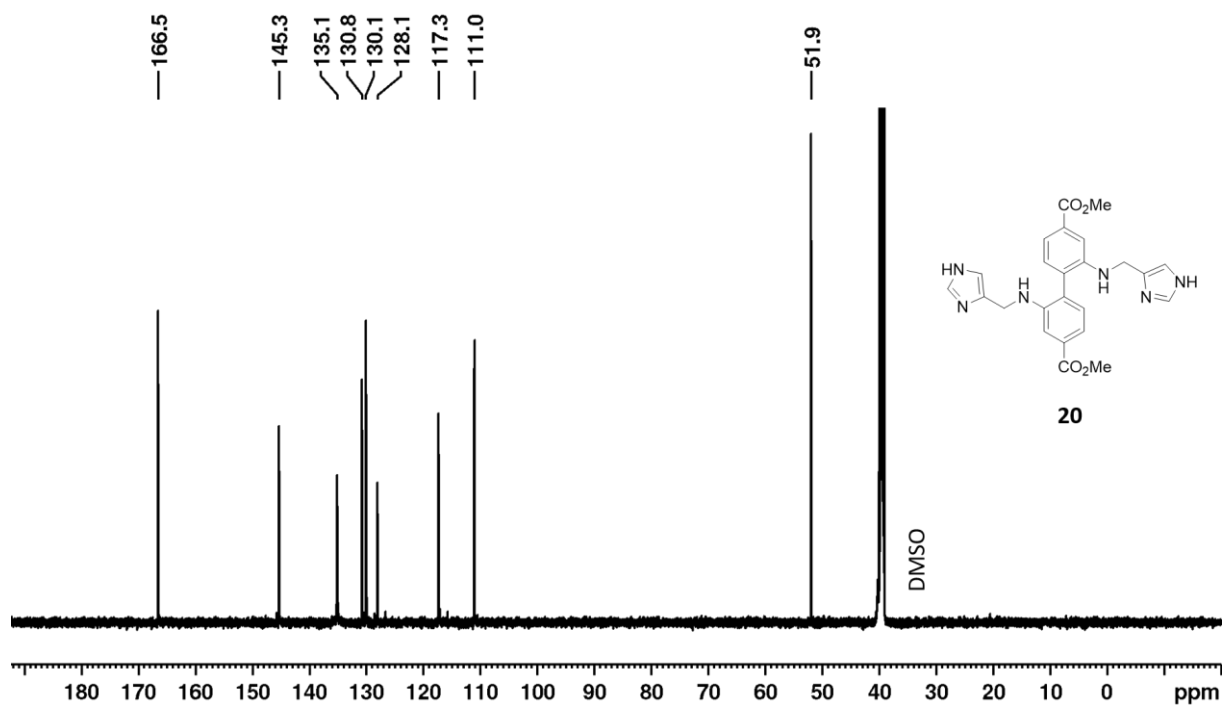
Figure 45. ^{13}C NMR spectrum (150 MHz, d_6-DMSO) of **20**.

Compound 28

Methyl 6-(4-(methoxycarbonyl)-2-aminophenyl) (**7**) was synthesised according to the procedure in the supporting information of Paper II. **7** (1.00 g, 3.49 mmol) and LiOH (0.335 g, 14.0 mmol, 4 equiv.) were stirred for a day in a solvent mixture of H_2O/THF/MeOH (2:2:1, 8 mL, 8 mL, 4 mL). The solvent volume was reduced and the solution was acidified with acetic acid to precipitate the product. The product was collected through filtration and washed with water. After drying overnight, the product was suspended in H_2O (ca. 30 mL) and stirred for 15 min. The product was collected through filtration and washed with H_2O and acetone. After drying in a vacuum oven, the product was obtained as an orange powder (0.820 g, 3.18 mmol, 91 %). The ^1H NMR spectrum showed traces of acetic acid (ca. 1 %).
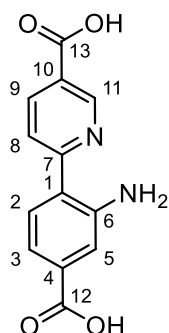
^1H NMR (d_6-DMSO, 600 MHz): δ[ppm] 13.04 (2H, *br*, s, CO_2**H**), 9.12 (1H, dd, $^4J_{H,H}$ = 2.3 Hz, $^5J_{H,H}$ = 0.75 Hz, H11), 8.32 (1H, dd, $^3J_{H,H}$ = 8.5 Hz, $^4J_{H,H}$ = 2.3 Hz, H9), 8.00 (1H, dd, $^3J_{H,H}$ = 8.7 Hz, $^5J_{H,H}$ = 0.66 Hz, H8), 7.74 (1H, d, $^3J_{H,H}$ = 8.3 Hz, H2), 7.44 (1H, d, $^4J_{H,H}$ = 1.7 Hz, H5), 7.16 (1H, dd, $^3J_{H,H}$ = 8.2 Hz, $^4J_{H,H}$ = 1.7 Hz, H3), 6.94 (2H, *br*, s, N**H**$_2$). ^{13}C NMR (d_6-DMSO, 150 MHz): δ[ppm] 167.3 (C12), 166.0 (C13), 161.3 (C7), 149.0 (C11), 148.2 (C6), 137.7 (C9), 132.3 (C4), 129.6 (C2), 123.9 (C10), 122.0 (C1), 121.7 (C8), 117.8 (C5), 116.1 (C3). HRMS *m/z* [M-H$^+$] ($C_{13}H_9N_2O_4^-$): Calcd: 257.0568 Found: 257.0569.
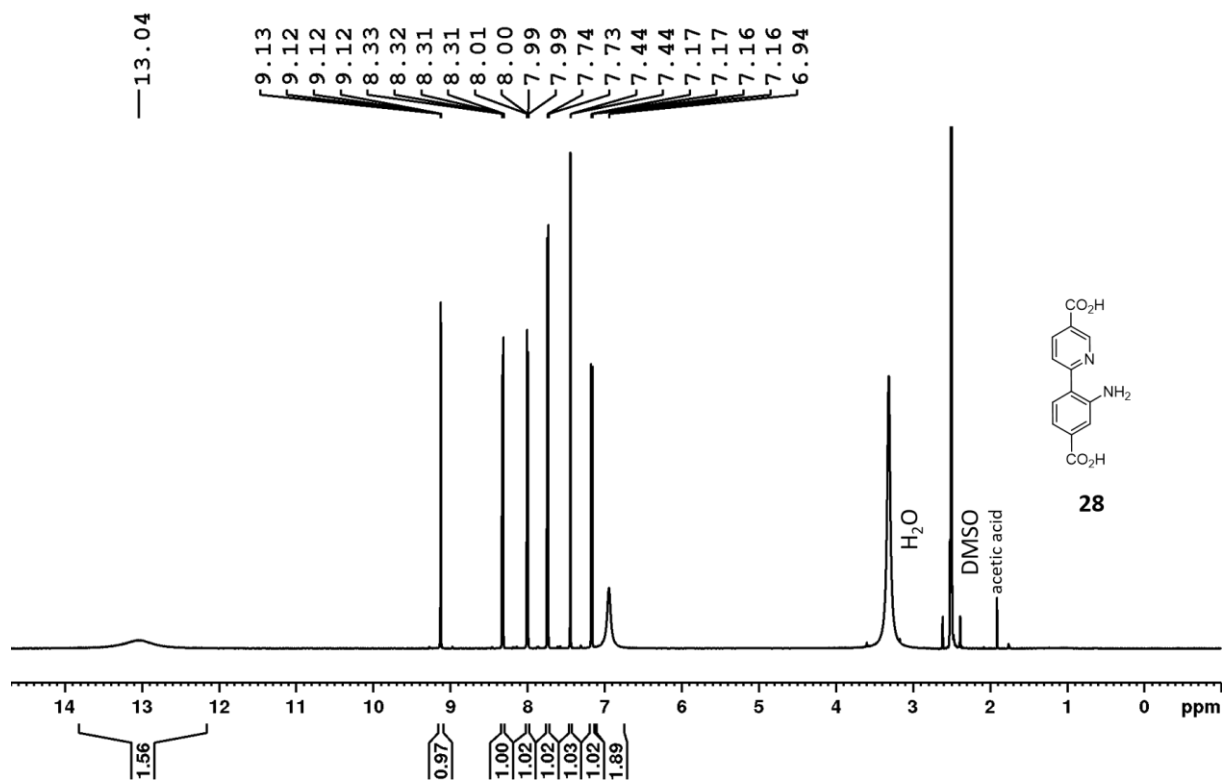
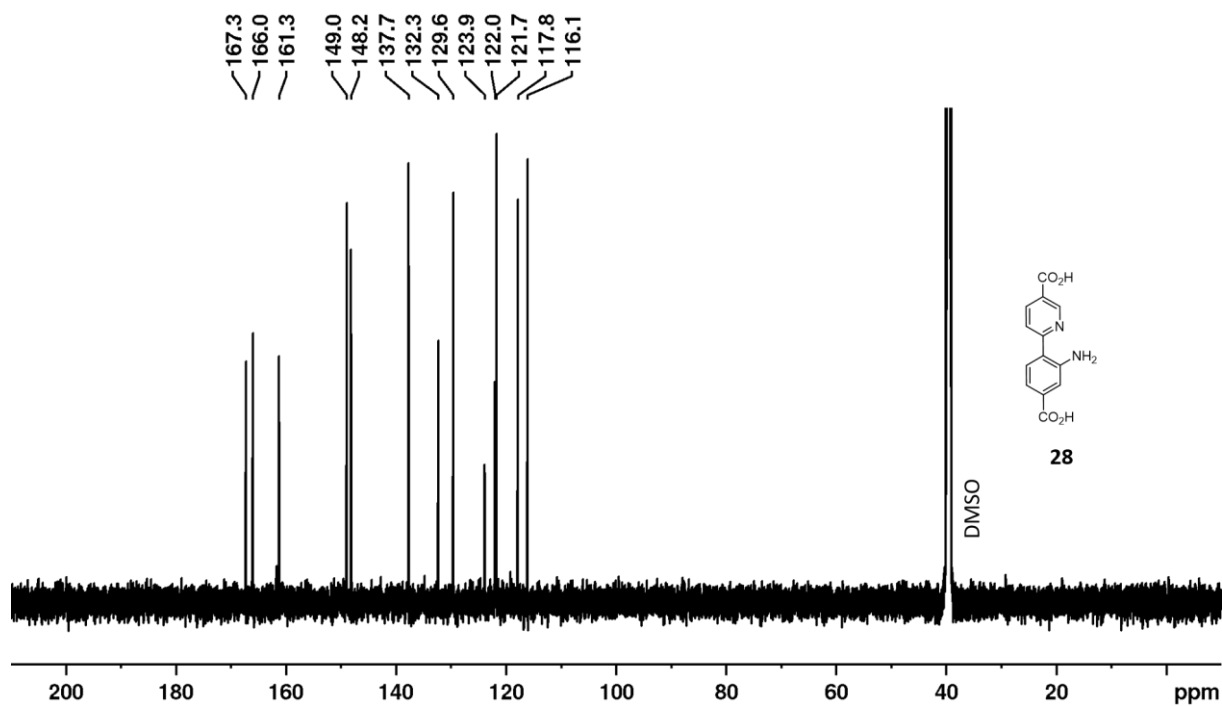Figure 46. ^{1}H NMR spectrum (600 MHz, d_6-DMSO) of **28**.

Figure 47. ^{13}C NMR spectrum (150 MHz, d_6-DMSO) of **28**.
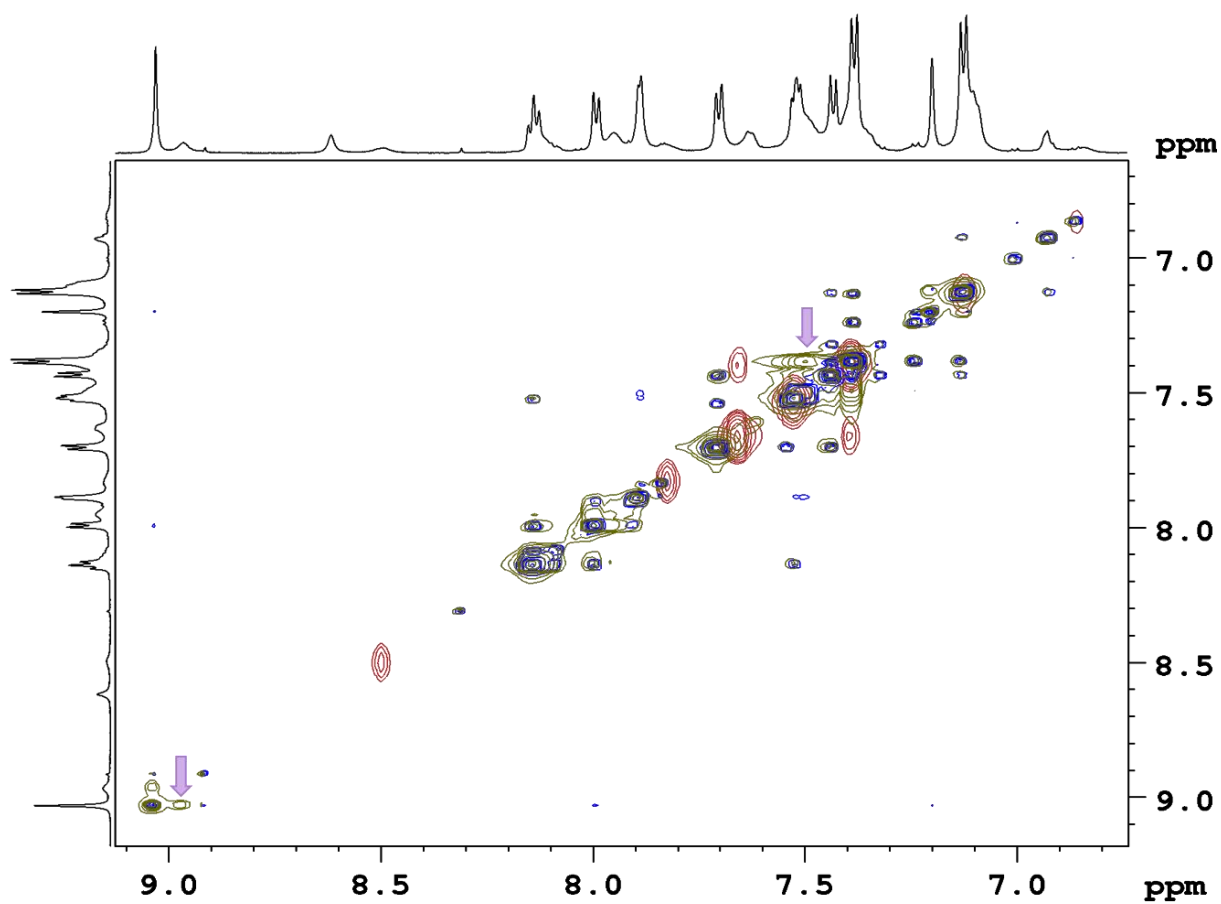
Other Data

Figure 48. Overlay of the NOESY/EXSY (d_6-DMSO, 600 MHz) spectra of complexes **1** (red) and **3** (blue) and a mixture of both (dark green). Two of the peaks that stem from neither complex and are only observed in the mixture are highlighted with a lavender arrow.
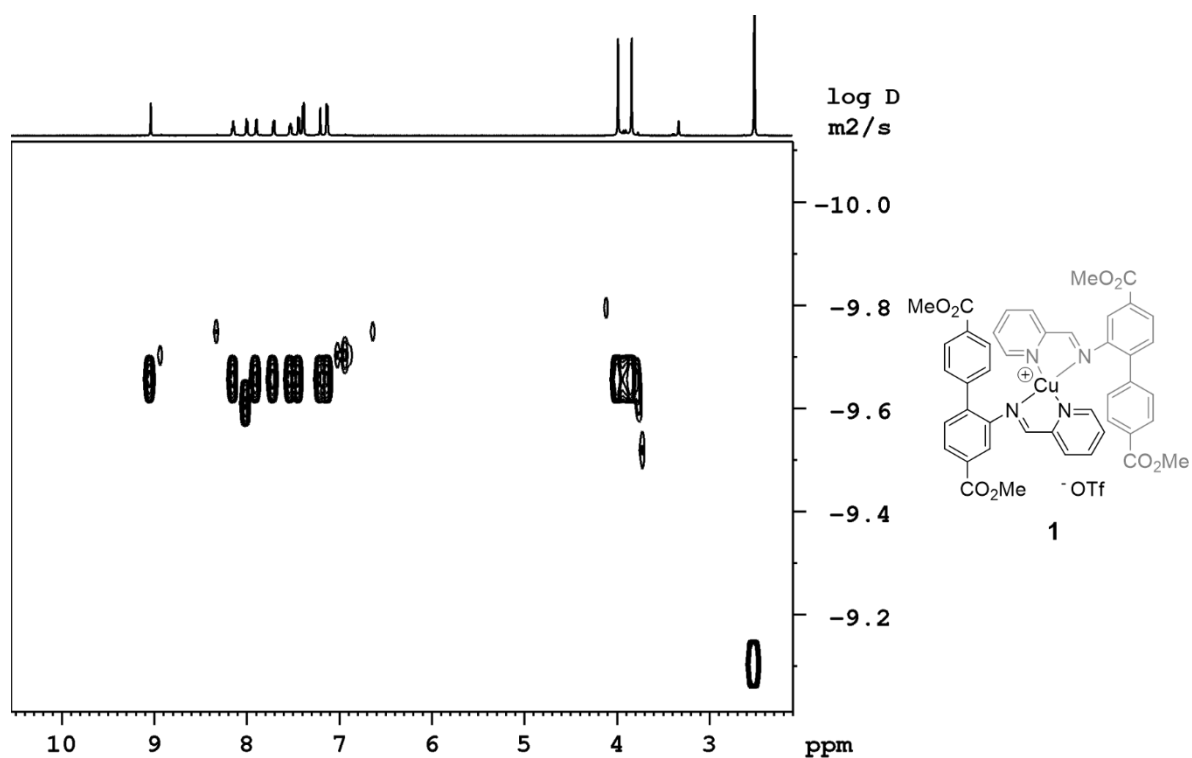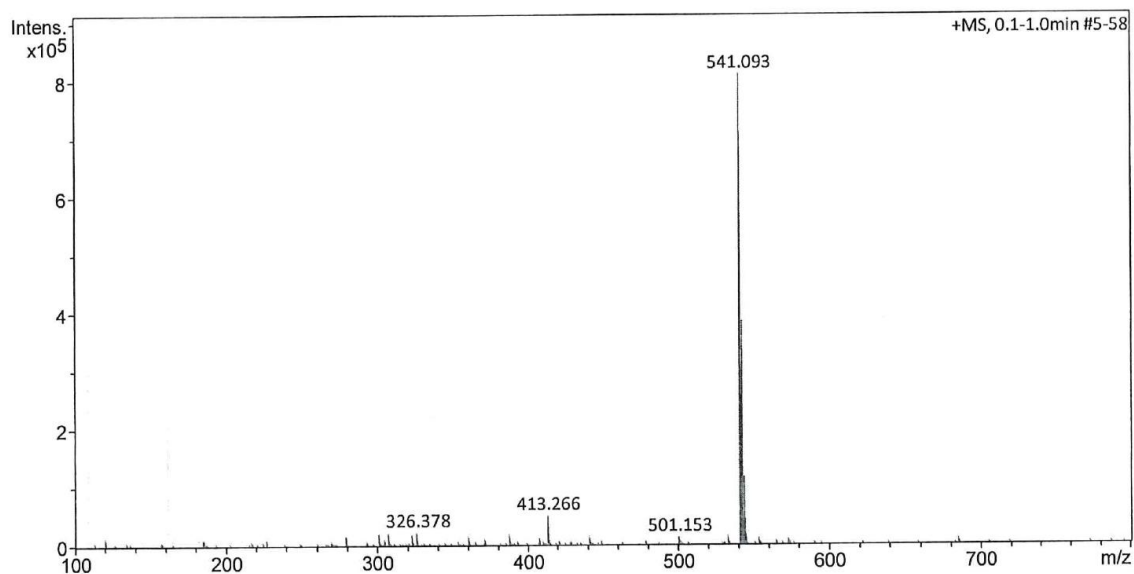
Figure 49. DOSY of **1** (600 MHz, d_6-DMSO).

Figure 50. ESI-MS spectrum of **11**. The peak at 413 m/z stems from the instrumentation.
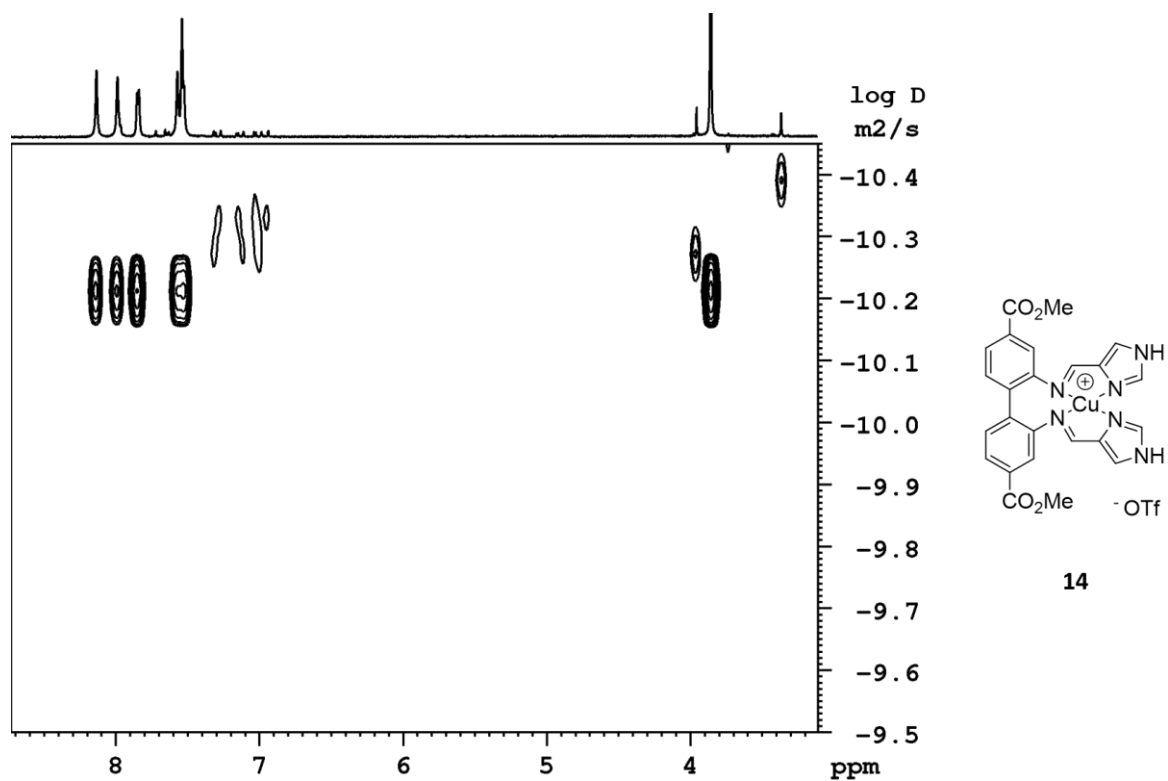
Figure 51. DOSY of **14** (600 MHz, CD₃CN).
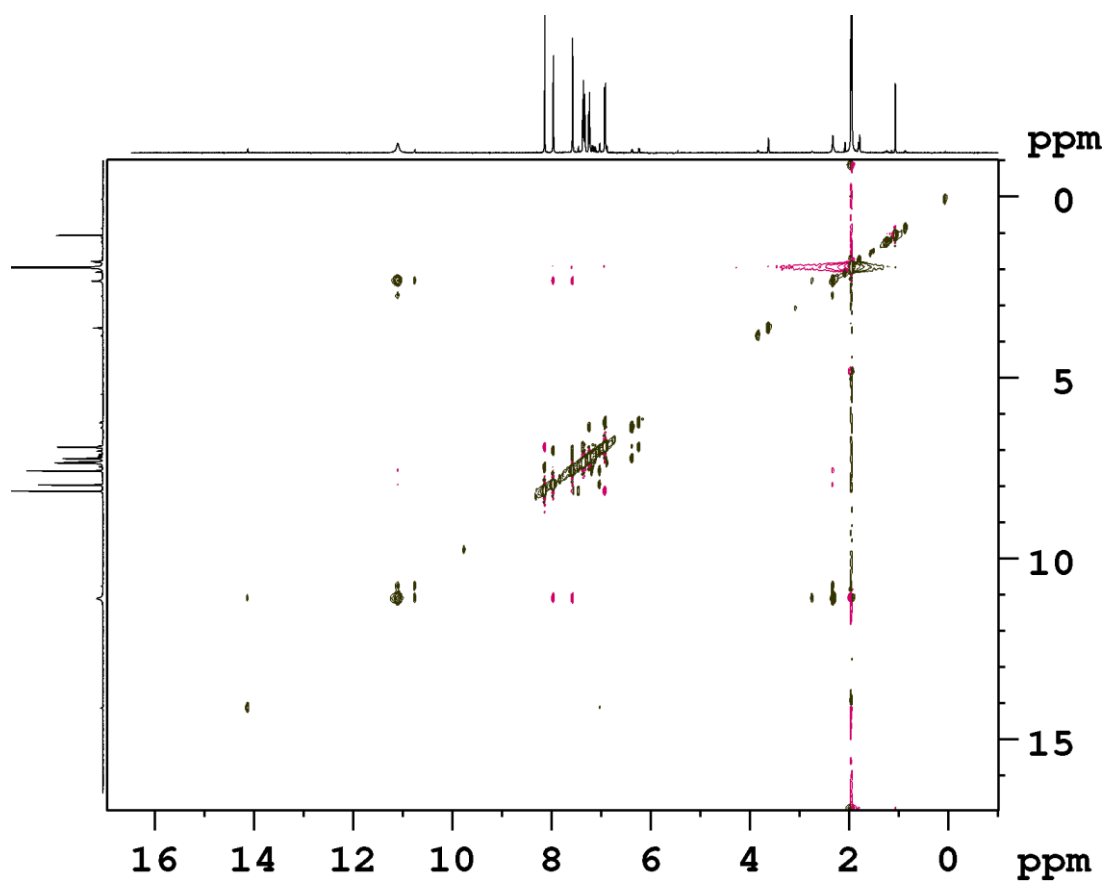
Figure 52. NOESY/EXSY of **18** at −34 °C (500 MHz, CD₃CN). EXSY peaks are in the same phase as the diagonal.

Table 5. Chemical shifts in d_6-DMSO of the protons in compound **11** (denoted **3** in Paper I, higher aggregates not included).
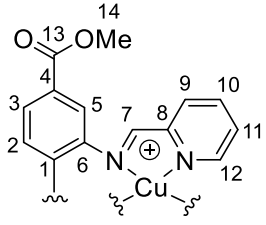
Proton #	Ligand δ [ppm]	Monomer δ [ppm]	Dimer δ [ppm]	Change upon dimerisation Δδ [ppm]
2	7.60	7.61	7.15	−0.46
3	7.94	7.91	7.27	−0.64
5	7.73	7.83	7.88	0.05
7	8.33	8.94	9.19	0.25
9	7.65	8.09	8.06	−0.03
10	7.83	8.26	8.10	−0.16
11	7.45	7.91	7.51	−0.40
12	8.55	8.90	7.44	−1.46
14	3.90	3.86	3.75	−0.11

Table 6. Chemical shifts in CD_2Cl_2 of the protons in the cyclohexane analogue of **11** reported by Ouali *et al.*[13] Numbering as reported in the same publication. The alkane protons 10 and 11 are not included, as they are reported as one common multiplet.
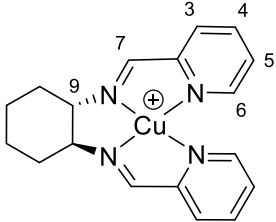
Proton #	Monomer δ [ppm]	Dimer δ [ppm]	Change upon dimerisation $\Delta\delta$ [ppm]
3	7.53	8.17 and 8.03	0.64 and 0.50
4	7.87	8.09 and 8.04	0.22 and 0.17
5	7.49	7.63 and 7.62	0.14 and 0.13
6	8.03	8.49 and 8.46	0.46 and 0.43
7	8.61	9.11 and 8.84	0.50 and 0.23
9	4.00	4.60 and 3.79	0.60 and −0.21

Table 7. Chemical shifts in CD₃CN of the protons in compound **18** at −34 °C (denoted **5** in Paper I). Chemical shifts of the supposed dimer were determined through EXSY.
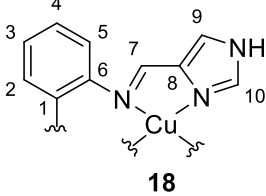
Proton #	Monomer δ [ppm]	Dimer δ [ppm]	Change upon dimerisation Δδ [ppm]
2,4 (overlap)	7.37	7.18, 6.90	−0.19, −0.47
3	7.25	6.39	−0.87
5	6.94	6.25	−0.69
7	8.15	7.47	−0.68
9	7.98	7.04	−0.94
10	7.59	7.20 and 7.04	−0.39 and −0.55
N**H**	11.12	10.77 and 14.15	−0.35 and 3.03

Table 8. Parameters of the fits in Figure 35. The fitting function is $y = a + bx^c$. The parameters a, b and c are given with their standard errors. c was not fixed.

Time	a	b	c
1 day	0.009 ± 0.004	0.013 ± 0.007	3 ± 1
2 days	0.008 ± 0.005	0.047 ± 0.008	2.3 ± 0.4
3 days	0.008 ± 0.005	0.053 ± 0.008	2.3 ± 0.3
4 days	0.019 ± 0.004	0.063 ± 0.007	3.1 ± 0.3

Table 9. Parameters of the fits in Figure 35. The fitting function is $y = a + bx^2$. The parameters a and b.

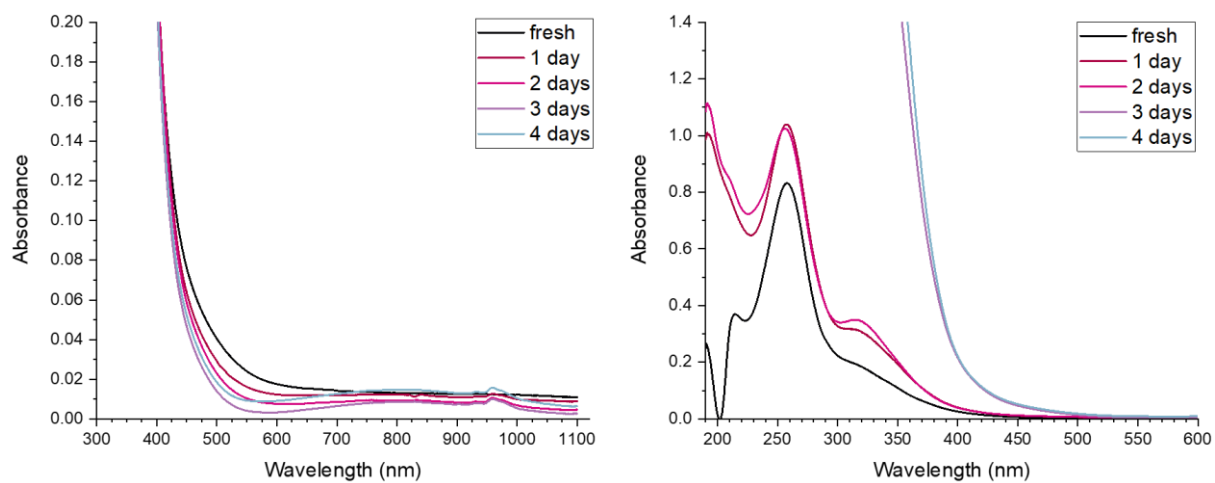| Time	a	b
1 day	0.006 ± 0.004	0.021 ± 0.003
2 days	0.006 ± 0.002	0.053 ± 0.002
3 days	0.005 ± 0.002	0.059 ± 0.002
4 days	0.005 ± 0.01	0.098 ± 0.009

Figure 53. UV/Vis spectra of the oxidation of **14** in acetonitrile at 0.15 mM. Left: Evolution of the d-d band. Right: Diluted 1:10.
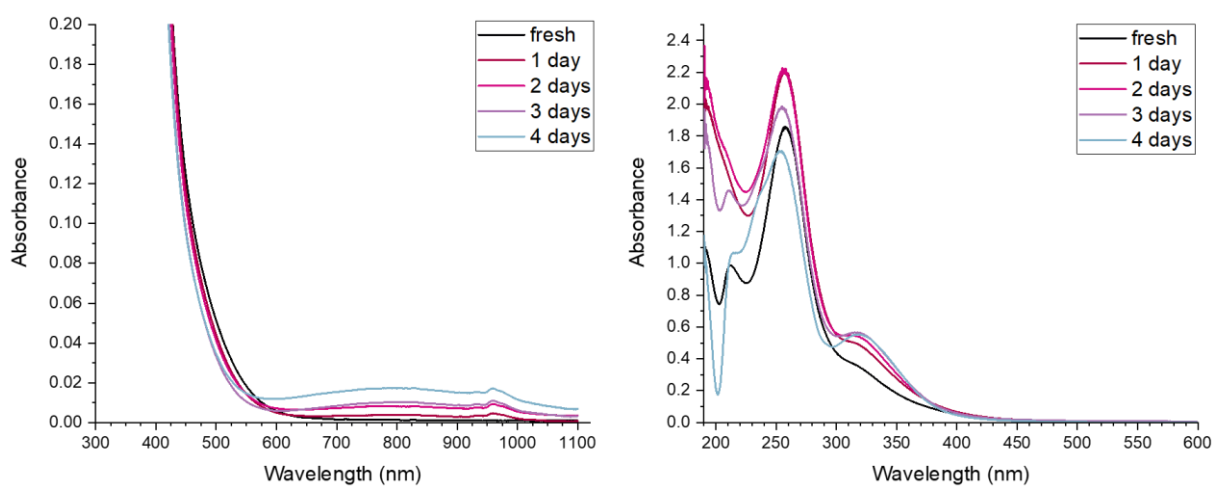

Figure 54. UV/Vis spectra of the oxidation of **14** in acetonitrile at 0.30 mM. Left: Evolution of the d-d band. Right: Diluted 1:10.
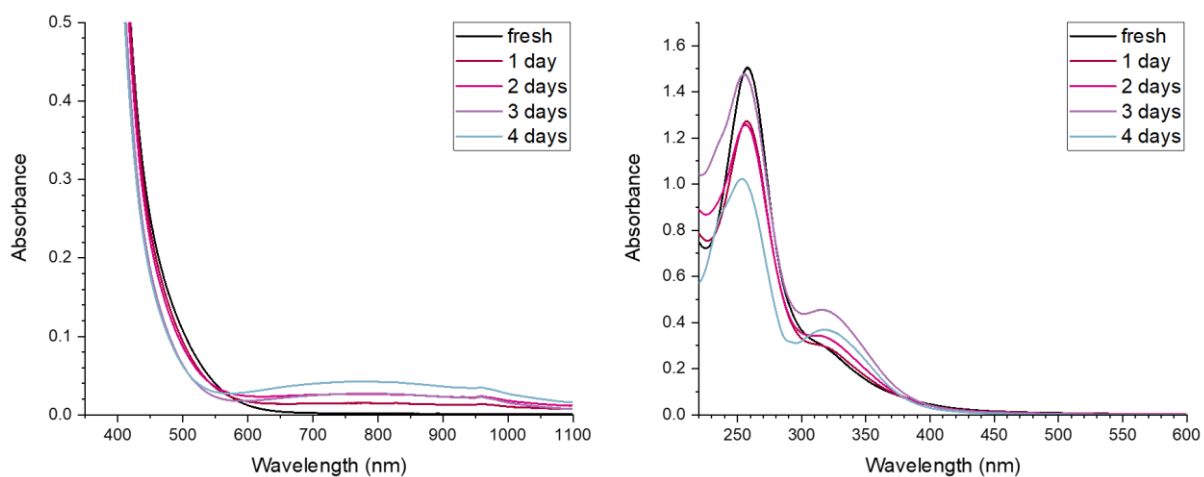
Figure 55. UV/Vis spectra of the oxidation of **14** in acetonitrile at 0.6 mM. Left: Evolution of the d-d band. Right: Diluted 1:30.
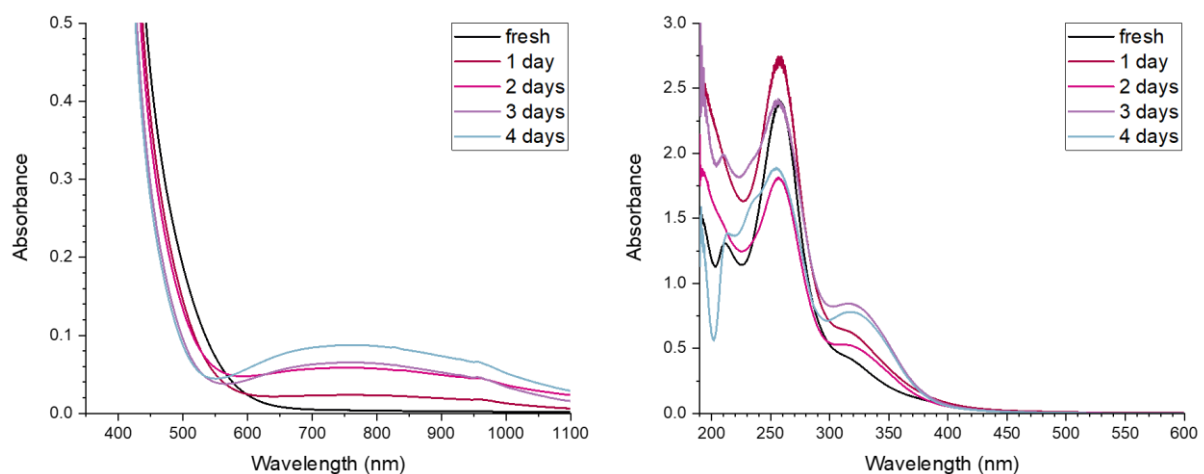

Figure 56. UV/Vis spectra of the oxidation of **14** in acetonitrile at 0.15 mM. Left: Evolution of the d-d band. Right: Diluted 1:30.
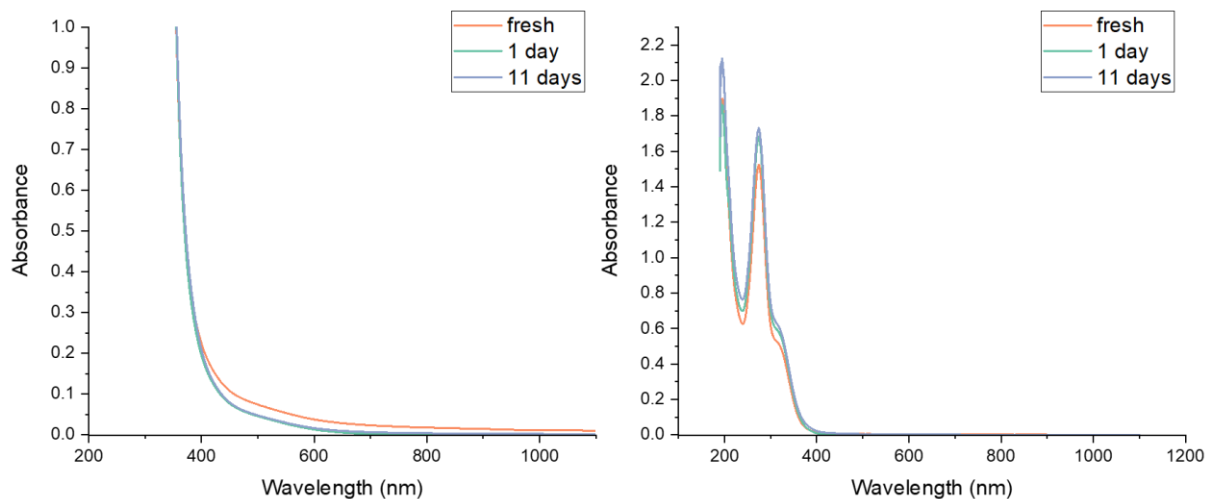
Figure 57. UV/Vis spectra of **3** in acetonitrile over time.
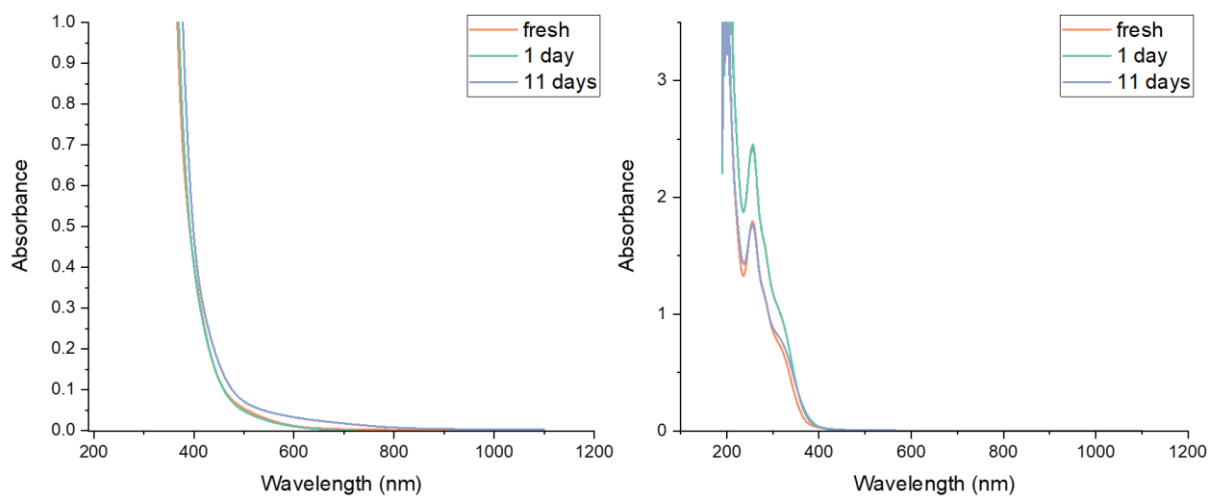
Figure 58. UV/Vis spectra of **5** in acetonitrile over time.

Autocorrect Propositions to Amuse the Adapt Reader

Adipic Acid	adipose acid
Aromats	aromas
Brønsted	Bronzed
CuOTf	coot
Denticity	dent city
Derivatisation	reprivatisation
Homoleptic	homoerotic
Metalated	mutilated
pi stacking	pistachios
salen	salon
tricoordinate	Trico ordinate

Appendix B: Papers I–IV

Appended are the final manuscript, the SI and the cover feature.

Paper II:

Appended are the manuscript and the SI, both are under preparation.

Paper III:

Appended are the manuscript and the SI, both are under preparation.

Appended is the final manuscript. For Paper IV, the SI was not appended as this thesis work only covers two of the compounds published in the Paper. The SI can be found online with the publication.

Paper I

Structural Elucidation, Aggregation, and Dynamic Behaviour of N,N,N,N-Copper(I) Schiff Base Complexes in Solid and in Solution: a Combined NMR, X-ray Spectroscopic and Crystallographic Investigation

Isabelle Gerz, Sergio Augusto Venturinelli Jannuzzi, Knut T. Hylland, Chiara Negri, David S. Wragg, Sigurd Øien-Ødegaard, Mats Tilset, Unni Olsbye, Serena DeBeer, Mohamed Amedjkouh

Cover Feature:
S. DeBeer, M. Amedjkouh and co-workers
Structural Elucidation, Aggregation, and Dynamic Behaviour of *N,N,N,N*-Copper(I) Schiff Base Complexes
in Solid and in Solution: a Combined NMR, X-ray Spectroscopic and Crystallographic Investigation

Structural Elucidation, Aggregation, and Dynamic Behaviour of *N,N,N,N*-Copper(I) Schiff Base Complexes in Solid and in Solution: A Combined NMR, X-ray Spectroscopic and Crystallographic Investigation
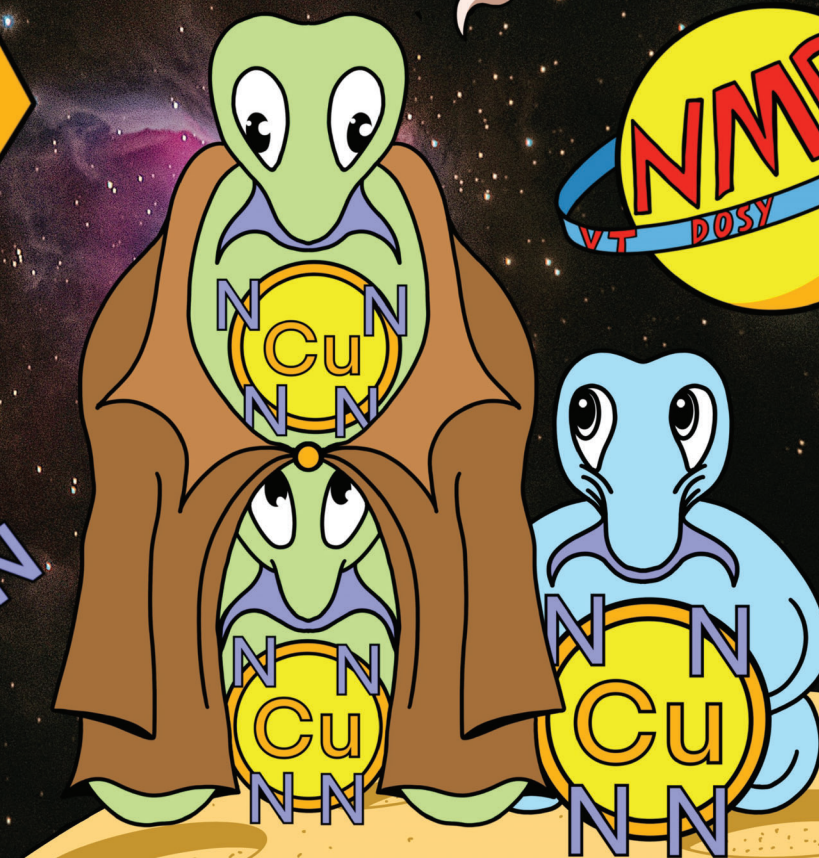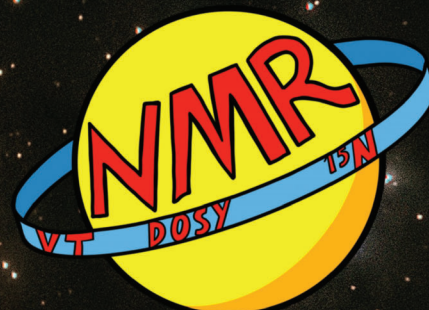
Isabelle Gerz,[a, b] Sergio Augusto Venturinelli Jannuzzi,[c] Knut T. Hylland,[a, b] Chiara Negri,[a, b] David S. Wragg,[a, b] Sigurd Øien-Ødegaard,[a, b] Mats Tilset,[a, b] Unni Olsbye,[a, b] Serena DeBeer,*[c] and Mohamed Amedjkouh*[a, b]

A series of Cu(I) complexes of bidentate or tetradentate Schiff base ligands bearing either 1-*H*-imidazole or pyridine moieties were synthesized. The complexes were studied by a combination of NMR and X-ray spectroscopic techniques. The differences between the imidazole- and pyridine-based ligands were examined by ^1H, ^{13}C and ^{15}N NMR spectroscopy. The magnitude of the $^{15}N_{imine}$ coordination shifts was found to be strongly affected by the nature of the heterocycle in the complexes. These trends showed good correlation with the obtained Cu—N_{imine} bond lengths from single-crystal X-ray diffraction measurements. Variable-temperature NMR experiments, in combination with diffusion ordered spectroscopy (DOSY) revealed that one of the complexes underwent a temperature-dependent interconversion between a monomer, a dimer and a higher aggregate. The complexes bearing tetradentate imidazole ligands were further studied using Cu K-edge XAS and VtC XES, where DFT-assisted assignment of spectral features suggested that these complexes may form polynuclear oligomers in solid state. Additionally, the Cu(II) analogue of one of the complexes was incorporated into a metal-organic framework (MOF) as a way to obtain discrete, mononuclear complexes in the solid state.

Introduction

Nitrogen-ligated copper complexes have been developed for a multitude of catalytic applications, ranging from water splitting[1–3] to C—X bond formation,[4,5] C—H activation,[6–11] and selective oxidations.[12–16] Enzymes with copper as a cofactor often combine the two latter aims and have inspired chemists to generate complexes with design elements taken from the active site of the enzyme. In this context, the histidine copper brace, a structural motif found in monooxygenases,[17–21] has

stood model for a range of complexes with aliphatic amines, amides or imines combined with heterocycles in the ligand.[22–27] The majority of bioinspired copper complexes are Cu(II) species,[23,26,28–30] while there are fewer examples in the Cu(I) oxidation state.[24,27,31] As Cu(I) complexes are closed-shell d10 species, the ligand field stabilization energy cannot dictate particularly favourable coordination environments for Cu(I), as it is the case for the cupric state.[32] In addition, heterocyclic copper complexes are prone to form assemblies – from simple dimers[33] to polynuclear aggregates[34,35] or even metal-organic frameworks (MOFs).[36,37] Polynuclear oligomers have been described and studied for copper complexes of multidentate imidazole[38–40] or pyridine[41] ligands. The diverse coordination numbers and geometries of Cu(I) species often demand a combination of spectroscopic and theoretical tools to describe their binding mode.[42] Given that oxidation is prevented, Cu(I) complexes are readily studied in solution by NMR, unlike their paramagnetic Cu(II) analogues. A particularly powerful NMR tool to evaluate coordination complexes bearing nitrogen ligands are ^{15}N coordination shifts; yet, they have been scarcely applied to copper compounds.[43,44] Although both stable isotopes of copper are NMR active nuclei, the applicability of both ^{63}Cu and ^{65}Cu NMR to copper complexes is limited to either highly symmetric complexes or CO-ligated species due to the extremely broad resonances for other types of complexes.[45,46] Other element-specific techniques, namely X-ray absorption (XAS) and emission (XES) spectroscopy,[47] are better-suited to observe the coordination centre through copper. Combined, they become particularly powerful to

[a] I. Gerz, Dr. K. T. Hylland, Dr. C. Negri, Dr. D. S. Wragg, Dr. S. Øien-Ødegaard, Prof. M. Tilset, Prof. U. Olsbye, Prof. M. Amedjkouh
Department of Chemistry,
University of Oslo
P. O. Box 1033 Blindern, 0315 Oslo, Norway
E-mail: mamou@kjemi.uio.no
[b] I. Gerz, Dr. K. T. Hylland, Dr. C. Negri, Dr. D. S. Wragg, Dr. S. Øien-Ødegaard, Prof. M. Tilset, Prof. U. Olsbye, Prof. M. Amedjkouh
Centre for Materials Science and Nanotechnology,
University of Oslo
P.O. Box 1126 Blindern, 0316 Oslo, Norway
[c] Dr. S. A. V. Jannuzzi, Prof. S. DeBeer
Department of Inorganic Spectroscopy,
Max Planck Institute for Chemical Energy Conversion
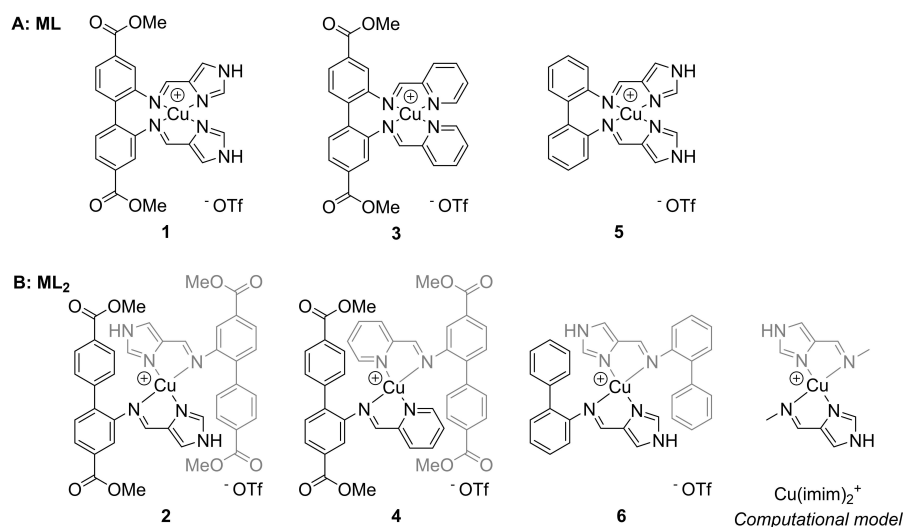Stiftstraße 34–36, 45470 Mülheim an der Ruhr, Germany
E-mail: serena.debeer@cec.mpg.de

Figure 1. Synthesized copper(I) complexes **1–6** and the computational model $Cu(imim)_2^+$. A: Complexes of the type ML bearing tetradentate ligands. B: Homoleptic ML_2 complexes with bidentate ligands.

identify key structural features of the complexes under study. To complement, density functional theory (DFT) calculations are presented to bring an in-depth assignment of spectral features in X-ray absorption and emission. In this article, we present the synthesis and characterisation of new copper(I) complexes bearing either bidentate *N,N* Schiff base ligands or tetradentate *N,N,N,N* Schiff base ligands (Figure 1). The heterocycle (either imidazole or pyridine) is connected to the biphenyl backbone through an imine – creating a 1,4-relationship between the coordinating nitrogen atoms. The biphenyl moiety of the complexes introduces a versatile backbone to tune the steric and electronic attributes of the system by established methods of organic chemistry. Notably, it introduces a possible anchor point for immobilization without strongly restraining the coordination geometry around the copper centre. Four of the herein reported complexes bear protected linker moieties in the form of methyl esters. The corresponding acids can function as linkers in metal-organic frameworks. Through the right choice of incorporation strategy, it can be ensured that isolated copper sites are created. Thereby MOF incorporation offers a pathway to circumvent the aforementioned aggregation, a common phenomenon for both, copper(I) and copper(II) complexes. We demonstrate the feasibility of MOF incorporation by post-synthetic linker modification for the copper(II) analogue of one of the complexes.
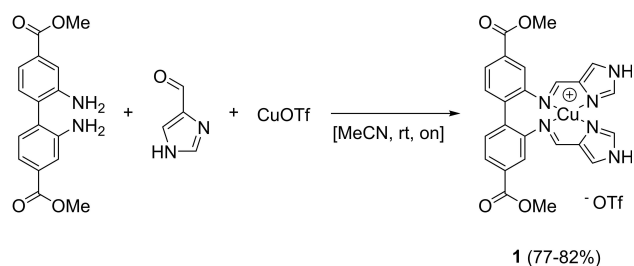
The solution behaviour of the complexes was studied by a combination of NMR techniques, namely ^{15}N NMR, diffusion ordered spectroscopy (DOSY) and variable temperature experiments. The findings on the copper ligation in solution were compared to those obtained from X-Ray characterisation of the solid state (single crystal XRD, XAS and XES). Finally, a DFT-assisted interpretation of the XAS and XES spectral features provides insight into the geometry around copper. Taken together the combined NMR, XRD and X-ray spectroscopic studies highlight the complexity of polynuclear Cu(I) structures

in both solid and solution states. The incorporation of the Cu(II)-analogue of one of these complexes into a MOF provides a clear future strategy for studying copper chemistry free of the complex aggregation behaviour reported herein.

Results and Discussion

Synthesis of Cu(I) Complexes

An obvious approach to obtain target **1** was to synthesize the ligand and subsequently metalate it with a Cu(I) salt. In literature, similar complexes have either been made by ligand synthesis and subsequent metalation,[48–50] or a one-pot synthesis.[51–53] Synthesizing the ligand for **1** by acid-catalysed condensation of 1*H*-imidazole-4-carbaldehyde with dimethyl 2,2'-diaminobiphenyl-4,4'-dicarboxylate resulted in poor yields. Therefore, condensation and metalation were attempted in one step (see Scheme 1), providing complex **1**. The synthesis is an overnight reaction at ambient temperature in acetonitrile, followed by a minimalistic work-up (filtration of the precipitated product). Complex **1** was isolated in good yields and high purity.

Scheme 1. Synthesis of complex **1**.

EurJIC
European Journal of Inorganic Chemistry

Full Papers
doi.org/10.1002/ejic.202100722

Chemistry Europe
European Chemical Societies Publishing

The complex was characterized by NMR, HRMS and elemental analysis. The ^{1}H NMR spectrum of **1** in d_6-DMSO shows six resonances in the aromatic region, each integrating for two protons. Additionally, there is one resonance at 13.35 ppm (imidazole NH, two protons) and one at 3.83 ppm (methyl group, six protons). The aldehyde and NH$_2$ resonances found in the starting materials are absent and instead, a resonance consistent with an imine was observed (8.31 ppm), correlating to a carbon resonance at 154.5 ppm in an HSQC experiment. The synthesis method depicted in Scheme 1 was extended to five more copper(I) complexes (**2–6**) (Figure 1). For all of them, MS showed an *m/z* consistent with the complex cation charged +1. The complexes were isolated in high purities (demonstrated by elemental analysis) and in fair to good yields. The resulting tetracoordinated complexes can be divided into two groups. The first group (**1**, **3** and **5**, Figure 1A) is of the type ML, where L is a tetradentate ligand. The other group (Figure 1B) consists of complexes **2**, **4** and **6**. Starting from 2-aminobiphenyls, the formation of ML$_2$ (L being a bidentate ligand) complexes was consistently observed by NMR, MS and elemental analysis. For compounds **2** and **4**, single crystal structures showed the coordination of two bidentate ligands (Figure 7, Figure S71). The preferential formation of ML$_2$ complexes has been reported before for bi- and tridentate ligands that coordinate through nitrogen to copper (I).[54,55]

NMR Studies of Dynamic Solution Behaviour: Ligand Exchange and Aggregation

All complexes were fully characterized by NMR, albeit the solution behaviour of some caused intricate NMR spectra (see Figure 2). Intriguingly, the choice of solvent not only affected the res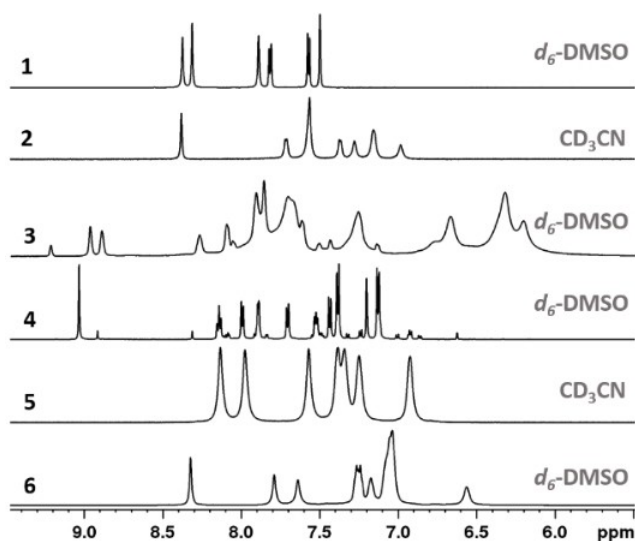onances' broadness and chemical shifts, but also the number of observable species (see below). Possible explanations for the solution behaviour are changes in ligation and/or conformation. Typical processes that induce ligation changes in copper(I) and other d^{10} species are solvent coordination, intermolecular ligand exchange and/or aggregation.[42,45,56–61] For reference purposes, the ligand of each complex was synthesized by adapting previously reported procedures for Schiff base ligands.[62]

Based on literature reports for similar ML$_2$-type complexes,[60,63,64] it seems likely that complexes **2**, **4** and **6** are in equilibrium with an ML complex and the free ligand. However, the ligand of **4** could not be identified as (one of the) minor species in the ^{1}H NMR spectrum of **4** in d_6-DMSO, while the observation of all three species (ML$_2$, ML and free ligand) in the mass spectra of the ML$_2$ complexes (see SI) supports the hypothesis. An NMR experiment on a sample containing both complex **2** and **4** did not only show the sum of both ^{1}H NMR spectra, but also peaks belonging to neither parent complexes or their free ligands (see Figure S67). The formation of the new species was too fast to be followed by NMR. Cross peaks resulting from chemical exchange between these new proton signals and signals from the parent complexes were observed in the NOESY/EXSY spectrum of the mixture (see Figure S68). Based on these observations, we speculate that the new species might be a heteroleptic complex bearing one imidazole and one pyridine ligand. Concluding, ligand exchange is likely to occur, but it seems to be a rapid process on the NMR time scale that does not explain the observation of multiple species in the ^{1}H NMR spectrum of **4** in d_6-DMSO.

The solution behaviour of **4** was further studied by variable temperature NMR (VT NMR). In order to lower the temperature without freezing the sample, the experiment was conducted in acetonitrile. The change of solvent altered the appearance of **4** at room temperature: Instead of multiple species, a single species with broadened peaks was observed (Figure 3, 25 °C).
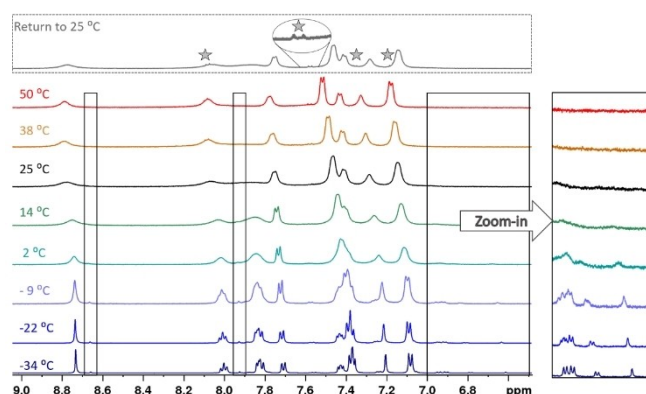

Figure 2. Aromatic region of the ^{1}H NMR spectra (600 MHz, 25 °C) of the copper(I) complexes synthesized in this work.

Figure 3. Aromatic region of the ^{1}H NMR spectra of **4** at different temperatures (CD$_3$CN, 500 MHz). Black boxes indicate some of the areas where the minor species is observable at low temperatures. The rightmost box is displayed with higher intensities for all spectra to improve visibility of the additional peaks. The top spectrum was recorded after the temperature experiment. It is largely consistent with the initial room temperature experiment, but traces of decomposition were observed (indicated by stars).

EurJIC
European Journal of Inorganic Chemistry

Full Papers
doi.org/10.1002/ejic.202100722

Chemistry Europe
European Chemical Societies Publishing

The sample was cooled down to $-34\,°C$ in increments of around $10\,°C$.

This resulted in narrower peaks and the evolution of additional peaks (boxes in Figure 3), similar to the room temperature measurement in d_6-DMSO. The species giving rise to the new peaks interconverts with the major species, as revealed by chemical exchange cross-peaks in a NOESY/EXSY experiment (see Figures S26 and S30) conducted at the lowest temperature ($-34\,°C$). These processes, which we were not able to identify unambiguously, were reversible: spectra acquired during step-wise temperature increase were identical to those during the cool-down process. Further temperature elevation above $25\,°C$ led to peak narrowing, but minute signs of decomposition were observed. The decomposition peaks persisted upon return to room temperature (stars in the top spectrum in Figure 3). Identification of the decomposition product for **4** (and other complexes) can be found in the SI (Figure S65). Otherwise, the spectrum regained its initial appearance. In summary, ligand exchange seems to be only identifiable process for the observations made for **2**, **4** and **6** in NMR.

The experiments discussed below on **1**, **3** and **5** showed that for the ML complexes a different phenomenon causes their non-trivial NMR spectra – the formation of polynuclear species. A VT NMR experiment was conducted on **3** in CD$_3$CN, yielding spectra with severe line broadening at all temperatures ($-34\,°C$ to $50\,°C$, Figures S61 and S62). A separate VT NMR experiment was therefore conducted in d_6-DMSO (Figure 4), showing a temperature dependent equilibrium between three species at room temperature:
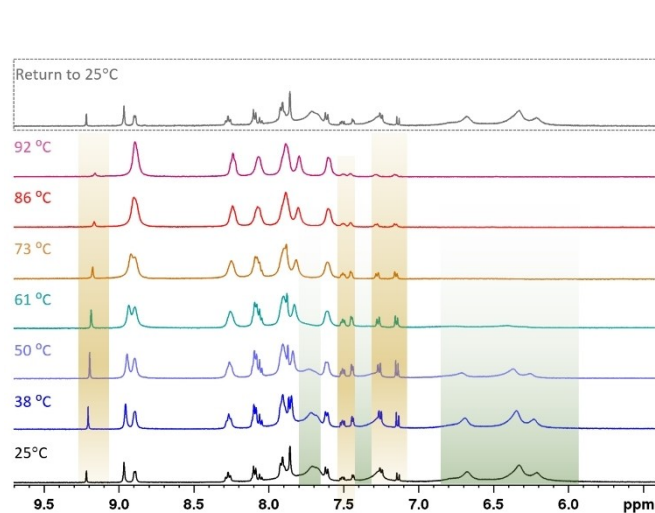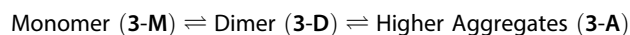
$$\text{Monomer (3-M)} \rightleftharpoons \text{Dimer (3-D)} \rightleftharpoons \text{Higher Aggregates (3-A)}$$

The room temperature spectrum featured two species with sharp resonances, of which the minor (**3-D**) integrates roughly to a third of the major species (**3-M**). Additionally, a species (**3-A**) with severely broadened resonances and a considerable upfield shift is observable. In the interval from $25\,°C$ to around $60\,°C$, the signal intensity of **3-A** (green highlights in Figure 4) decreases. The aggregates seem to mainly break up into dimers, as **3-D**'s intensity gain (brown highlights in Figure 4) comes at the expense of the aggregate's intensity. As temperature is further increased, **3-D** is minimised again until the entropically favoured **3-M** dominates the spectrum at $90\,°C$. The changes were reversible and return to room temperature reproduced the initial room temperature spectrum. The assignment of the involved species was supported by a DOSY experiment (Figure 5), as the three species have different diffusion coefficients. **3-M** diffuses fastest, closely followed by **3-D**. On the other hand, **3-A** diffuses significantly slower. Evans *et. al* obtained good correlations between the molecular weight and the diffusion coefficients of small molecules without heavy atoms (not heavier than sulphur) by applying the Stokes-Einstein-Gierer-Wirtz estimation (SEGWE).[65,66] Despite copper violating the requirement for light atoms, the diffusion coefficients calculated by this method support the assignment of monomeric and dimeric species for **3-M** and **3-D** (Figure 5). Furthermore, it allowed identifying **3-A** as higher aggregates with an estimated average composition of around twenty monomeric units.

In d_6-DMSO, the ^{1}H NMR spectrum of **1** shows one species alone. In CD$_3$CN however, there were minor species observable at room temperature in addition to the major species. A VT NMR experiment, ranging from $25\,°C$ to $-34\,°C$, was conducted in acetonitrile, to see if aggregation behaviour could be identified for **1** (Figure 6). The additional minor species became more prominent upon temperature decrease and reached
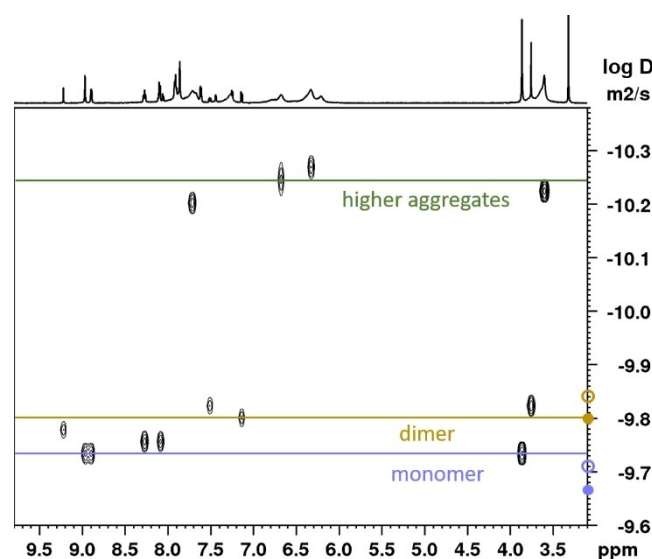

Figure 4. Aromatic region of the ^{1}H NMR spectra of **3** at different temperatures (500 MHz, d_6-DMSO). At room temperature, three species are observable. Above $70\,°C$, the broad resonances of **3-A** have disappeared and only **3-M** and **3-D** remain. At the highest temperature, **3-M** dominates the spectrum. As the $25\,°C$ spectrum after the temperature elevation (top spectrum) is equal to the initial $25\,°C$ spectrum before the VT NMR experiment (bottom spectrum), the observed processes are reversible.

Figure 5. Diffusion ordered spectroscopy (DOSY) of **3** (600 MHz, d_6-DMSO). Circles on the y-axis indicate calculated diffusion coefficients for the monomer and dimer (full circles for the complex cations, hollow circles for the ion pairs). The coefficients were calculated using the SEGWE D/MW calculator developed by Evans and et al.[65,66]
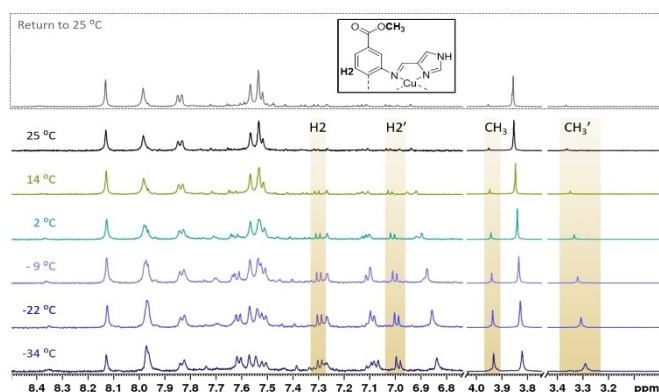
EurJIC
European Journal of Inorganic Chemistry

Full Papers
doi.org/10.1002/ejic.202100722

Chemistry Europe
European Chemical Societies Publishing

Figure 6. Partial ^{1}H NMR spectra of **1** at different temperatures (500 MHz, CD$_3$CN). One of the minor species shows two sets of signals, here highlighted for the methyl group and H2, a proton on the biphenyl backbone. As the room temperature spectrum after the temperature decrease (top spectrum) is equal to the initial room temperature spectrum before the VT NMR experiment (bottom spectrum), the observed processes are reversible.

similar intensities to those of the major species at the lowest investigated temperature. As the peaks of the minor species do not increase in parallel, more than one minor species must be present. The identification of the minor species is complicated by the amount and overlap of resonances. At intermediate temperatures (2 °C and −9 °C), only one of them has risen significantly above the baseline. Therefore, we will focus our discussion on these spectra.

Most of the minor species' aromatic resonances were shifted upfield compared to those of the major species, similarly to what was seen for most of **3-D**'s aromatic resonances with respect to those of **3-M**. While **3-D** showed as many resonances as **3-M**, indicating magnetic equivalency of the resonances in the ligand, this was not observed for the minor species of **1**. Instead, two sets of resonances were observed, as highlighted for the methyl group and one of the phenyl protons (H2) in Figure 6. There are literature examples of dimeric copper(I) complexes either maintaining or losing the magnetic equivalency of their tetradentate pyridine Schiff base ligands.[33,51] The postulation of the dimeric nature of this species is not only based on the twofold set of resonances and the upfield shifts for most aromatic resonances, but also the strong difference between the two shifts of each pair of proton resonances. This is especially pronounced for the NH proton and the methyl group. While one of the resonances has a similar shift to the corresponding resonance in the major species, the other is located further away (at −9 °C: $\Delta\delta$CH$_3$ = +0.11 and −0.51; $\Delta\delta$NH = +3.36 and −0.26). Solvent coordination or partial decoordination can be ruled out as the source of magnetic inequivalency by the pronounced effect on the remote methyl groups. A more likely explanation are ring currents caused by aromatic rings placed in spatial proximity by the dimerization.

A VT NMR experiment for **5** in acetonitrile revealed similar processes as seen for **1** to be operative (see Figures S63 and S64). At room temperature, one species with broad resonances was observed, but minor species were detected at temperatures

below 2 °C. In d_6-DMSO, complex **5**'s resonances were even broader than in acetonitrile (Figure S32). Overall, the VT NMR experiments suggest dimerization and possibly even the presence of higher oligomers for **1** and **5** (see spectra at the two lowest temperatures in Figure 6). While the aggregation behaviour of **3** could be studied well by means of NMR, the low intensities of the minor species paired with the additional complexity of the ^{1}H NMR spectra of **1** and **5** in acetonitrile at lower temperatures complicated the complete assignment of these species. The different appearances of **1**, **3** and **5** in different solvents show that the aggregation behaviour is influenced by the solvent. Ouali *et al.* found that acetonitrile was non-innocent in the dimerization process of a complex closely related to **3** (the imines are connected through a cyclohexyl bridge instead of the biphenyl),[67] and the same is likely for other coordinating solvents, such as DMSO. Studying the complexes' solid behaviour allows to remove solvent effects and the interactions between complexes may be augmented by the naturally higher concentration. Despite numerous attempts, no crystals suitable for single crystal XRD could be obtained for any of the ML complexes. To gain further insights into polynuclear assemblies of **1** and **5**, they were investigated through the Cu K-edge (see below).

^{15}N Coordination Shifts

The nitrogen shifts in NMR are good descriptors of the coordination centre in *N*-ligated coordination complexes.[43,44] Due to the low sensitivity and natural abundance of ^{15}N, the nitrogen shifts were determined indirectly through ^{1}H-^{15}N HMBC experiments. The complexes' ^{15}N shifts seem to form two groups according to the heterocycle they are based on (see Table 1). The pyridine-based complexes have upfield δ^{15}N$_{imine}$ shifts relative to the imidazole-based compounds. The type of complex, ML or ML$_2$, seems to have little effect on the nitrogen shifts when they bear the same heterocycle. **1**, **2** and **6** have similar nitrogen NMR shifts (δ^{15}N$_{imine}$ ≈ −85 ppm; δ^{15}N$_{IM}$ ≈ −171 ppm; δ^{15}N$_{AZ}$ ≈ −205 ppm). Even though **5** was measured in another solvent (acetonitrile), the nitrogen shifts resemble those of the other imidazole-bearing copper complexes. The pyridine-based complexes **3-M** and **4** also have similar shifts to each other, with δ^{15}N$_{imine}$ ≈ −92 ppm and δ^{15}N$_{pyridine}$ ≈ −128 ppm. However, the nitrogen shifts of **3-D**, δ^{15}N$_{imine}$ = −107.7 ppm and δ^{15}N$_{pyridine}$ = −105.3 ppm, are quite different compared to those of **3-M**.

The effect of the copper ligation manifests itself in the coordination shifts $\Delta\delta^{15}$N, which are calculated from the difference of the nitrogen shift in the free ligand and in the complex.[43,44] Coordination shifts were obtained for **1**, **2**, **3**, **4** and **6**. The ligand of **5** was not soluble in acetonitrile, while the NMR resonances of the complex were severely broadened in DMSO and methanol. As ^{15}N NMR coordination shifts are solvent-dependent,[68] no coordination shift was calculated.

The resonances corresponding to **3-A** are likely too broad to show defined crosspeaks in ^{1}H-^{15}N HMBC, but the coordination shifts for both, **3-M** and **3-D**, were obtained. The $\Delta\delta^{15}$N$_{imine}$ are

EurJIC
European Journal of Inorganic Chemistry

Full Papers
doi.org/10.1002/ejic.202100722

Chemistry Europe
European Chemical
Societies Publishing

Table 1. ^{15}N NMR shifts in ppm. The spectra are recorded in d_6-DMSO, unless noted otherwise. All shifts are reported relative to an external nitromethane standard. Coordination shifts $\Delta\delta^{15}$N, if obtained, are given in squared brackets. ^{1}H-^{15}N HMBC spectra of complexes **1–6** and their ligands are given in the SI.

| Compound	$\delta^{15}N_{imine}$ [$\Delta\delta^{15}N_{imine}$]	$\delta^{15}N_{pyridine}$ [$\Delta\delta^{15}N_{pyridine}$]	$\delta^{15}N_{IM}$ [$\Delta\delta^{15}N_{IM}$]	$\delta^{15}N_{AZ}$ [$\Delta\delta^{15}N_{AZ}$]
1	−83.2 [−13.7]		−173.4 [−57.3]	−203.7 [+7.1]
2	−86.0 [−16.1]		−171.7 [−55.2]	−205.6
3-M	−89.6 [−41.7]	−128.6 [−67.0]		
3-D	−107.7 [−59.8]	−105.3 [−43.7]		
4	−94.0 [−46.1]	−126.8 [−64.3]		
5[a]	−79.1		−170.5	−211.4
6	−86.1 [−21.1]		−170.0 [−52.8]	−206.1 [+3.5]

[a] measured in acetonitrile.

−41.7 ppm for **3-M** and −59.8 ppm for **3-D**, while the $\Delta\delta^{15}N_{pyridine}$ are −67.0 ppm and −43.7 ppm respectively (Table 1). This suggests that the copper-imine bond is strengthened at the expense of the copper-pyridine bond upon dimerization. Van Stein *et al.* found $\Delta\delta^{15}N_{imine} = -47.0$ ppm and $\Delta\delta^{15}N_{pyridine} = -36.1$ ppm for a closely related dimeric copper compound (the imines are connected through an ethyl bridge instead of the biphenyl) in methanol.[33] The magnitudes of the coordination shifts differ somewhat, but the greater effect on N_{imine} compared to $N_{pyridine}$ is in good agreement with **3-D**'s coordination shifts, further supporting **3-D**'s dimeric nature. Complex **4**'s coordination shifts are similar to those of **3-M**, as anticipated from the similarity in absolute shifts.

The imidazole complexes have smaller $\Delta\delta^{15}N_{imine}$ (−13.7 ppm for **1**, −16.1 ppm for **2** and −21.1 ppm for **6**) than the pyridine-based complexes reported herein. The coordinating nitrogen of the imidazole is strongly affected ($\Delta\delta^{15}N_{IM} = -57.3$ ppm for **1**, $\Delta\delta^{15}N_{IM} = -55.2$ ppm for **2** and $\Delta\delta^{15}N_{IM} = -52.8$ ppm for **6**), while the NH is barely influenced ($\Delta\delta^{15}N_{AZ} = +7.1$ for **1** and $\Delta\delta^{15}N_{AZ} = +3.8$ ppm for **6**), consistent with this nitrogen not being involved in the coordination to copper.

Single-Crystal XRD

It was possible to obtain crystals suitable for single crystal XRD analysis by recrystallizing **4** from MeCN/toluene (Figure 7).

The tetracoordinated environment surrounding copper is an intermediate geometry between square-planar and tetrahedral, as determined by the structure's τ_4'-value ($\tau_4' = 0.50$). τ_4' is a geometry index for tetracoordinated complexes that adapts values between 0 (square planar) and 1 (tetrahedral).[69,70] The imine–N–copper bonds (N1–Cu: 2.054(2) Å; N3–Cu: 2.085(2) Å) are slightly longer than the pyridine–N–copper bonds (N2–Cu: 2.028(2) Å; N4–Cu: 2.021(2) Å). These bond lengths are in very good agreement with the $\Delta\delta^{15}$N of **4**, where both, imine and pyridine nitrogen, showed considerable coordination shifts, with the pyridine undergoing the larger change upon ligation. The crystal structure of **4** shows large differences between the two ligands, despite their identical connectivity. For one, the
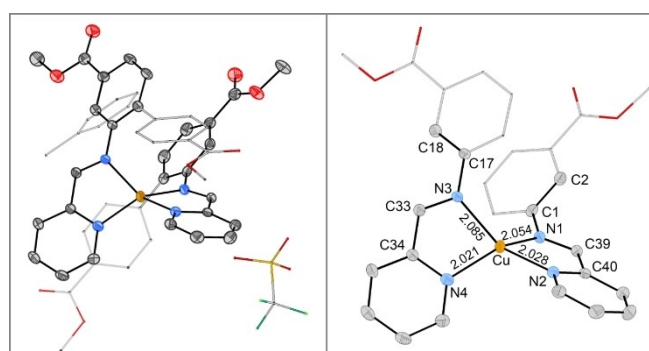
Figure 7. ORTEP plots of **4** (ellipsoids at 50% probability). The asymmetric unit contains the complex cation, the non-coordinating anion and a solvent molecule (toluene). Hydrogen atoms are omitted and parts of the structure are represented as sticks for clarity. Selected bond lengths: (Cu–N1: 2.054(2) Å; Cu–N2: 2.028(2) Å; Cu–N3: 2.085(2) Å; Cu–N4: 2.021(2) Å).

bond lengths to copper differ not only between the types of nitrogen but also between the two ligands, creating an unsymmetric environment around copper (see Figure 7, right side). The lack of symmetry is even clearer when comparing the dihedral angles between the imine and the adjacent phenyl ring, which were measured to be −27.1(4)° (C33–N3–C17–C18) and −42.8(4)° (C39–N1–C1–C2) respectively. Each pyridine ring π-stacks with the non-imine-bearing phenyl ring of the other ligand in the same complex. Together with the co-crystallisation of a solvent molecule (toluene), these interactions can account for the distortions from a symmetric arrangement of the two identical ligands around copper. Additionally, crystallisation of complex **2** from MeCN/Et$_2$O resulted in fine needles that afforded a preliminary crystal structure (see SI for more details). The imine-copper bonds (2.21(2) Å and 2.32(2) Å) were elongated compared to those in **4**. These elongated, thus weaker, N_{imine}–Cu bonds in **2** compared to **4** are in line with smaller $\Delta\delta^{15}N_{imine}$ for the imidazole-based complexes compared to the pyridine-based complexes. Contrarily, the imidazole-copper bonds were 1.915(12) Å and 1.929(12) Å, so considerably shorter than the pyridine-copper bonds in **4**. The triflate counterion

does not coordinate to either **2** or **4**, but for **2** a hydrogen bond to the imidazole-NH was noted.

X-ray Absorption and Emission Spectroscopy

While ^{1}H, ^{13}C and ^{15}N NMR provided structural information based on the ligands' nuclei, X-ray spectroscopy was employed to furnish structural insights through the selective interrogation of the Cu centre and its surrounding. Of special interest were the tetracoordinate copper imidazole complexes **1** and **5**, as they could not be crystallised and their solution behaviour hinted agglomeration. While the monomers were the dominating species in solution at room temperature, a different situation might be found for the solid state, where the copper centres are in closer proximity to each other and solvent effects are absent. The Cu K-edge X-ray absorption spectra (XAS) for complexes **1** and **5** in solid state are shown in Figure 8.

As expected for closed-shell d^{10} systems, no 1s to 3d pre-edge feature are observed in the XAS spectra. The lowest lying transitions at 8984.5 and 8987.8 eV are attributed to dipole allowed 1s–4p transitions. These features are informative of the Cu(I) coordination symmetry based on the seminal work by Kau *et al.*[71] Two-coordinate linear Cu(I) are characterized by a sharp and very intense peak at ca. 8984 eV (intensities of ca. 1 *vs* normalized edge jump), whereas four-coordinate tetrahedral species give rise to much weaker rising edge features at higher energies (intensities of ca. 0.8). See SI for further information. The intensity of the rising edge features in **1** and **5** are most consistent with four-coordinate Cu(I) complexes.[71] The position of the K-edge taken as the first inflection point is 8982.2 eV for both complexes. Moreover, both spectra show at least two features at 8984.8 and 8988.0 eV, although in **5** the rising edge features are less intense. An intermediate feature at 8986.0 eV is more noticeable in **1** than in **5**. The overall profile indicates that
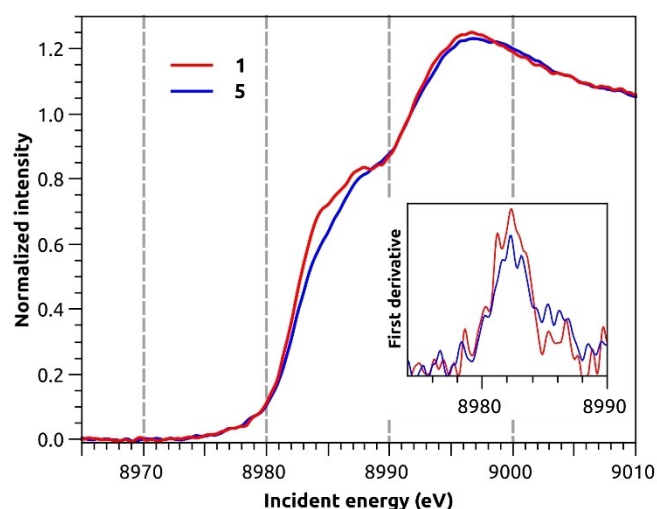
the Cu sites in these two complexes are tetracoordinated centres with similarly distorted geometries. To gain further insight into the coordination environment, the X-ray emission spectra (XES) of **1** and **5** were collected and Figure 9 presents the valence-to-core (VtC) XES region. The VtC region is of special interest because it involves transitions from filled valence orbitals, i.e. those above Cu(3p) up to the HOMO. For this reason, it carries information on the identity of bound ligands and local geometry.[72] The K$\beta_{2,5}$ features of **1** and **5** are characterized by two sharp peaks at 8973.1 and 8976.0 eV, the latter being somewhat less intense in **5**. Complex **1** presents more intense shoulders at ca. 8967 and 8982 eV, which may be associated with the additional methyl ester groups in the complex. The Kβ'' features, appearing at ~8958 eV, are rather weak and broad for both complexes. The overall similarity between **1** and **5** also agrees with the findings of the ^{15}N NMR study discussed above.

Calculations

Motivated by the consistent quantitative agreement between experimental and calculated VtC spectra demonstrated in previous studies,[72–77] calculations on DFT optimized structures were pursued. Based on the evidence from the Cu K-edge XAS that **1** and **5** are tetracoordinated, models of the Δ atropisomer of the cations of **1** and **5** were built. The optimizations with PBE0 functional converged to two conformers: a near two-coordinate seesaw geometry (**1**-seesaw, **5**-seesaw) with two elongated Cu–N$_{imine}$ bonds and a tetracoordinate near T$_d$ geometry (**1**-T$_d$, **5**-T$_d$), see Figure S76. Key geometrical parameters are shown in Table 2. Given the small energy difference between conformers, a small model that ignores the ligand backbone and has the imine connecting to a methyl group instead was built. The structure is shown in Figure 1B and the optimized geometry is marked in red in Figure 10. With it, we
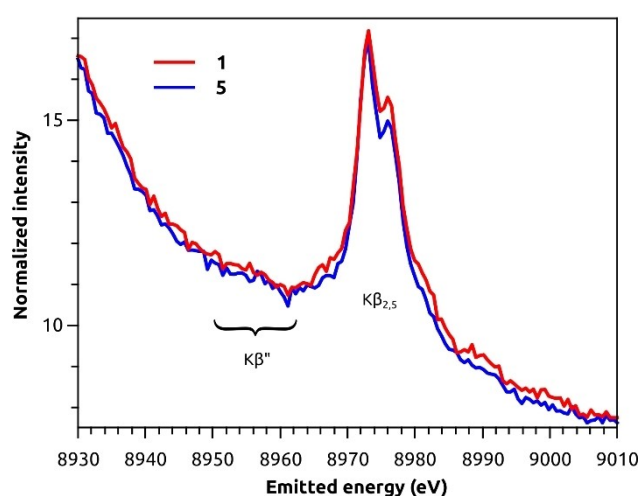

Figure 8. Cu K-edge X-ray absorption spectra of **1** (red) and **5** (blue) calibrated versus the first inflection point of Cu foil at 8980.3 eV. The first derivative (inset) highlights the first inflection point of the samples at 8982.2 eV for both.

Figure 9. Valence-to-core X-ray emission spectra of **1** (red) and **5** (blue). The intensity was normalized to the maximum of the K$\beta_{1,3}$ (shown in Figure S75) and multiplied by 1000.

EurJIC
European Journal of Inorganic Chemistry

Full Papers
doi.org/10.1002/ejic.202100722

Chemistry Europe
European Chemical
Societies Publishing

Table 2. Key parameters of $Cu(imim)_2^+$ model, **1** and **5** obtained by DFT. Imidazole and imine nitrogens are N_{IM} and N_{imine} respectively. $K\beta_{2,5}$ peak intensities were taken relative to the onset intensity at 8961.1 eV in all cases.

	Cu–N_{IM} [Å][a]	Cu–N_{imine} [Å][a]	N_{IM}–Cu–N_{IM}' [°]	N_{imine}–Cu–N_{imine}' [°]	τ_4, τ_4'[b]	Splitting of calc. $K\beta_{2,5}$ peaks [eV][c]	Intensity ratio of calc. $K\beta_{2,5}$ peaks	Relative energy[f] [kcal/mol]
$Cu(imim)_2^+$	2.00	2.11	137	112	0.70, 0.66	3.7	0.70[d,e]	–
1-T_d	1.93	2.14	143	85	0.63, 0.58	4.0	0.56[d]	0.0
1-seesaw	1.86	2.41	176	68	0.56, 0.34	4.1	0.19[d]	0.4
5-T_d	1.94	2.13	140	87	0.63, 0.40	4.2	0.44[e]	0.0
5-seesaw	1.86	2.38	167	70	0.57, 0.40	4.3	0.34[e]	−1.7

[a] Average distances. [b] Limiting values for T_d: $\tau_4 = \tau_4' = 1$, for seesaw: $\tau_4 \sim 0.43$, $\tau_4' \sim 0.24$.[69,70,78] [c] Exp. splitting for **1** and **5**: 2.9 eV. [d] Exp. ratio for **1**: 0.75. [e] Exp. ratio for **5**: 0.67. [f] Electronic energy relative to the respective T_d geometry at PBE0/def2-TZVP level.
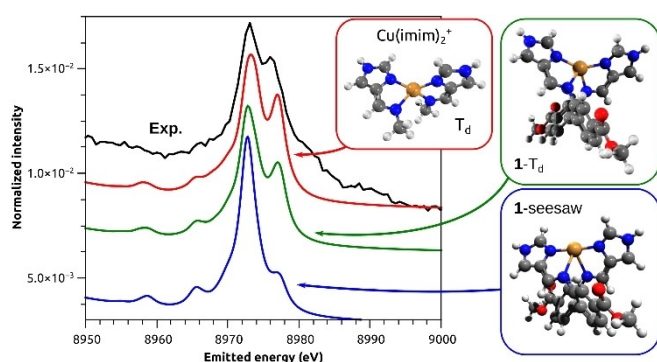

Figure 10. Experimental VtC XES spectrum of **1** and calculated spectra on the optimized geometries obtained at PBE0/def2-TZVP level shown in ball-and-stick models. Key parameters are presented in Table 2. Calculated spectra were obtained with Lorentzian line shape on individual transitions (sticks not shown), 2.5 eV line width, shifted by 134.4 eV, scaled so that the red trace matched the intensity of the main $K\beta_{2,5}$ peak and offset down to improve visualisation.

investigated the flexibility of the bis(imidazole)imine moieties and the correlation with VtC XES features.

The calculated VtC XES spectrum of the small model $Cu(imim)_2^+$ in its near tetrahedral energy minimum showed the greatest similarity with the experimental spectrum (Figure 10) with respect to the relative ratio of the $K\beta_{2,5}$ peaks (0.70 vs 0.75 observed experimentally) and splitting of the $K\beta_{2,5}$ peaks (3.7 eV vs 2.9 eV observed experimentally). The ratio was defined as the intensity ratio between the peaks at 8976.0 eV and 8973.1, relative to the intensity at the onset 8961.1 eV. The spectrum of **1**-T_d is in reasonable agreement, but the intensity ratio is lower (0.56) and the splitting is larger (4.0 eV) than the experimental values. Lastly, **1**-seesaw gave a sharp and strong $K\beta_{2,5}$ with a much less intense second peak. The same trends were found for **5** as well.

Based on these findings, the actual coordination environment of **1** and **5** in solid state should approach tetrahedral with two Cu–N_{IM} bond length on the order of 1.9–2.0 Å and two slightly longer Cu–N_{imine} of 2.1–2.2 Å. These bond lengths are comparable to those found in the preliminary single crystal structure of **2**. Given the high similarity between all imidazole

complexes found by ^{15}N NMR, they are expected to have similar Cu–N bond lengths. The distorted T_d geometry also agrees with the rising edge profile observed experimentally in the XAS, whereas a seesaw geometry would approach a two-coordinate site and would have produced a stronger peak at lower energies.

As both, T_d and seesaw geometries were found to be stable for both **1** and **5**, with small relative energies between them, the existence of near degenerate conformation minima was explored. Attempts to find the minimum energy path between the two minima failed using the nudged elastic band method,[79] which converged to barrierless paths in both cases. Optimisations with B3LYP converged to only the seesaw conformer for both complexes. These findings are indicative of a shallow potential energy surface. As the PBE0 structures transition between T_d and seesaw, the Cu–N_{IM} bonds contract by 0.07 Å and the Cu–N_{imine} bonds expand almost four-fold as much, by 0.27 Å.

The predicted VtC spectra of the conformers are very distinct with respect to the intensity of the high-energy $K\beta_{2,5}$ feature, which motivated further investigation of its intensity along the conformational change. As the $Cu(imim)_2^+$ model reproduces the VtC XES spectra obtained for either **1** or **5** and because their XAS spectra are similar, the simplified structure was deemed as a good representation of the imidazole-based complexes reported herein. A series of constrained optimizations with the angle between copper and N_{IM} varying from 137.09° (near-T_d energy minimum) to 180.0° was performed to capture the $T_d \rightarrow$ seesaw transition. Figure 11 presents the energy profile along the potential energy surface scan for $Cu(imim)_2^+$, as well as the calculated VtC XES and XAS for each point. Notably, the high-energy $K\beta_{2,5}$ peak (Figure 11b) decreases while the feature at the rising edge (Figure 11c) increases as the geometry approaches seesaw conformation.

These results emphasize the complementary nature of the VtC XES and XAS data for assigning local site symmetry.

The role of d-p orbital mixing for the VtC XES intensities was investigated computationally. The molecular orbitals involved in the main transitions are depicted in Figure 12. The main peak is predominantly formed by two transitions to the core hole: from
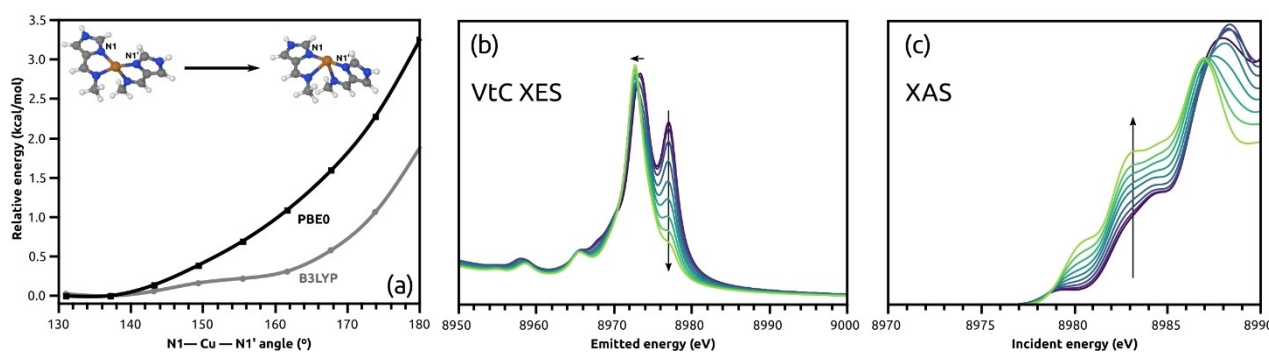
EurJIC
European Journal of Inorganic Chemistry

Full Papers
doi.org/10.1002/ejic.202100722

**Chemistry
Europe**
European Chemical
Societies Publishing

Figure 11. (a) Relaxed potential energy surface scan of the small model, calculated (b) VtC XES and (c) XAS spectra along the N_{IM}-Cu—N_{IM}' angle, on PBE0 geometries. The arrow indicates the trend from near tetrahedral to seesaw conformation. The energy shift in (b) is 134.4 eV and in (c) is 97.0 eV.
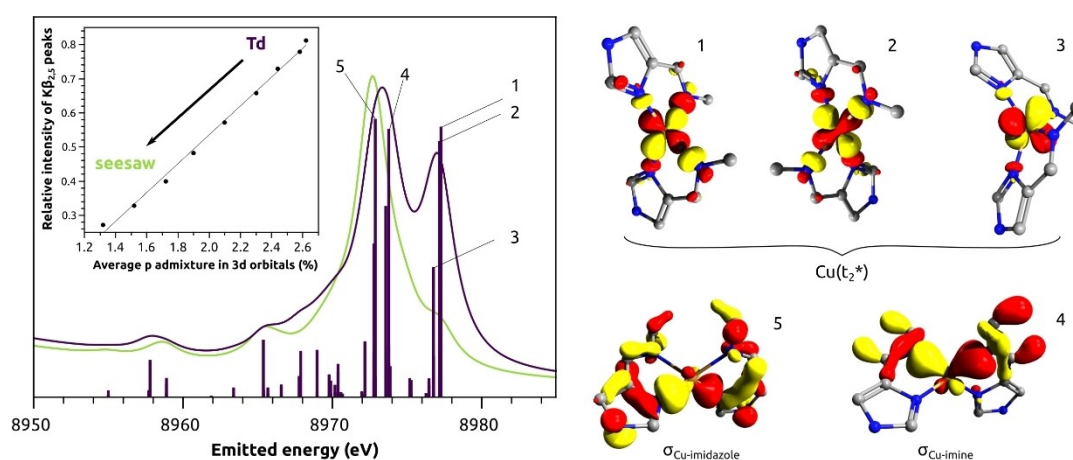

Figure 12. Computed transition intensities for Cu(imim)$_2$$^+$ model in T_d conformation and molecular orbitals corresponding to selected transitions. Hydrogens were omitted for clarity. The inset shows the correlation between the relative intensity of the two $K\beta_{2,5}$ peaks and the average p character in the filled molecular orbital with main 3d character (HOMO to HOMO-4). Isovalue: 0.05 e/au^3.

Cu–N_{IM} sigma bonding orbital (5) and from the Cu–N_{imine} bonding orbital (4) lying 0.9 eV above. As indicated in Table 2, the Cu–N_{imine} bond is considerably elongated in seesaw geometry, which decreases the intensity of transition 4, causing the main peak to shift toward lower energies, thus increasing the splitting. The fact that the Cu–N_{imine} bonding molecular orbital is almost 1 eV higher than the Cu–N_{IM} counterpart indicates that the Cu–N_{imine} bonds are weaker. These findings are in very good agreement with the ^{15}N NMR data, where imidazole complexes showed larger $|\Delta\delta^{15}N|$ for N_{IM} than for N_{imine}. More noticeably, the geometry-sensitive high-energy peak of the $K\beta_{2,5}$ is due to emissions of filled Cu(3d) molecular orbitals (1–3), more precisely from the $\sigma(t_2^*)$ set formed by the antibonding combination with N donor orbitals. This agrees well with our earlier observations of VtC XES of Cu(I)-binding proteins.[74] The inset in Figure 12 shows the relative ratio of the $K\beta_{2,5}$ peaks as a function of the average p contribution in all mainly 3d molecular orbitals. The correlation corroborates that the intensity mechanism of valence-to-1s transitions is dictated by the extent of p–d mixing of the valence orbital (3d). In the T_d limit, the mixing is maximized as all 4p orbitals have the same t_2 symmetry as the three 3d orbitals. The mixing deteriorates as

one approaches the seesaw limit with p_z becoming more antibonding and $p_{x,y}$ set contribution to the bonding lessens. Hence, while Cu(I) complexes have no 1s-to-3d pre-edge feature in the XAS, the 3d-to-1s feature in the VtC XES serves effectively as an "inverted pre-edge", as also previously observed in Zn[80] and Cu[74,81] and low valent Fe[82] VtC XES.

Finally, it is worth comparing the experimental XAS and VtC XES of **1** and **5** in light of the trends obtained computationally with the small model. The lower intensity of the rising edge feature of **5** in comparison to **1** would indicate that **5** approaches the T_d limit better than **1**, which would imply that the high-energy $K\beta_{2,5}$ feature in the VtC XES of **5** should have been more intense than **1**. However, this is not observed in the experimental spectra.

Concluding, the combination of NMR studies in solution and the X-ray spectroscopic studies on solids for the imidazole ML complexes underlines the well-established flexibility of Cu(I) complexes in terms of symmetry and coordination numbers.[32] For the ML complexes, this can result in the coexistence of multiple, interconverting species. In that case, some of the experimental observations are necessarily merged trends of the individual species' behaviour. A thorough computational study

EurJIC
European Journal of Inorganic Chemistry

Full Papers
doi.org/10.1002/ejic.202100722

Chemistry Europe
European Chemical
Societies Publishing

involving explicit solvation effects, multiple complexes and a systematic conformational search would be needed to mirror the compounds' intricate behaviour, but lies beyond the scope of this work. Furthermore, the concomitance of species can limit their value in catalytic studies as mechanisms may become difficult to decipher.[67,83] This creates an incentive to isolate the copper sites: If dimerization and oligomerisation are prevented, a more well-defined copper site can be obtained. A possibility to achieve this spatial isolation is the incorporation into a rigid framework. The heterogenisation accompanying the incorporation of the copper complexes into a metal-organic framework (MOF) is desirable in light of potential catalytic applications.[84]

Incorporation of Complex 1b into the MOF UiO-67

The corresponding carboxylic acids of the complexes that bear ester groups can function as linkers in metal-organic frameworks, e.g. UiO-67, a MOF with outstanding stability.[85] The NMR experiments reported herein were well-suited for Cu(I) complexes in solution. The environment, and thereby the oxidation state, of the Cu centre is more challenging to control during synthesis or modification of a metal-organic framework. Furthermore the d–d transition of Cu(II) complexes offers a convenient way to follow the incorporation of the metal by comparing the transmission spectrum of the molecular complex to the direct reflectance spectrum of the functionalised MOF. The Cu(II) analogue of **1** was synthesized from Cu(OTf)$_2$ and characterized by elemental analysis, HRMS and UV/Vis (see SI, compound **1b**). It showed an absorbance band at 670 nm (104 L·mol^{-1}cm^{-1}), comparable to literature reports of similar Cu(II) complexes.[53] Due to its paramagnetic nature, complex **1b** has extremely broadened peaks that merge into the baseline in ^{1}H NMR. Complex **1b** was reduced to complex **1** with ascorbic

acid in an NMR experiment, showing that the synthesis yields the same ligand regardless of the oxidation state of the copper salt used (Figure S66). Taking these considerations into account, the extensibility of this work's synthesis protocol to MOF functionalisation is demonstrated by the incorporation of Cu(II) complex **1b** into UiO-67. The highly acidic conditions during MOF synthesis would result in hydrolysis of the imine bond in the ligand. Therefore, post-synthetic linker modification (PSLM) of a MOF containing 2,2'-diaminobiphenyl-4,4'dicarboxylic acid (bpdc-(NH$_2$)$_2$) as a linker is the most suitable method of incorporation. Additionally, PSLM ensures that only mononuclear copper sites are obtained, as the biphenyl backbone is already anchored to the framework and only one complex can form per linker. Due to the poor stability of UiO-67-(NH$_2$)$_2$,[86] that has 100% of bpdc-(NH$_2$)$_2$, the synthetic procedure was applied to UiO-67 with mixed linkers. Literature for the related UiO-67-NH$_2$ (only one amino group), found much higher stability for MOF with 20% than for 100% amino functionalised linker.[87] This is consistent with the observations for amino-functionalisation of UiO-66, which has the shorter terephthalic acid as a linker.[88,89] UiO-67-(NH$_2$)$_2$-10% was obtained following a synthetic procedure described elsewhere.[90] The 10% amino-functionalisation are taken from the ratio of linkers during synthesis, actual incorporation is somewhat lower (SI). The diamino-functionalised MOF was shaken in an acetonitrile solution of 1H-imidazole-4-carbaldehyde and Cu(OTf)$_2$ overnight. After washing and drying, a light green MOF was obtained. The incorporation of the complex was confirmed by the good agreement of the UV/Vis spectra of the modified MOF and complex **1b** (Figure 13A), as well as EDX, elemental analysis and TGA.

^{1}H NMR of the digested MOF showed the imidazole aldehyde and bpdc-(NH$_2$)$_2$. The complex itself was therefore submitted to the alkaline digestion conditions and was found
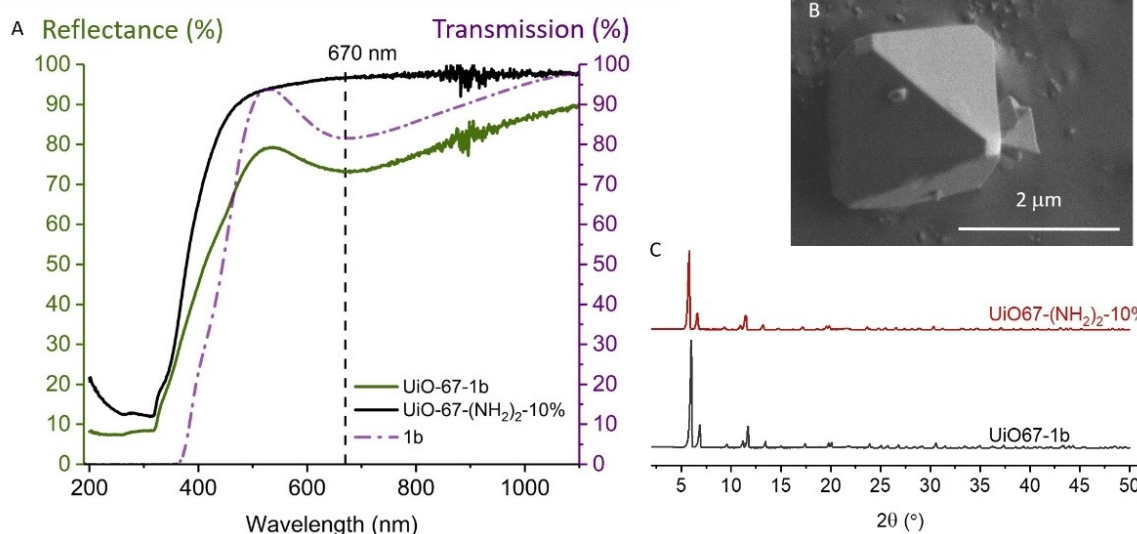

Figure 13. Incorporation of complex **1b** into UiO-67. **A**. UV/Vis: DR of the mixed linker MOF (UiO-67-(NH$_2$)$_2$-10%; black) and the MOF after PSLM (green), resulting in the formation of complex **1b** inside the MOF. The plot is overlaid with the transmission spectrum of **1b** in solution (0.86 mM; purple). **B**. Secondary electron image of UiO-67-1b. **C**. Powder XRD of the mixed linker MOF (UiO-67-(NH$_2$)$_2$-10%; black) and the MOF after PSLM (UiO-67-1b; red).

EurJIC
European Journal of Inorganic Chemistry

Full Papers
doi.org/10.1002/ejic.202100722

Chemistry Europe
European Chemical
Societies Publishing

to hydrolyse completely. The structural integrity of the copper-functionalised MOF UiO-67-1b was not compromised by the post-synthetic linker modification, as shown by powder XRD and SEM (Figure 13B and C).

Conclusion

A series of new copper complexes was synthesized. The *N,N,N,N*-coordinated copper(I) complexes were readily obtained via a one-pot synthesis that avoids time-consuming work-ups and stabilizes the imine ligand. Bidentate ligands were found to form ML_2 complexes, while tetradentate ligands formed ML complexes. The ligand design with ester-substituents on the biphenyl backbone is a key feature for later incorporation of the complex into the MOF UiO-67. Post-synthetic linker modification is the incorporation method of choice for these complexes, as it is compatible with the synthesis protocol, the stability of the complexes and allows to form the copper complexes on spatially isolated sites.

The molecular copper complexes themselves were studied by combined multinuclear NMR techniques, elucidating their solution behaviour. For the ML_2 complexes, NMR experiments suggested that they undergo ligand exchange in solution, in agreement with literature reports of Cu(I) complexes of bidentate ligands.[60,63,64] For the ML complexes, the formation of polynuclear species was studied by a combination of NMR techniques. Van Stein *et al.* reported a dimeric copper(I) complex of a tetradentate pyridine Schiff base ligand with a cyclohexyl backbone,[33] which Ouali *et al.* found to be inter-converting with a monomeric complex.[67] The closely related complex **3** with a biphenyl backbone formed both, the monomeric species **3-M** and the dimeric species **3-D**. Interestingly, we also found a third coexisting species, the higher aggregate **3-A**. The temperature-dependent interconversion of these three species was studied in d_6-DMSO, and the species' identity was confirmed through diffusion ordered spectroscopy (DOSY). Unlike literature reports on copper(I) amide complexes,[35] we did not observe defined oligomers of intermediate size between dimer and higher aggregates. **1** and **5** also formed dimers and potentially further polynuclear species (from VT NMR at lower temperatures) in acetonitrile, although to a lesser extent than **3**.

The nitrogen coordination shifts ($\delta^{15}N_{complex} - \delta^{15}N_{ligand}$) of the complexes showed that the copper coordination environment is dictated by the heterocycle (pyridine *vs* imidazole). Interestingly, $\Delta\delta^{15}N$ were barely affected by substitution on the phenyl rings and denticity of the ligand and the consequential ML or ML_2 formulation. The coordination shifts of **3-M** and **3-D** gave a glimpse at the changes the copper centre undergoes upon dimerization: the bond with the imine is strengthened while the bond with the heterocycle is weakened. All $\Delta\delta^{15}N$ were in good agreement with the bond length in the crystal structures of **2** and **4** and the computational model $Cu(imim)_2^+$. This suggests that the crystal structures are representative for the bond lengths of the copper(I) complexes of the respective heterocycle-Schiff base ligand. Both, single crystal XRD and

$\Delta\delta^{15}N$, show a more symmetrical coordination environment for the (monomeric) pyridine complexes than the imidazole complexes. Given the good agreement of the ^{15}N NMR experiments with the other experiments reported herein, we hope that this work encourages others to investigate more copper(I) complexes through ^{15}N NMR spectroscopy.

The imidazole-bearing ML complexes **1** and **5** were subjected to a combined XAS and XES study. The supporting DFT calculations converged to two structures for each mono-nuclear complex cation, a distorted T_d and a seesaw geometry. The experimental XAS and Valence-to-Core XES spectra showed better agreement with **1**-T_d and **5**-T_d than the corresponding seesaw geometries. However, the experimental data was reproduced even more accurately by the simplified $Cu(imim)_2^+$ model. The imidazole moieties are perpendicular to each other in $Cu(imim)_2^+$, which is a highly unfavourable conformation for monomers of **1** and **5**, where the imidazole-imine moieties are constrained by the biaryl backbone. In polynuclear species, the coordinating nitrogens do not necessarily originate from the same ligand. The good agreement between the experimental data and the $Cu(imim)_2^+$ model might therefore hint at an amplification of the polynuclear character in solid state. This is expected from the absence of solvent interactions and the naturally higher concentration of copper sites.

The combination of element-specific techniques has allowed the notorious aggregation behaviour of copper(I) complexes to be studied. As many related complexes are studied for catalytic applications, the herein reported results underline the necessity for caution when establishing structure-reactivity relationships from selective characterisation methods, such as single crystal structures. This work paves the way for future investigations of the complexes and the copper-functionalised MOF as catalysts for C—H activation.

Experimental Section

Synthesis and Characterization. All syntheses involving Cu(I) species were carried out in an Ar-filled UNIlab pro glovebox from MBraun. All solvents used were degassed with the freeze-pump-thaw technique (3 cycles). CuOTf, $CuOTf_2$, the respective aldehydes, biphenyl-2,2'-diamine and biphenyl-2-amine were purchased from commercial sources and used as received. Dimethyl 2-amino-biphenyl-4,4'-dicarboxylate and dimethyl 2,2'-diaminobiphenyl-4,4'-dicarboxylate were synthesized according to literature.[58,62] See SI for instrumentation, as well as procedures and characterisation data for all compounds. **Example (1)**.
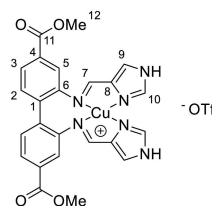
A mixture of dimethyl 2,2'-diaminobiphenyl-4,4'-dicarboxylate (0.50 mmol, 150 mg), CuOTf (0.50 mmol, 106 mg, 1 equiv.) and 1*H*-imidazole-4-carbaldehyde (1.0 mmol, 96 mg, 2 equiv.) were stirred in acetonitrile (3 mL) overnight. The solid was collected through filtration and washed with acetonitrile (2 mL) and diethyl ether

(4 mL). Residual solvent was left to evaporate over night to yield **1** as an ochre solid. Yield: 77–82%. ^{1}H NMR (600 MHz, d_6-DMSO): δ = 13.35 (2H, s, NH), 8.37 (2H, s, H10), 8.31 (2H, s, H7), 7.89 (2H, s, H9), 7.81 (2H, dd, $^3J_{H,H}$ = 7.9 Hz, $^4J_{H,H}$ = 1.5 Hz, H3), 7.57 (2H, d, $^3J_{H,H}$ = 7.9 Hz, H2), 7.49 (2H, d, $^4J_{H,H}$ = 1.2 Hz, H5), 3.83 ppm (6H, s, H12); ^{13}C NMR (150 MHz, d_6-DMSO): δ = 165.5 (C11), 154.5 (C7), 147.6 (C6), 138.7 (C10), 137.7 (C8), 133.7 (C1), 132.3 (C2), 130.0 (C4), 125.3 (C3), 123.0 (C9), 120.7 (q, $^1J_{C-F}$ = 322 Hz, CF$_3$) 120.3 (C5), 52.3 ppm (C12); ^{15}N{^{1}H} NMR (800 MHz, d_6-DMSO): δ = −83.2 (N$_{imine}$), −173.4 (N$_{IM}$), −203.7 ppm (N$_{AZ}$); LRMS (ESI): m/z (%): 519.083 (100), [^{63}CuL]$^+$, 521.082 (46) [^{65}CuL]$^+$; HRMS (ESI): m/z calcd for C$_{24}$H$_{20}$CuN$_6$O$_4^+$: 519.0837 [^{63}CuL]$^+$; found: 519.0833; elemental analysis calcd (%) for C$_{25}$H$_{20}$CuF$_3$N$_6$O$_7$S: C 44.88, H 3.01, N 12.56; found: C, 44.57; H, 3.06; N, 12.44.

DOSY measurement. The DOSY spectrum was collected on a Bruker AVII600 with Z-gradient probe with the stebpgp1s pulse sequence with 16 transitions. The diffusion period Δ was 90 ms and the gradient pulse duration (p30, $^1/_2$·δ) was 2.45 ms. Spinning was off. The data were analysed using the Diffusion option in the Bruker Dynamics Center.[91] The fitting is based on user-defined integrals and areas with signal overlap were not included for analysis (see SI). The theoretical diffusion constants were obtained through the SEGWE D/MW calculator developed and made available by Evans *et. al.*[65,66]

Single-crystal X-ray diffraction. Full details of the data collection, structure solution and refinement for each compound are contained in the cif files.

Deposition Numbers 2048292 (**2**) and 2048291 (**4**) contain the supplementary crystallographic data for this paper. These data are provided free of charge by the joint Cambridge Crystallographic Data Centre and Fachinformationszentrum Karlsruhe Access Structures service www.ccdc.cam.ac.uk/structures. The data are summarized in Table S3, SI.

X-ray absorption measurements. XAS spectra were collected with an *easyXES100-extended* laboratory spectrometer (easyXAFS, LLC, Seattle, USA) using a 100 W tungsten cathode source operating at 25 kV accelerating potential.[92,93] A circular aperture of 0.5 mm diameter was placed in front of the source to improve resolution. A helium flight path encompassing the Rowland circle area was used to reduce the X-ray attenuation in air. A circularly bend Si(553) crystal with 1 m radius was used as monochromator. The samples were diluted to 3% mass fraction of copper in boron nitride in a N$_2$-filled glovebox, ground, packed into a plastic cell (5 mm diameter, 1 mm thickness) and sealed with Kapton tape. The transmitted photons in the 8920–9200 eV range were detected by a Vortex detector. The samples were measured under constant stream of dry N$_2$ flow to hinder permeation of air into the cells. At least ten scans were acquired consecutively with 0.1 eV step across Cu K-edge region and spaced data points before and after for normalization. Each scan was inspected individually for radiation damage and oxidation and then averaged together. The incident flux (I$_0$) was measured in the same way without any sample. The energy axis of all spectra was calibrated versus the first inflection point of copper foil spectrum at 8980.3 eV measured in the same conditions. The final spectra were obtained with the ln(I$_0$/I$_1$) relationship and normalized in the Athena software. A three-point smoothing was applied to improve clarity, while the spectral features were neither suppressed nor introduced (see Figure S73).

Considering that **5** is more susceptible to air oxidation than **1**, successive spectra of **5** were collected for longer time (Figure S74). Decay in the intensity of the rising edge feature was observed starting at the 13th scan, meaning that oxidative damage is mitigated in the first 10 scans averaged in the final spectrum.

X-ray emission measurements. Samples for X-ray emission spectroscopy were prepared in a N$_2$-filled glovebox by grinding the compounds and packing the powders into 0.5-mm thick aluminium cells, which were sealed with 38 μm thick Kapton tape and kept in inert atmosphere until the measurement. The data were collected at the PINK tender X-ray beamline at BESSY II synchrotron at Helmholtz-Zetrum Berlin, during commissioning mode operation, at room temperature. The setup is the same as described previously.[94,95] The incoming energy was 9500 eV with a bandwidth of 95 eV, estimated flux of ~8×10^{12} photons/s, beam size of 500× 30 μm (H×V). The analyser was a von Hamos with one cylindrically bent diced Si(444) crystal with 246 mm radius. The data were acquired in continuous snake-like scan mode at 100.0 μm/s rate with 20 passes on the surface of the sample. The spectrum of each pass was compared with the previous to inspect for radiation-induced damage. Spectra showing unaltered features were averaged and presented herein. To assure that undamaged data were collected, radiation damage was intentionally induced to provide data of damaged sample as followed by exposing single spots to 60 times longer than the data collection scans. The detector was a 1028-pixel Eiger with 75 μm pixel size. The energy calibration was done with data collected on a CuCl sample also measured at ESRF/ ID26, where the spectrometer was calibrated with a series of scattering lines across Cu XES range. A linear polynomial was fitted to correlate the energy of three VtC peaks (8972.5, 8976.4, 8981.9 eV) and Kβ$_{1,3}$ (8903.2 eV) peak with the detector channel. The intensity was normalized to the Kβ$_{1,3}$ maximum and multiplied by 1000.

Molecular modelling. All calculations were performed with the ORCA electronic structure package version 4.2.1.[96] Geometry optimizations were carried out using restricted density functional calculations with B3LYP[97–100] and PBE0[101–103] exchange-correlation functionals, the Douglas-Kroll-Hess scalar-relativistic all-electron adapted versions of Aldrichs' triple-zeta quality basis set (def2-TZVP),[104] resolution of identity with the general-purpose SARC/J[105] auxiliary basis set and the chain of sphere approximations to speed up HF exchange calculation. The functionals were chosen based on literature reports[106] and the basis set due to the usual convergence with respect to the geometry at the triple zeta level. Scalar relativistic effects were included by the Douglas-Kroll-Hess Hamiltonian. Dispersion corrections were included by Grimme's atom-pairwise dispersion correction with Becke-Johnson damping.[107,108] The optimization thresholds were specified by the "TightOpt" keyword. Optimizations of **1** and **5** starting from a near tetrahedral initial guess converged to seesaw conformations with B3LYP, but stayed at near tetrahedral symmetry with PBE0. Optimization of the B3LYP seesaw geometries with PBE0 gave another minimum at a seesaw conformation. The energy minima were attested by the absence of imaginary vibrational modes in the Hessian calculation. Potential energy calculations were computed with relaxed surface scans along the angle formed by the binding imidazole nitrogens and Cu atom. Pre-K-edge X-ray absorption spectra were calculated by time-dependent DFT within Tamm-Dancoff approximation with B3LYP functional on PBE0-optimized geometries.[109] The oscillator strengths were computed based on the sum of the electric dipole, magnetic dipole and electric quadrupole contributions. The transitions were assigned based on the inspection of the natural transition orbitals. Valence-to-core X-ray emission spectra were calculated on PBE0-optimized geometries by a one-electron DFT-based approach[77] with BP86[98,110,111] functional and corrected for spin-orbit coupling.[75,112] In this case, the core properties basis set CP(PPP) was assigned to the metal and the radial integration accuracy was increased. The SCF convergence criteria were in all cases set according to the "TightSCF" keyword. Avogadro was used to visualize structures and plot of molecular orbitals. The atomic

orbital contributions to the molecular orbitals were obtained with the aid of loewdin_plotter.[113]

Conflict of Interest

The authors declare no conflict of interest.

Keywords: Aggregation · Copper · NMR spectroscopy · X-ray absorption spectroscopy · X-ray emission spectroscopy

[1] S. Liu, Y.-J. Lei, Z.-J. Xin, Y.-B. Lu, H.-Y. Wang, *J. Photochem. Photobiol. A* **2018**, *355*, 141–151.

[2] J. Shen, X. Zhang, M. Cheng, J. Jiang, M. Wang, *ChemCatChem* **2020**, *12*, 1302–1306.

[3] P. Garrido-Barros, I. Funes-Ardoiz, S. Drouet, J. Benet-Buchholz, F. Maseras, A. Llobet, *J. Am. Chem. Soc.* **2015**, *137*, 6758–6761.

[4] F. Monnier, M. Taillefer, *Angew. Chem. Int. Ed.* **2009**, *48*, 6954–6971; *Angew. Chem.* **2009**, *121*, 7088–7105.

[5] A. Shafir, P. A. Lichtor, S. L. Buchwald, *J. Am. Chem. Soc.* **2007**, *129*, 3490–3491.

[6] K. Hirano, M. Miura, *Chem. Lett.* **2015**, *44*, 868–873.

[7] T. Aneeja, M. Neetha, C. M. A. Afsina, G. Anilkumar, *RSC Adv.* **2020**, *10*, 34429–34458.

[8] X.-X. Guo, D.-W. Gu, Z. Wu, W. Zhang, *Chem. Rev.* **2015**, *115*, 1622–1651.

[9] B. Schönecker, T. Zheldakova, C. Lange, W. Günther, H. Görls, M. Bohl, *Chem. Eur. J.* **2004**, *10*, 6029–6042.

[10] H.-Q. Do, R. M. K. Khan, O. Daugulis, *J. Am. Chem. Soc.* **2008**, *130*, 15185–15192.

[11] A. E. Wendlandt, A. M. Suess, S. S. Stahl, *Angew. Chem. Int. Ed.* **2011**, *50*, 11062–11087; *Angew. Chem.* **2011**, *123*, 11256–11283.

[12] M. Suzuki, *Acc. Chem. Res.* **2007**, *40*, 609–617.

[13] S. Schindler, *Eur. J. Inorg. Chem.* **2000**, 2311–2326.

[14] S. Itoh, *Acc. Chem. Res.* **2015**, *48*, 2066–2074.

[15] J. Y. Lee, R. L. Peterson, K. Ohkubo, I. Garcia-Bosch, R. A. Himes, J. Woertink, C. D. Moore, E. I. Solomon, S. Fukuzumi, K. D. Karlin, *J. Am. Chem. Soc.* **2014**, *136*, 9925–9937.

[16] J. I. van der Vlugt, F. Meyer, in *Organometallic Oxidation Catalysis. Topics in Organometallic Chemistry* (Eds.: F. Meyer, C. Limberg), Springer, Berlin, Heidelberg, **2007**, pp. 191–240.

[17] R. J. Quinlan, M. D. Sweeney, L. L. Leggio, H. Otten, J.-C. N. Poulsen, K. S. Johansen, K. B. R. M. Krogh, C. I. Jørgensen, M. Tovborg, A. Anthonsen, T. Tryfona, C. P. Walter, P. Dupree, F. Xu, G. J. Davies, P. H. Walton, *PNAS* **2011**, *108*, 15079–15084.

[18] G. R. Hemsworth, E. J. Taylor, R. Q. Kim, R. C. Gregory, S. J. Lewis, J. P. Turkenburg, A. Parkin, G. J. Davies, P. H. Walton, *J. Am. Chem. Soc.* **2013**, *135*, 6069–6077.

[19] F. L. Aachmann, M. Sørlie, G. Skjåk-Bræk, V. G. H. Eijsink, G. Vaaje-Kolstad, *PNAS* **2012**, *109*, 18779–18784.

[20] L. Cao, O. Caldararu, A. C. Rosenzweig, U. Ryde, *Angew. Chem. Int. Ed.* **2018**, *57*, 162–166; *Angew. Chem.* **2018**, *130*, 168–172.

[21] M. O. Ross, F. MacMillan, J. Wang, A. Nisthal, T. J. Lawton, B. D. Olafson, S. L. Mayo, A. C. Rosenzweig, B. M. Hoffman, *Science* **2019**, *364*, 566–570.

[22] I. Garcia-Bosch, *Synlett* **2017**, *28*, 1237–1243.

[23] A. L. Concia, M. R. Beccia, M. Orio, F. T. Ferre, M. Scarpellini, F. Biaso, B. Guigliarelli, M. Réglier, A. J. Simaan, *Inorg. Chem.* **2017**, *56*, 1023–1026.

[24] I. Garcia-Bosch, M. A. Siegler, *Angew. Chem. Int. Ed.* **2016**, *55*, 12873–12876; *Angew. Chem.* **2016**, *128*, 13065–13068.

[25] C. E. Elwell, N. L. Gagnon, B. D. Neisen, D. Dhar, A. D. Spaeth, G. M. Yee, W. B. Tolman, *Chem. Rev.* **2017**, *117*, 2059–2107.

[26] A. Fukatsu, Y. Morimoto, H. Sugimoto, S. Itoh, *Chem. Commun.* **2020**, *56*, 5123–5126.

[27] S. C. Bete, C. Würtele, M. Otte, *Chem. Commun.* **2019**, *55*, 4427–4430.

[28] P. J. Donoghue, A. K. Gupta, D. W. Boyce, C. J. Cramer, W. B. Tolman, *J. Am. Chem. Soc.* **2010**, *132*, 15869–15871.

[29] S. Muthuramalingam, D. Maheshwaran, M. Velusamy, R. Mayilmurugan, *J. Catal.* **2019**, *372*, 352–361.

[30] A. C. Neira, P. R. Martínez-Alanis, G. Aullón, M. Flores-Alamo, P. Zerón, A. Company, J. Chen, J. B. Kasper, W. R. Browne, E. Nordlander, I. Castillo, *ACS Omega* **2019**, *4*, 10729–10740.

[31] E. Ramírez, M. K. Hossain, M. Flores-Alamo, M. Haukka, E. Nordlander, I. Castillo, *Eur. J. Inorg. Chem.* **2020**, 2798–2808.

[32] M. A. Carvajal, J. J. Novoa, S. Alvarez, *J. Am. Chem. Soc.* **2004**, *126*, 1465–1477.

[33] G. C. Van Stein, G. Van Koten, K. Vrieze, C. Brevard, *Inorg. Chem.* **1984**, *23*, 4269–4278.

[34] H. Nierengarten, J. Rojo, E. Leize, J.-M. Lehn, A. V. Dorsselaer, *Eur. J. Inorg. Chem.* **2002**, 573–579.

[35] S. Sung, D. C. Braddock, A. Armstrong, C. Brennan, D. Sale, A. J. P. White, R. P. Davies, *Chem. Eur. J.* **2015**, *21*, 7179–7192.

[36] M. Eddaoudi, D. F. Sava, J. F. Eubank, K. Adil, V. Guillerm, *Chem. Soc. Rev.* **2014**, *44*, 228–249.

[37] Y.-L. Hou, S.-X. Li, R. W.-Y. Sun, X.-Y. Liu, S. W. Ng, D. Li, *Dalton Trans.* **2015**, *44*, 17360–17365.

[38] Y. Sunatsuki, Y. Motoda, N. Matsumoto, *Coord. Chem. Rev.* **2002**, *226*, 199–209.

[39] T. Higa, M. Moriya, Y. Shimazaki, T. Yajima, F. Tani, S. Karasawa, M. Nakano, Y. Naruta, O. Yamauchi, *Inorg. Chim. Acta* **2007**, *360*, 3304–3313.

[40] W. A. Alves, G. Cerchiaro, A. Paduan-Filho, D. M. Tomazela, M. N. Eberlin, A. M. Da Costa Ferreira, *Inorg. Chim. Acta* **2005**, *358*, 3581–3591.

[41] K. T. Potts, M. Keshavarz, K. F. S. Tham, H. D. Abruna, C. R. Arana, *Inorg. Chem.* **1993**, *32*, 4422–4435.

[42] C. He, G. Zhang, J. Ke, H. Zhang, J. T. Miller, A. J. Kropf, A. Lei, *J. Am. Chem. Soc.* **2013**, *135*, 488–493.

[43] L. Pazderski, in *Annual Reports on NMR Spectroscopy* (Ed.: G. A. Webb), Academic Press, London, **2013**, pp. 33–179.

[44] L. Pazderski, in *Annual Reports on NMR Spectroscopy* (Ed.: Atta-ur-Rahman), Academic Press, London, **2020**, pp. 151–284.

[45] R. M. Gschwind, *Chem. Rev.* **2008**, *108*, 3029–3053.

[46] M. Kujime, T. Kurahashi, M. Tomura, H. Fujii, *Inorg. Chem.* **2007**, *46*, 541–551.

[47] J. K. Kowalska, F. A. Lima, C. J. Pollock, J. A. Rees, S. DeBeer, *Isr. J. Chem.* **2016**, *56*, 803–815.

[48] J. Schnödt, J. Manzur, A.-M. García, I. Hartenbach, C.-Y. Su, J. Fiedler, W. Kaim, *Eur. J. Inorg. Chem.* **2011**, 1436–1441.

[49] D. K. Seth, S. Bhattacharya, *Polyhedron* **2011**, *30*, 2438–2443.

[50] E. Lagerspets, K. Lagerblom, E. Heliövaara, O.-M. Hiltunen, K. Moslova, M. Nieger, T. Repo, *J. Mol. Catal.* **2019**, *468*, 75–79.

[51] J. Hamblin, L. J. Childs, N. W. Alcock, M. J. Hannon, *J. Chem. Soc. Dalton Trans.* **2002**, 164–169.

[52] T. Tanaka, Y. Sunatsuki, T. Suzuki, *Inorg. Chim. Acta* **2020**, *502*, 119373.

[53] M. Mimura, T. Matsuo, T. Nakashima, N. Matsumoto, *Inorg. Chem.* **1998**, *37*, 3553–3560.

[54] J. Becker, P. Gupta, F. Angersbach, F. Tuczek, C. Näther, M. C. Holthausen, S. Schindler, *Chem. Eur. J.* **2015**, *21*, 11735–11744.

[55] M. Lerch, M. Weitzer, T.-D. J. Stumpf, L. Laurini, A. Hoffmann, J. Becker, A. Miska, R. Göttlich, S. Herres-Pawlis, S. Schindler, *Eur. J. Inorg. Chem.* **2020**, 3143–3150.

[56] K. Schober, H. Zhang, R. M. Gschwind, *J. Am. Chem. Soc.* **2008**, *130*, 12310–12317.

[57] S. Ay, R. E. Ziegert, H. Zhang, M. Nieger, K. Rissanen, K. Fink, A. Kubas, R. M. Gschwind, S. Bräse, *J. Am. Chem. Soc.* **2010**, *132*, 12899–12905.

[58] K. T. Hylland, S. Øien-Ødegaard, R. H. Heyn, M. Tilset, *Eur. J. Inorg. Chem.* **2020**, 3627–3643.

[59] K. T. Hylland, I. Gerz, D. S. Wragg, S. Øien-Ødegaard, M. Tilset, *Eur. J. Inorg. Chem.* **2021**, 1869–1889.

[60] B. Herzigkeit, B. M. Flöser, T. A. Engesser, C. Näther, F. Tuczek, *Eur. J. Inorg. Chem.* **2018**, 3058–3069.

[61] G. Forte, I. P. Oliveri, G. Consiglio, S. Failla, S. D. Bella, *Dalton Trans.* **2017**, *46*, 4571–4581.

[62] K. T. Hylland, S. Øien-Ødegaard, M. Tilset, *Eur. J. Org. Chem.* **2020**, 4208–4226.

[63] A. J. J. Lennox, S. Fischer, M. Jurrat, S.-P. Luo, N. Rockstroh, H. Junge, R. Ludwig, M. Beller, *Chem. Eur. J.* **2016**, *22*, 1233–1238.

[64] Y. Zhang, M. Heberle, M. Wächtler, M. Karnahl, B. Dietzek, *RSC Adv.* **2016**, *6*, 105801–105805.

[65] R. Evans, Z. Deng, A. K. Rogerson, A. S. McLachlan, J. J. Richards, M. Nilsson, G. A. Morris, *Angew. Chem. Int. Ed.* **2013**, *52*, 3199–3202; *Angew. Chem.* **2013**, *125*, 3281–3284.

[66] R. Evans, G. Dal Poggetto, M. Nilsson, G. A. Morris, *Anal. Chem.* **2018**, *90*, 3987–3994.

[67] A. Ouali, M. Taillefer, J.-F. Spindler, A. Jutand, *Organometallics* **2007**, *26*, 65–74.

[68] R. Kleinmaier, S. Arenz, A. Karim, A.-C. C. Carlsson, M. Erdélyi, *Magn. Reson. Chem.* **2013**, *51*, 46–53.

[69] D. Rosiak, A. Okuniewski, J. Chojnacki, *Polyhedron* **2018**, *146*, 35–41.

[70] A. Okuniewski, D. Rosiak, J. Chojnacki, B. Becker, *Polyhedron* **2015**, *90*, 47–57.

[71] L. S. Kau, D. J. Spira-Solomon, J. E. Penner-Hahn, K. O. Hodgson, E. I. Solomon, *J. Am. Chem. Soc.* **1987**, *109*, 6433–6442.

[72] C. J. Pollock, S. DeBeer, *Acc. Chem. Res.* **2015**, *48*, 2967–2975.

[73] G. E. Cutsail, N. L. Gagnon, A. D. Spaeth, W. B. Tolman, S. DeBeer, *Angew. Chem. Int. Ed.* **2019**, *58*, 9114–9119; *Angew. Chem.* **2019**, *131*, 9212–9217.

[74] V. Martin-Diaconescu, K. N. Chacón, M. U. Delgado-Jaime, D. Sokaras, T.-C. Weng, S. DeBeer, N. J. Blackburn, *Inorg. Chem.* **2016**, *55*, 3431–3439.

[75] B. Lassalle-Kaiser, T. T. Boron, V. Krewald, J. Kern, M. A. Beckwith, M. U. Delgado-Jaime, H. Schroeder, R. Alonso-Mori, D. Nordlund, T.-C. Weng, D. Sokaras, F. Neese, U. Bergmann, V. K. Yachandra, S. DeBeer, V. L. Pecoraro, J. Yano, *Inorg. Chem.* **2013**, *52*, 12915–12922.

[76] R. Alonso-Mori, J. Kern, D. Sokaras, T.-C. Weng, D. Nordlund, R. Tran, P. Montanez, J. Delor, V. K. Yachandra, J. Yano, U. Bergmann, *Rev. Sci. Instrum.* **2012**, *83*, 073114.

[77] N. Lee, T. Petrenko, U. Bergmann, F. Neese, S. DeBeer, *J. Am. Chem. Soc.* **2010**, *132*, 9715–9727.

[78] L. Yang, D. R. Powell, R. P. Houser, *Dalton Trans.* **2007**, 955–964.

[79] O.-P. Koistinen, V. Ásgeirsson, A. Vehtari, H. Jónsson, *J. Chem. Theory Comput.* **2019**, *15*, 6738–6751.

[80] O. McCubbin Stepanic, J. Ward, J. E. Penner-Hahn, A. Deb, U. Bergmann, S. DeBeer, *Inorg. Chem.* **2020**, *59*, 13551–13560.

[81] H. Lim, M. L. Baker, R. E. Cowley, S. Kim, M. Bhadra, M. A. Siegler, T. Kroll, D. Sokaras, T.-C. Weng, D. R. Biswas, D. M. Dooley, K. D. Karlin, B. Hedman, K. O. Hodgson, E. I. Solomon, *Inorg. Chem.* **2020**, *59*, 16567–16581.

[82] M. U. Delgado-Jaime, S. DeBeer, M. Bauer, *Chem. Eur. J.* **2013**, *19*, 15888–15897.

[83] R. Berg, B. F. Straub, *Beilstein J. Org. Chem.* **2013**, *9*, 2715–2750.

[84] A. Bavykina, N. Kolobov, I. S. Khan, J. A. Bau, A. Ramirez, J. Gascon, *Chem. Rev.* **2020**, *120*, 8468–8535.

[85] J. H. Cavka, S. Jakobsen, U. Olsbye, N. Guillou, C. Lamberti, S. Bordiga, K. P. Lillerud, *J. Am. Chem. Soc.* **2008**, *130*, 13850–13851.

[86] N. Ko, J. Hong, S. Sung, K. E. Cordova, H. J. Park, J. K. Yang, J. Kim, *Dalton Trans.* **2015**, *44*, 2047–2051.

[87] A. M. Rasero-Almansa, A. Corma, M. Iglesias, F. Sánchez, *ChemCatChem* **2014**, *6*, 3426–3433.

[88] S. M. Chavan, G. C. Shearer, S. Svelle, U. Olsbye, F. Bonino, J. Ethiraj, K. P. Lillerud, S. Bordiga, *Inorg. Chem.* **2014**, *53*, 9509–9515.

[89] W. Kleist, F. Jutz, M. Maciejewski, A. Baiker, *Eur. J. Inorg. Chem.* **2009**, 3552–3561.

[90] G. Kaur, *Optimization of UiO-67 Type Metal-Organic Frameworks for Catalysis, PhD Thesis*, Oslo University, **2020**.

[91] "*Non-Frequency Dimension NMR Analysis Software | Bruker*," can be found under https://www.bruker.com/en/products-and-solutions/mr/nmr-software/dynamics-center.html, **2021**.

[92] G. T. Seidler, D. R. Mortensen, A. J. Remesnik, J. I. Pacold, N. A. Ball, N. Barry, M. Styczinski, O. R. Hoidn, *Rev. Sci. Instrum.* **2014**, *85*, 113906.

[93] E. P. Jahrman, W. M. Holden, A. S. Ditter, D. R. Mortensen, G. T. Seidler, T. T. Fister, S. A. Kozimor, L. F. J. Piper, J. Rana, N. C. Hyatt, M. C. Stennett, *Rev. Sci. Instrum.* **2019**, *90*, 024106.

[94] N. Levin, S. Peredkov, T. Weyhermüller, O. Rüdiger, N. B. Pereira, D. Grötzsch, A. Kalinko, S. DeBeer, *Inorg. Chem.* **2020**, *59*, 8272–8283.

[95] Z. Mathe, O. M. Stepanic, S. Peredkov, S. DeBeer, *Chem. Sci.* **2021**, *12*, 7888–7901.

[96] F. Neese, *Wiley Interdiscip. Rev.: Comput. Mol. Sci.* **2018**, *8*, e1327.

[97] C. Lee, W. Yang, R. G. Parr, *Phys. Rev. B* **1988**, *37*, 785–789.

[98] A. D. Becke, *Phys. Rev. A* **1988**, *38*, 3098–3100.

[99] A. D. Becke, *J. Chem. Phys.* **1993**, *98*, 5648–5652.

[100] P. J. Stephens, F. J. Devlin, C. F. Chabalowski, M. J. Frisch, *J. Phys. Chem.* **1994**, *98*, 11623–11627.

[101] J. P. Perdew, Y. Wang, *Phys. Rev. B* **1992**, *45*, 13244–13249.

[102] J. P. Perdew, K. Burke, M. Ernzerhof, *Phys. Rev. Lett.* **1996**, *77*, 3865–3868.

[103] J. P. Perdew, M. Ernzerhof, K. Burke, *J. Chem. Phys.* **1996**, *105*, 9982–9985.

[104] F. Weigend, R. Ahlrichs, *Phys. Chem. Chem. Phys.* **2005**, *7*, 3297–3305.

[105] F. Weigend, *Phys. Chem. Chem. Phys.* **2006**, *8*, 1057–1065.

[106] A. J. Johansson, M. R. A. Blomberg, P. E. M. Siegbahn, *Inorg. Chem.* **2006**, *45*, 1491–1497.

[107] S. Grimme, S. Ehrlich, L. Goerigk, *J. Comput. Chem.* **2011**, *32*, 1456–1465.

[108] S. Grimme, J. Antony, S. Ehrlich, H. Krieg, *J. Chem. Phys.* **2010**, *132*, 154104.

[109] S. DeBeer George, T. Petrenko, F. Neese, *J. Phys. Chem. A* **2008**, *112*, 12936–12943.

[110] S. H. Vosko, L. Wilk, M. Nusair, *Can. J. Phys.* **1980**, *58*, 1200–1211.

[111] J. P. Perdew, *Phys. Rev. B* **1986**, *33*, 8822–8824.

[112] M. A. Beckwith, M. Roemelt, M.-N. Collomb, C. DuBoc, T.-C. Weng, U. Bergmann, P. Glatzel, F. Neese, S. DeBeer, *Inorg. Chem.* **2011**, *50*, 8397–8409.

[113] "*ORCA / orca-helpers*," can be found under https://gitlab.gwdg.de/orca-helpers/orca-helpers, **2021**.

Supporting Information

Contents

2

General Considerations

All syntheses involving Cu(I) species were carried out in an Ar-filled UNIlab pro glovebox from MBraun. All solvents used with copper(I) species were degassed with the freeze-pump-thaw technique (3 cycles). CuOTf, CuOTf$_2$, the respective aldehydes, biphenyl-2,2'-diamine and biphenyl-2-amine were purchased from commercial sources and used as received. Dimethyl 2-aminobiphenyl-4,4'-dicarboxylate and dimethyl 2,2'-diaminobiphenyl-4,4'-dicarboxylate were synthesized according to literature.[1,2] Yield ranges for the copper complexes were determined from triplets of each synthesis. Melting points, if measured, are uncorrected and were measured on a Stuart SMP10 instrument. NMR spectra were recorded on the following Bruker instruments: DPX300, AVIII400, DRX500, AVI600, AVII600, AVIIIHD800. ^{1}H and ^{13}C NMR spectra are referenced to residual solvent signals. ^{15}N NMR signals are referenced to an external nitromethane standard. ^{19}F NMR signals are referenced to an internal C$_6$F$_6$ standard. For the DOSY measurement, the calibration of the Z-gradient probe was verified for the HDO peak in D$_2$O. All NMR spectra were recorded at ambient temperature, unless specified. The NMR samples of compounds containing copper were prepared in the glovebox in commercial 9 inch NMR tubes. The samples were transferred out of the glovebox with the adapter depicted in **Figure S1**. The sample was connected to a vacuum line and the solvent was frozen with liquid nitrogen. The tube was flame sealed under vacuum.

Figure S1. Reusable adapter to seal NMR tubes for samples in high boiling point solvents. This adapter has been developed by Elijah Aller.

MS (ESI) was recorded on a Bruker maXis II ETD spectrometer. Elemental analysis was performed by Mikroanalytisches Laboratorium Kolbe, Oberhausen, Germany. UV/Vis measurements were performed on a Specord 200 Plus instrument for solutions, and on a UV-3600 UV-Vis-NIR Spectrophotometer from Shimadzu for solids. Powder X-ray diffraction was performed with a Bruker D8 Discover diffractometer, using Cu $K_{\alpha 1}$ radiation selected by a Ge (111) Johanssen monochromator. Thermogravimetric analysis was conducted on a NETZSCH STA 449 F3 Jupiter, ramping from 30 to 900 °C with a 10 K/min ramping rate. The samples were under a stream of synthetic air, consisting of a 20 ml/min flowrate of N_2 and 5 mL/min flowrate of O_2. SEM images were taken on a Hitachi SU8230 Field Emission Scanning Electron Microscope (FE-SEM). Single crystal diffraction data were acquired on a Bruker D8 Venture equipped with a Photon 100 detector, and using Mo Kα radiation (λ = 0.71073 Å) from an Incoatec iµS microsource. Data reduction was performed with the Bruker Apex3 Suite, the structures were solved with ShelXT and refined with ShelXL.[3,4] Olex2 was used as user interface.[5] The cif files were edited with enCIFer v. 1.4.[6] and molecular graphics were produced with Diamond v. 4.6.2.

Synthesis and Characterization of Compounds

Compound 1

A mixture of dimethyl 2,2'-diaminobiphenyl-4,4'-dicarboxylate (0.50 mmol, 150 mg), CuOTf (0.50 mmol, 106 mg, 1 equiv.) and 1*H*-imidazole-4-carbaldehyde (1.0 mmol, 96 mg, 2 equiv.) were stirred in acetonitrile (3 mL) overnight. The solid was collected through filtration and washed with 2 mL acetonitrile and 4 mL diethyl ether. Residual solvent was left to evaporate over night to yield **1** as an ochre solid. Yield: 77-82 %.
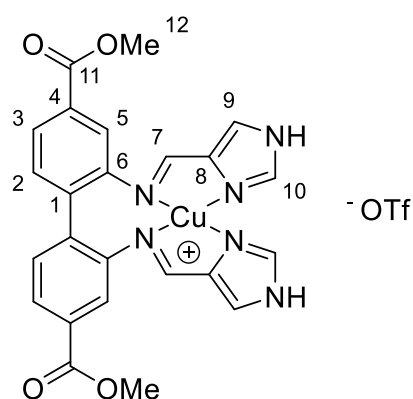
^{1}H NMR (d_6-DMSO, 600 MHz): δ 13.35 (2H, s, N**H**), 8.37 (2H, s, H10), 8.31 (2H, s, H7), 7.89 (2H, s, H9), 7.81 (2H, dd, $^3J_{H,H}$ = 7.9 Hz, $^4J_{H,H}$ = 1.5 Hz, H3), 7.57 (2H, d, $^3J_{H,H}$ = 7.9 Hz, H2), 7.49 (2H, d, $^4J_{H,H}$ = 1.2 Hz, H5), 3.83 (6H, s, H12). ^{13}C NMR (d_6-DMSO, 150 MHz): δ 165.5 (C11), 154.5 (C7), 147.6 (C6), 138.7 (C10), 137.7 (C8), 133.7 (C1), 132.3 (C2), 130.0 (C4), 125.3 (C3), 123.0 (C9), 120.7 (q,$^1J_{C-F}$ = 322 Hz, **CF₃**) 120.3 (C5), 52.3 (C12). ^{15}N{^{1}H} NMR (800 MHz, d_6-DMSO): δ −83.2 (N$_{imine}$), −173.4 (N$_{IM}$), −203.7 (N$_{AZ}$). ESI-MS: *m/z* 519.083 (100 %, [^{63}CuL]$^+$), 521.082 (46 %, [^{65}CuL]$^+$). HRMS *m/z* [^{63}CuL$^+$] (C₂₄H₂₀CuN₆O₄$^+$): Calcd: 519.0837 Found: 519.0833. Anal. Calcd: C, 44.88; H, 3.01; N, 12.56 Found: C, 44.57; H, 3.06; N, 12.44.
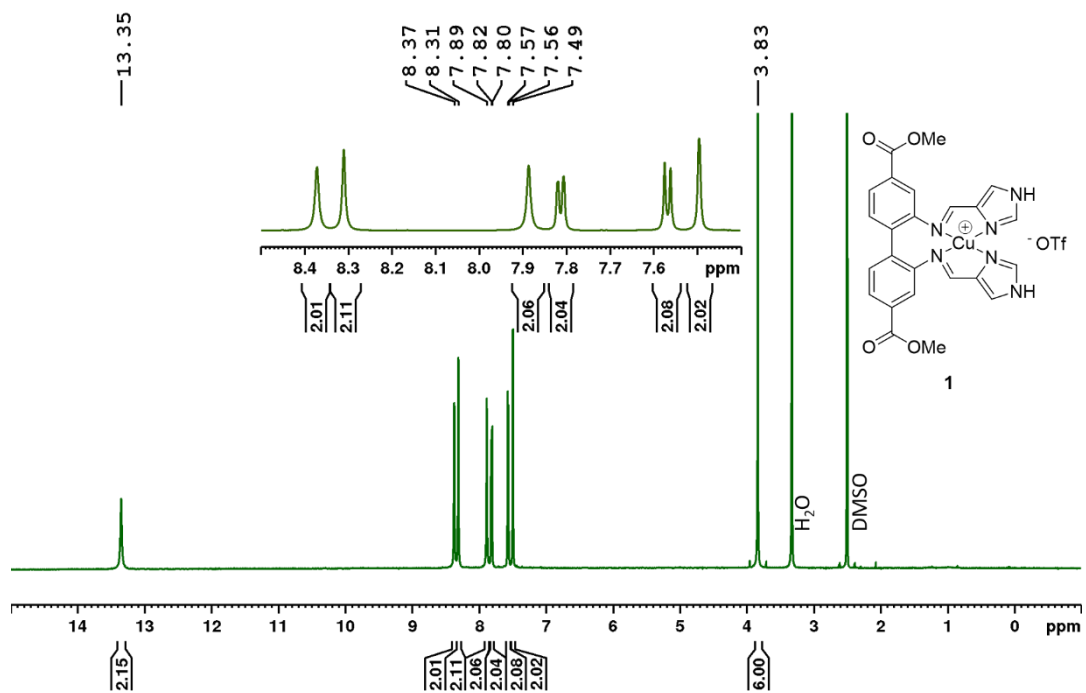
Figure S2. ^{1}H NMR (600 MHz, d_{6}-DMSO) of **1**.
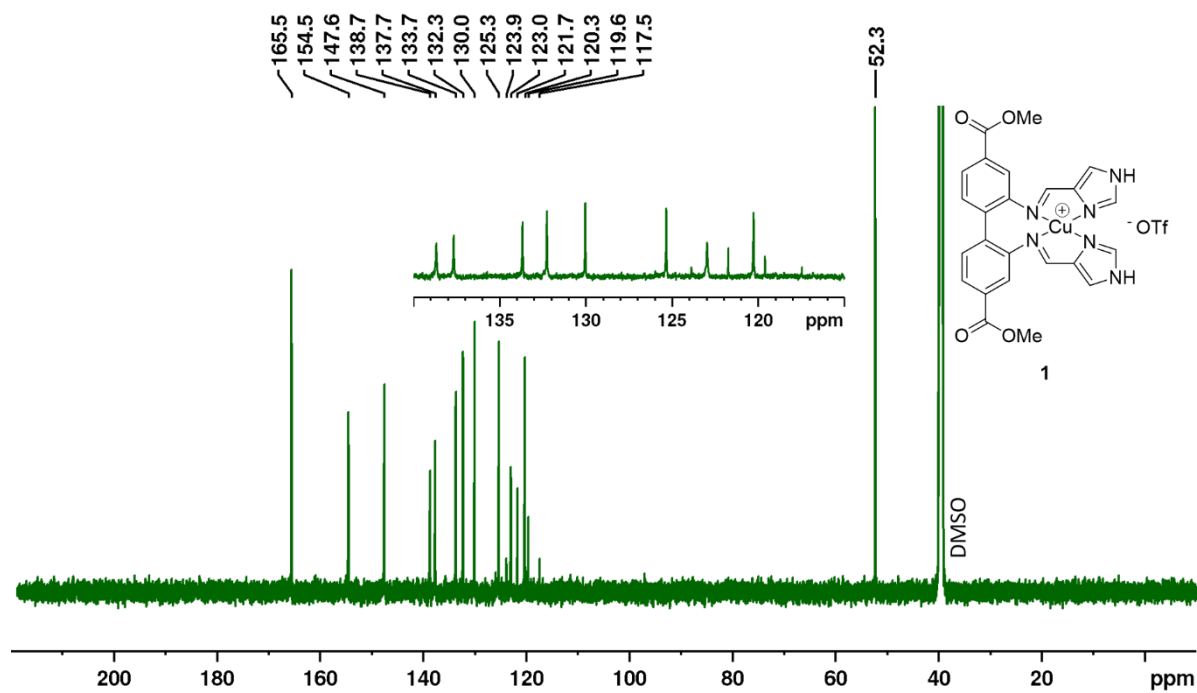
Figure S3. ^{13}C NMR (150 MHz, d_{6}-DMSO) of **1**.
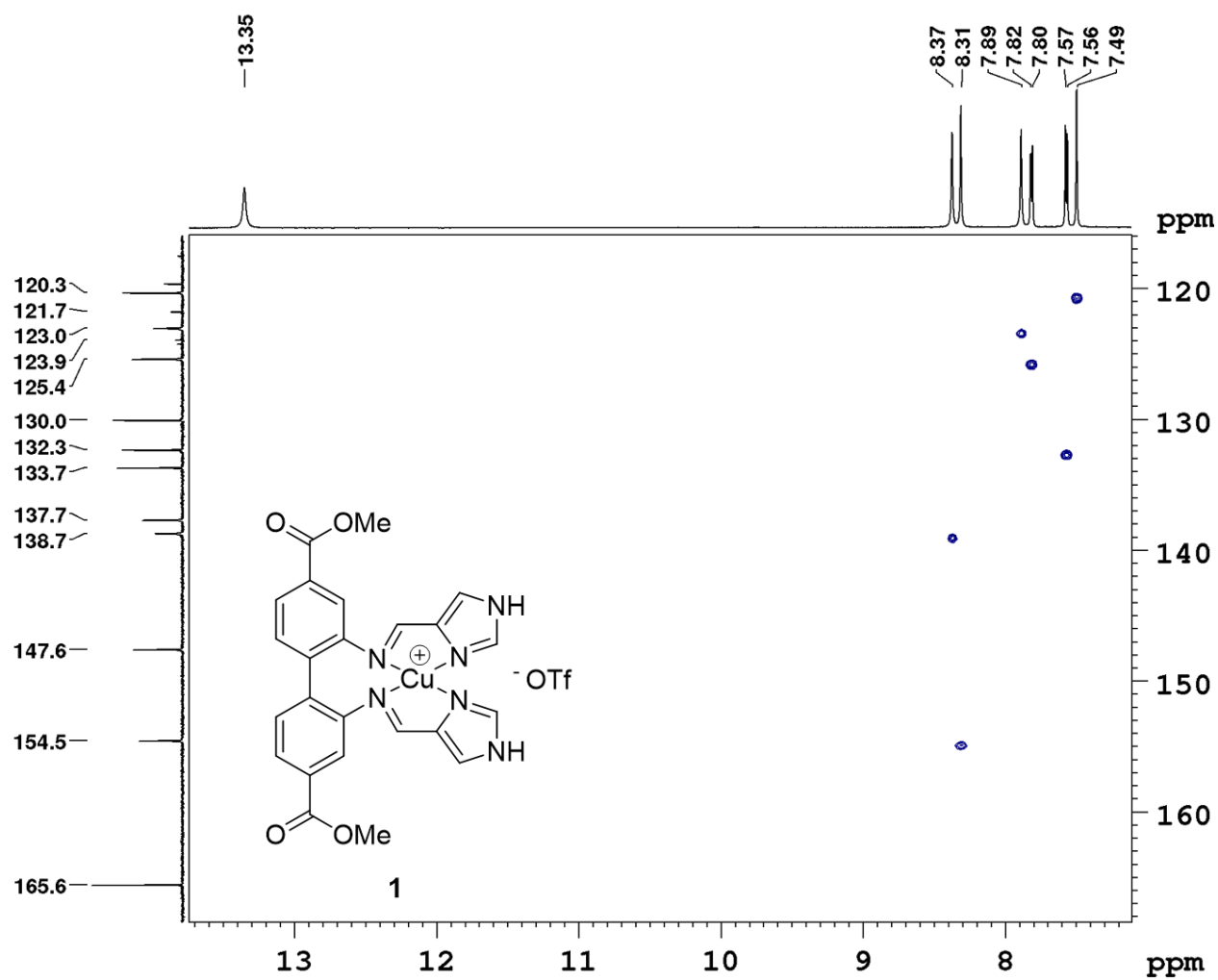
Figure S4. HSQC spectrum (600 MHz, d_6-DMSO) of **1**.
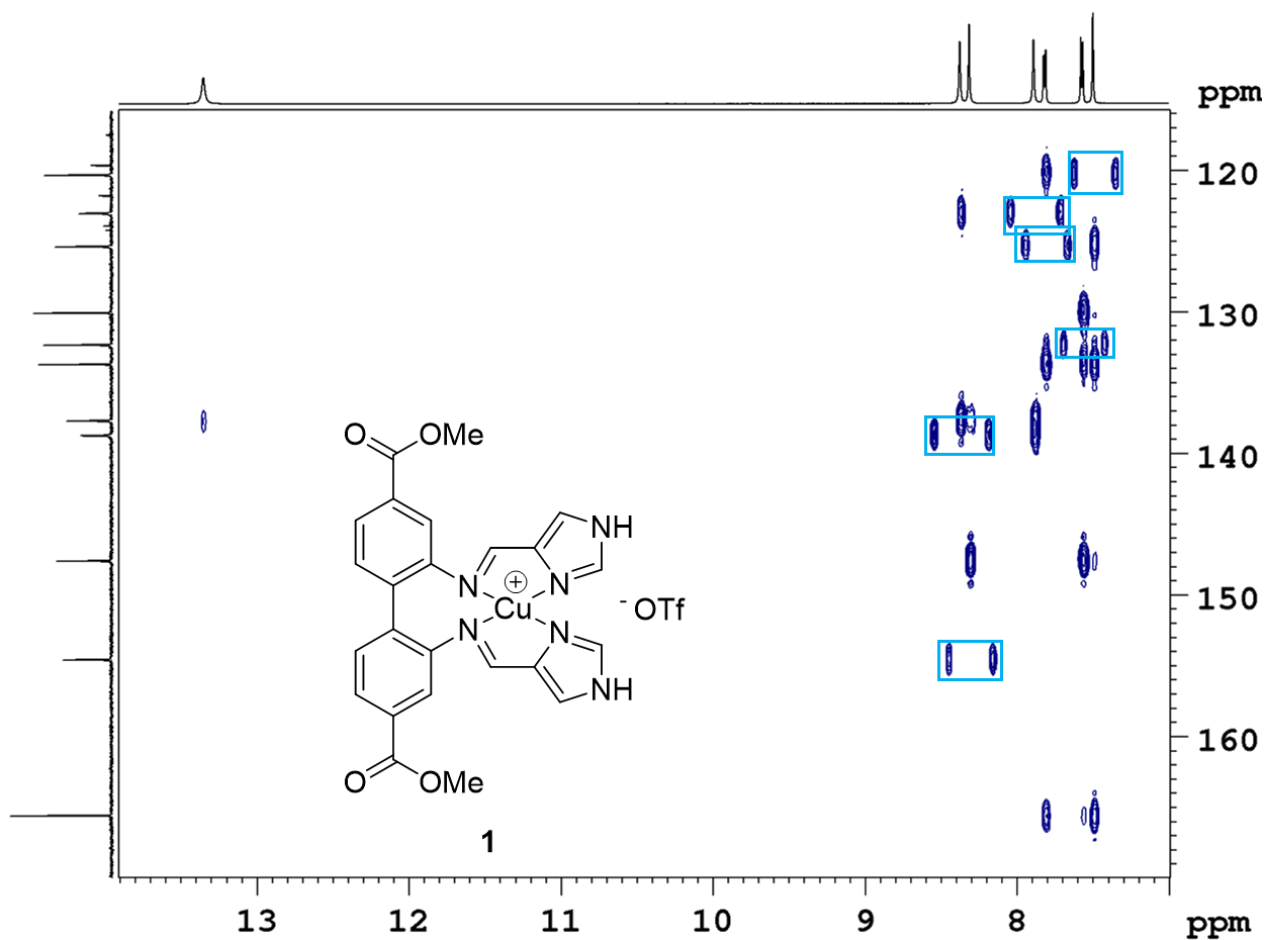
Figure S5. HMBC spectrum (600 MHz, d_6-DMSO) of **1**. Doublets originating from HSQC correlations are framed for clarity.
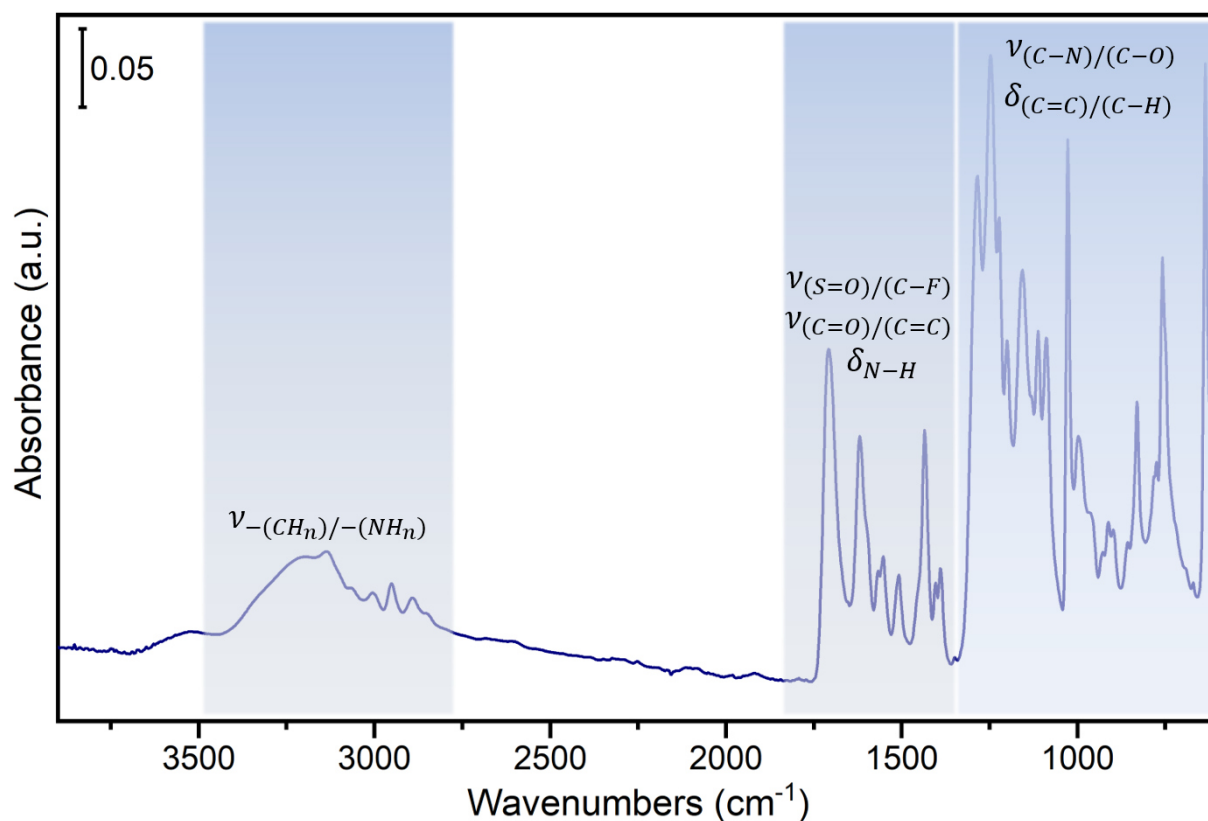
Figure S6. ATR spectrum of **1**, with reported range for the frequencies of the main functional groups.

Figure S6 reports the ATR spectrum for complex **1**. The spectrum shows the frequencies for the main functional groups present in the molecule. In the high frequencies region we can observe the contribution from the stretching modes of –*CH* and –*NH* groups, while in the 1700-1300 cm^{-1} region we can identify the frequencies of the stretching modes of carboxylic *C=O* and of the *C=C* bonds. Those signals are superimposed with the contribution from *S=O* and *C–F* stretching modes from the triflate group and with the bending modes of –*NH* groups. In the low frequencies region fall the bands related to the stretching modes of *C–N* and *C–O*, as well as those of the bending modes of *C=C* and *C–H*. Due to the structure of complex **1**, the peaks expected on the basis of the functional groups present are significantly overlapped in the entire spectral range, not allowing for a peak-to-peak assignment. The characteristic frequencies for the *Cu–N* stretching modes are expected to be in the Far-Infrared region (and consequently not accessible).

Compound 1b

A mixture of dimethyl 2,2'-diaminobiphenyl-4,4'-dicarboxylate (1.00 mmol, 300 mg), Cu(OTf)$_2$ (1.00 mmol, 362 mg, 1 equiv.) and 1*H*-imidazole-4-carbaldehyde (2.00 mmol, 192 mg, 2 equiv.) were stirred in MeOH (3 mL) overnight. The solvent was removed under reduced pressure. After drying in a vacuum oven at 50 °C overnight, **1b** was obtained as a dark green solid. Yield: 94-97 %.
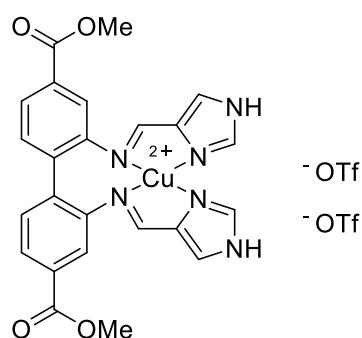
M.p. 206 °C. HRMS *m/z* [CuL^{2+}] (C$_{24}$H$_{20}$CuN$_6$O$_4$$^{2+}$): Calcd: 259.5416 Found: 259.5418. Anal. Calcd: C, 38.17; H, 2.46; N, 10.27 Found: C, 37.65; H, 2.51; N, 10.01. UV/Vis (MeCN): $\varepsilon_{670\,nm} = 104$ L·mol^{-1}cm^{-1}

Figure S7. UV/Vis spectra of **1b** measured in MeCN.

Compound 2

A mixture of CuOTf (0.18 mmol, 37 mg, 1 equiv.), dimethyl 2-aminobiphenyl-4,4'-dicarboxylate (0.35 mmol, 100 mg, 2 equiv.) and 1*H*-imidazole-4-carbaldehyde (0.35 mmol, 37 mg, 2 equiv.) were stirred in acetonitrile (3 mL) overnight. Diethyl ether (4 mL) was added, and the precipitated solid was collected through filtration and washed with diethyl ether (2 mL). Residual solvent was left to evaporate over night to yield **2** as a brown solid. Yield: 71-80 %.

^{1}H NMR (600 MHz, CD$_3$CN): δ 10.80 (2H, s, N**H**), 8.38 (2H, s, H7), 7.71 (2H, d, $^3J_{H,H}$ = 7.0 Hz, H3), 7.56 (6H, m, overlap H imidazole and H phenyl), 7.37 (2H, d, $^3J_{H,H}$ = 6.4 Hz, H2), 7.28 (2H, s, H imidazole) 7.16 (4H, s, H phenyl), 6.98 (2H, s, H5), 3.93 (6H, s, CO$_2$C**H**$_3$), 3.91 (6H, s, CO$_2$C**H**$_3$).^{1}H NMR (600 MHz, d_6-DMSO): δ 13.07 (2H, s, N**H**), 8.49 (2H, s, H7), 7.82 (2H, s, H9), 7.66 (2H, d, $^3J_{H,H}$ = 7.1 Hz, H3), 7.53 (6H, m, overlap H10 and H15), 7.39 (2H, d, $^3J_{H,H}$ = 7.3 Hz, H2), 7.13 (4H, s, H14), 6.86 (2H, s, H5), 3.90 (6H, s, CO$_2$C**H**$_3$), 3.88 (6H, s, CO$_2$C**H**$_3$). ^{13}C NMR (150 MHz, CD$_3$CN): δ 167.3 (C17), 166.6 (C11), 154.1 (C7), 147.6 (C6), 142.9 (C13), 139.5 (C1), 139.4 (*br*, C8) 137.9 (*br*, **C**H imidazole), 131.5 (C4), 130.9 (C2), 130.8 (**C**H phenyl), 129.9 (C16), 129.1 (**C**H phenyl), 127.9 (C3), 122.5 (*br*, **C**H imidazole), 122.2 (m*, ^1J = 321 Hz, **C**F$_3$), 121.3 (C5), 52.9 (CO$_2$**C**H$_3$), 52.8 (CO$_2$**C**H$_3$). ^{19}F NMR (376 MHz, CD$_3$CN): δ −79.8 (C**F**$_3$). ^{15}N{^{1}H} NMR (800 MHz, d_6-DMSO): δ −86.0 (N$_{imine}$), −171.7 (N$_{IM}$), −205.6 (N$_{AZ}$). ESI-MS: *m/z* 386.111 (38 %, [L+Na]$^+$), 426.051 (78 %, [^{63}CuL]$^+$), 428.049

12

(34 %, $[^{65}CuL]^+$), 789.173 (100 %, $[^{63}CuL_2]^+$), 791.172 (51 %, $[^{65}CuL_2]^+$). HRMS m/z $[^{63}CuL_2^{2+}]$ ($C_{40}H_{34}CuN_6O_8^+$): Calcd: 789.1734 Found: 789.1726. Anal. Calcd: C, 52.42; H, 3.65; N, 8.95 Found: C, 52.05; H, 3.77; N, 8.84. * d visible, expected q

Figure S8. ^{1}H NMR (600 MHz, CD$_3$CN) of **2**.
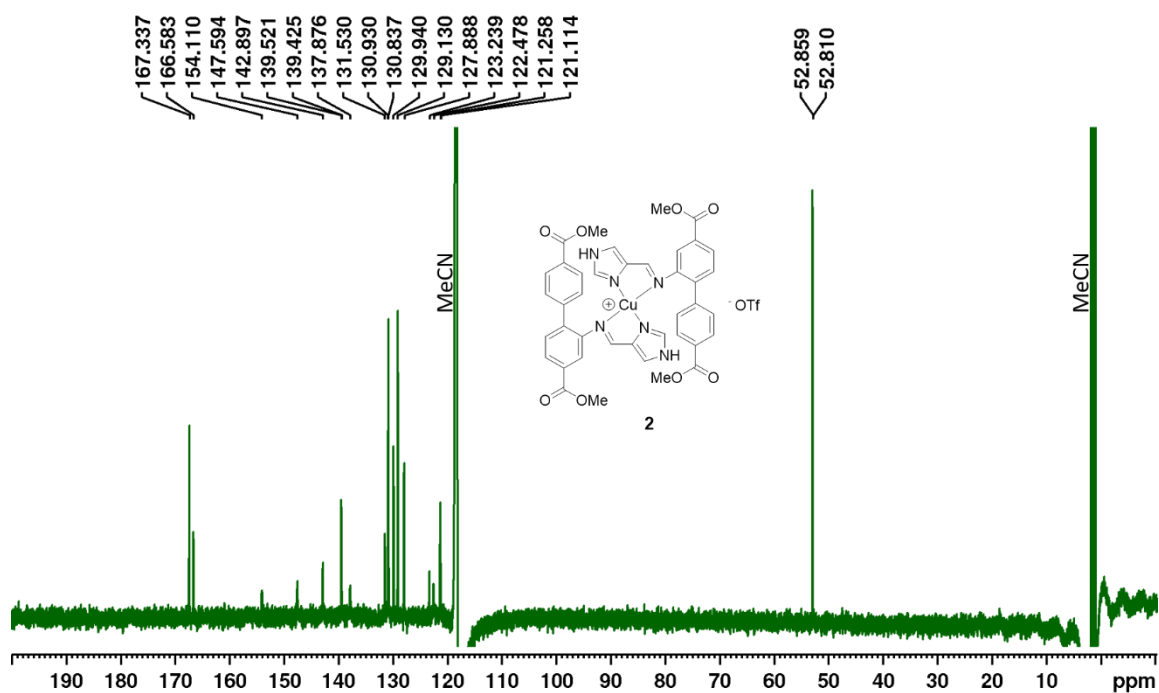
Figure S9. ^{1}H NMR (600 MHz, d_6-DMSO) of **2**.

Figure S10. ^{13}C NMR (150 MHz, CD$_3$CN) of **2** (15360 scans, d1= 8 s).

14

Figure S11. Detail of the ^{13}C NMR spectrum of **2**. The relatively sharp peaks at 123.2 ppm and 121.1 ppm are most likely originating from the counter ion (SO$_3$CF$_3$ $^-$). A low intensity quartet (with a 1:3:3:1 intensity ratio) can appear as a doublet, with only the inner peaks distinguished from the baseline.

Figure S12. ^{19}F NMR (376 MHz, CD$_3$CN) of **2** with hexafluorobenzene as internal standard.

Compound 3

A mixture of dimethyl 2,2'-diaminobiphenyl-4,4'-dicarboxylate (0.33 mmol, 100 mg), CuOTf (0.33 mmol, 70 mg, 1 equiv.) and picolinaldehyde (0.66 mmol, 72 mg, 64 µL, 2 equiv.) were stirred in MeCN (3 mL) overnight. Et$_2$O (4 mL) were added. The solid was collected through filtration and washed with Et$_2$O (2 mL). Residual solvent was left to evaporate over night to yield **3** as a dark green solid. Yield: 63-85 %.

HRMS *m/z* [^{63}CuL$^+$] (C$_{28}$H$_{22}$CuN$_4$O$_4^+$): Calcd: 541.0932 Found: 541.0932 Anal. Calcd: C, 50.40; H, 3.21; N, 8.11 Found: C, 50.14; H, 3.22; N, 8.09.

The presence of multiple species (**3-M**, **3-D**, **3-A**) at room temperature impeded the assignment of resonances by classical NMR full characterization techniques (Figure S13-S18). At higher temperatures, only **3-M** and **3-D** were present, which facilitated structure elucidation. For the assignments of the major (**3-M**) and minor (**3-D**) species observed in the ^{1}H NMR spectrum of complex **3** in d_6-DMSO at room temperature, spectra collected at other temperatures were consulted (25 °C to 92 °C). The assigned NMR resonances belonging to each species (**3-M** and **3-D**) are listed separately below. NMR data for **3-A** are not listed.

NMR Data for **3-M**

^{1}H NMR (800 MHz, d_6-DMSO): δ 8.94 (2H, s, H7), 8.90 (2H, s, H12), 8.26 (2H, s, H10), 8.08-8.09 (2H, m, H9), 7.90-7.92 (4H, m, H3 and H11), 7.83 (2H, s, H5), 7.61 (2H, s, H2), 3.87 (6H, s, H14). All resonances were significantly broadened at 55 °C, and no fine structure could be detected. ^{13}C NMR (200 MHz, d_6-DMSO): δ 165.1 (C13), 162.4 (C7), 150.1 (C12), 149.8 (C8), 146.0 (C6), 138.7 (C10), 132.9 (C2), 130.5 (C4), 129.2 (C11), 128.8 (C9), 126.1 (C3), 120.6 (C5), 52.1 (C14). The resonance corresponding to C1 was not observed. ^{15}N{^{1}H} NMR (800 MHz, d_6-DMSO): δ −89.6 (N$_{imine}$), −128.6 (N$_{pyridine}$).

NMR Data for **3-D**

^{1}H NMR (800 MHz, d_6-DMSO): δ 9.19 (4H, s, H7), 8.10 (4H, m, H10), 8.06 (4H, d, $^3J_{H,H}$ = 7.7 Hz, H9), 7.88 (4H, s, H5), 7.50-7.51 (4H, m, H11), 7.44 (4H, d, $^3J_{H,H}$ = 4.4 Hz, H12), 7.27 (4H, dd, $^3J_{H,H}$ = 7.8 Hz, $^4J_{H,H}$ = 1.0 Hz, H3), 7.15 (4H, d, $^3J_{H,H}$ = 7.8 Hz, H2), 3.77 (12H, s, H14). For some of the resonances, specifically those corresponding to H10 and H5, the integrals are less accurate because of overlap with resonances corresponding to **3-A**. ^{13}C NMR (200 MHz, d_6-DMSO): δ 164.2 (C13), 163.9 (C7), 148.6 (C8), 147.7 (C12), 145.6 (C6), 138.0 (C10), 137.0 (C1), 132.3 (C2), 130.2 (C4), 128.3 (C11), 128.2 (C9), 127.8 (C3), 121.4 (C5), 51.9 (C14). ^{15}N{^{1}H} NMR (800 MHz, d_6-DMSO): δ −105.3 (N$_{pyridine}$), −107.7 (N$_{imine}$).

In addition, one resonance corresponding to the triflate anion was observed at δ 120.5 (d, q expected, $^1J_{C,F}$ = 322 Hz) in the ^{13}C NMR spectrum of **3**.

Figure S13. ^{1}H NMR (600 MHz, d_6-DMSO) of **3**.

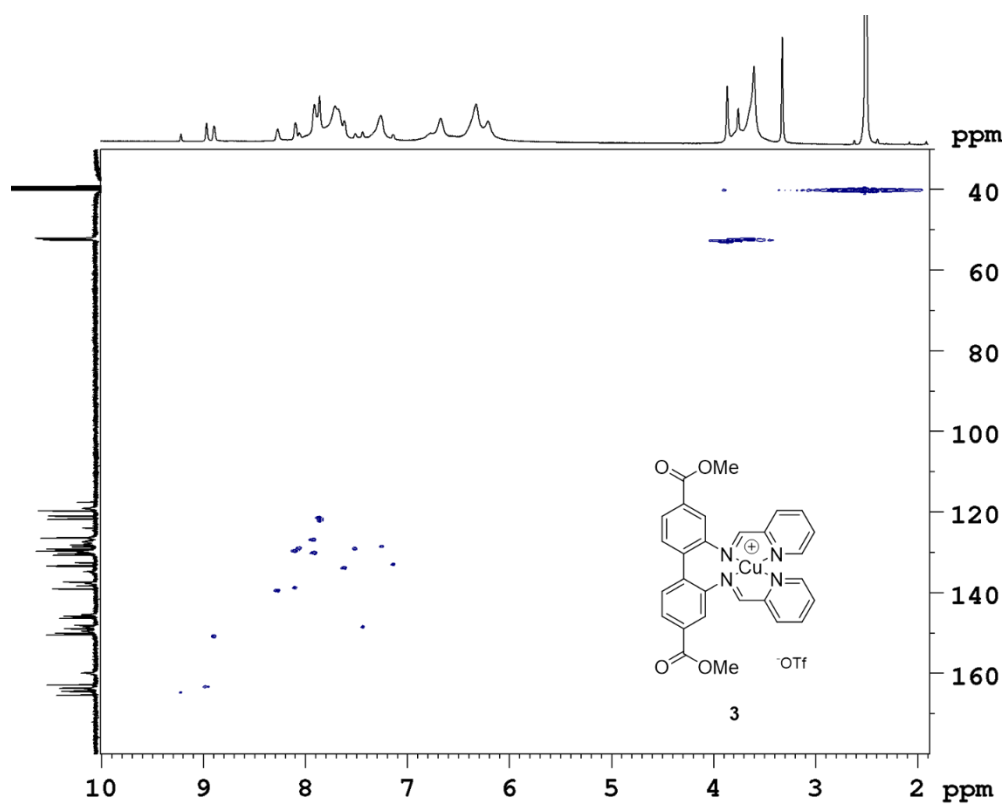**Figure S14**. ^{13}C NMR (150 MHz, d_6-DMSO) of **3**.

Figure S15. HSQC (600 MHz, *d₆*-DMSO) of **3**.
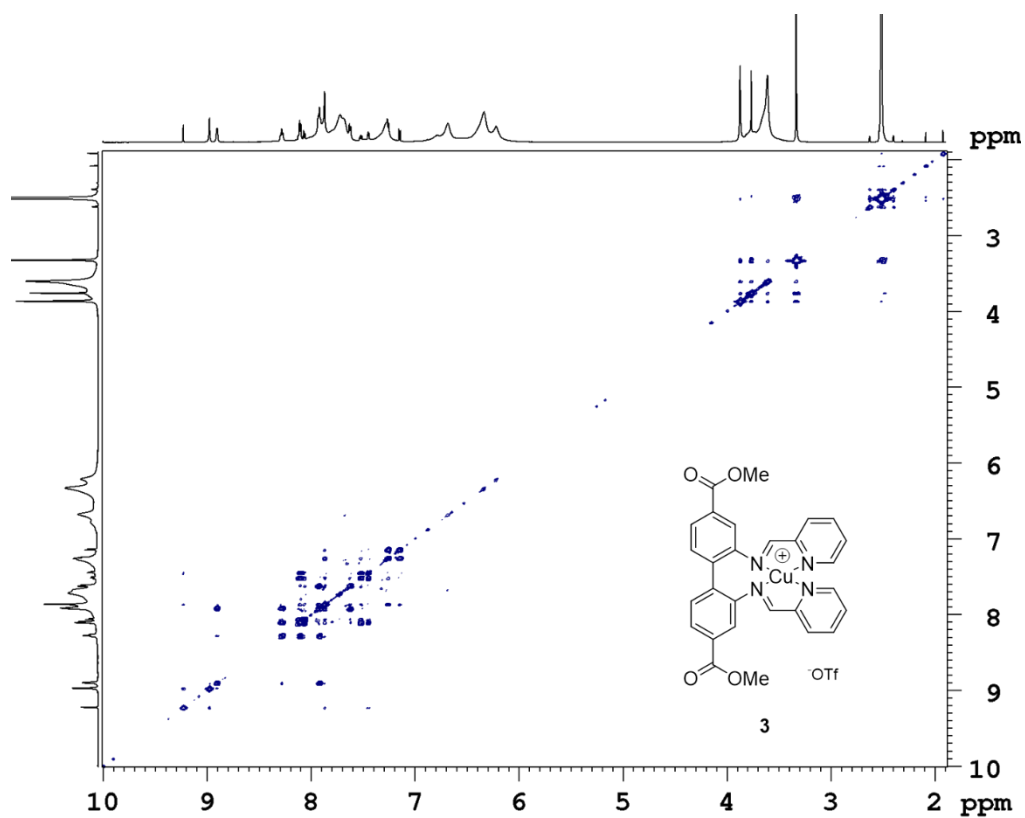

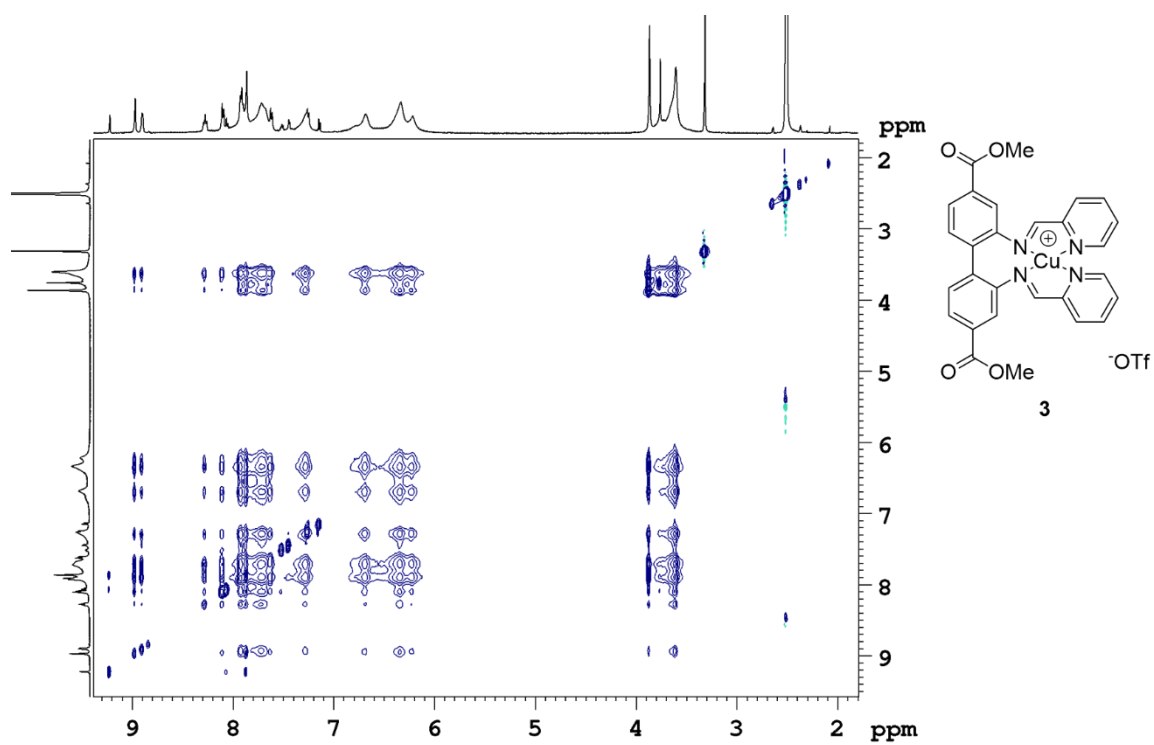**Figure S16.** COSY (600 MHz, *d₆*-DMSO) of **3**.

19

Figure S17. NOESY/EXSY (500 MHz, d_6-DMSO) of **3**. No correlations that clearly indicate

exchange between **3-M** and **3-D** could be identified, as opposed to the NOESY/EXSY spectrum
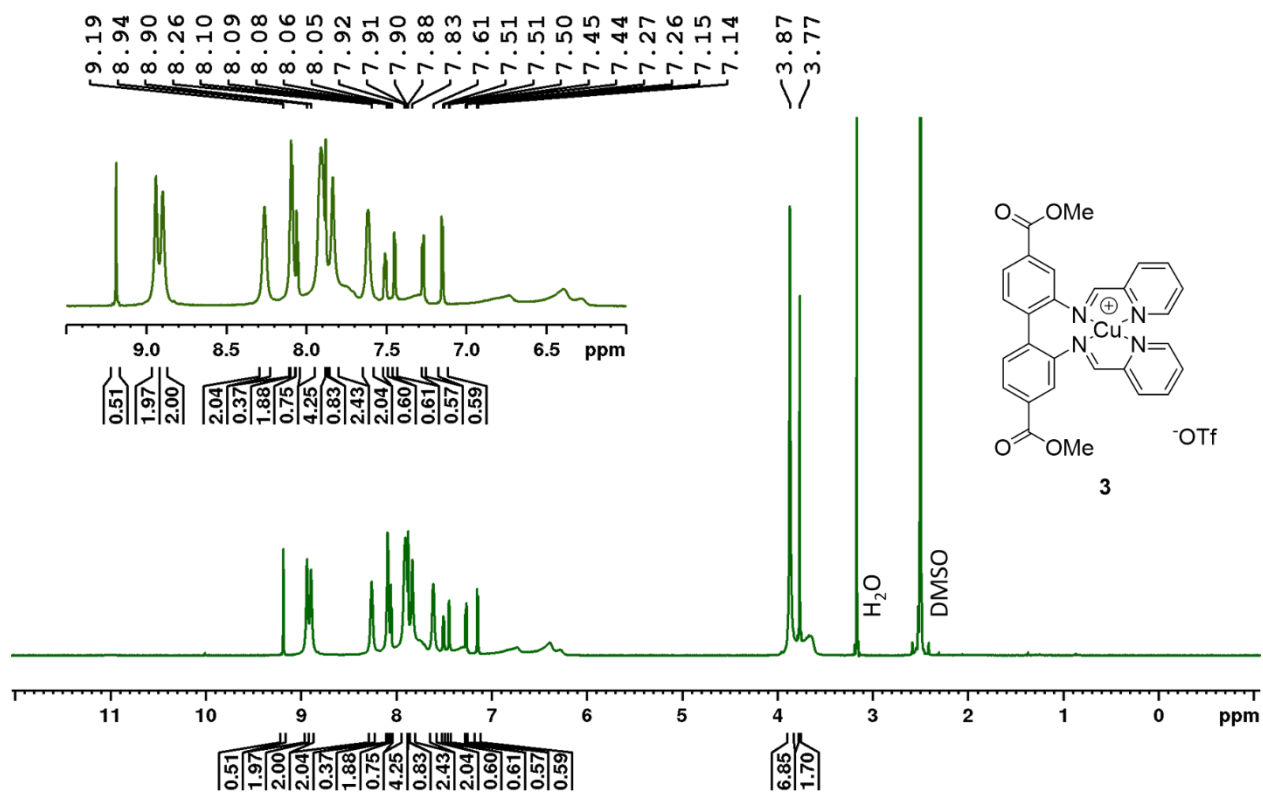
collected at 92 °C (Figure S21).

Figure S18. ^{1}H NMR (800 MHz, d_6-DMSO, 55 °C) of **3**.

Figure S19. ^{1}H NMR (500 MHz, d_6-DMSO, 92 °C) of **3**.

Figure S20. ^{13}C NMR (200 MHz, d_6-DMSO, 55 °C) of **3**.

Figure S21. NOESY/EXSY (500 MHz, d_6-DMSO, 92 °C) of **3**. The exchange peaks (black cross-peaks) between the major species (**3-M**) and the minor species (**3-D**) suggest the species are interconverting.

Compound 4

A mixture of CuOTf (0.175 mmol, 37 mg, 1 equiv.), dimethyl 2-aminobiphenyl-4,4'-dicarboxylate (0.350 mmol, 100 mg, 2 equiv.) and picolinaldehyde (0.350 mmol, 38 mg, 33 µL, 2 equiv.) were stirred in 2 mL MeCN overnight. 6 mL of Et$_2$O were added. The precipitated solid was collected through filtration and washed with 2 mL Et$_2$O. Residual solvent was left to evaporate over night to yield **4** as a dark green solid. Yield: 67-87 %.

NMR Data for Compound **4** in CD$_3$CN

^{1}H NMR (600 MHz, CD$_3$CN): δ 8.77 (*br*, 1H, s, H7) 8.06 (*br*, 1H, s, H pyridine), 7.87 (*br*, 2H, s, H pyridine), 7.75 (1H, d, $^3J_{H,H}$ = 5.6 Hz, H3), 7.46 (2H, s, H17), 7.41 (1H, d, , $^3J_{H,H}$ = 6.1 Hz, H2) 7.28 (1H, s, H5), 7.14 (2H, s, H16), 3.99 (6H, s, H14), 3.83 (6H, s, H20), missing: H pyridine. ^{13}C NMR (150 MHz, CD$_3$CN): δ 166.8 (C19), 166.3 (C13), 161.6* (*br*, C7), 150.8* (*br*, C pyridine), 146.1 (C6), 141.9 (C15), 140.2 (C1), 138.7*, (*br*, C pyridine) 138.6* (*br*, C pyridine), 131.9 (C4), 131.3 (C2), 130.8 (C16), 130.4 (C18), 129.39 (C17), 129.35 (C3), 122.35 (q, ^1J= 320 Hz, **C**F$_3$), 122.34 (C5), 53.0 (C14), 52.7 (C20). ESI-MS: *m/z* 375.134 (100 %, [L+H]$^+$), 437.056 (40 %, [^{63}CuL]$^+$), 439.055 (18 %, [^{65}CuL]$^+$), 811.183 (26 %, [^{63}CuL$_2$]$^+$), 813.183 (13 %, [^{65}CuL$_2$]$^+$). HRMS *m/z* [^{63}CuL$_2$$^{2+}$] (C$_{44}H_{36}CuN_4O_8$$^+$): Calcd: 811.1824 Found: 811.1825 Anal. Calcd: C, 56.22; H, 3.77; N, 5.83 Found: C, 56.08; H, 3.68; N, 5.75. *=detected through HSQC.
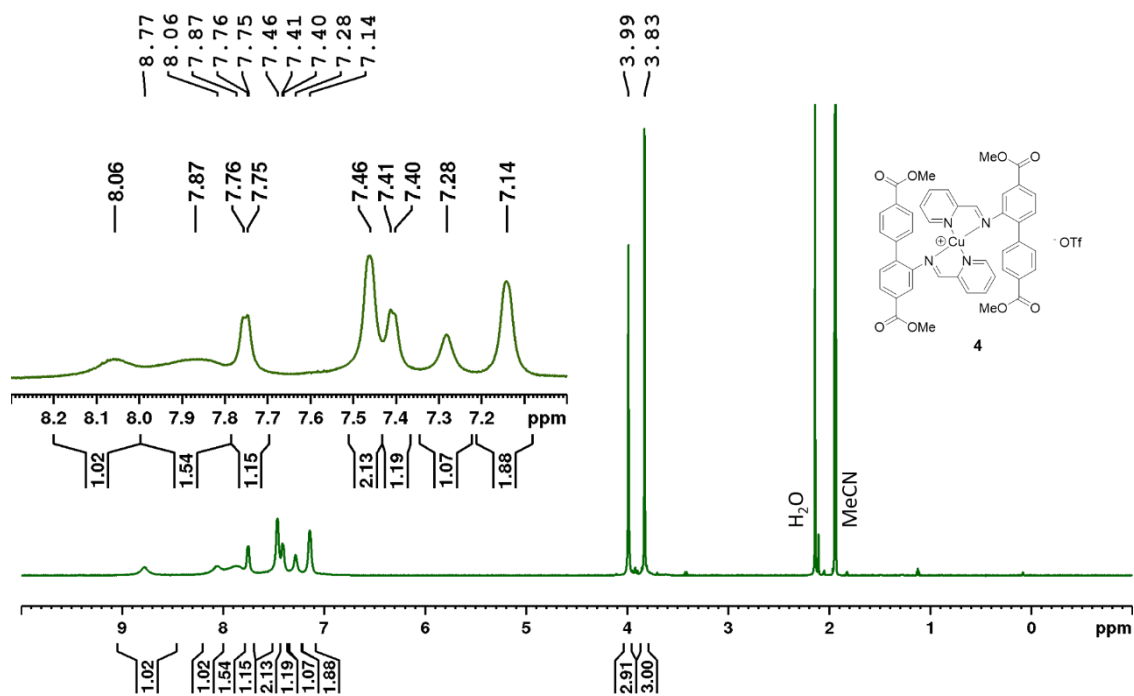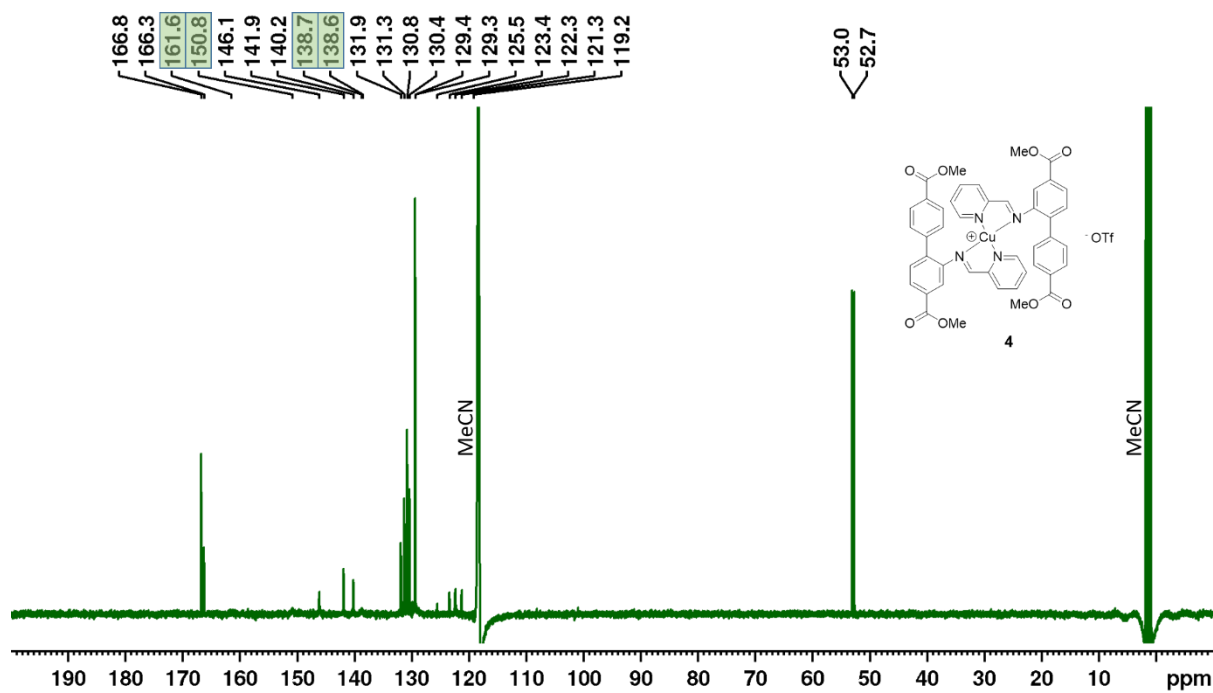
Figure S22. ^{1}H NMR (600 MHz, CD$_3$CN) of **4**.

Figure S23. ^{13}C NMR (150 MHz, CD$_3$CN) of **4**. Peaks localized through HSQC are highlighted.
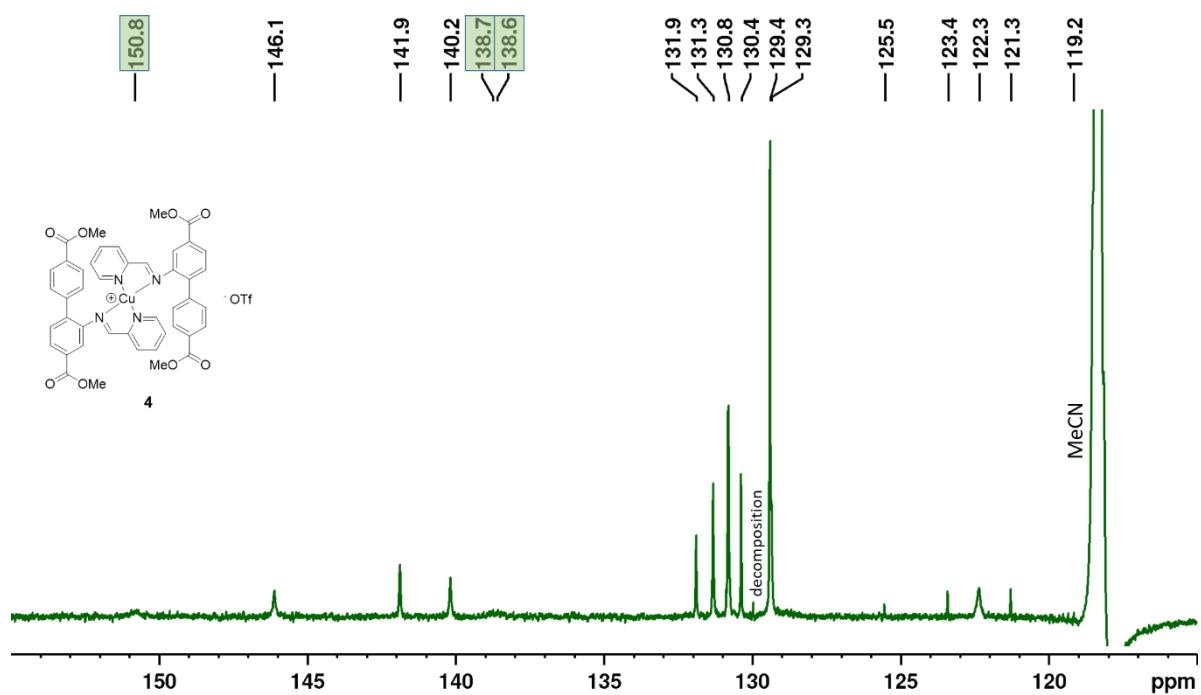
24

Figure S24. Detail of the ^{13}C NMR (150 MHz, CD$_3$CN) spectrum of **4**. Peaks localized through HSQC are highlighted.
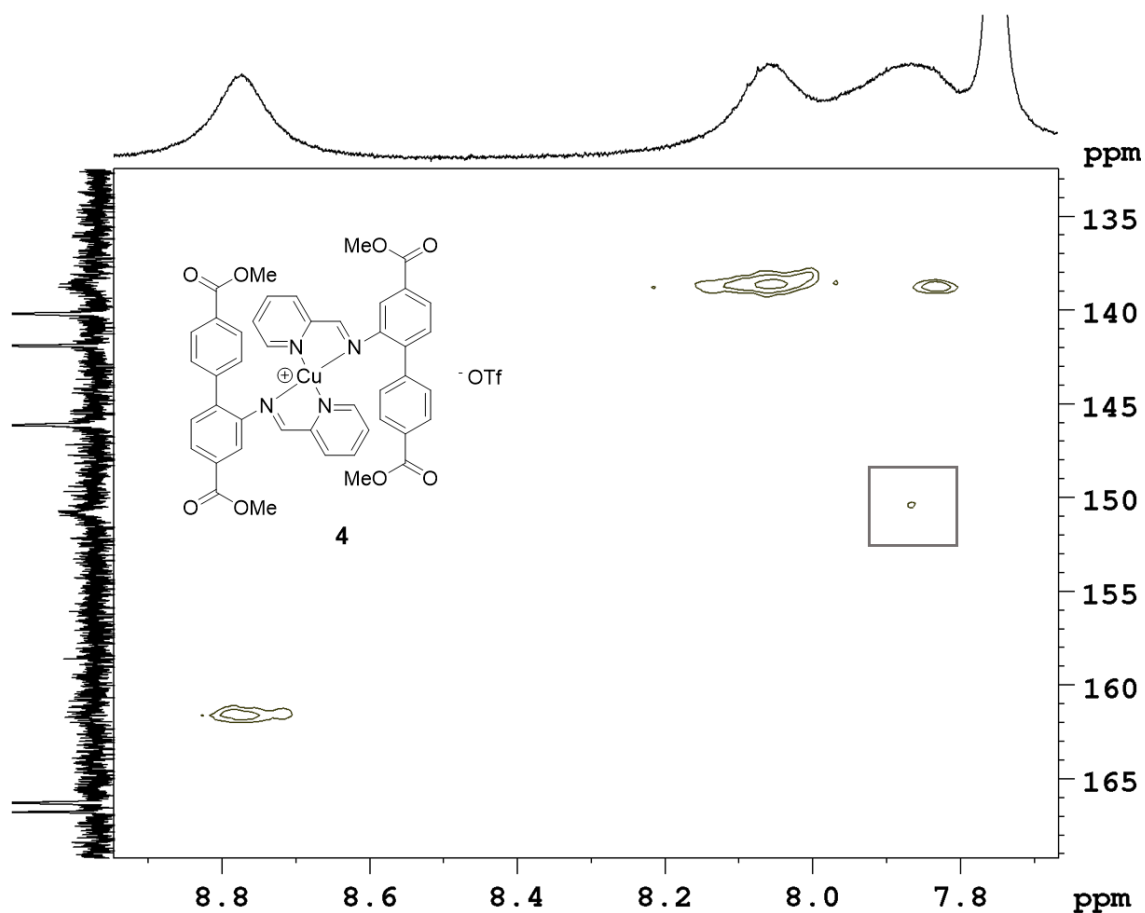
Figure S25. HSQC (600 MHz, CD$_3$CN) of **4** showing the carbons detected through HSQC.

Compound **4** showed minor species besides the main peaks in both, d_6-DMSO (at ambient temperature) and CD$_3$CN (at low temperatures). In order to see if the minor species and the major species interconvert, NOESY/EXSY experiments were conducted in both solvents (**Figure S26** and **Figure S30**). Both show correlations between the minor and the major species. In acetonitrile, the phase of the exchange peaks differs from the NOEs at room temperature. NOEs were only observed for the major species.
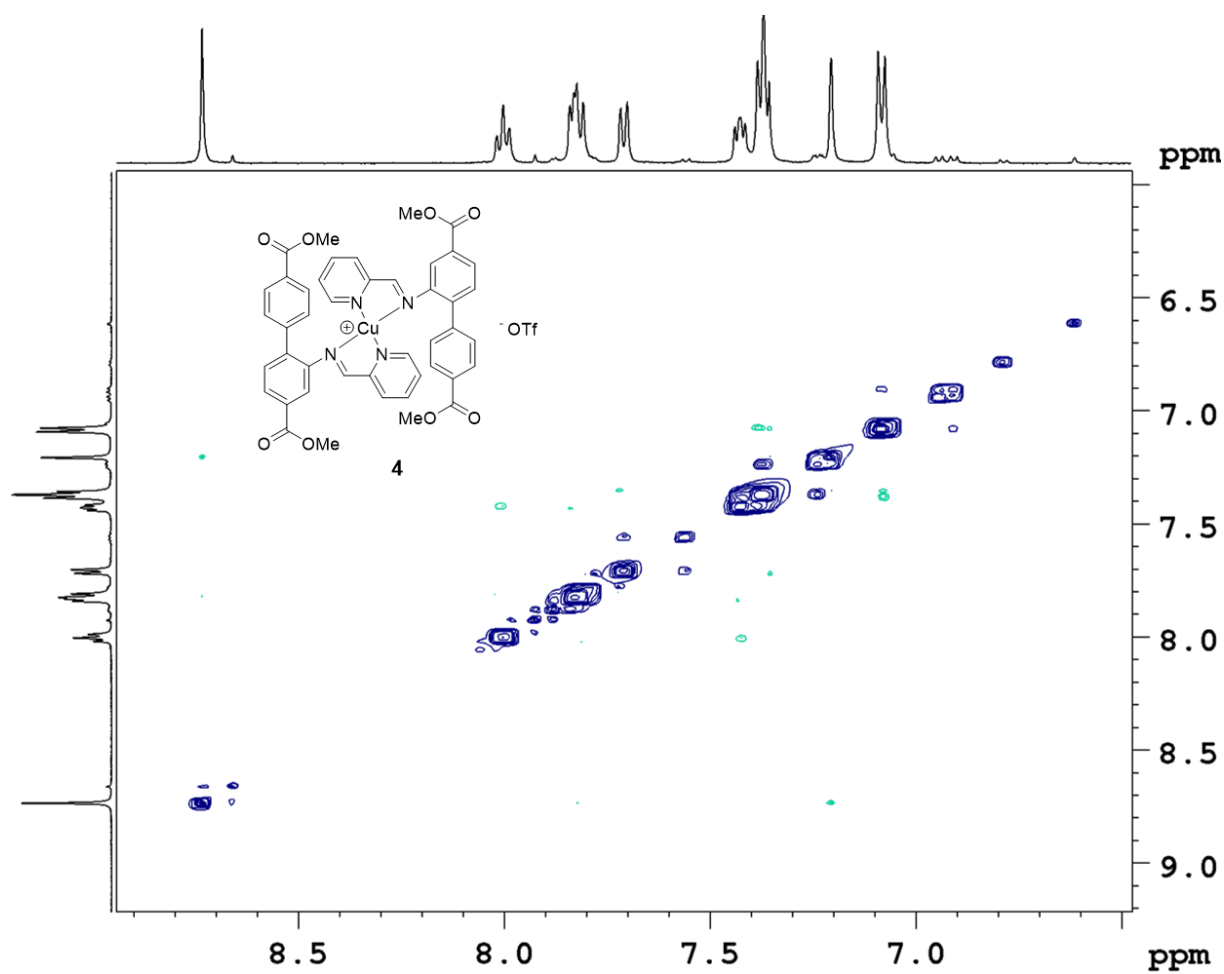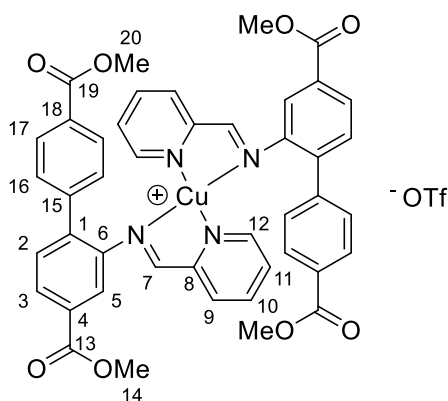
Figure S26. NOESY/EXSY (500 MHz, CD₃CN) of **4** at -34 °C showing chemical exchange (positive peaks off the diagonal) between the major species and the minor species. At higher temperatures, these peaks coalesced into a broadened peak.

NMR Data for Compound **4** in *d6*-DMSO

In the ^{1}H NMR spectrum of **4** in *d6*-DMSO, one or more minor species were observed in addition to the major species. Only NMR data for the major species are given below.

^{1}H NMR (600 MHz, *d6*-DMSO): δ 9.03 (2H, s, H7), 8.12-8-15 (2H, m, H10), 7.99 (2H, d, $^3J_{H,H}$ = 7.6 Hz, H9), 7.89 (2H, d, $^3J_{H,H}$ = 4.4 Hz, H12), 7.70 (2H, d, $^3J_{H,H}$ = 7.9 Hz, H3), 7.51-7.53 (2H, m, H11), 7.43 (2H, d, $^3J_{H,H}$ = 7.9 Hz, H2), 7.38 (4H, d, $^3J_{H,H}$ = 8.0 Hz, H17), 7.19 (2H, s, H5), 7.12 (4H, d, $^3J_{H,H}$ = 8.0 Hz, H16), 3.97 (6H, s, H14), 3.83 (6H, s, H20). ^{13}C NMR (150 MHz, *d6*-DMSO): δ 165.2 (C19), 164.8 (C13), 161.2 (C7), 149.5 (C8), 149.1 (C12), 144.7 (C6), 140.4 (C15), 138.6 (C1), 137.8 (C10), 130.1 (C2), 130.0 (C4), 129.5 (C16), 128.5 (C18), 128.2 (C9), 127.9 (C11 + C17), 127.8 (C3), 120.9 (C5), 120.6 (q, $^1J_{C,F}$ = 321 Hz, CF$_3$), 52.2 (C14), 51.9 (C20). ^{15}N{^{1}H} NMR (600 MHz, *d6*-DMSO): δ −94.0 (N$_{imine}$), −126.8 (N$_{pyridine}$).

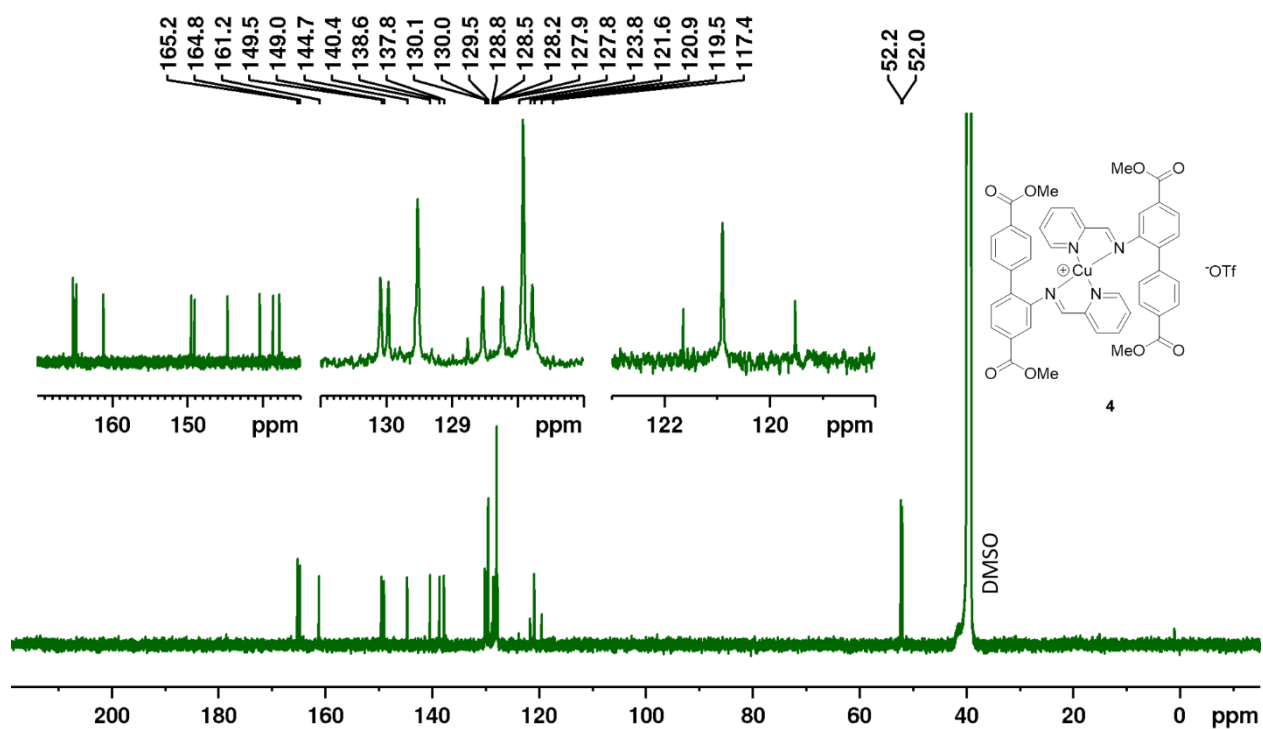**Figure S27**. ^1H NMR (600 MHz, d_6-DMSO) of **4**.

Figure S28. ^{13}C NMR (150 MHz, d_6-DMSO) of **4**.
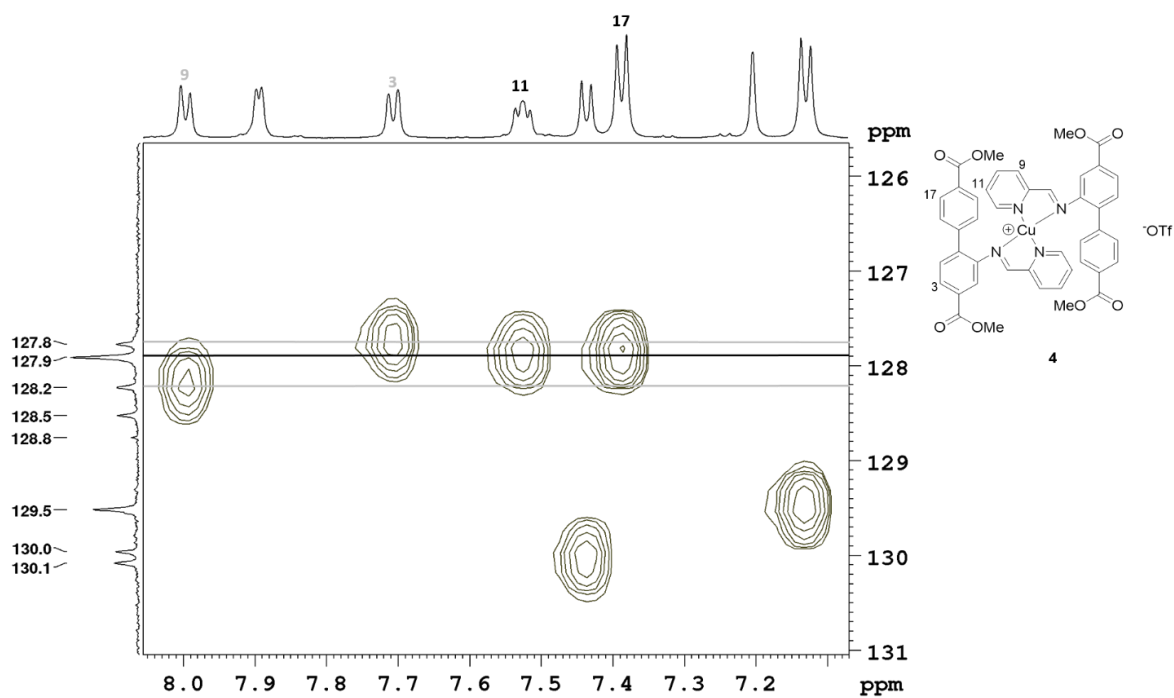
Figure S29. HSQC (600 MHz, d_6-DMSO) of **4**. The resonances corresponding to H11 and H17 both show a correlation to the resonance at δ 127.9, suggesting overlapping ^{13}C resonances.
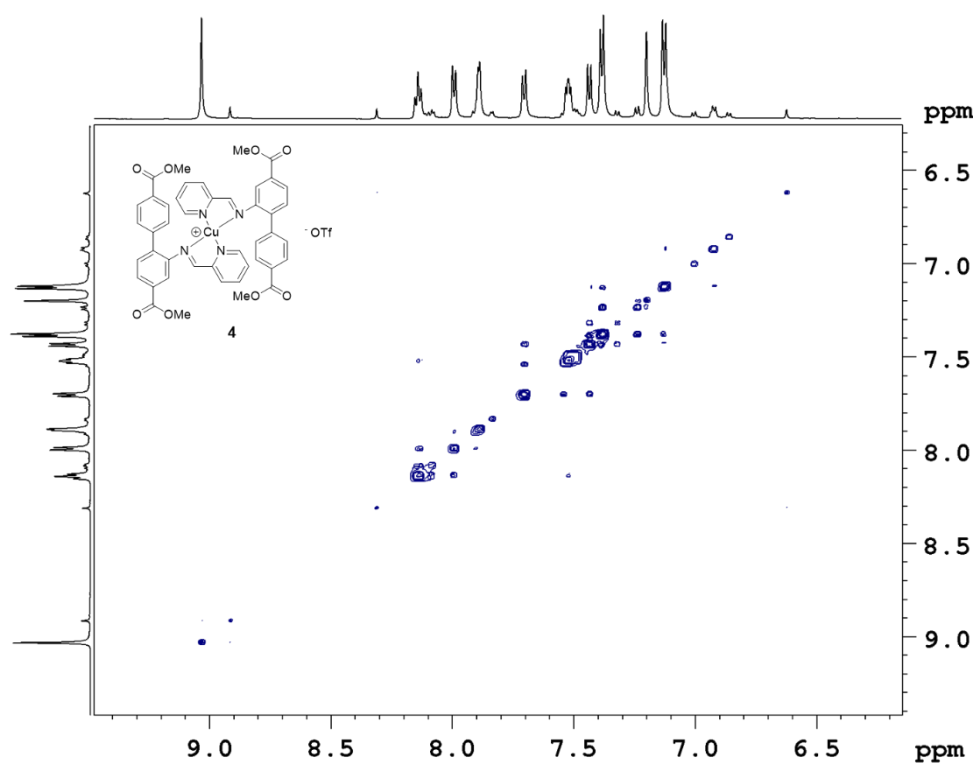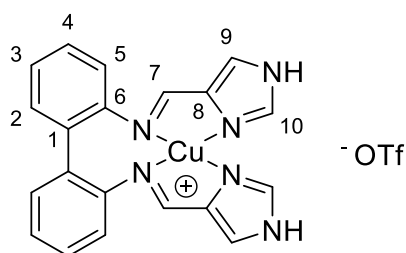

Figure S30. NOESY/EXSY (600 MHz, d_6-DMSO) of **4** at ambient temperature, showing chemical exchange and NOEs in the same phase.

30

Compound 5

A mixture of biphenyl-2,2'-diamine (0.54 mmol, 100 mg), CuOTf (0.54 mmol, 115 mg, 1 equiv.) and 1H-imidazole-4-carbaldehyde (1.08 mmol, 104 mg, 2 equiv.) were stirred in MeCN (3 mL) overnight. Et_2O (4 mL) was added and the solid was collected through filtration and washed (2x 1 mL Et_2O). Residual solvent was left to evaporate over night to yield **5** as a brown solid. Yield: 60-69 %.

^{1}H NMR (600 MHz, CD_3CN): δ 11.01 (2H, N**H**), 8.13 (2H, H7), 7.97 (2H, H10), 7.57 (2H, H9), 7.38 (2H, H2), 7.34 (2H, H4), 7.25 (2H, H3), 6.92 (2H, H5). ^{13}C NMR (150 MHz, CD_3CN): δ 154.1 (C7), 148.5 (C6), 139.3 (C8), 138.7 (C10), 133.0 (C2), 131.4 (C1), 129.5 (C4), 126.3 (C3), 122.2 (m*, $^1J_{C,F}$ = 325 Hz, **CF**$_3$), 122.1 (C9), 120.4 (C5). ^{15}N{^{1}H} NMR (800 MHz, CD_3CN): δ −79.1 (N$_{imine}$), −170.5 (N$_{IM}$), −211.4 (N$_{AZ}$). HRMS m/z [^{63}CuL$^+$] (C$_{20}$H$_{16}$CuN$_6^+$): Calcd: 403.0727 Found: 403.0715 Anal. Calcd: C, 45.61; H, 2.92; N, 15.20 Found: C, 45.73; H, 2.92; N, 15.19.
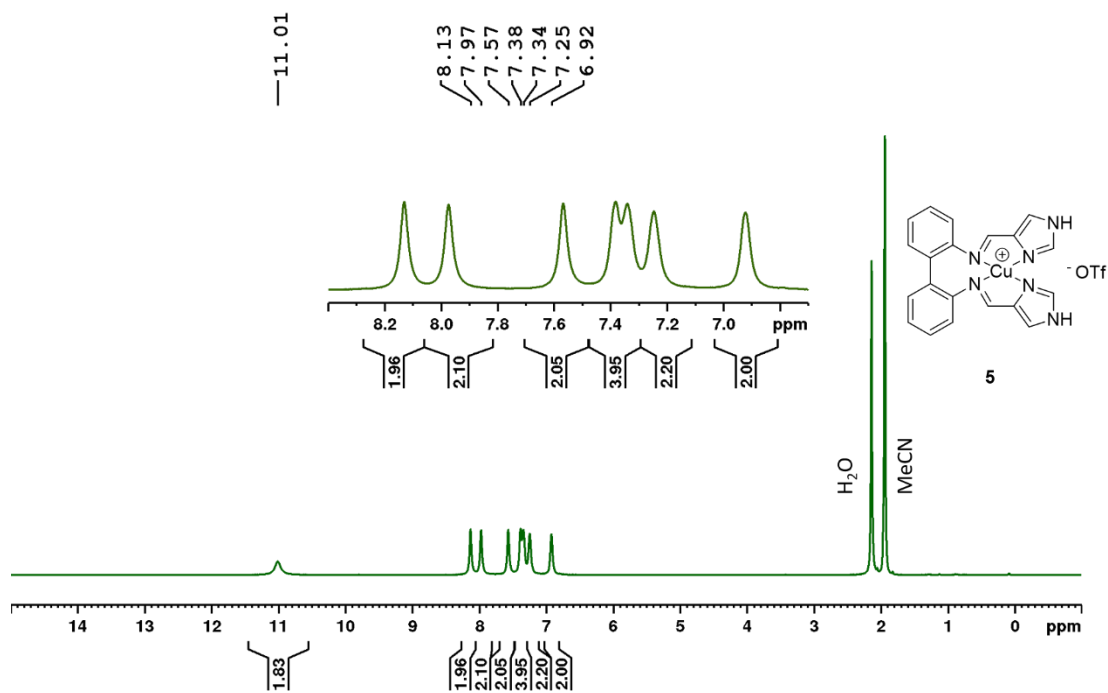
* d visible, expected q

Figure S31. ^{1}H NMR (600 MHz, CD$_3$CN) of **5**.
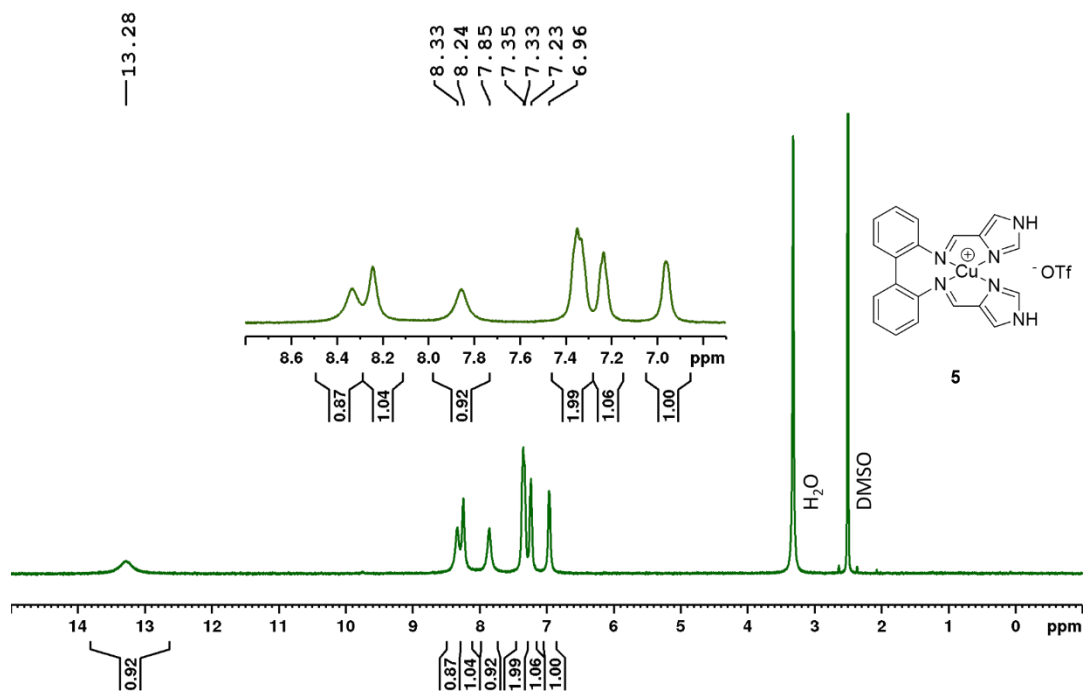

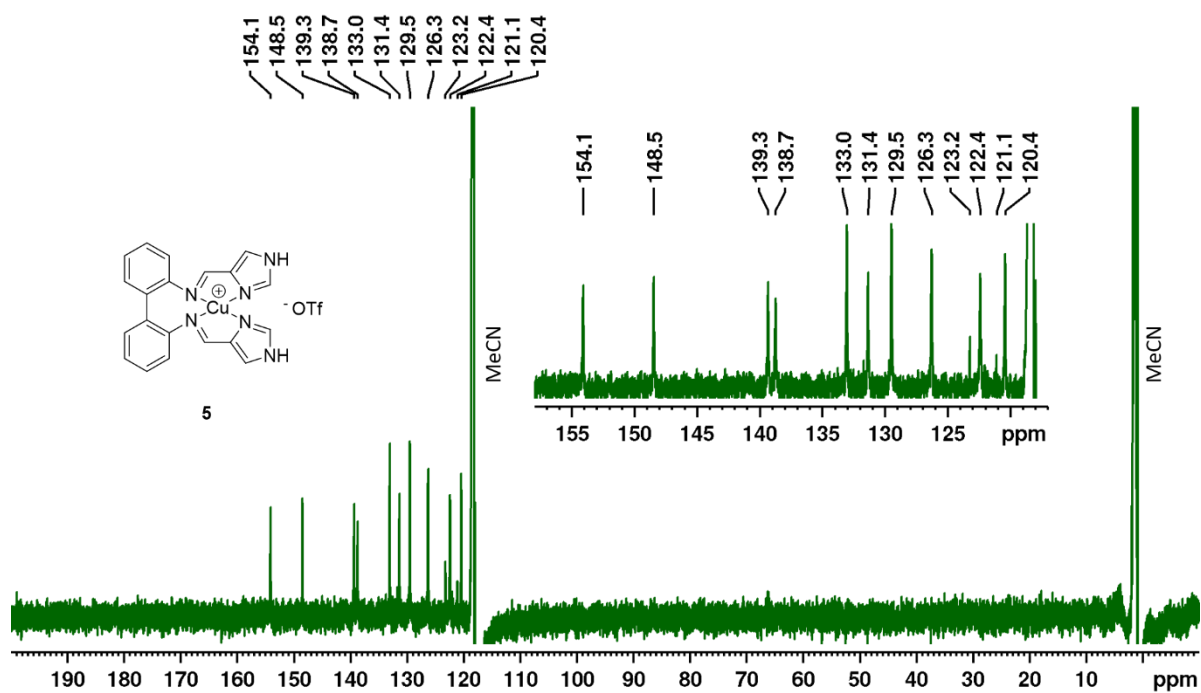**Figure S32**. ^{1}H NMR (500 MHz, d$_6$-DMSO) of **5**. The peaks are broader compared to the measurement in CD$_3$CN.

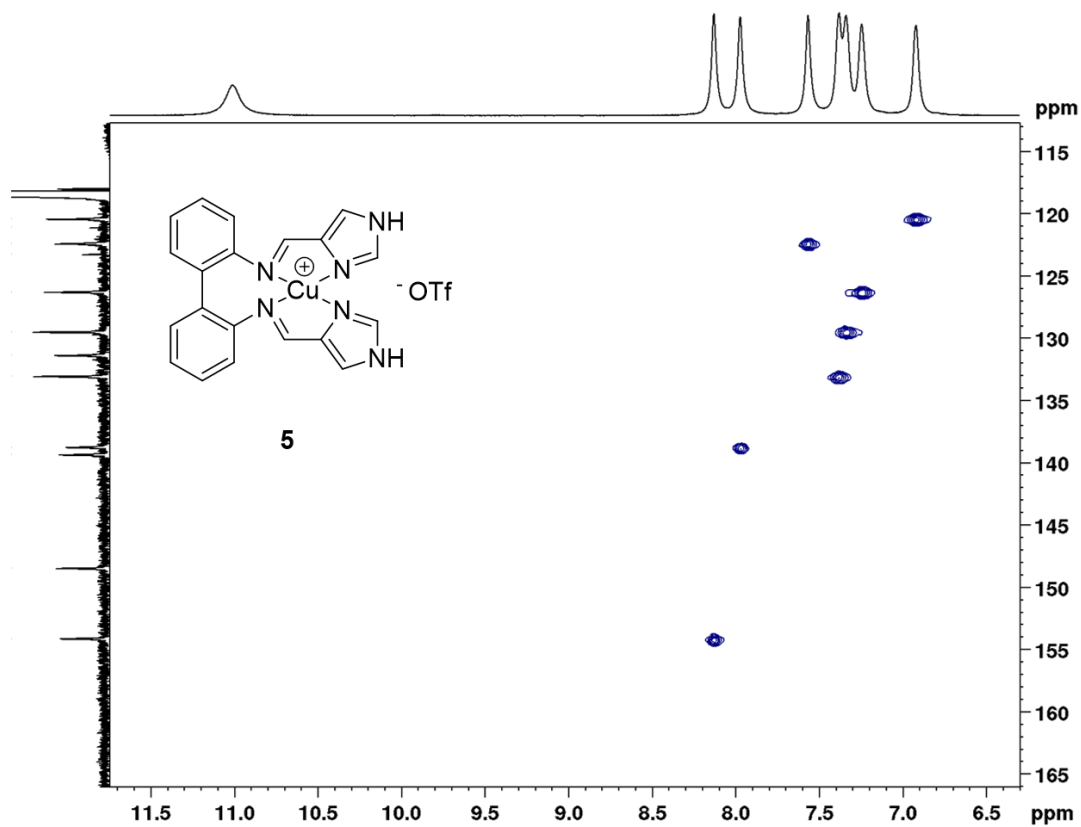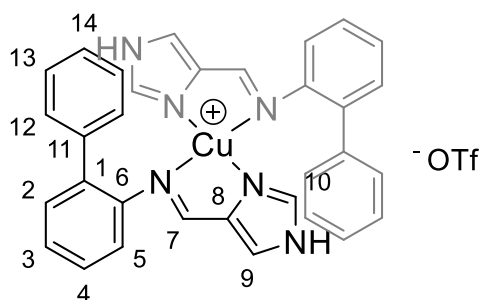**Figure S33.** ^{13}C NMR (150 MHz, CD$_3$CN) of **5**.

Figure S34. HSQC (600 MHz, CD$_3$CN) of complex **5**.

Compound 6

A mixture of CuOTf (0.30 mmol, 63 mg, 1 equiv.), biphenyl-2-amine (0.59 mmol, 100 mg, 2 equiv.) and 1*H*-imidazole-4-carbaldehyde (0.59 mmol, 57 mg, 2 equiv.) were stirred in MeCN (2 mL) overnight. The formed solid was collected through filtration and washed with Et$_2$O (2 mL). Residual solvent was left to evaporate over night to yield **6** as an orange solid. Yield: 64-72 %.

^{1}H NMR (*d$_6$*-DMSO, 600 MHz): δ 13.03 (2H, s, N**H**), 8.32 (2H, s, H7), 7.79 (2H, s, H9), 7.64 (2H, s, H10), 7.25 (4H, m, H2, H3), 7.17 (2H, m, H4), 7.05 (10H, m, H12-14), 6.56 (2H, m, H5). ^{13}C NMR (*d$_6$*-DMSO, 150 MHz): δ 153.7 (C7), 147.2 (C6), 138.3 (C11), 138.0 (C8), 137.4 (C10), 134.0 (C1), 130.0 (C2), 129.2 (**C**H phenyl), 128.2 (C4), 127.5 (**C**H phenyl), 126.5 (**C**H phenyl), 125.9 (C3), 121.9 (C9), 120.7 (q, $^1J_{C,F}$ = 322 Hz, **C**F$_3$), 120.6 (C5). ^{15}N{^{1}H} NMR (800 MHz, *d$_6$*-DMSO): δ −86.1 (N$_{imine}$), −170.0 (N$_{IM}$), −206.1 (N$_{AZ}$). ESI-MS: *m/z* 248.118 (100 %, [L+H]$^+$), 270.100 (63 %, [L+Na]$^+$), 310.040 (11 %, [^{63}CuL]$^+$), 312.038 (5 %, [^{65}CuL]$^+$), 557.150 (9 %, [^{63}CuL$_2$]$^+$), 559.149 (4 %, [^{65}CuL$_2$]$^+$). HRMS *m/z* [^{63}CuL$_2$$^{2+}$] (C$_{32}H_{26}CuN_6$$^+$): Calcd: 557.1509 Found: 557.1499. Anal. Calcd: C, 56.05; H, 3.71; N, 11.88 Found: C, 55.88; H, 3.69; N, 11.78.

Figure S35. ^{1}H NMR (600 MHz, d_6-DMSO) of **6**.
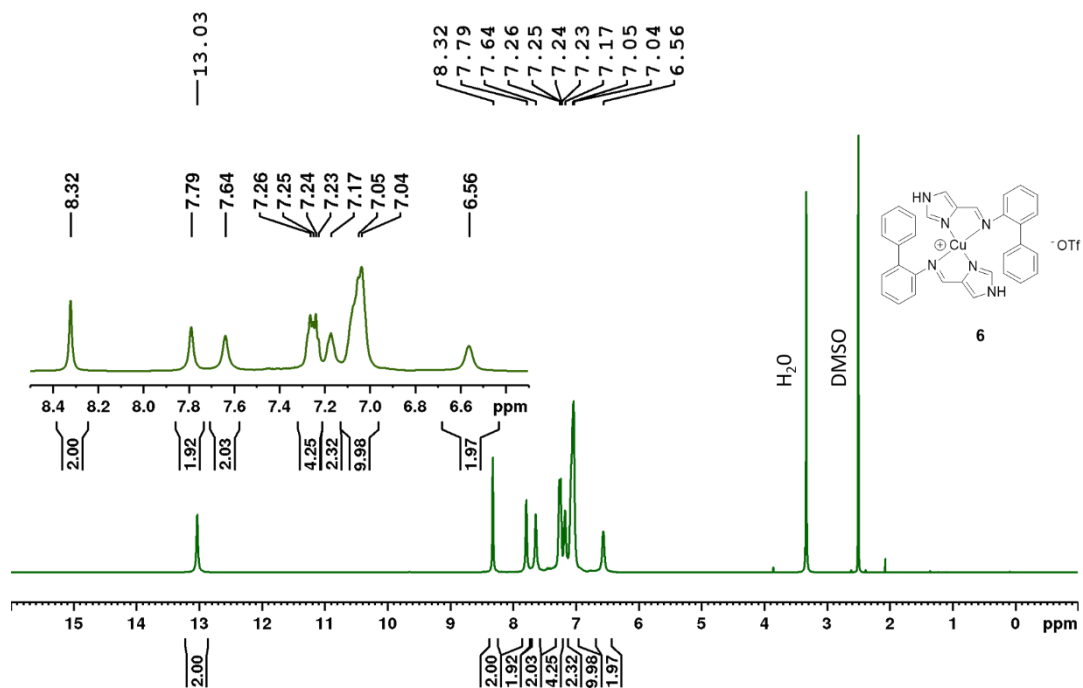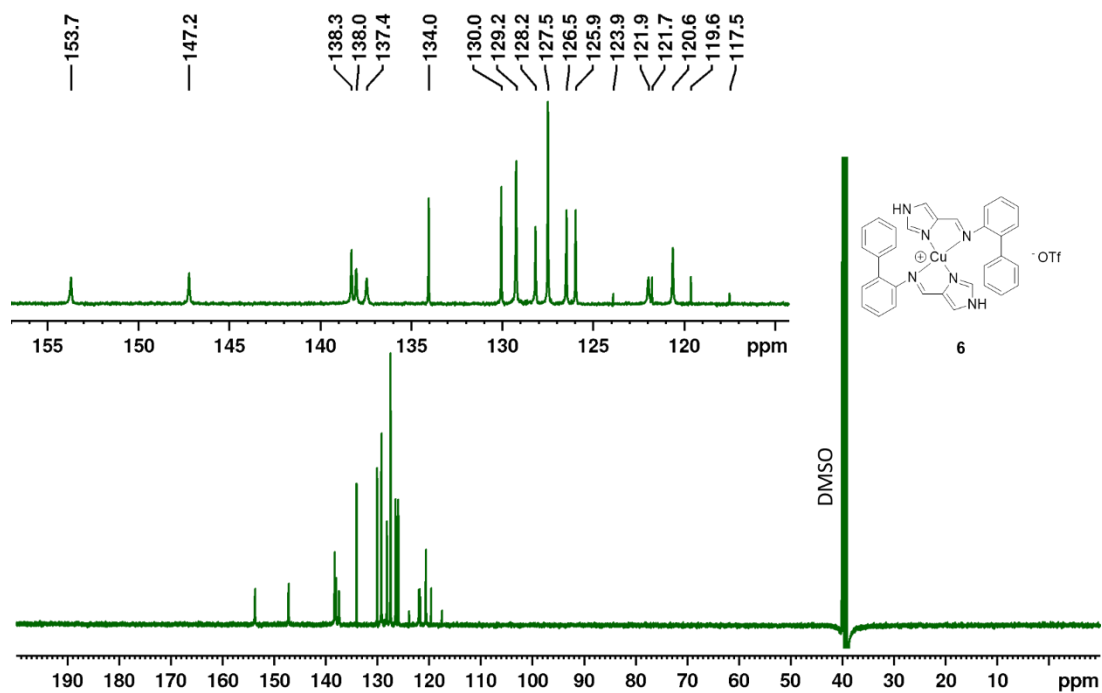

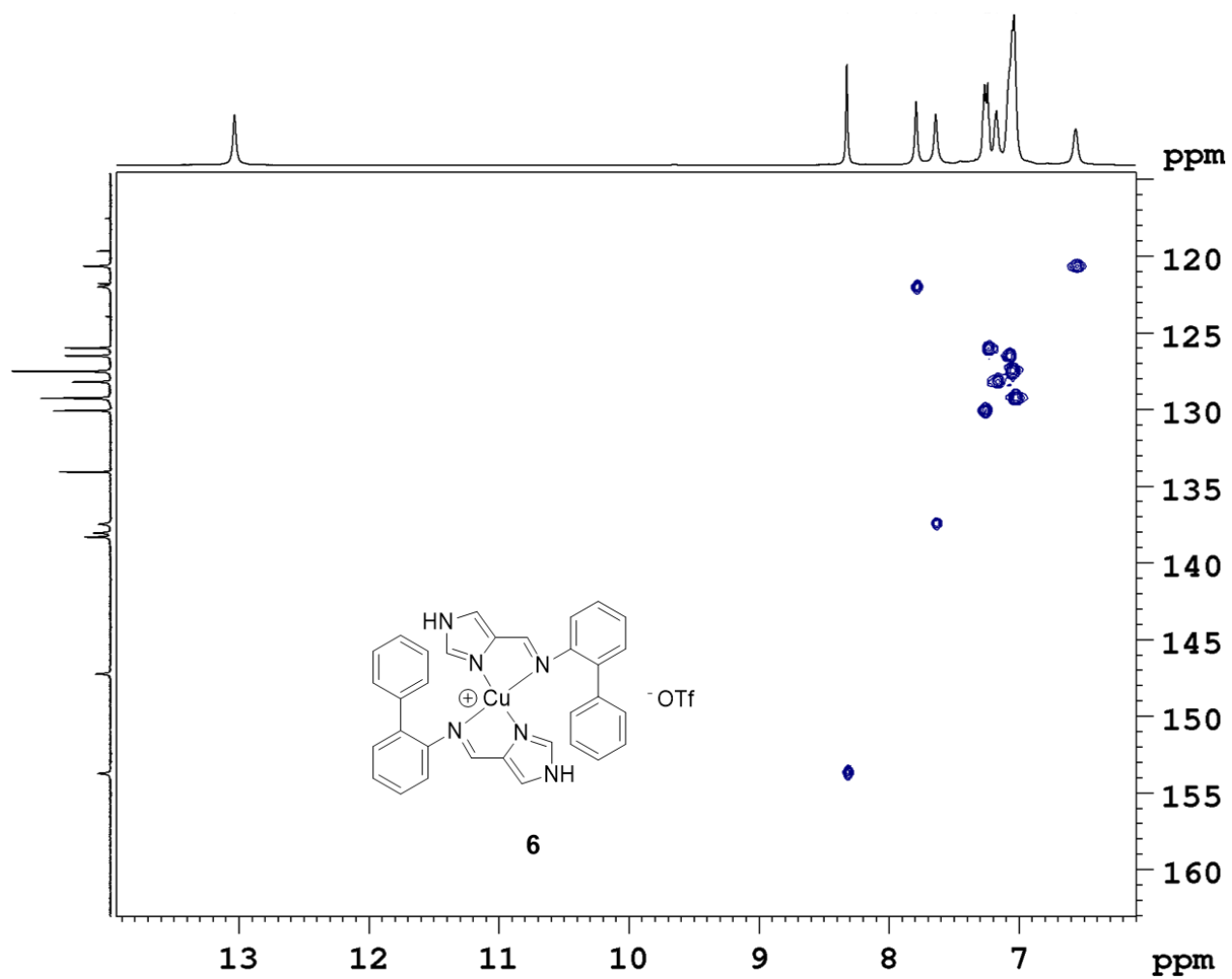**Figure S36**. ^{13}C NMR (150 MHz, d_6-DMSO) of **6**.

Figure S37. HSQC (600 MHz, *d₆*-DMSO) of **6**.

Synthesis of Ligands

The synthesis of ligands **L1-L6** was adapted from previously reported procedures for Schiff base ligands.[1]

[A]: The diamine (1.00 mmol) and the respective aldehyde (2.20 mmol, 2.2 equiv.) were suspended in dry EtOH. 3 drops of formic acid were added. The mixture was stirred for 20 h and the precipitated product was collected through filtration. The product was washed with dry EtOH and dried in a vacuum oven at 70 °C over night.

[B]: The amine (1.00 mmol) and the respective aldehyde (1.05 mmol, 1.05 equiv.) were suspended in dry EtOH. 3 drops of formic acid were added. The mixture was stirred for 20 h and the precipitated product was collected through filtration. The product was washed with dry EtOH and dried in a vacuum oven at 70 °C over night.

The ligands bearing imidazole moieties (**L1**, **L2**, **L5**, **L6**) showed concentration-dependent NMR spectra. In order to minimize the line-broadening, the spectra were recorded at low concentrations (ca. 0.5-1 mg in 0.6 mL of d_6-DMSO). Incomplete carbon spectra were obtained for these compounds, even after prolonged experiment time on high-field instruments. In HSQC, two correlations were observed for some protons (H7, H9 and H10), indicating conformational changes and/or intermolecular hydrogen bonding associated with the imine and imidazole groups in the molecules. The broadened resonances observed for **L1, L2, L5** and **L6** are in accordance with NMR data for imidazole Schiff bases found in the literature.[7–9] Therefore, only ^{1}H NMR spectra and ^{1}H-^{15}N HMBC are reported.

L1

L1 was obtained as a colourless to pale yellow solid from ligand synthesis procedure A after recrystallization from acetonitrile (23% yield).
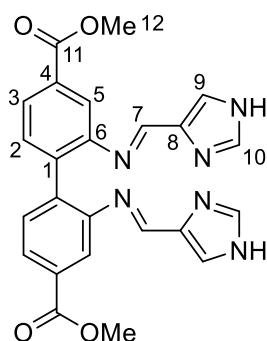
M.p. > 220 °C (decomposes). ^{1}H NMR (600 MHz, d_6-DMSO): δ 12.48 (*br*, 2H, s, N**H**), 8.20 (2H, s, H7), 7.81 (2H, d, $^3J_{H,H}$ = 7.7 Hz, H3), 7.72 (2H, s, H10), 7.51 (2H, s, H5), 7.5-7.1 (*br*, 2H, H9), 7.46 (2H, d, $^3J_{H,H}$ = 7.6 Hz, H2). ^{15}N{^{1}H} NMR (800 MHz, d_6-DMSO): δ −69.5 (N_{imine}), −116.1 (N_{IM}), −210.8 (N_{AZ}). HRMS (ESI) *m/z* ($C_{24}H_{20}N_6O_4$ + Na^+): Calcd: 479.1438 Found: 479.1438. Anal. Calcd: C, 63.15; H, 4.42; N, 18.41 Found: C, 62.87; H, 4.45; N, 18.38.
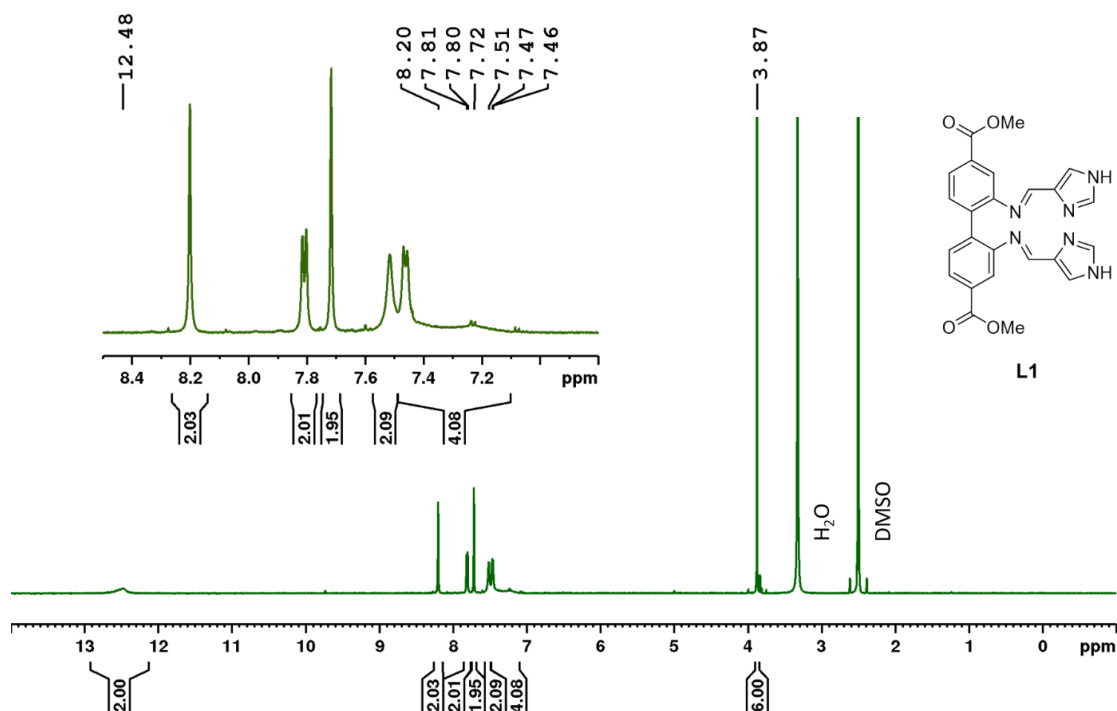
Figure S38. ^{1}H NMR (600 MHz, d_6-DMSO) of **L1**.

38

L2

L2 was obtained as a colourless solid from ligand synthesis procedure B after two-fold recrystallization from toluene (33 % yield).
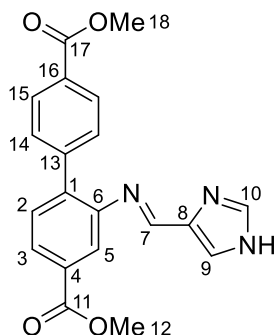
M.p. 191-193 °C (decomposes). ^{1}H NMR (600 MHz, d_6-DMSO): δ 12.67 (*br*, 1H, s, N**H**), 8.49 (1H, s, H7), 7.98 (2H, d, $^3J_{H,H}$ = 8.4 Hz, H15), 7.88 (1H, dd, $^3J_{H,H}$ = 8.0 Hz, $^4J_{H,H}$ = 1.5 Hz, H3), 7.81 (1H, s, H10), 7.7-7.6 (5H, overlapping m, H14, H2, H3, H9), 3.89 (3H, s, CO$_2$C**H$_3$**), 3.87 (3H, s, CO$_2$C**H$_3$**). ^{15}N{^{1}H} NMR (800 MHz, d_6-DMSO): δ −69.9 (N$_{imine}$), −116.5 (N$_{IM}$). ^{15}N shifts originate from two separate HMBC experiments at different concentrations. N$_{AZ}$ not found. HRMS (ESI) *m/z* (C$_{20}$H$_{17}$N$_3$O$_4$ + Na$^+$): Calcd: 386.1111 Found: 386.1111. Anal. Calcd: C, 66.11; H, 4.72; N, 11.56 Found: C, 65.95; H, 4.71; N, 11.48.
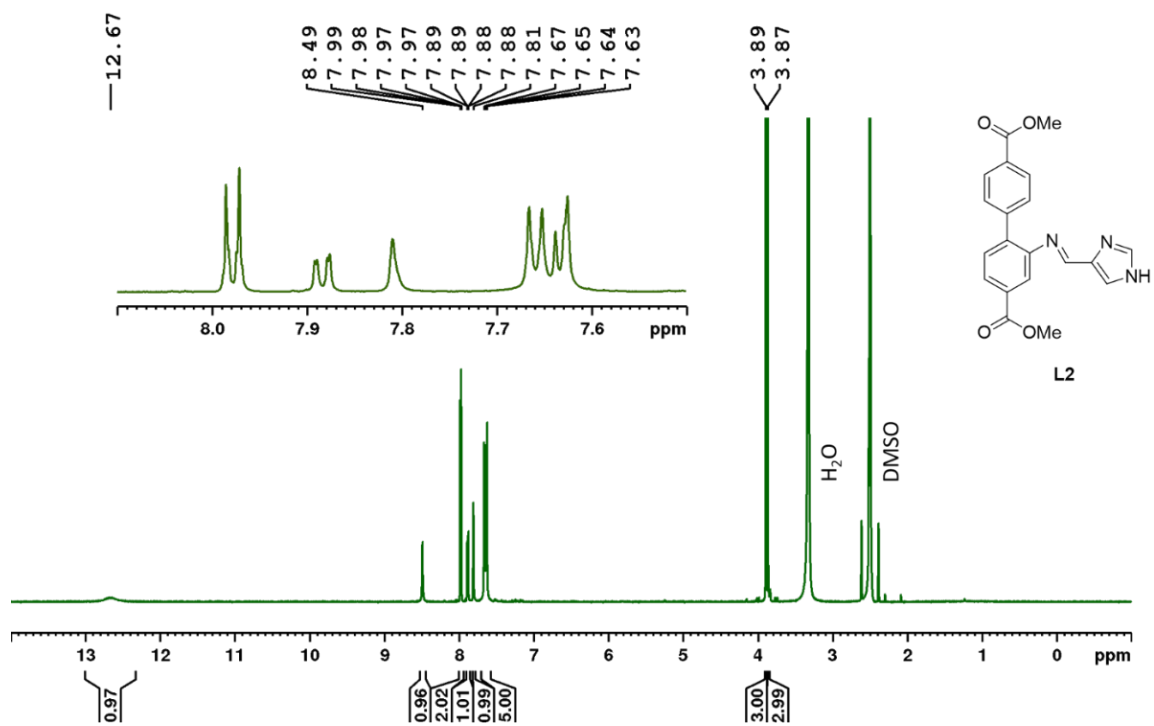
Figure S39. ^{1}H NMR (600 MHz, d_6-DMSO) of **L2**.

L3

L3 was synthesized according to ligand synthesis procedure A. After recrystallization from toluene, **L3** was obtained as pale yellow solid (82% yield).
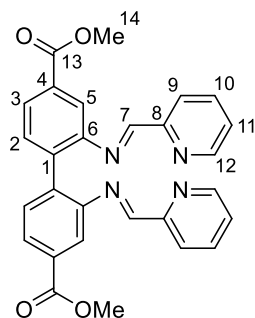
M.p. 219-222 °C (decomposes). ^{1}H NMR (600 MHz, d_6-DMSO): δ 8.55 (2H, ddd, $^3J_{H,H}$ = 4.8 Hz, $^4J_{H,H}$ = 1.6 Hz, $^5J_{H,H}$ = 0.9 Hz, H12), 8.33 (2H, s, H7), 7.94 (2H, dd, $^3J_{H,H}$ = 7.9 Hz, $^4J_{H,H}$ = 1.7 Hz, H3), 7.83 (2H, ddd, $^3J_{H,H}$ = 7.7 Hz, $^4J_{H,H}$ = 1.6 Hz, H10), 7.73 (2H, d, $^4J_{H,H}$ = 1.6 Hz, H5), 7.65 (2H, dd, $^3J_{H,H}$ = 8.0 Hz, $J_{H,H}$ = 0.9 Hz, H9), 7.60 (2H, d, $^3J_{H,H}$ = 7.9 Hz, H2), 7.45 (2H, ddd, $^3J_{H,H}$ = 7.5 Hz and 4.8 Hz, $^4J_{H,H}$ = 1.2 Hz, H11), 3.90 (6H, s, H14). ^{13}C NMR (150 MHz, d_6-DMSO): δ 165.8 (C13), 162.0 (C7), 153.4 (C8), 149.7 (C6), 149.5 (C12), 137.7 (C1), 137.0 (C10), 131.4 (C2), 130.6 (C4), 126.4 (C3), 125.7 (C11), 121.2 (C9), 118.8 (C5), 52.3 (C14). ^{15}N{^{1}H} NMR (800 MHz, d_6-DMSO): δ −47.9 (N$_{imine}$), −61.6 (N$_{pyridine}$). HRMS (ESI) m/z (C$_{28}$H$_{22}$N$_4$O$_4$ + Na$^+$): Calcd: 501.1532 Found: 501.1533. Anal. Calcd: C, 70.28; H, 4.63; N, 11.71 Found: C, 69.92; H, 4.61; N, 11.64.

Figure S40. ^{1}H NMR (600 MHz, d_6-DMSO) of **L3**.

Figure S41. ^{13}C NMR (150 MHz, d_6-DMSO) of **L3**.
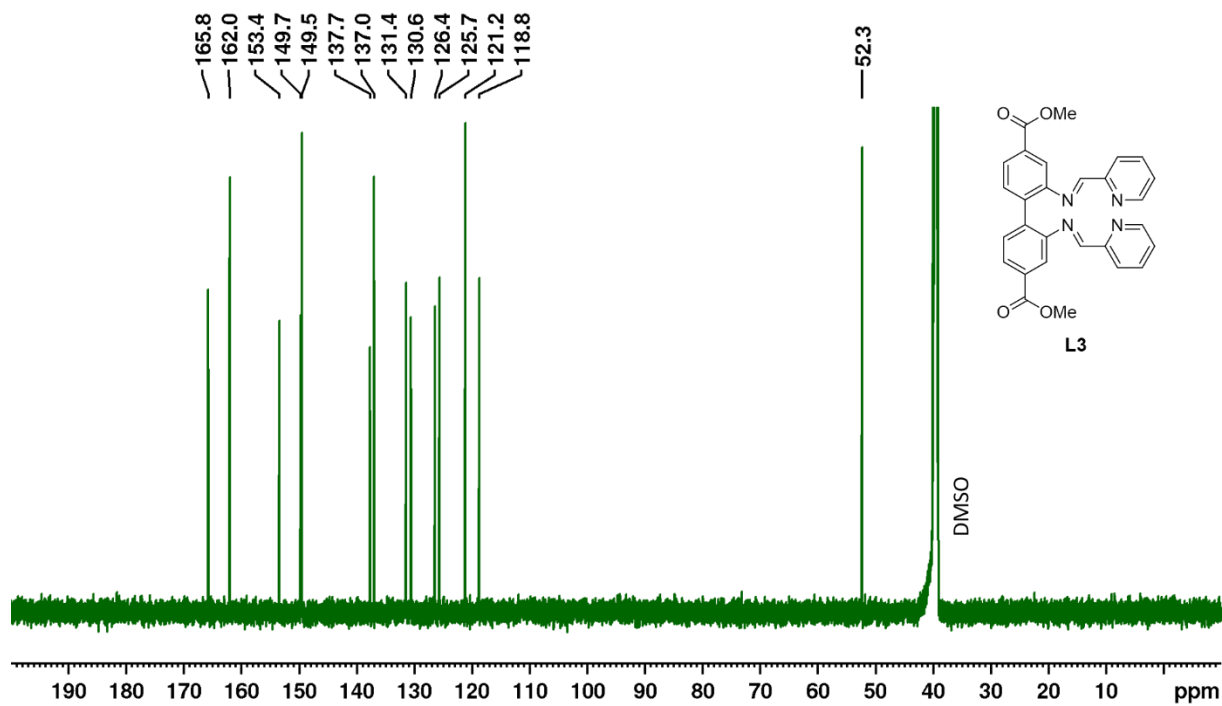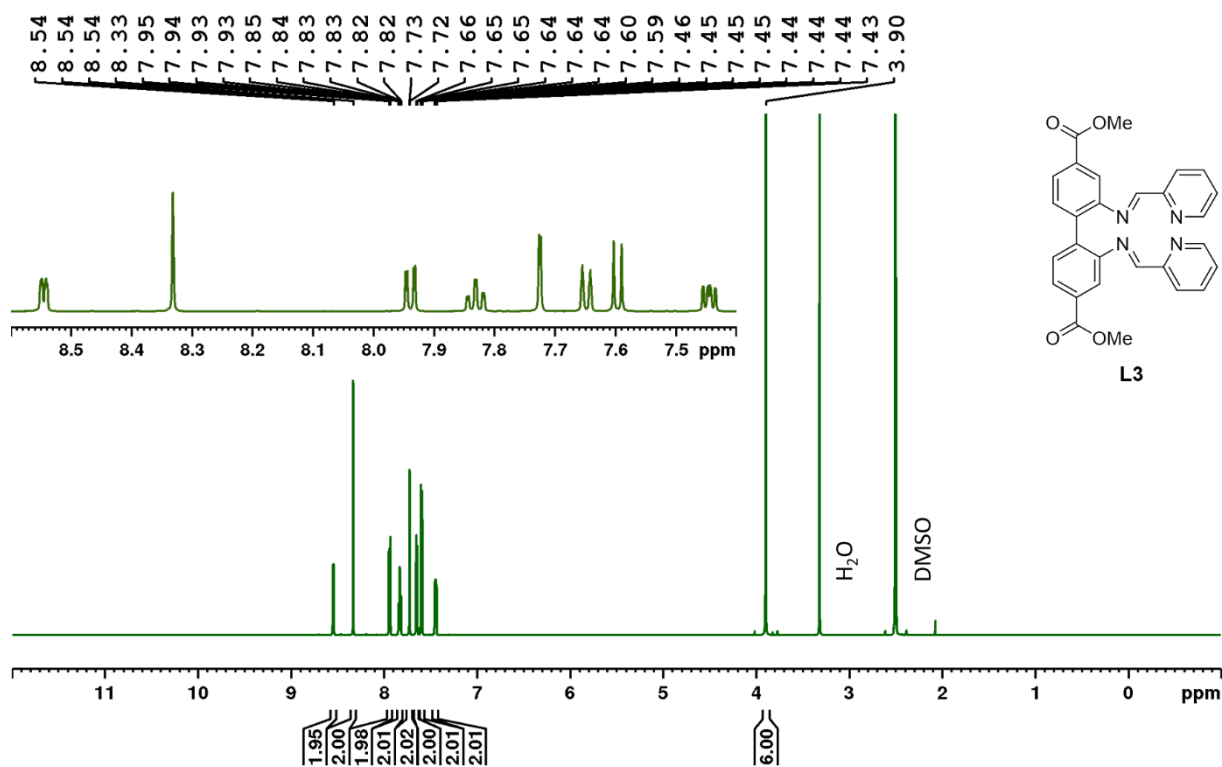
L4

L4 was obtained from ligand synthesis procedure B as a colourless solid (77-84 % yield).
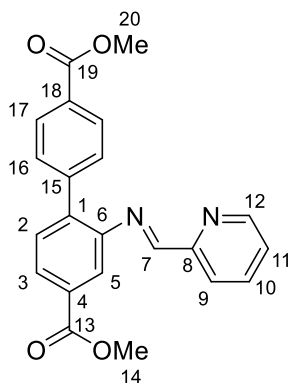
M.p. 176-178 °C. ^{1}H NMR (600 MHz, d_6-DMSO): δ 8.73 (1H, m, H12), 8.67 (1H, s, H7), 8.00 (2H, d, $^3J_{H,H}$ = 8.4 Hz, H17), 7.97 (1H, dd, $^3J_{H,H}$ = 8.0 Hz, $^4J_{H,H}$ = 1.7 Hz, H3), 7.94-7.89 (2H, overlapping m, H9 and H10), 7.73 (1H, d, $^4J_{H,H}$ = 1.6 Hz, H5), 7.69 (1H, d, $^3J_{H,H}$ = 8.0 Hz, H2), 7.67 (2H, d, $^3J_{H,H}$ = 8.5 Hz, H16), 7.53 (1H, m, H11), 3.91 (3H, s, H14), 3.87 (3H, s, H20). ^{13}C NMR (150 MHz, d_6-DMSO): δ 166.0 (C19), 165.6 (C13), 162.7 (C7), 153.7 (C8), 149.7 (C12), 148.6 (C6), 142.6 (C15), 138.2 (C1), 137.2 (C10), 130.6 (C2), 130.5 (C4), 130.3 (C16), 128.7 (C17), 127.1 (C3), 125.9 (C11), 121.5 (C9), 119.6 (C5), 52.4 (C14), 52.2 (C20), missing: C18. ^{15}N{^{1}H} NMR (600 MHz, d_6-DMSO): δ –47.9 (N$_{imine}$), −62.5 (N$_{pyridine}$). HRMS (ESI) *m/z* (C$_{22}$H$_{18}$N$_2$O$_4$ + Na$^+$): Calcd: 397.1158 Found: 397.1159. Anal. Calcd: C, 70.58; H, 4.85; N, 7.48 Found: C, 70.51; H, 4.88; N, 7.46.
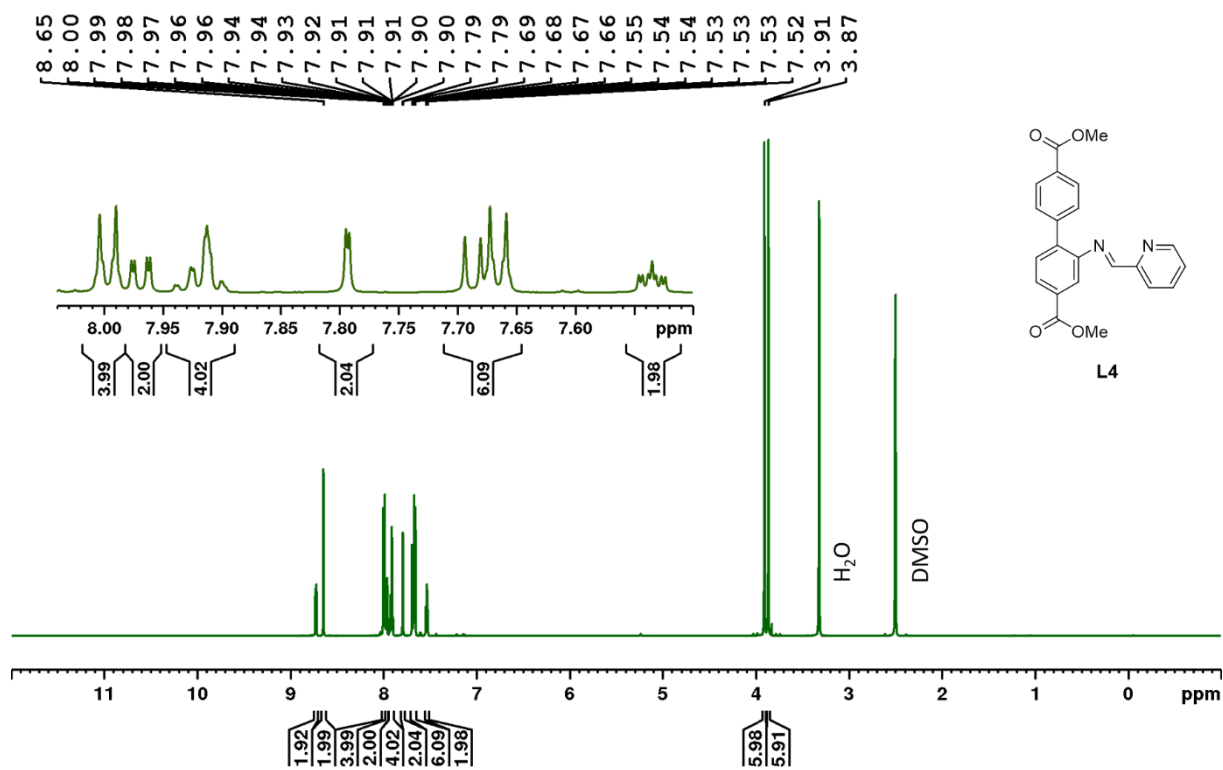
Figure S42. ^{1}H NMR (600 MHz, d_6-DMSO) of **L4**.
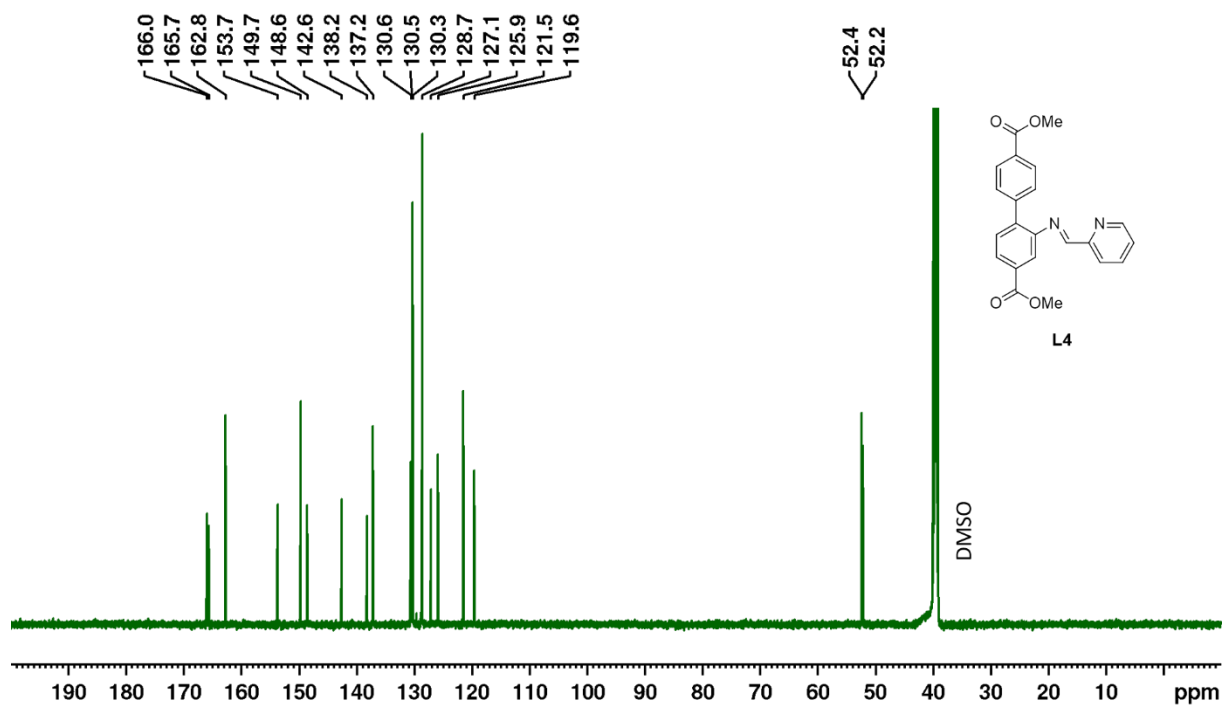
Figure S43. ^{13}C NMR (150 MHz, d_6-DMSO) of **L4**.

L5

L5 was obtained from ligand synthesis procedure A as a colourless solid (79-91 % yield).
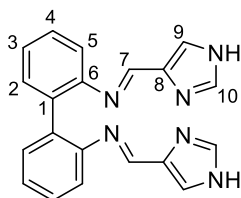
M.p. 230-231 °C (decomposes). ^{1}H NMR (600 MHz, d_6-DMSO): δ 12.45 (*br*, 2H, N**H**), 8.09 (2H, s, H7), 7.69 (2H, s, H10), 7.4-7.1 (*br*, 2H, H9), 7.33 (2H, dd, $^{3}J_{H,H}$ = 7.5 Hz, , H3), 7.26 (2H, d, $^{3}J_{H,H}$ = 7.2 Hz, H5), 7.19 (2H, dd, $^{3}J_{H,H}$ = 7.3 Hz, H4), 6.92 (2H, d, $^{3}J_{H,H}$ = 7.7 Hz, H2). ^{15}N{^{1}H} NMR (800 MHz, d_6-DMSO): δ −63.4 (N$_{imine}$), −117.0 (N$_{IM}$). N$_{AZ}$ not found. HRMS (ESI) *m/z* (C$_{20}$H$_{16}$N$_6$ + Na^{+}): Calcd: 363.1328 Found: 363.1329. Anal. Calcd: C, 70.57; H, 4.74; N, 24.69 Found: C, 70.41; H, 4.73; N, 24.61.
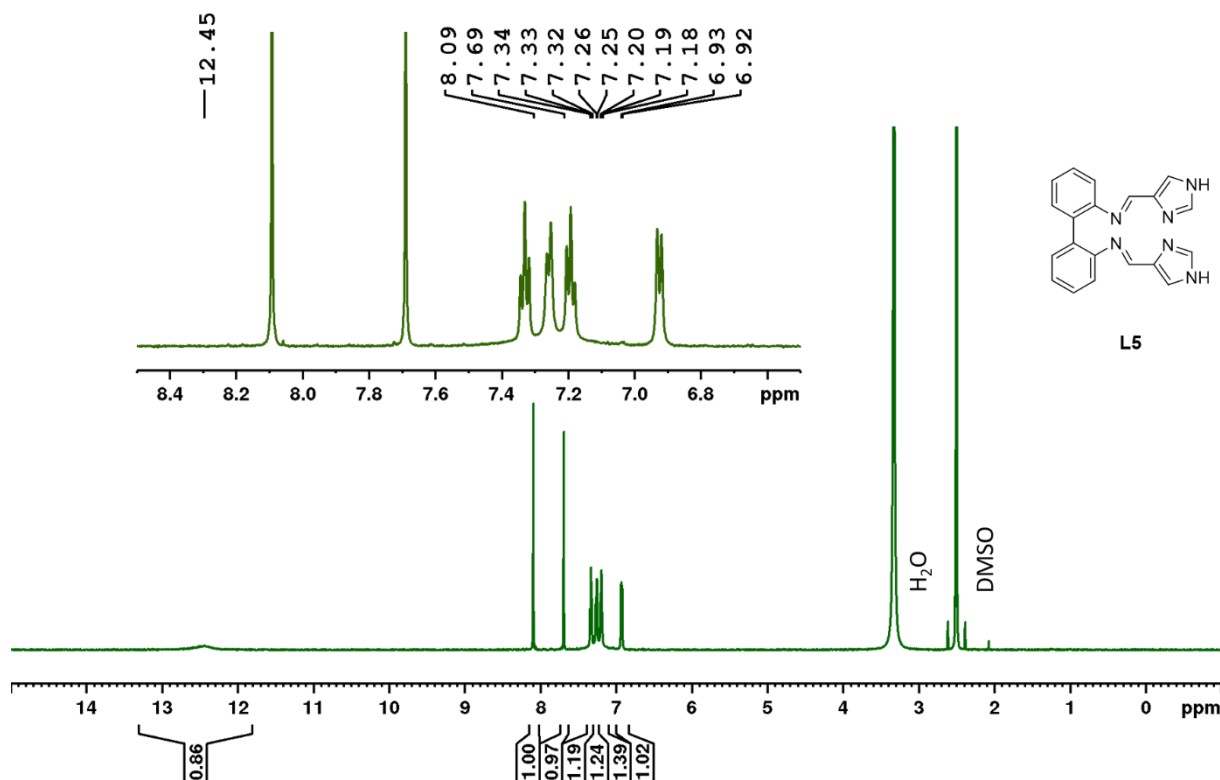
Figure S44. ^{1}H NMR (600 MHz, d_6-DMSO) of **L5**.

L6

L6 was obtained from ligand synthesis procedure B as an off-white solid (34-41 % yield).
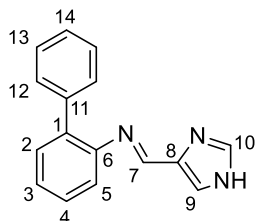
M.p. 189-190 °C (decomposes). ^{1}H NMR (600 MHz, d_6-DMSO): δ 12.65 (*br*, 1H, s, N**H**), 8.39 (1H, s, H7), 7.77 (1H, s, H10), 7.57 (*br*, 1H, s, H9), 7.47-7.33 (6H, overlap of phenyl-**H**), 7. ^{15}N{^{1}H} NMR (800 MHz, d_6-DMSO): δ −65.0 (N$_{imine}$), −117.2 (N$_{IM}$), −209.6 (N$_{AZ}$). HRMS (ESI) *m/z* (C$_{16}$H$_{13}$N$_3$ + Na$^+$): Calcd: 270.1001 Found: 270.1002. Anal. Calcd: C, 77.71; H, 5.30; N, 16.99 Found: C, 77.25; H, 5.27; N, 16.91.
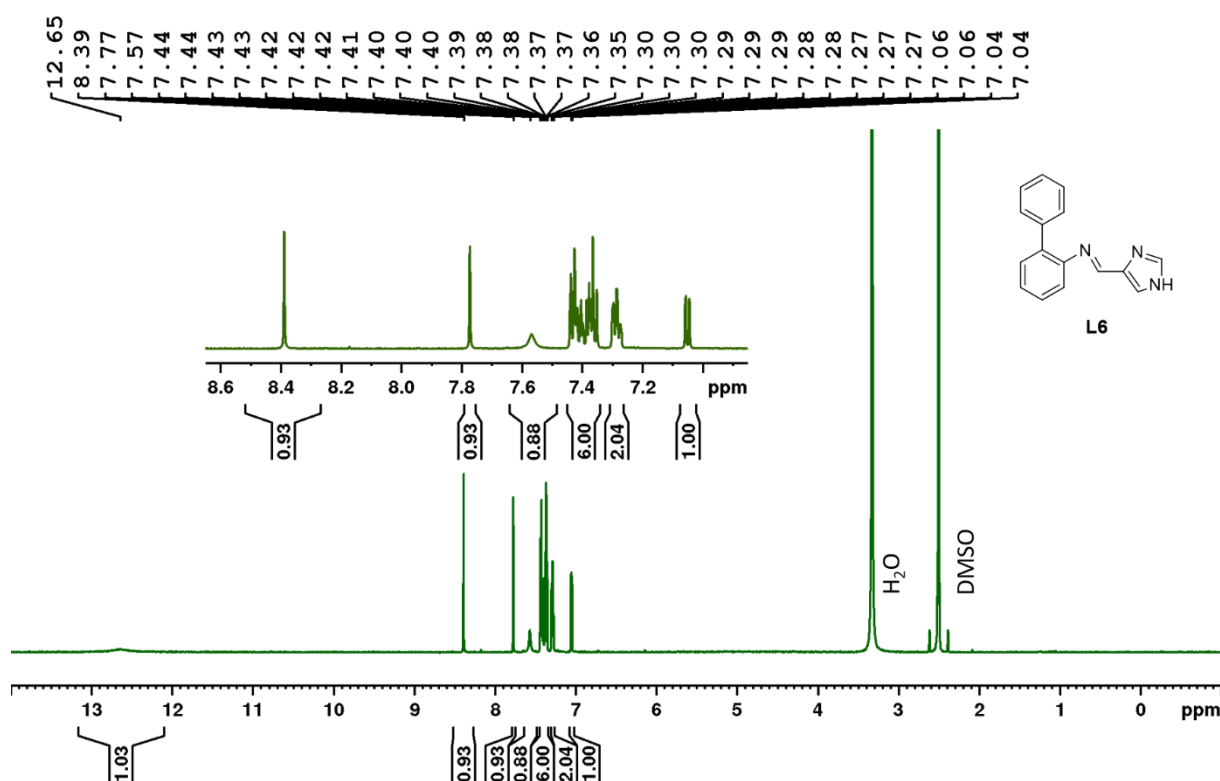
Figure S45. ^{1}H NMR (600 MHz, d_6-DMSO) of **L6**.

^{1}H-^{15}N HMBC
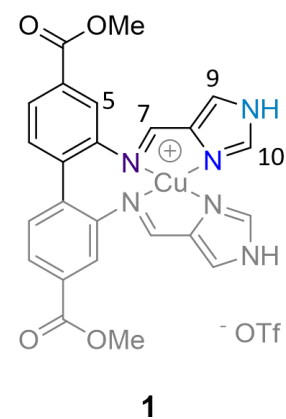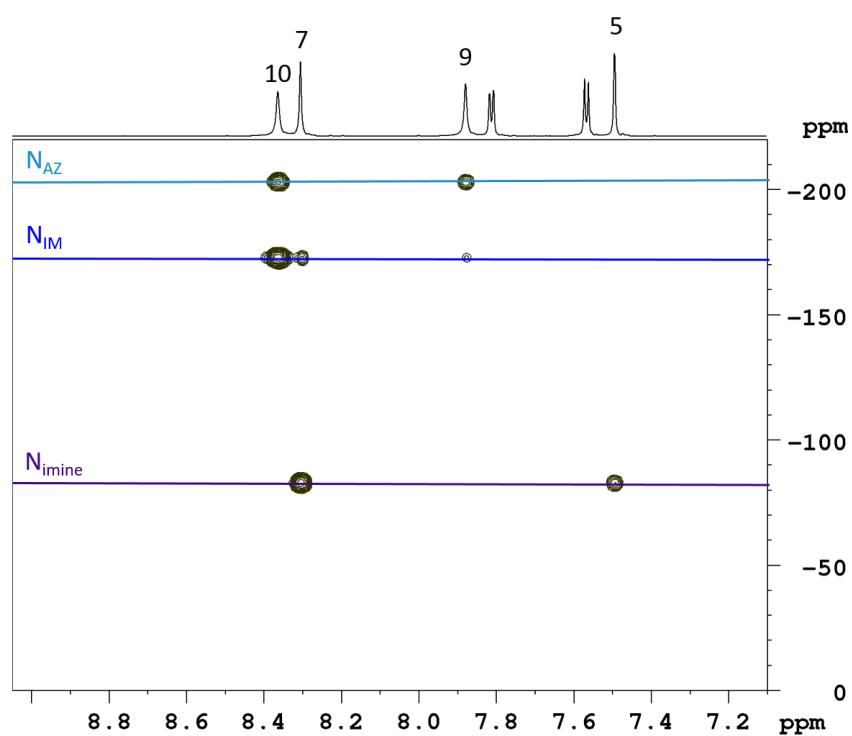
Figure S46. ^{1}H-^{15}N HMBC (800 MHz, d_6-DMSO) of **1**.
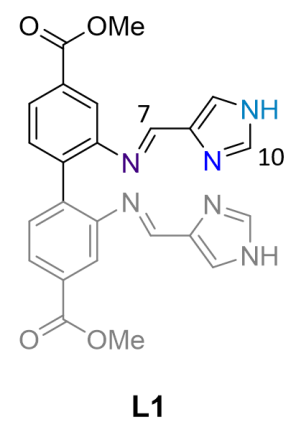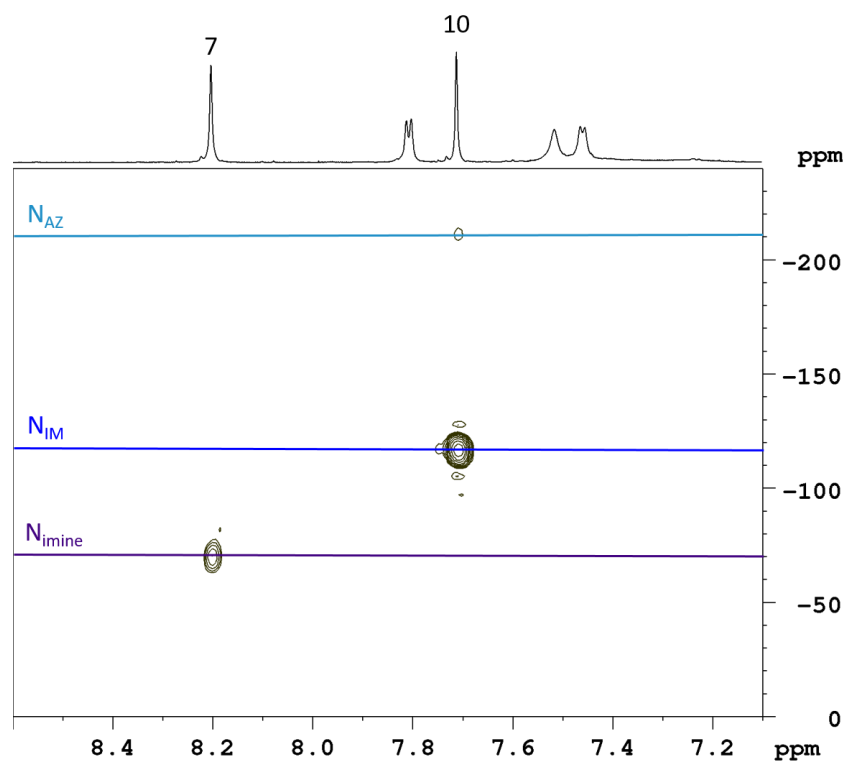
Figure S47. ^{1}H-^{15}N HMBC (800 MHz, d_6-DMSO) of **L1**.
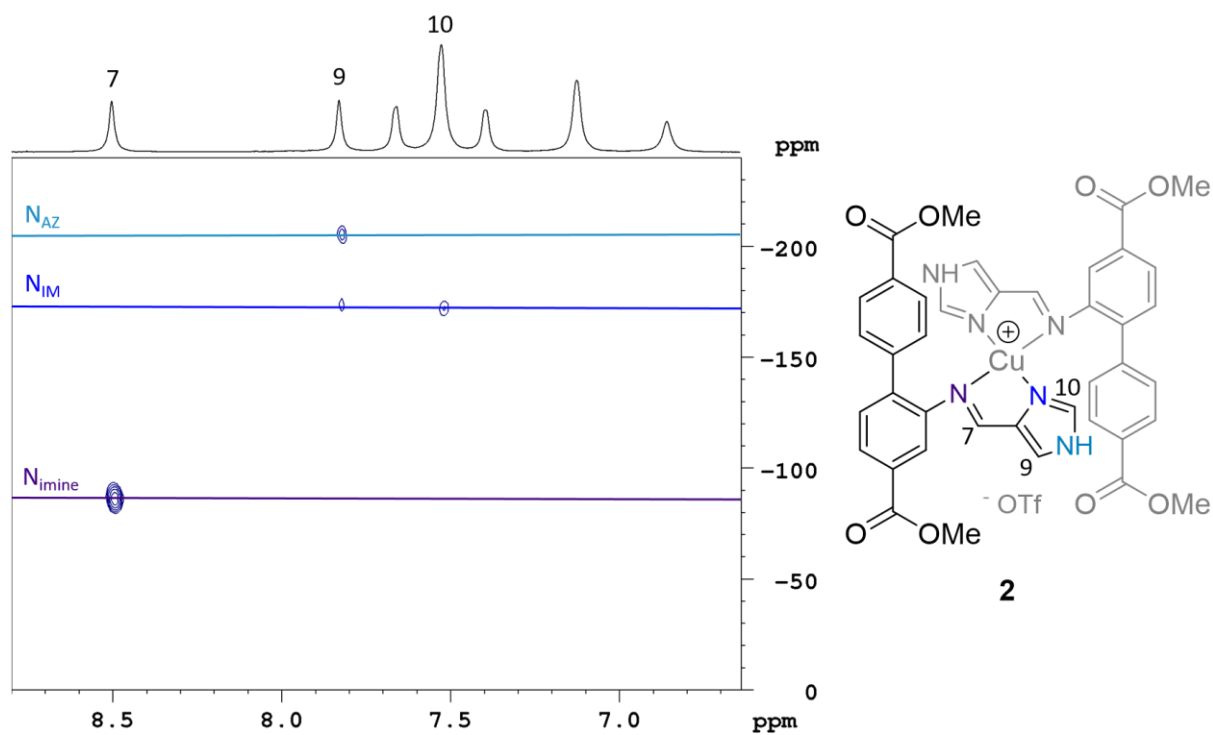
Figure S48. ^{1}H-^{15}N HMBC (800 MHz, d_6-DMSO) of **2**.
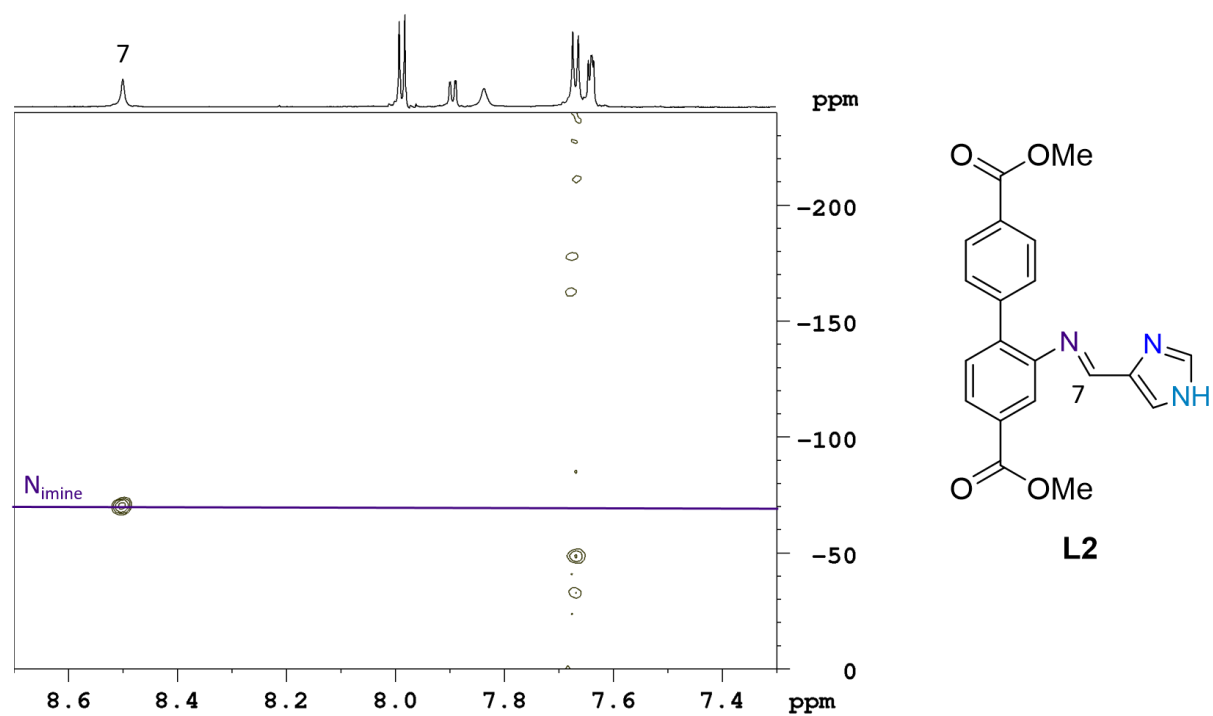
Figure S49. ^{1}H-^{15}N HMBC (800 MHz, d_6-DMSO) of **L2** (~0.5 mg of sample).
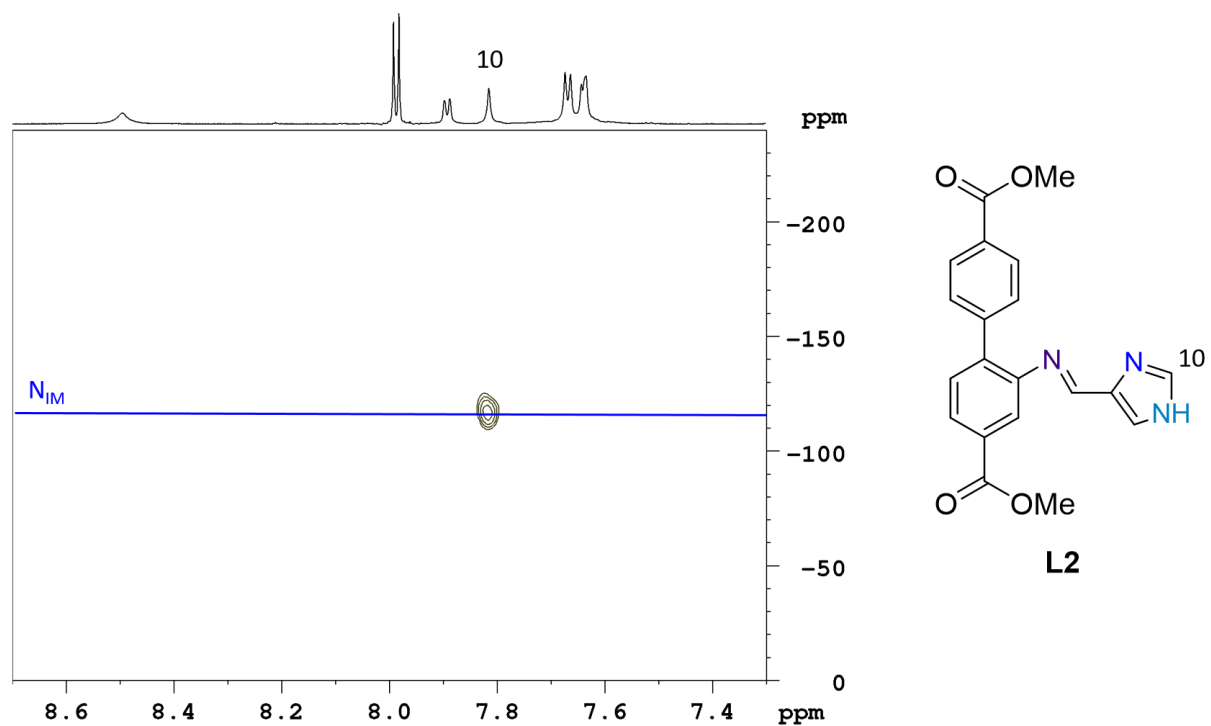
Figure S50. ^{1}H-^{15}N HMBC (800 MHz, d_6-DMSO) of **L2** (~1 mg of sample).
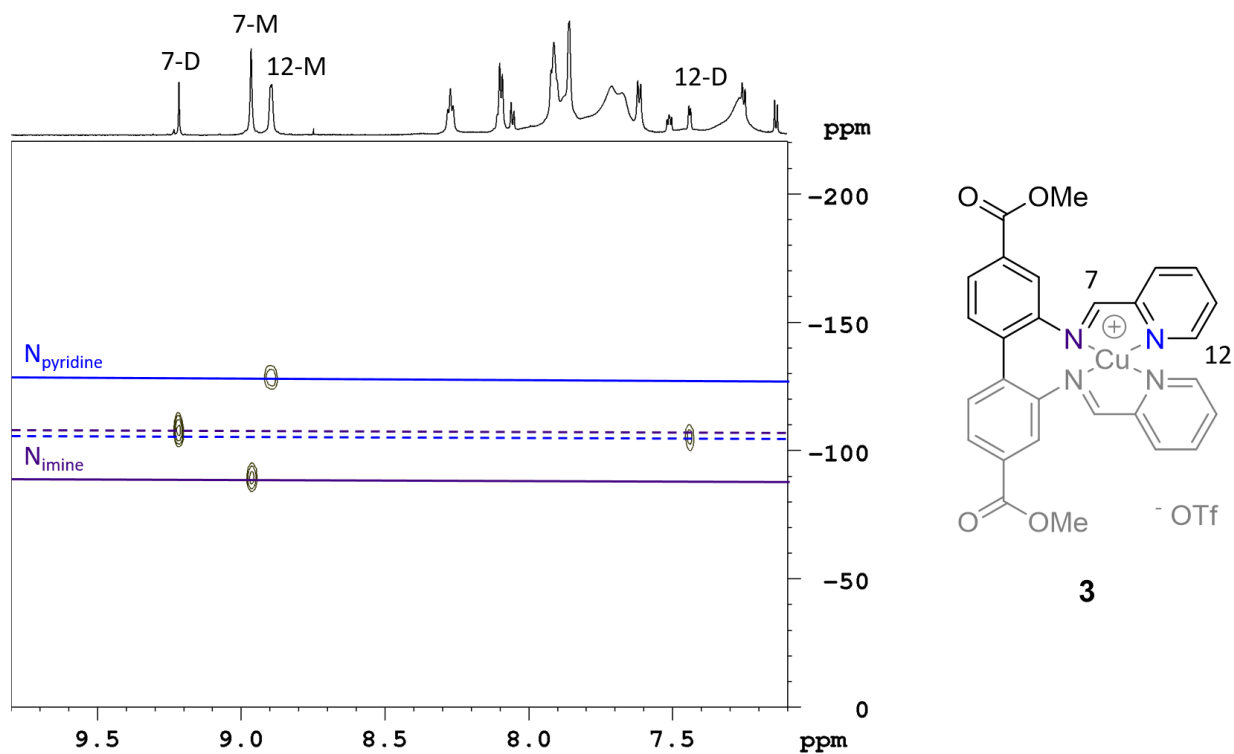
Figure S51. ^{1}H-^{15}N HMBC (800 MHz, d_6-DMSO) of **3**. Solid lines designate the ^{15}N shifts belonging to **3-M**, while dotted lines designate the ^{15}N shifts of **3-D**.
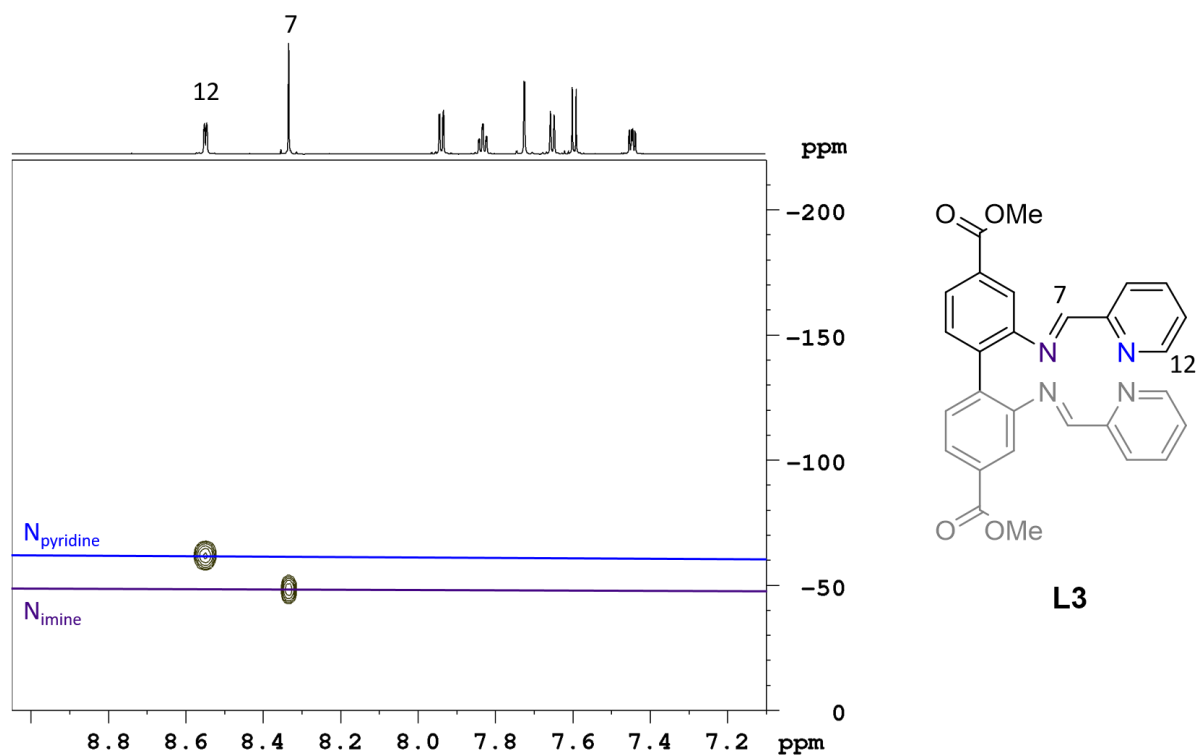
Figure S52. ^{1}H-^{15}N HMBC (800 MHz, d_6-DMSO) of **L3**.
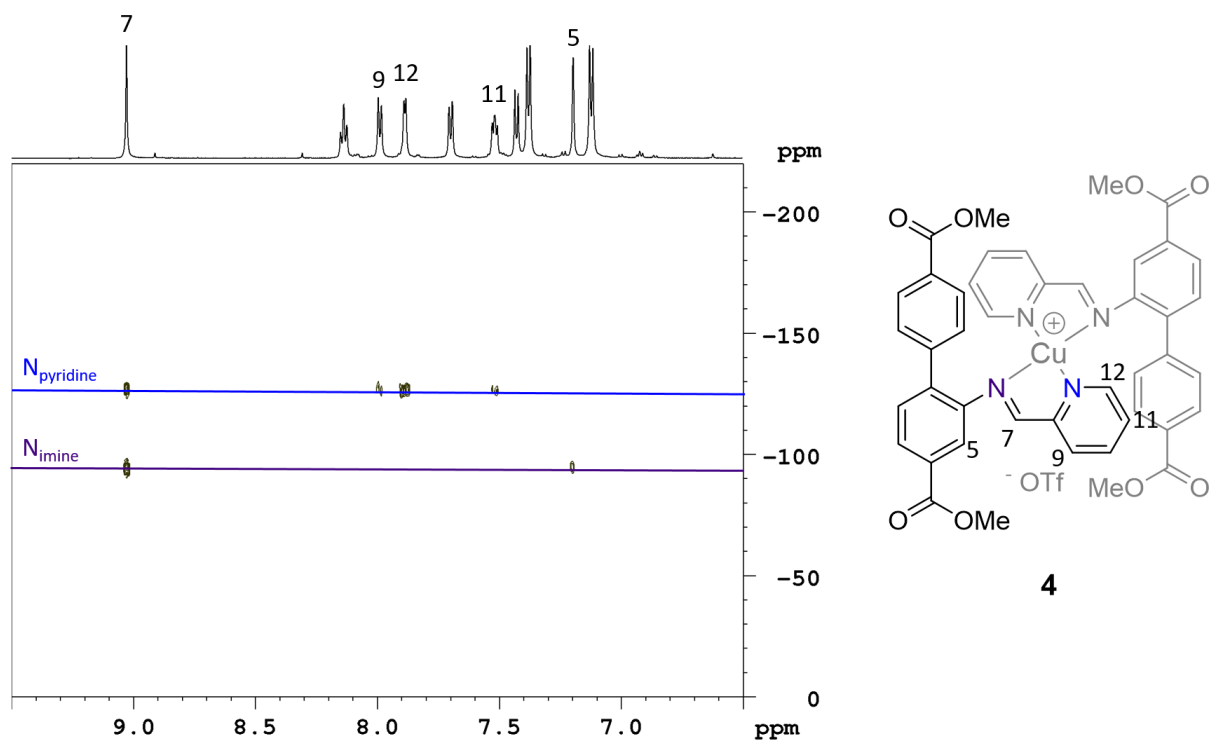
Figure S53. ^{1}H-^{15}N HMBC (600 MHz, d_6-DMSO) of **4**.
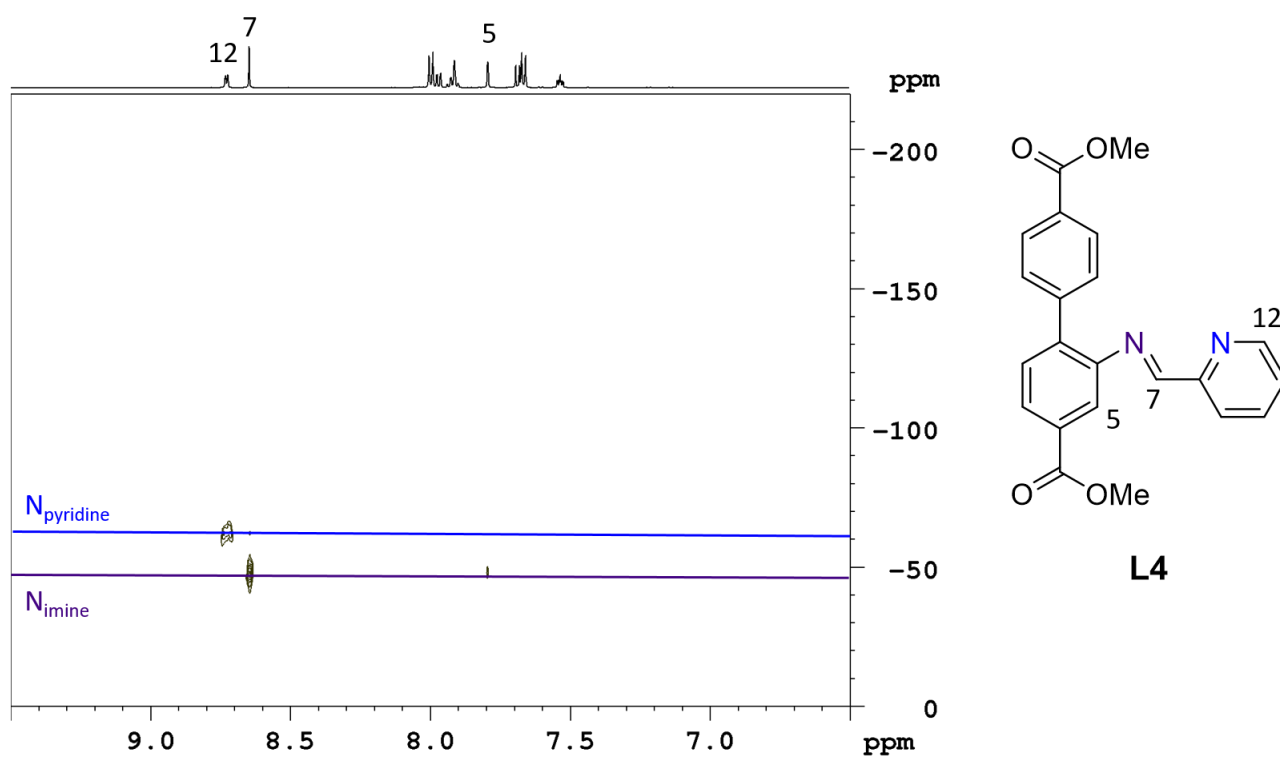
Figure S54. ^{1}H-^{15}N HMBC (600 MHz, d_6-DMSO) of **L4**.
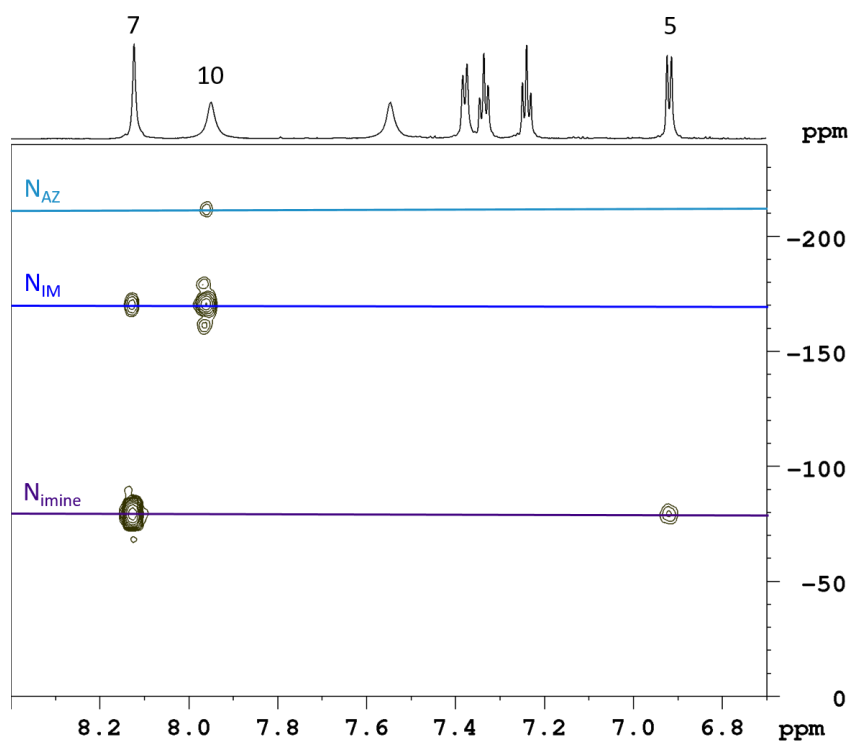
Figure S55. ^1H-^{15}N HMBC (800 MHz, CD$_3$CN) of **5**.
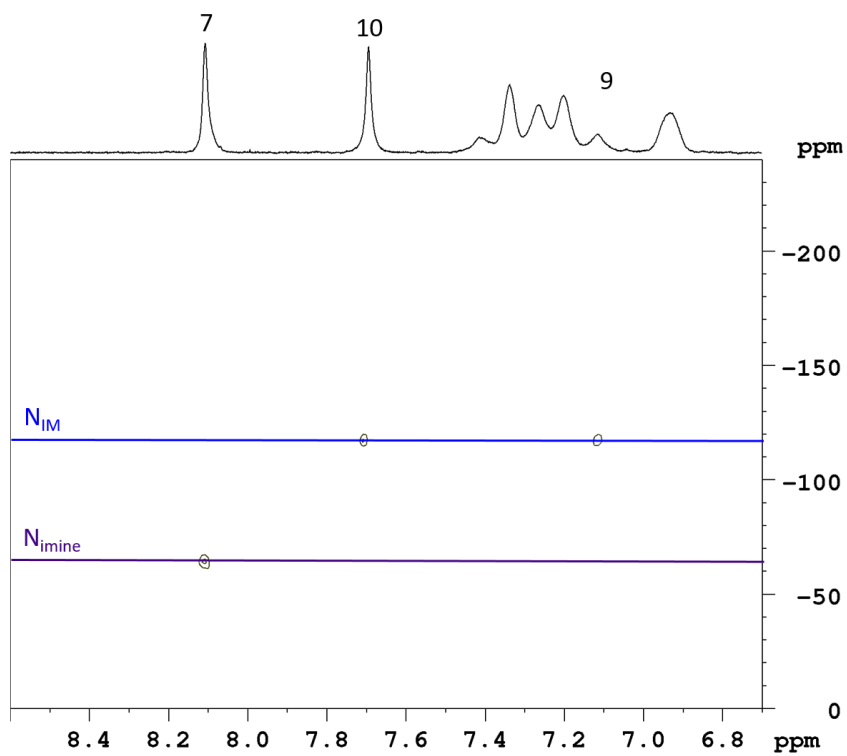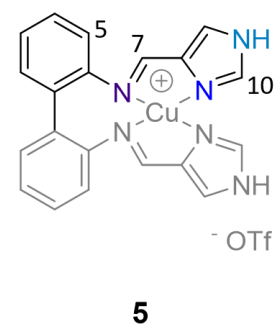
Figure S56. ^1H-^{15}N HMBC (800 MHz, d_6-DMSO) of **L5**.
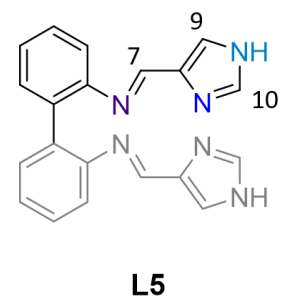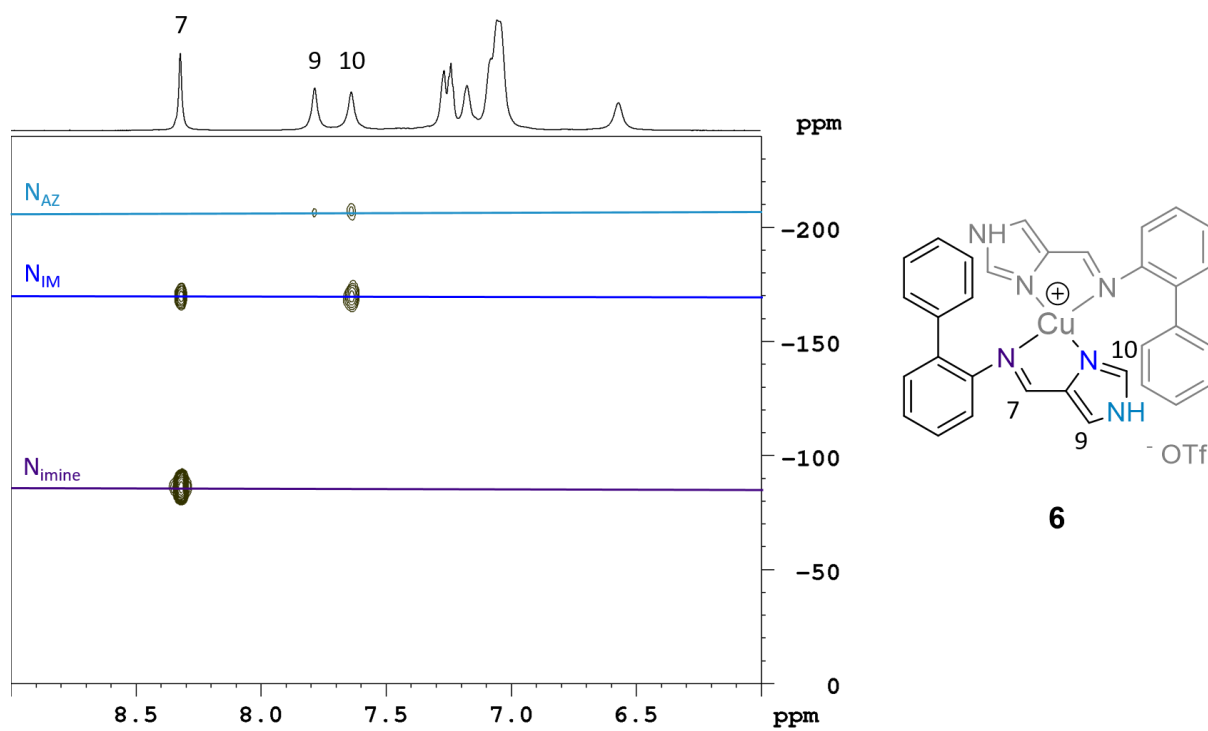
Figure S57. ^{1}H-^{15}N HMBC (800 MHz, d_6-DMSO) of **6**.
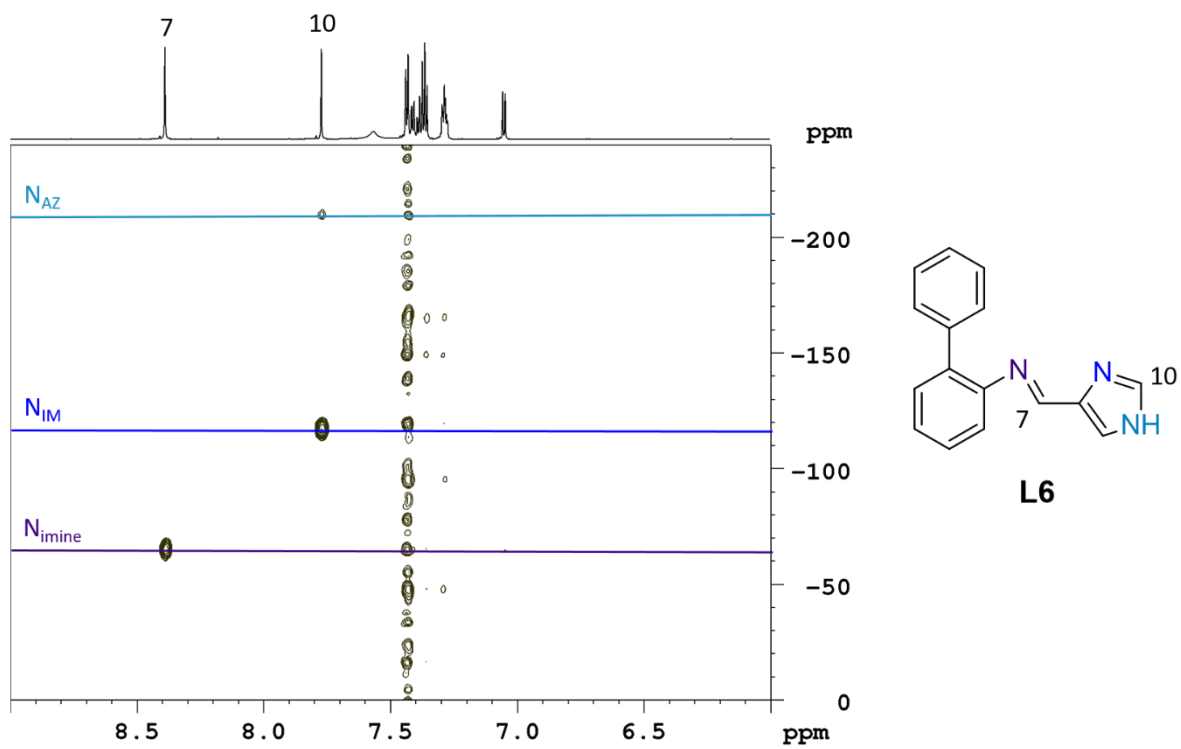
Figure S58. ^{1}H-^{15}N HMBC (800 MHz, d_6-DMSO) of **L6**.

Variable Temperature NMR Experiments

All variable temperature NMR experiments were measured on a Bruker DRX500 instrument. The reversibility of the observed processes was assessed by comparison of the room temperature spectrum (black spectrum) before and after the temperature experiments (grey spectrum on top). The temperature of the variable temperature NMR experiments was measured indirectly by correction of the displayed probe temperature to independently measured temperatures (or extrapolated temperatures for the temperatures above the boiling point of methanol) using a Delta OHM HD9214 thermometer fitted into a NMR tube containing CD_3OD/CH_3OH. Because of this, small deviations from the exact temperature cannot be excluded.

Compound 1
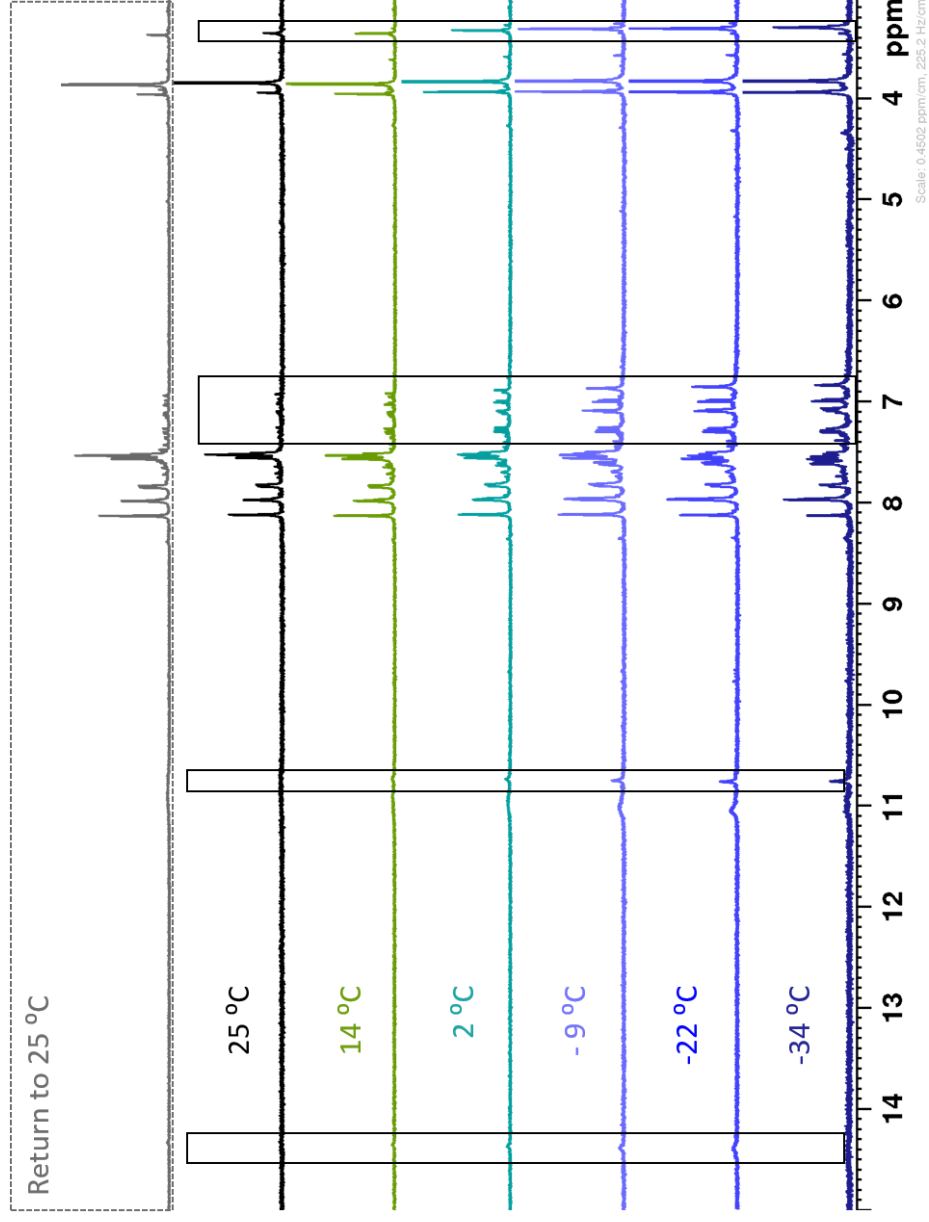
Figure S59. ^{1}H NMR (CD$_3$CN, 500 MHz) spectra of **1** at different temperatures. Boxes highlight the minor species rising at lower temperatures.

55
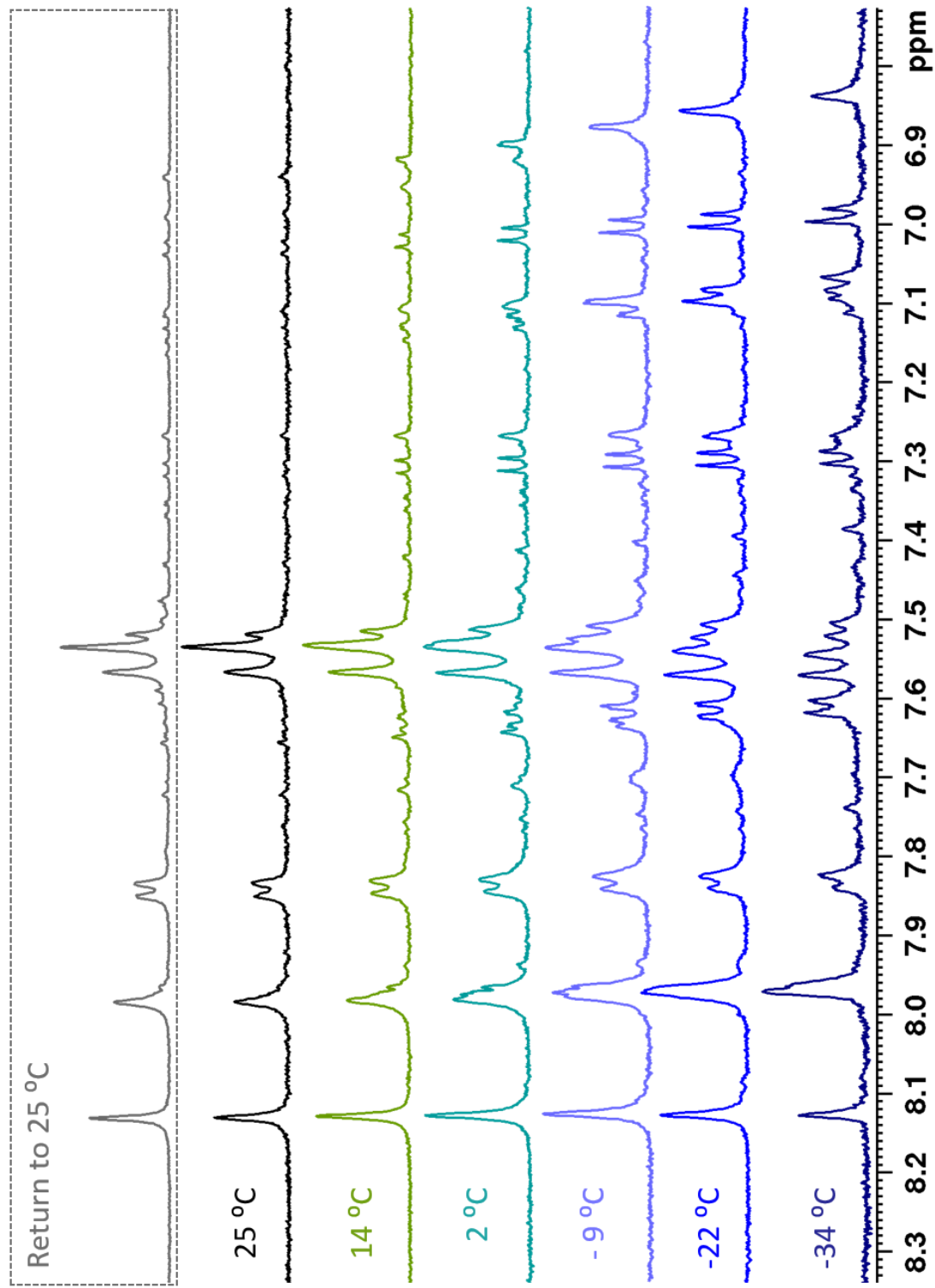
Figure S60. Aromatic region of the ^{1}H NMR (CD$_3$CN, 500 MHz) spectra of **1** at different temperatures.

56
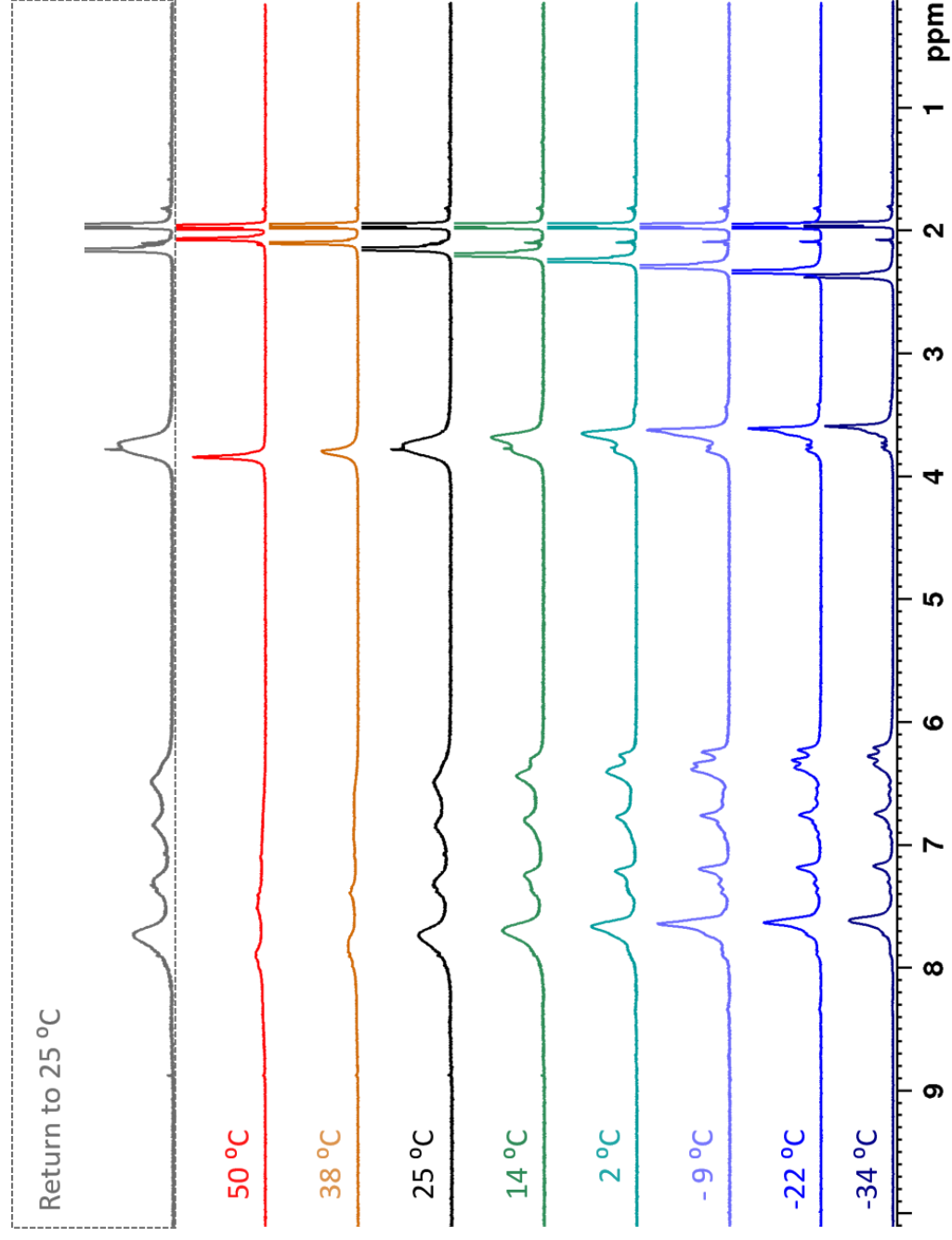
Compound 3

Figure S61. ^{1}H NMR (CD$_3$CN, 500 MHz) spectra of **3** at different temperatures.

57
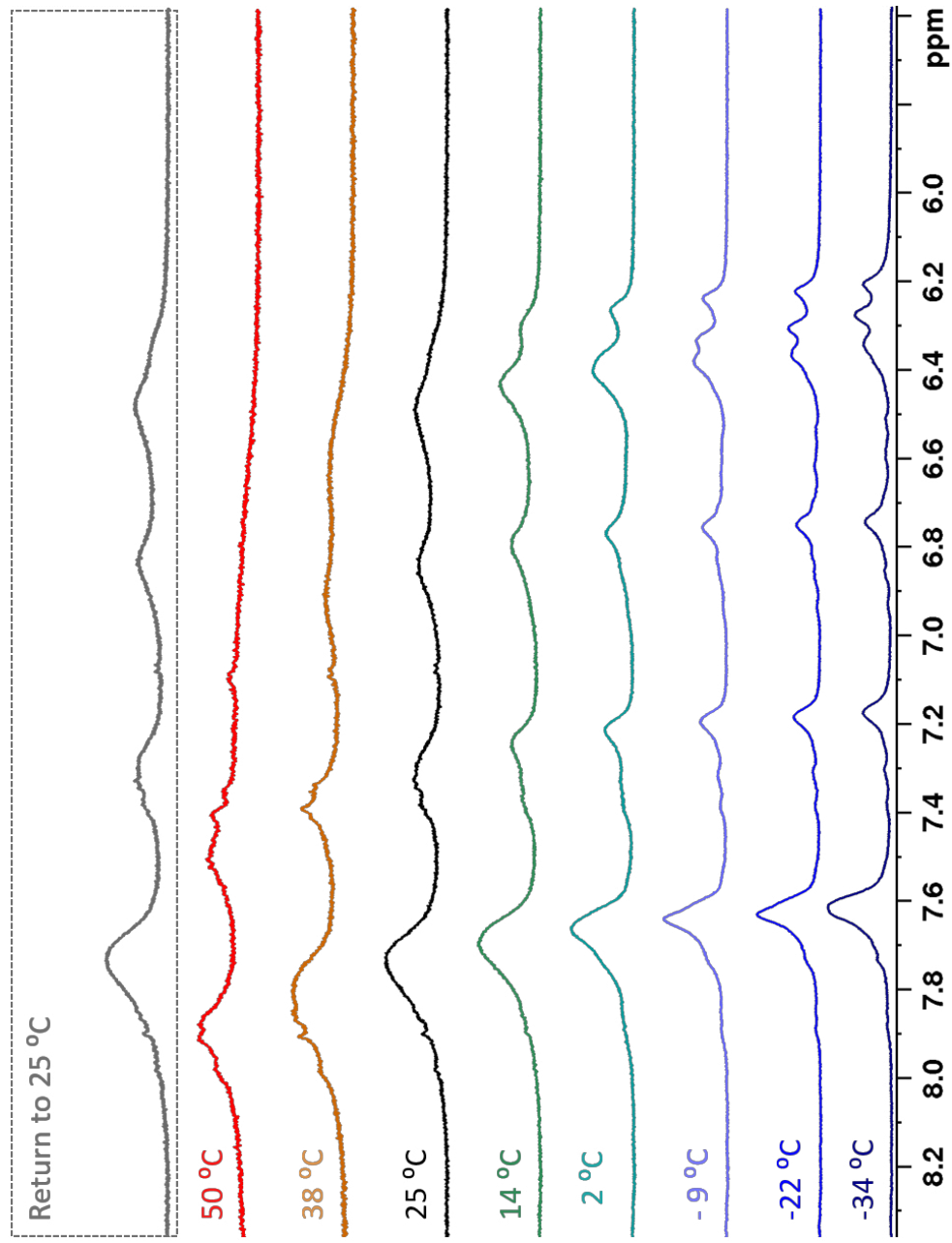
Figure S62. Aromatic region of the ^1H NMR (CD$_3$CN, 500 MHz) spectra of **3** at different temperatures. The peaks merge into the baseline at higher temperatures.

58

Compound 5
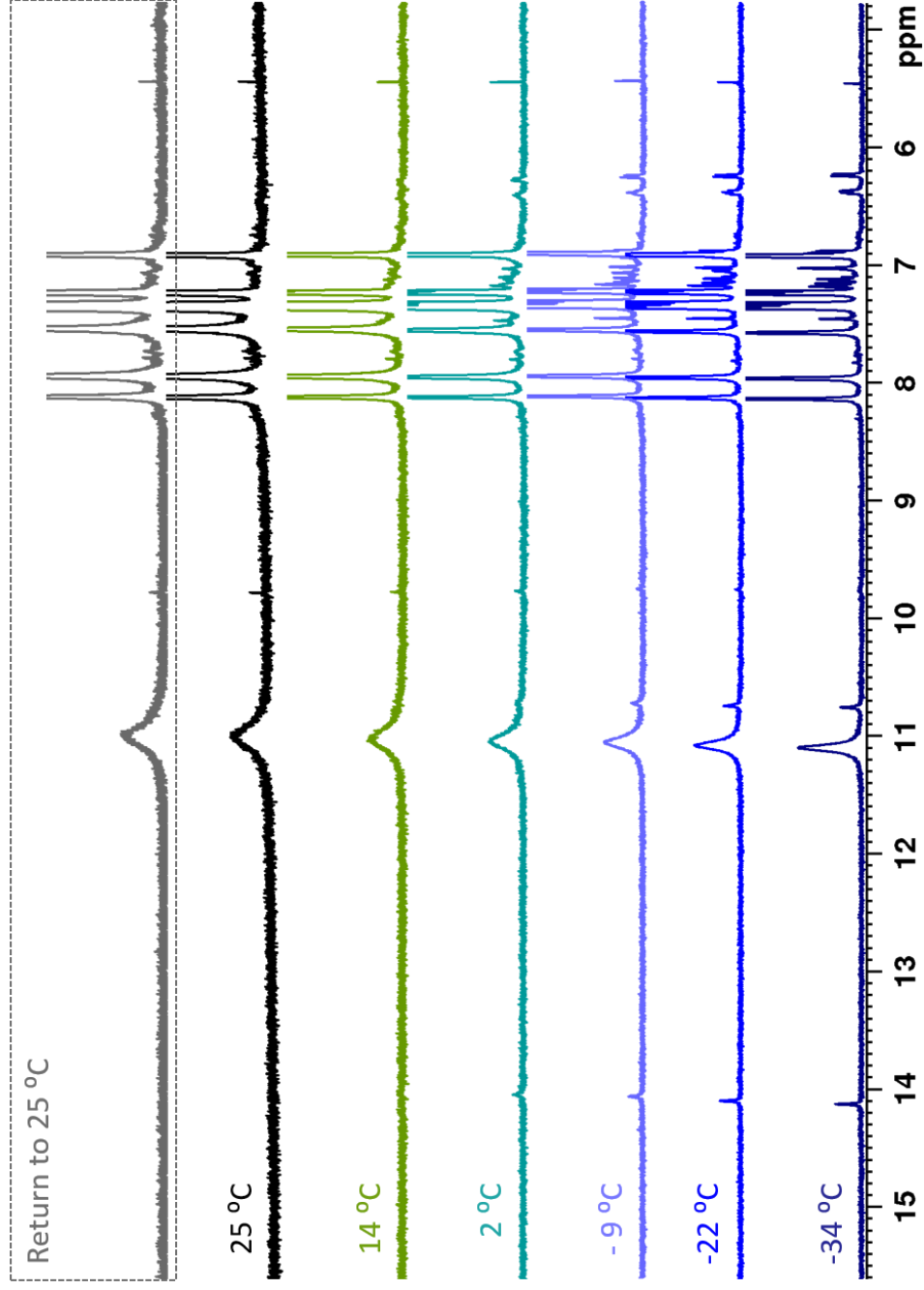
Figure S63. ^{1}H NMR (CD$_3$CN, 500 MHz) spectra of **5** at different temperatures.

Return to 25 °C

25 °C

14 °C

2 °C

- 9 °C

-22 °C

-34 °C

ppm

59
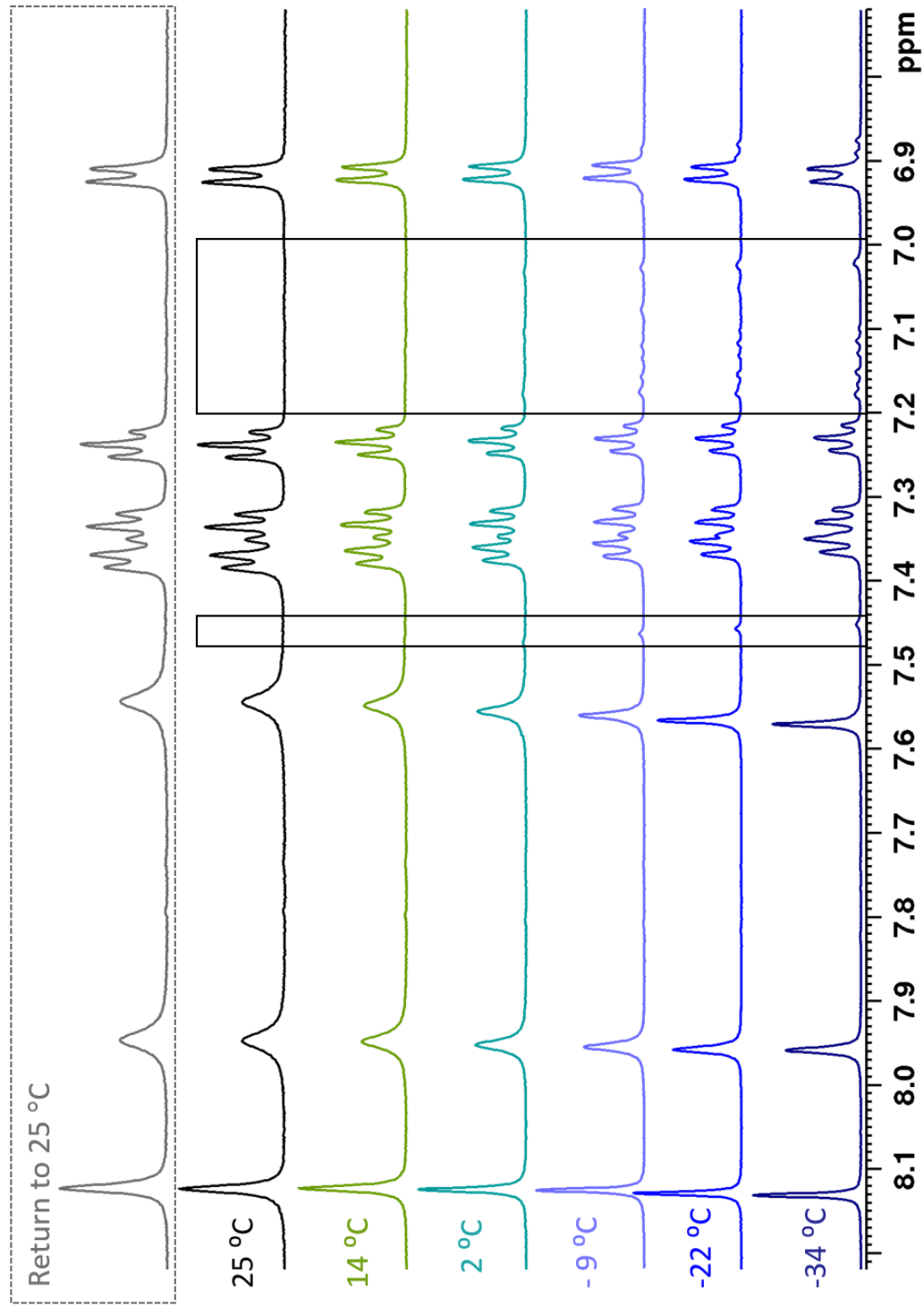
Figure S64. Aromatic region of the ^1H NMR (CD_3CN, 500 MHz) spectra of **5** at different temperatures. Boxes highlight the minor species rising at lower temperatures.

60

Decomposition During Longer NMR Experiments

We observed that complexes with considerable line broadening decomposed during NMR analysis. A sealed NMR sample of **1** remained unchanged even after months, while **2**, **4**, **5**, and **6** partially showed traces of the starting materials during NMR experiments longer than a day. A juxtaposition of the ^{1}H NMR spectra of the complexes after prolonged NMR experiments and the amines they were synthesized from shows good agreement between the decomposition peaks and the amine for all four complexes (Figure S65). In combination with the simultaneous rise of an aldehyde peak, it is evident that the decomposition can be attributed to hydrolysis of the imine bond. The hydrolysis of the complexes could have been prevented by use of dry NMR solvents. However, the stability of the complexes was of interest and the decomposition was minor enough to not impede full NMR characterisation.
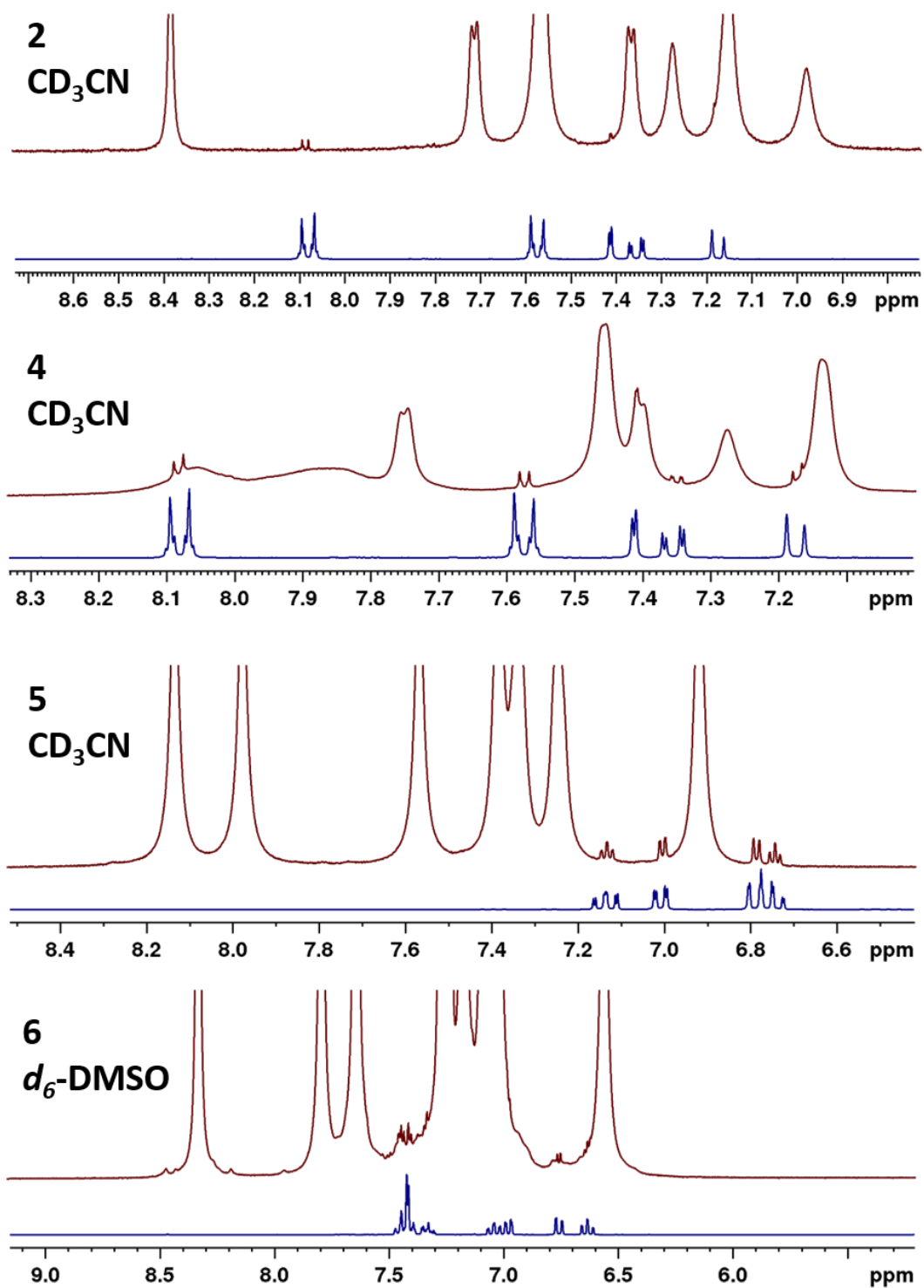
Figure S65. ^{1}H NMR (600 MHz) spectra of compounds **2**, **4**, **5** and **6** after full NMR analysis (ca.1 ½ days, in brown) stacked over the spectrum of the amine they were synthesizes from (in blue). The decomposition can therefore be attributed to hydrolysis of the imine.

Reduction of complex **1b** with ascorbic acid to form complex **1**
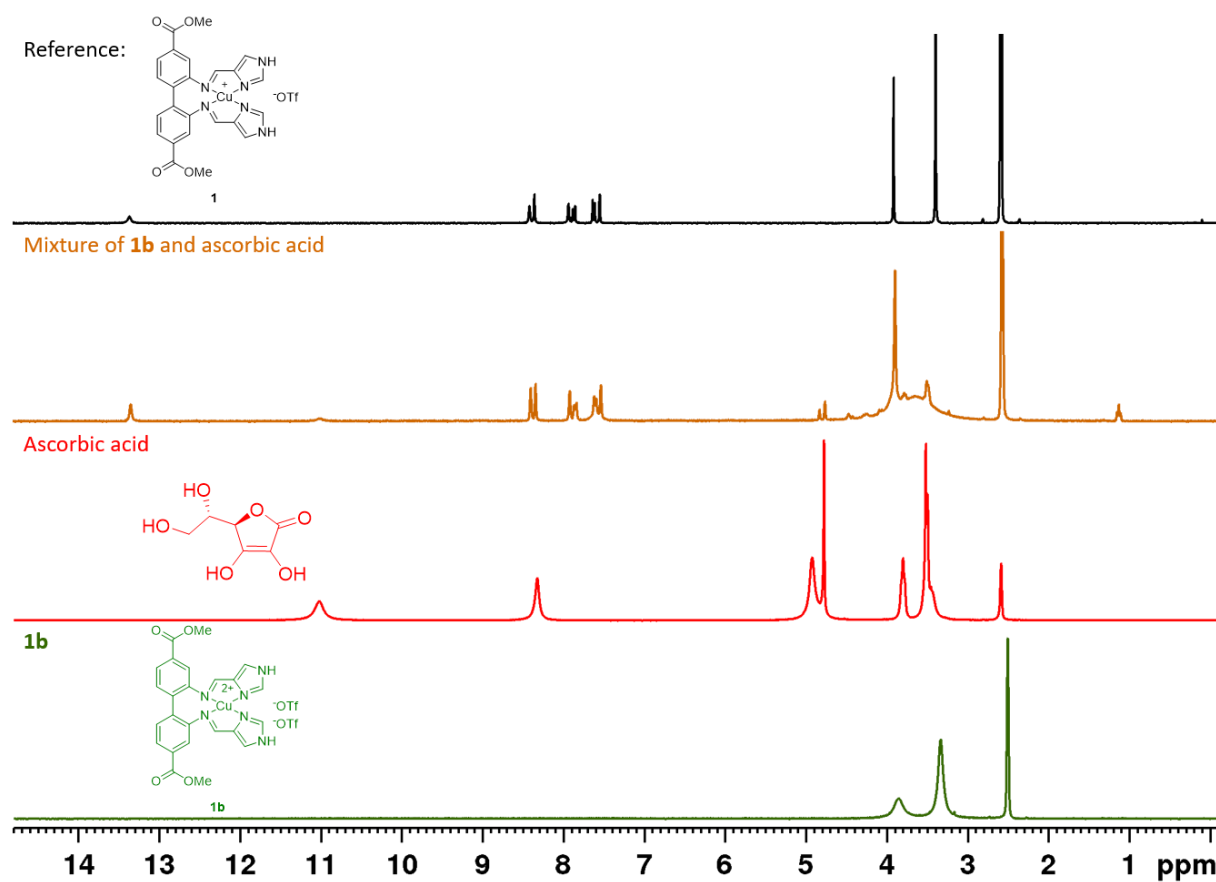
Figure S66. NMR experiment (d_6-DMSO, 300 MHz) showing the relation between complex **1b** and complex **1**. A solution of complex **1b** (green solution, bottom spectrum) was mixed with an ascorbic acid solution (colorless solution, 2nd spectrum from the bottom), giving rise to sharp peaks and causing a color change (yellow solution, 3rd spectrum from the bottom). The newly formed peaks are in good agreement with the peaks observed for the corresponding copper(I) complex **1** (top spectrum).

Ligand exchange NMR experiments

It is likely that the ML$_2$ complexes are in equilibrium with the corresponding ML complex and the free ligand. This is exemplified in Scheme S1 for complex **2**.
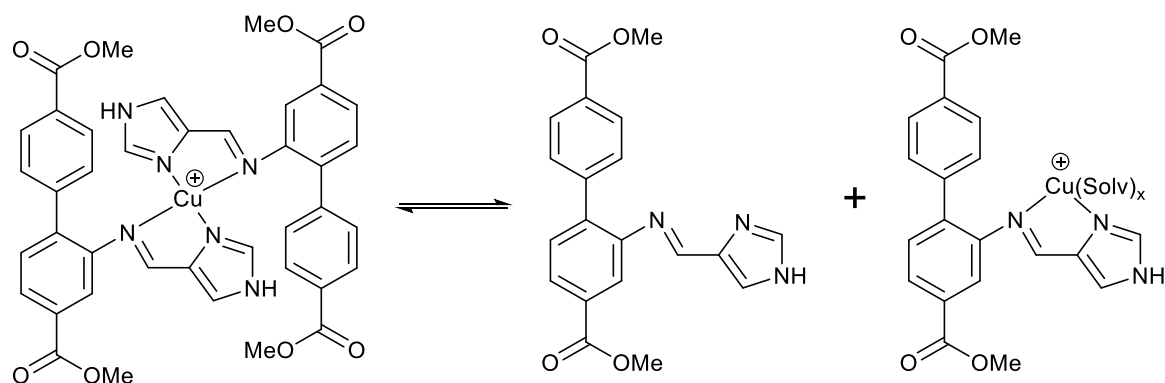
Scheme S1. Equilibrium of ML$_2$ complex **2** with the free ligand and the resulting ML complex. The ML complex might have x solvent molecules as additional ligand(s).

In order to probe if ligands can exchange from one complex to the other, a mixture of **2** and **4** was measured in d_6-DMSO. The mixture showed peaks that could not be attributed to either species or the free ligands. The spectral appearance of the mixture did not change from the first measurement (ca. 5 min after mixing) to the last measurement (next day).
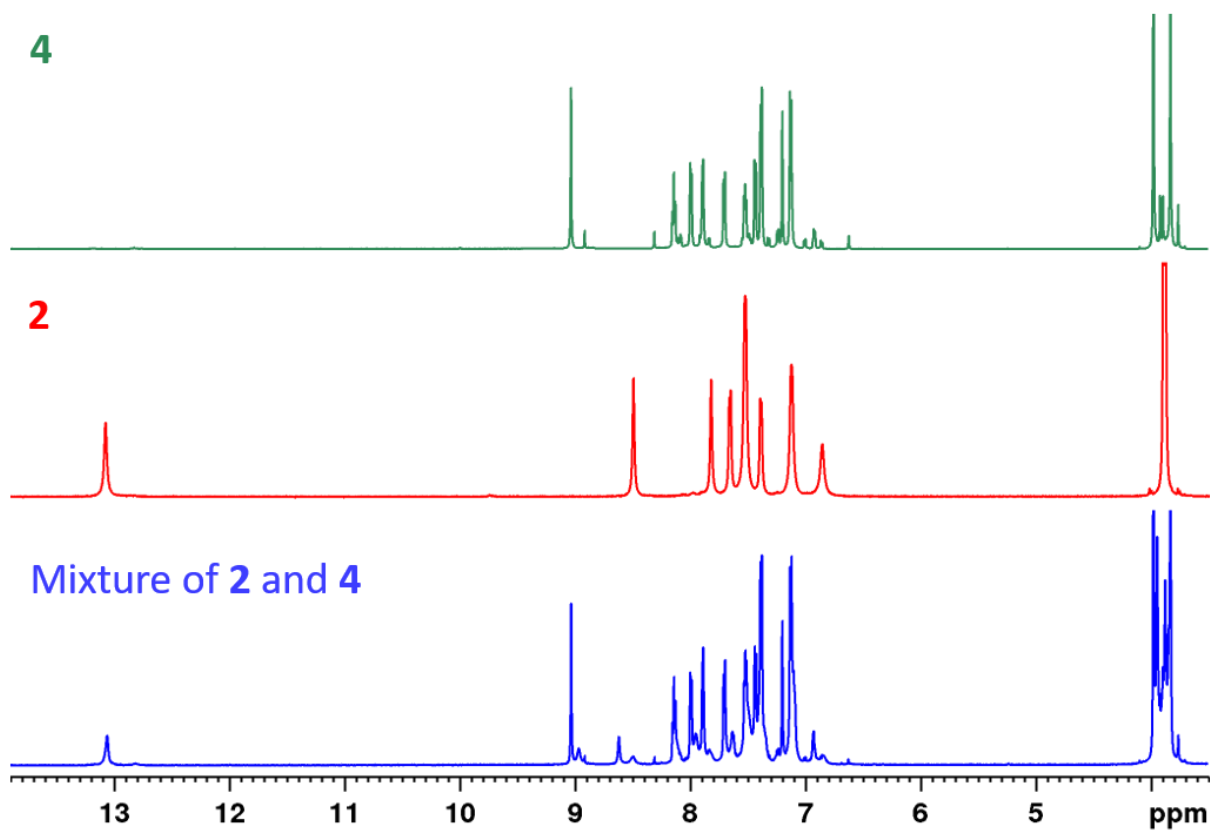
Figure S67. Overlay of the ^{1}H NMR (d_6-DMSO, 600 MHz) spectra of complexes **2** (middle) and **4** (top) and a mixture of both (bottom).
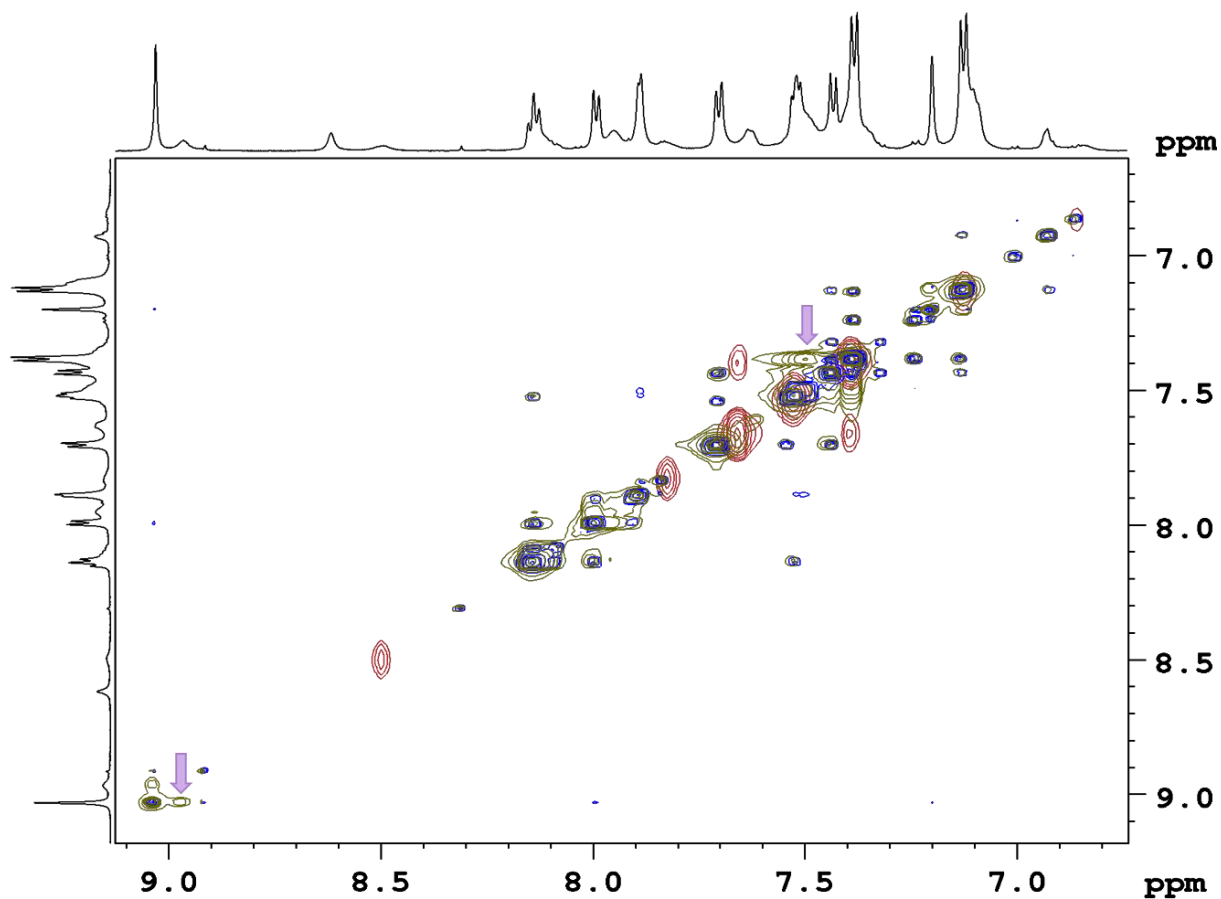
Figure S68. Overlay of the NOESY/EXSY (d_6-DMSO, 600 MHz) spectra of complexes **2** (red) and **4** (blue) and a mixture of both (dark green). Two of the peaks that stem from neither complex and are only observed in the mixture are highlighted with a lavender arrow.

Diffusion Ordered Spectroscopy (DOSY)
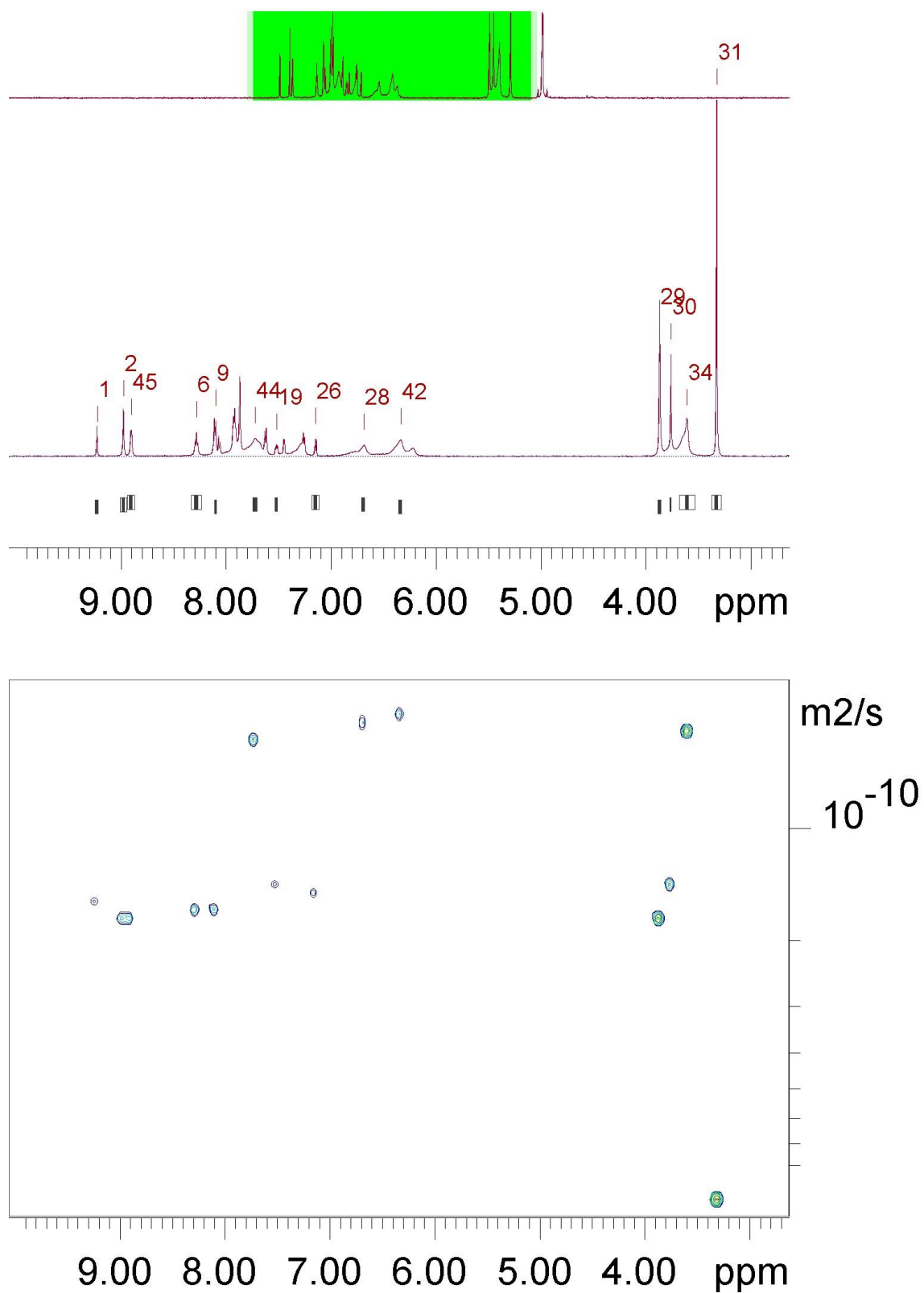
Figure S69. User-defined integration areas to calculate the DOSY spectrum of **3**.

Table S1. DOSY parameters used in the Bruker Dynamics Center.

Fitted function:	f (x) = Io * exp (-D * x^2 * gamma^2 * littleDelta^2 (bigDelta-littleDelta/3)* 10^4
used gamma:	26752 rad/(s*Gauss)
used little delta:	0.0049000 s
used big delta:	0.089900 s
used gradient strength:	variable
Random error estimation of data:	RMS per spectrum (or trace/plane)
Systematic error estimation of data:	worst case per peak scenario
Fit parameter Error estimation method:	from fit using calculated y uncertainties
Confidence level:	95%
Used Gradient strength:	all values (including replicates) used

Table S2. Peak list as generated by the Diffusion function in the Bruker Dynamics Center.[10]

Peak name	F2 [ppm]	D [m2/s]	error
1	9.228	1.58e-10	2.290e-12
2	8.976	1.77e-10	1.472e-12
6	8.281	1.67e-10	1.610e-12
9	8.097	1.65e-10	9.936e-13
19	7.520	1.40e-10	2.264e-12
26	7.146	1.50e-10	2.952e-12
28	6.688	5.08e-11	2.771e-12
29	3.867	1.75e-10	3.513e-13
30	3.760	1.39e-10	5.457e-13
31	3.325	9.62e-10	1.126e-12
32	2.508	7.18e-10	3.764e-13
34	3.606	5.43e-11	8.708e-13
42	6.336	5.05e-11	1.876e-12
44	7.720	5.84e-11	1.331e-12
45	8.902	1.76e-10	1.500e-12

70
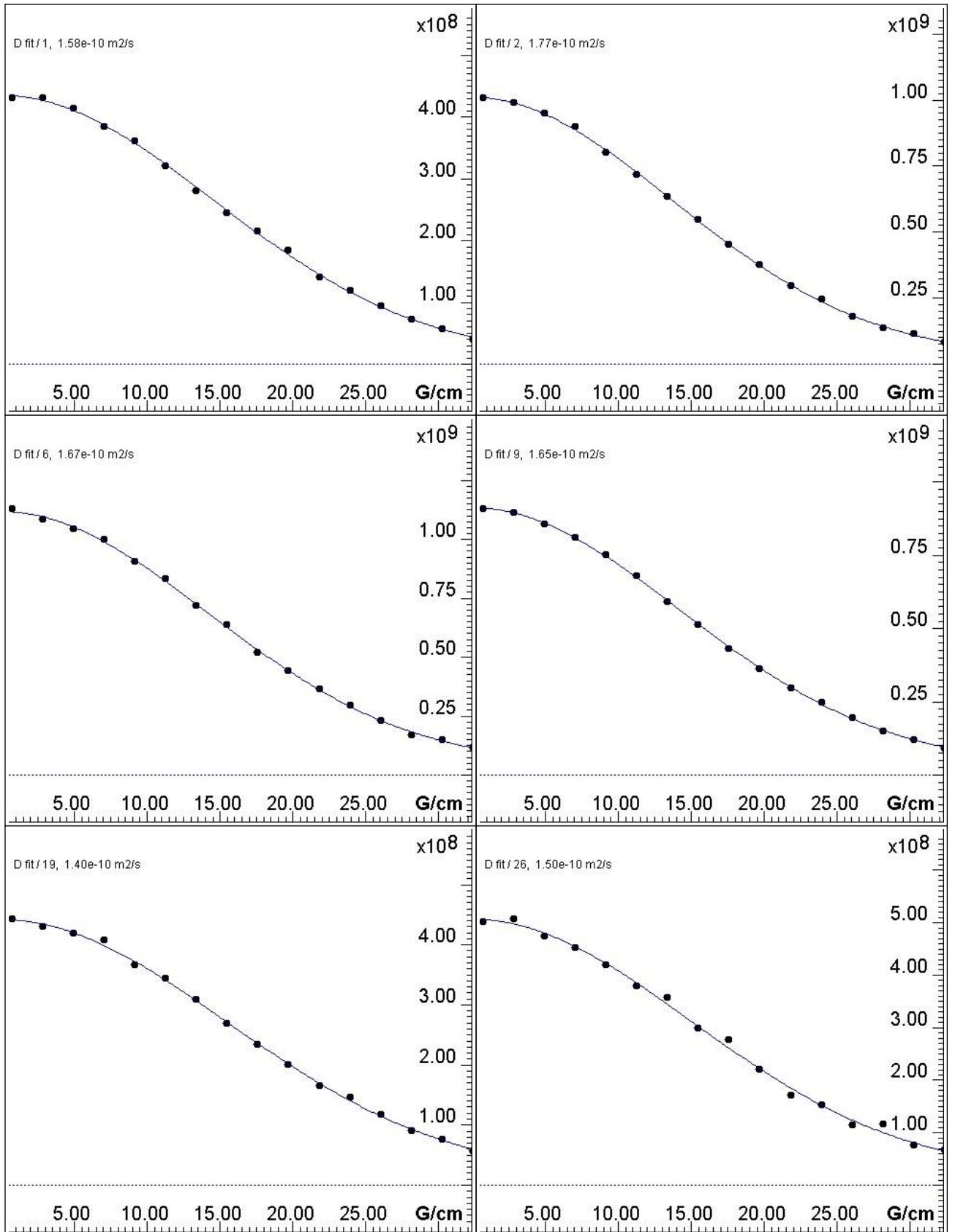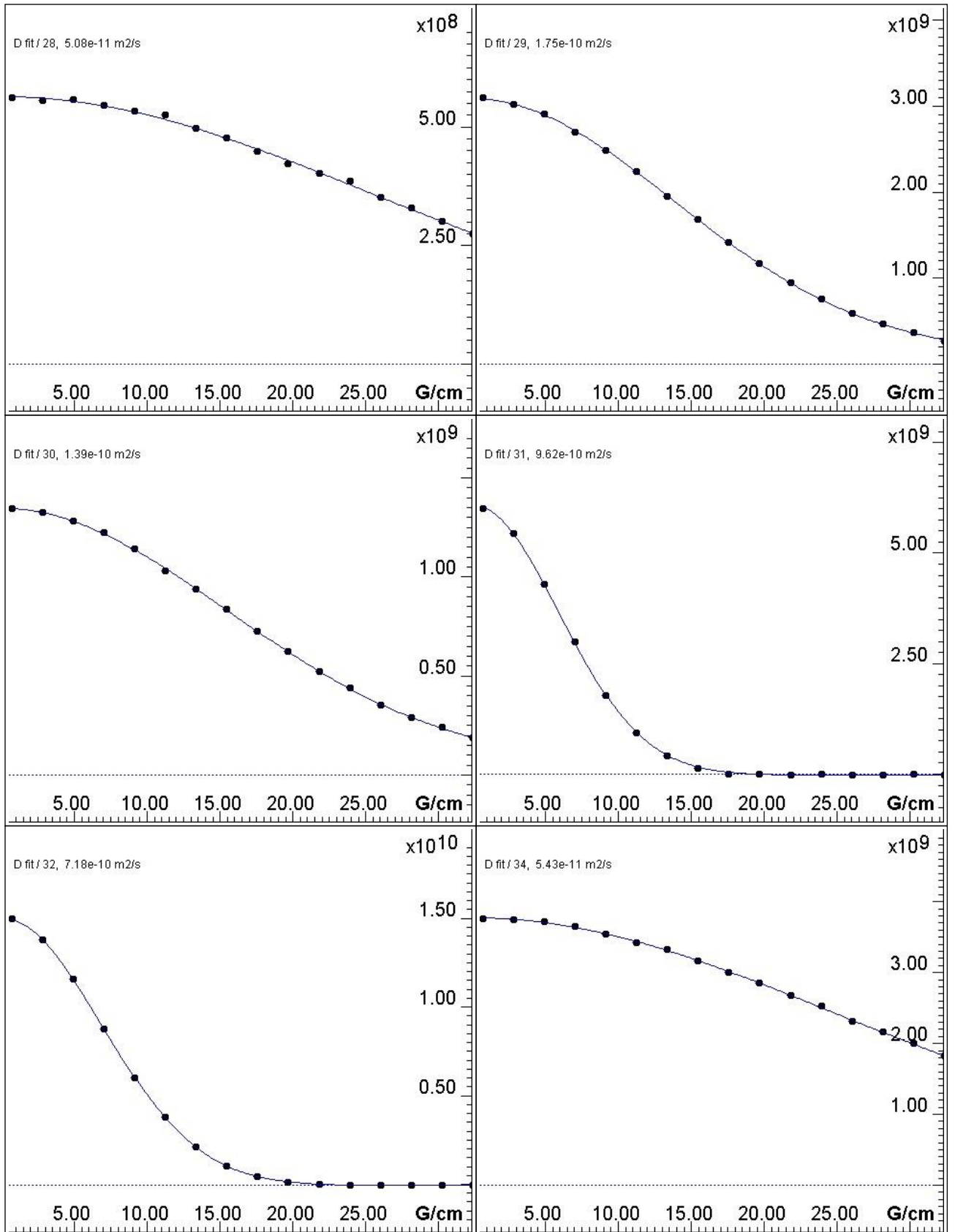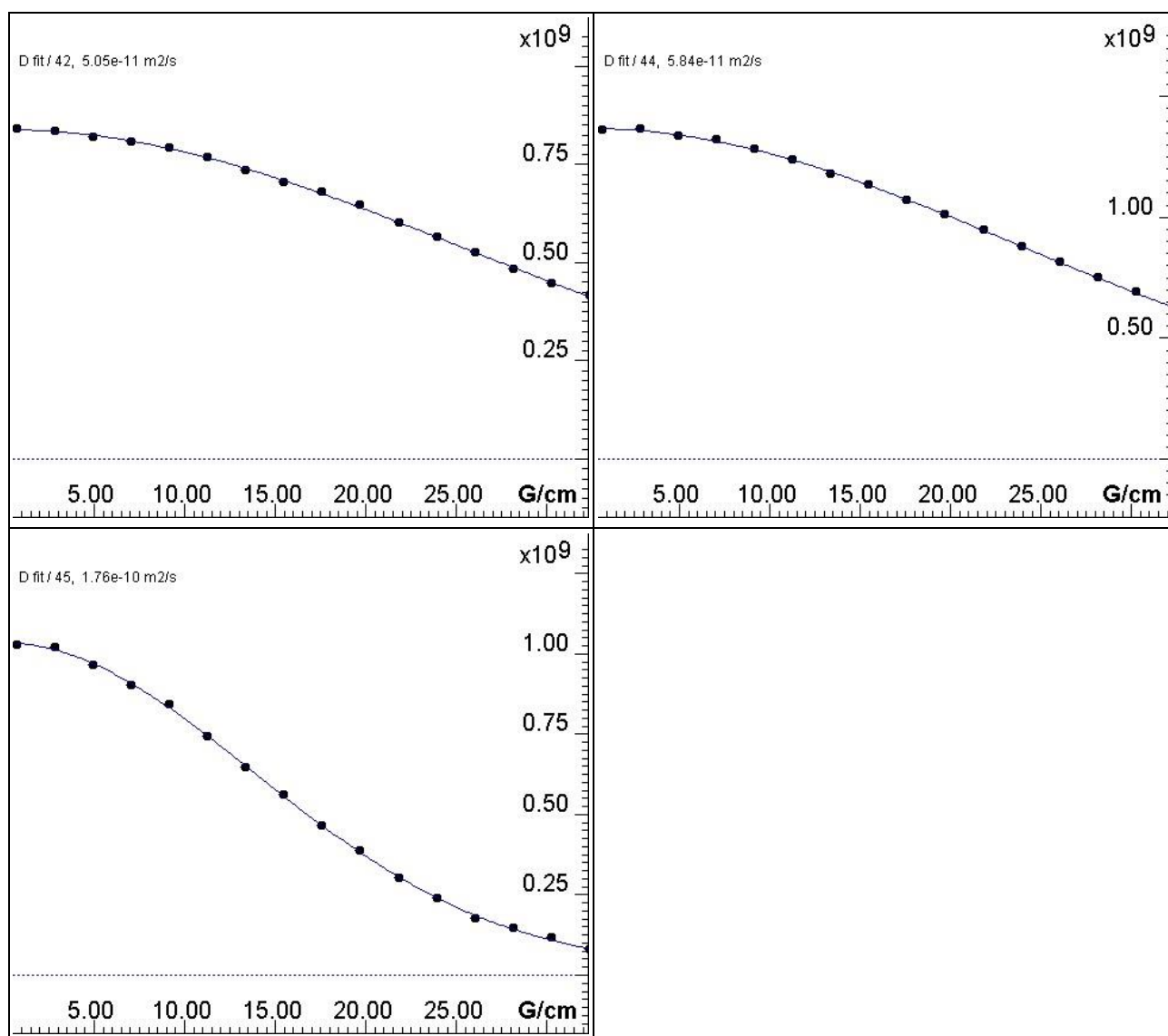
Figure S70. The integrals for selected integration areas at different gradient strength (dots) and their fits (lines). For peak numbering, see **Table S2**.

Crystallographic Data

Compound 2

We made several attempts to crystallize **2**, using different solvent combinations. The only measurable crystals were obtained by vapour diffusion of diethyl ether into a solution of **2** in acetonitrile. The crystals were very thin plates that diffracted poorly. Every crystal we checked was twinned with two diffracting domains, related by a two-fold rotation about the reciprocal c-axis (normal to the ab plane). The diffraction signals were too weak to allow twin integration, so the twin law was applied during structure refinement. The structure contains a solvent accessible void, and attempts to model a solvent molecule (e.g. a linear hydrocarbon) resulted in solvate species with unphysical bond lengths. The location of the inversion centre in this void made accurate solvate structure determination impossible. PLATON/SQUEEZE solvent mask was applied instead.[11] The somewhat high R-factor is attributed to the twinning and poor diffraction ability of the crystal.
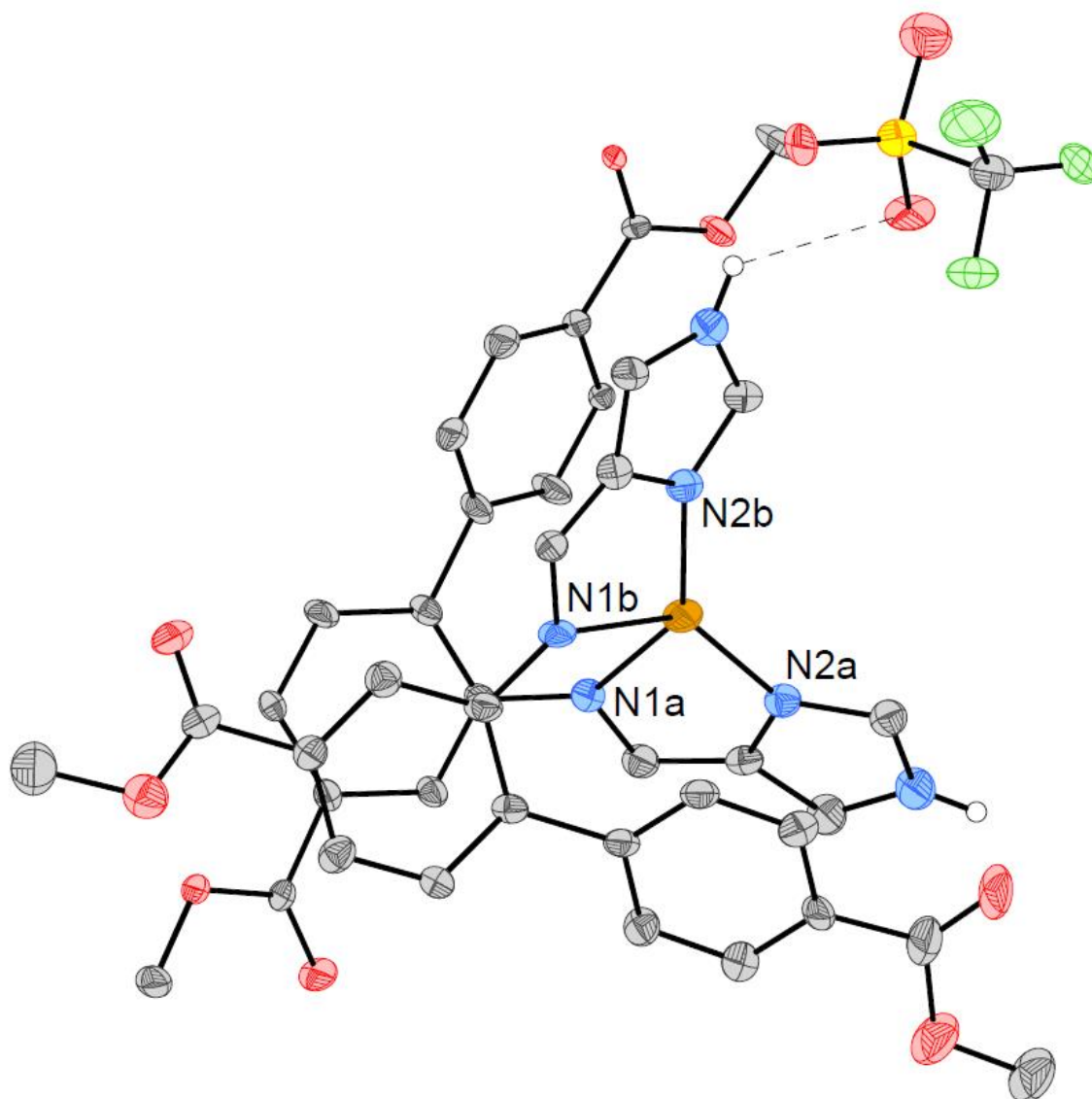
Figure S71. ORTEP plot of compound **2** with 50% probability ellipsoids [ig-62-(2048292)]. Selected bond lengths: N1a-Cu: 2.21(2) Å; N1b-Cu: 2.32(2) Å; N2a-Cu: 1.929(12) Å; N2b-Cu: 1.915(12) Å. Averaged τ_4'=0.60 ± 0.02.[12,13] The hydrogen bond between the imidazole-NH and the triflate anion has a length of 2.76 Å and a NHO angle of 118 °.

Compound 4

Single crystals suitable for single crystal X-Ray diffraction were obtained by vapour diffusion of toluene into a solution of **4** in a toluene/acetonitrile mixture.
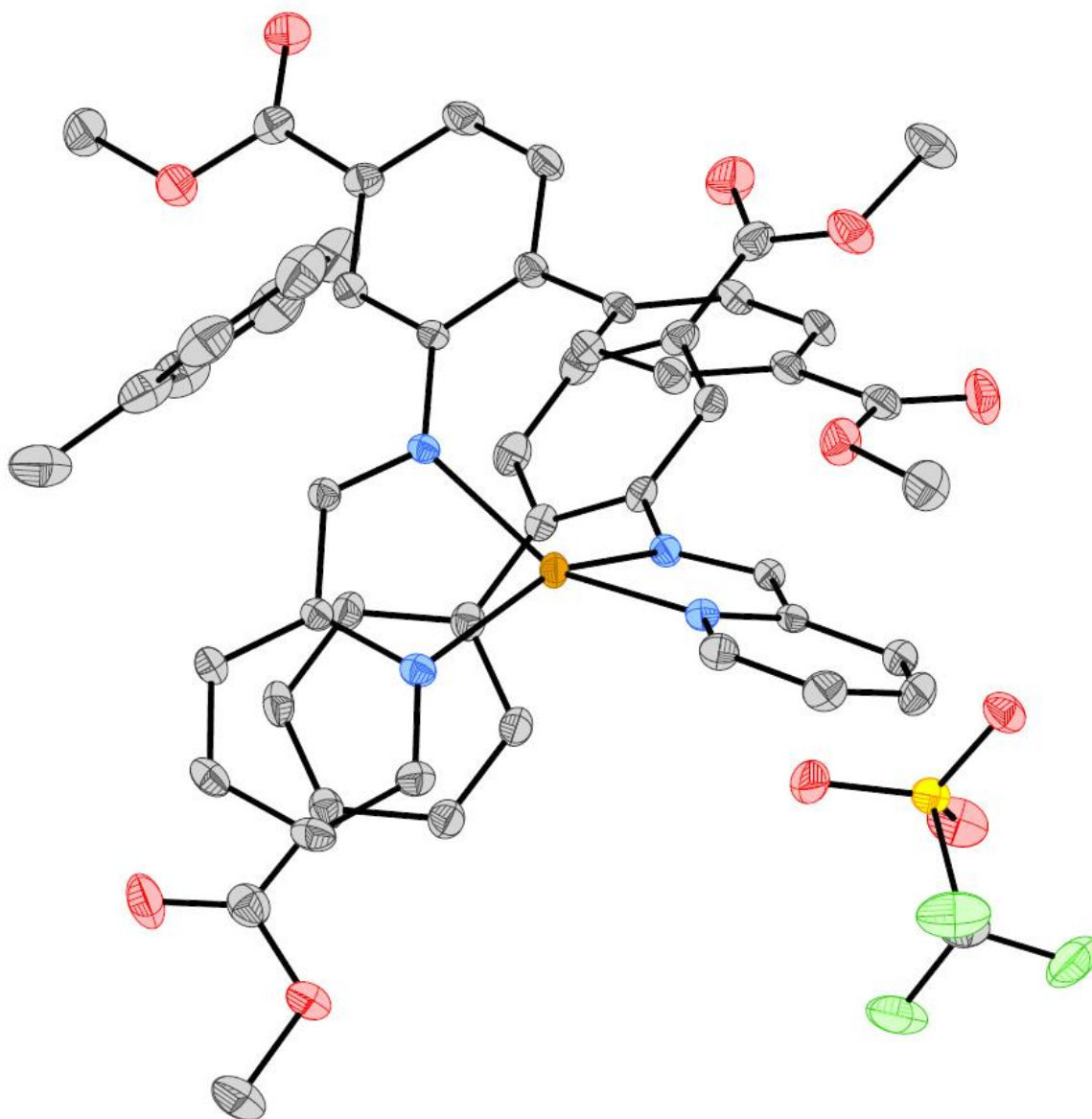
Figure S72. ORTEP plot of compound **4** with a co-crystalized solvent molecule (toluene) with 50% probability ellipsoids [ig-0124-(2048291)].

Table S3. Crystal and refinement data for compounds **2** and **4**.

	ig-62-(2048292)	ig-0124-(2048291)
	2	**4** **co-crystallized with toluene**
Crystal data		
Chemical formula	$C_{40}H_{34}CuN_6O_8 \cdot CF_3O_3S$	$C_{44}H_{36}CuN_4O_8 \cdot CF_3O_3S \cdot C_7H_8$
M_r	939.34	1053.51
Crystal system, space group	Triclinic, *P-1*	Monoclinic, *Cc*
Temperature (K)	100	105
a, b, c (Å)	11.839 (7), 12.740 (8), 15.296 (9)	18.2548 (13), 17.2687 (12), 15.2341 (11)
α, β, γ (°)	76.222 (13), 88.825 (13), 81.925 (13)	90, 92.665 (2), 90
V (Å³)	2218 (2)	4797.2 (6)
Z	2	4
Radiation type	Mo $K\alpha$	Mo $K\alpha$
μ (mm⁻¹)	0.62	0.58
Crystal size (mm)	0.27 × 0.05 × 0.01	1.5 × 0.25 × 0.25
Data collection		

Diffractometer	Bruker D8 Venture/Photon100 detector	Bruker D8 Venture/Photon100 detector
Absorption correction	Multi-scan	Multi-scan
	SADABS2016/2 (Bruker,2016/2) was used for absorption correction. wR2(int) was 0.1273 before and 0.0870 after correction. The Ratio of minimum to maximum transmission is 0.8092. The λ/2 correction factor is Not present.	*SADABS2016*/2 (Bruker,2016/2) was used for absorption correction. wR2(int) was 0.1372 before and 0.0401 after correction. The Ratio of minimum to maximum transmission is 0.8463. The λ/2 correction factor is Not present.
T_{min}, T_{max}	0.602, 0.744	0.631, 0.746
No. of measured, independent and observed [I > 2σ(I)] reflections	16219, 3434, 2826	36839, 14513, 12732
R_{int}	0.107	0.035
θ_{max} (°)	19	30.6
$(\sin \theta/\lambda)_{max}$ (Å^{-1})	0.457	0.716
Refinement		
$R[F^2 > 2\sigma(F^2)]$, $wR(F^2)$, S	0.145, 0.408, 1.87	0.041, 0.097, 1.02
No. of reflections	3434	14513
No. of parameters	507	654
No. of restraints	738	2
H-atom treatment	H-atom parameters constrained	H-atom parameters constrained
$\Delta\rho_{max}$, $\Delta\rho_{min}$ (e Å^{-3})	1.33, −0.97	0.42, −0.32
Absolute structure	–	Flack x determined using 5408 quotients [(I+)-(I-)]/[(I+)+(I-)] (Parsons, Flack and Wagner, Acta Cryst. B69 (2013) 249-259).
Absolute structure parameter	–	−0.003 (7)

XAS

Two-coordinate linear arrangement destabilizes 4pz with respect to the doubly-degenerate 4px,y set. As 4px,y remain non-bonding, they retain high p character, which raises the intensity of the 1s-4px,y transition through the electric dipole mechanism, at energies below that of the 1s-4pz transition. In contrast, as one approaches the tetrahedral limit, the 4p set comes close to triply degeneracy and is allowed to mix with 3dxy,xz,yz set as they all transform as T2. As t2 orbitals in Td complexes are antibonding, 1s-4p transitions are shifted to higher energies relative to 1s-4px,y in D∞h.[14]
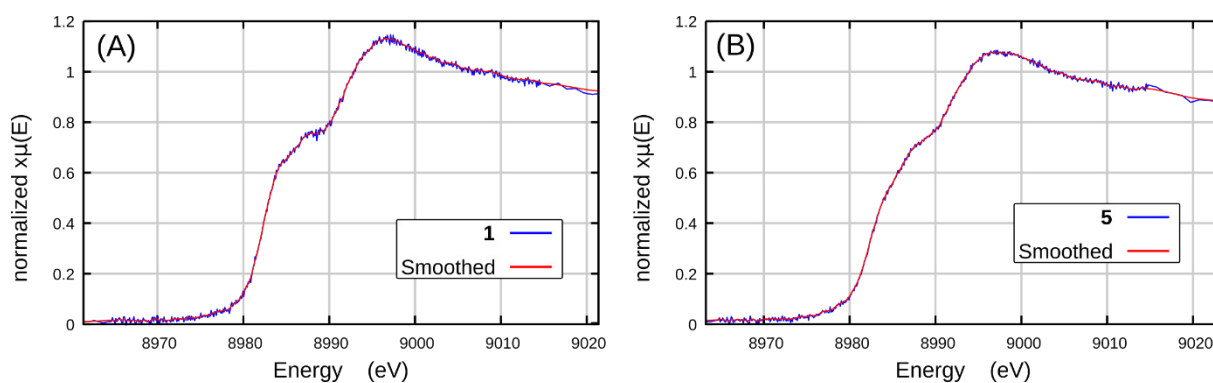
Figure S73. Average of 10 Cu K-edge XAS scans of **1** (A) and **5** (B) in blue overlaid with the respective smoothed spectra in red, as produced by three-point smoothing algorithm with 9 repetitions in Athena software of the Demeter package.[15]
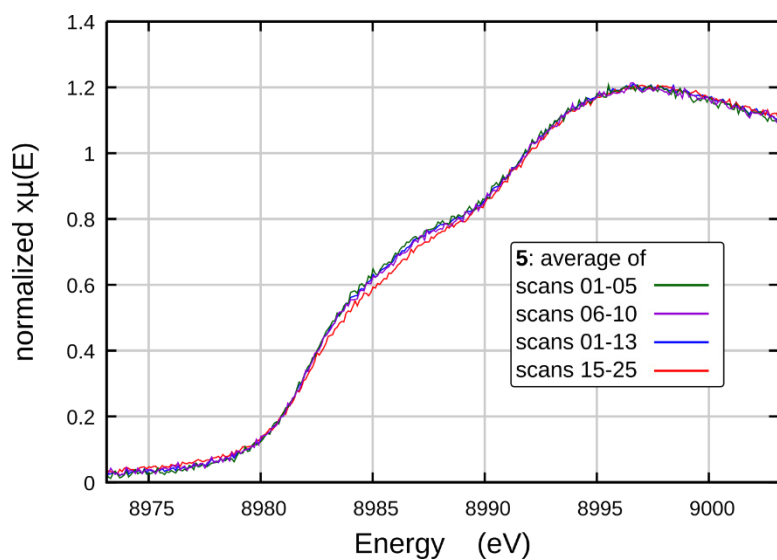
Figure S74. Damage study of **5** in Cu K-edge XAS region. Averages of scans 1 to 5 (green trace) overlaps with the averages of scans 6 to 10 (purple) and 1 to 13 (blue), while scans beyond 15th start to show noticeable decrease in the intensity, as evidenced by the average of scans 15 to 25 in red. Such changes were attributed to decomposition most probably due to slow air permeation into the cell.

XES
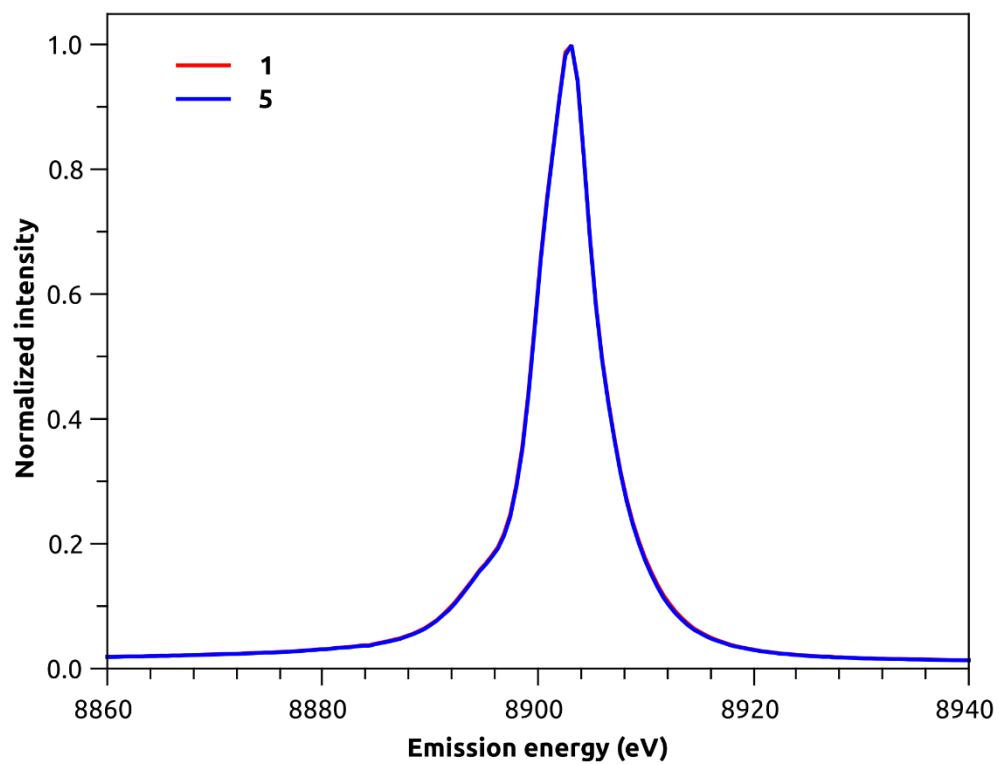
Figure S75. Non-resonant X-ray emission spectra of **1** and **5** in the mainline region.

DFT
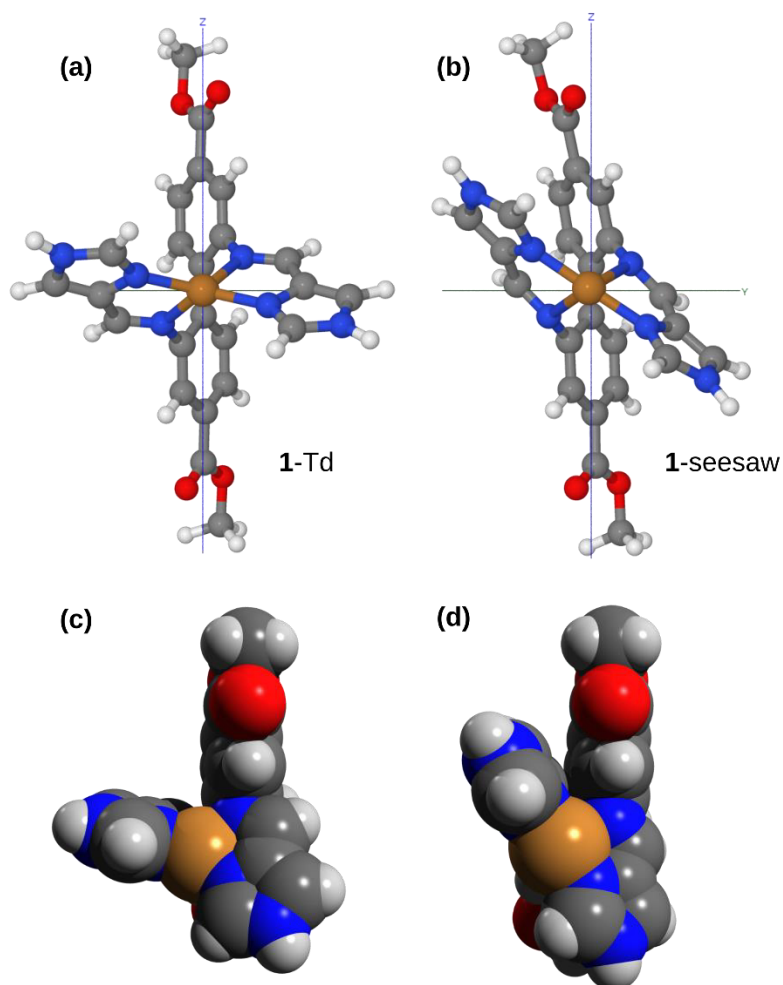
Figure S76. View along the C_2 axis (x) of the DFT optimized structures of (a) **1**-T_d and (b) **1**-seesaw. The vertical axis (z) is biphenyl C-C bond. Space-filling models showing the van der Waals radii of the atoms in (c) **1**-T_d and (d) **1**-seesaw.

MOF Incorporation

Synthetic procedure for UiO-67-(NH$_2$)$_2$-10%

2,2' diaminobiphenyl 4,4'dicarboxylic acid was synthesized according to literature.[16] ZrCl$_4$ (1.00 g, 4.29 mmol, 1 equiv.) was carefully dissolved in a beaker containing DMF (ca. 100 mL) and distilled water (230µL). The solution was heated and benzoic acid (4.72 g, 38.7 mmol, 9 equiv.) was dissolved under stirring. Thereafter, 2,2'-diaminobiphenyl-4,4'-dicarboxylic acid (0.12 g, 0.44 mmol, 0.1 equiv.) was added to the DMF solution. The mixture was transferred to a round bottom flask containing biphenyl-4,4'-dicarboxylic acid (0.94 g, 3.88 mmol, 0.9 equiv.). It was stirred overnight at 138 ºC with a fitted condenser. The solids were collected through filtration and washed with hot DMF (200 mL) and acetone (150 mL). After drying in an oven at 150 ºC overnight, the product was obtained as a pale yellow solid (1.31 g).

Synthetic procedure for UiO-67-1b

A 10 mL centrifuge tube with UiO-67-(NH$_2$)$_2$-10% (500 mg, ~0.14 mmol diamino-functionalisation), Cu(OTf)$_2$ (50 mg, 0.14 mmol), 1*H*-imidazole-4-carbaldehyde (30 mg, 31 mmol) and acetonitrile (5 mL) was shaken at 500 rpm over night. The resulting mixture was centrifuged and the supernatant removed. The solid was washed three times with acetonitrile (addition of 5 mL acetonitrile, resuspension of the solid, shaken for 30 min at 500 rpm, centrifugation and removal of the supernatant). The last two washing steps were not coloured (see Figure S77). The pristine MOF was dried for 24 h in a vacuum oven at 80 °C, yielding 488 mg of UiO-67-**1b**.
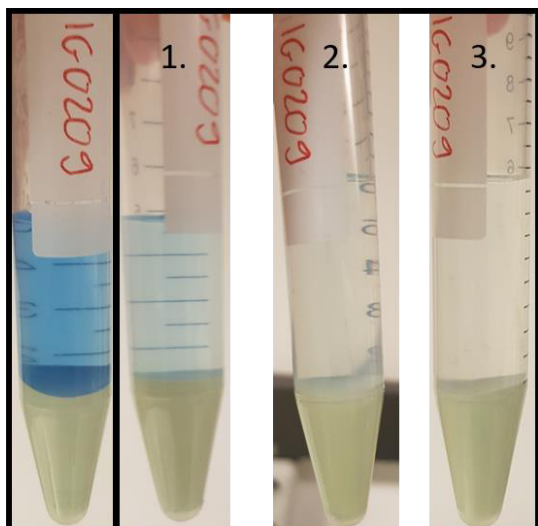
Reaction mixture   Washing steps

Figure S77. Centrifuge tube with the synthesized MOF. Left: Reaction mixture after centrifugation with blue supernatant. Right: Centrifugation after each washing step; while the first washing step still has a faint blue supernatant, the second and third washing step yielded colourless supernatants.

NMR

Ca. 25 mg of sample were digested in 1 mL of 0.1 M NaOD in D_2O overnight. For **1b** and UiO-67-1b, an excess of ascorbic acid was added, resulting in a colour change from green to yellow.

The proof of the incorporation of **1b** by so-called digestion NMR could not be made, as the complex does not tolerate the strongly basic digestion conditions (bottom spectrum in Figure S78) and hydrolyses into aldehyde and amine. However, digested UiO-67-1b contained aldehyde and diamine in similar quantities (Figure S78), supporting incorporation of the complex. The digestion NMR was also useful to estimate the actual percentage of bpdc-$(NH_2)_2$ in UiO-67-$(NH_2)_2$-10%. The quantification of the linkers in the NMR spectra is complicated by the presence of multiple species that can be attributed to bpdc-$(NH_2)_2$. This is likely due to reactions with e.g. formate (that is generated during MOF synthesis from DMF).[17] The estimation of the amount of bpdc-$(NH_2)_2$ incorporated was therefore attempted on a group of signals that can be attributed to the proton located next to the amino groups (Figure S78, blue box). Its integral was 3-4% of that of the signals belonging to bpdc in the spectra of the digested MOFs (Figure S78), suggesting an incorporation of 6-8% (the bpdc signals account for four protons each). This is consistent with the reported values.[18]
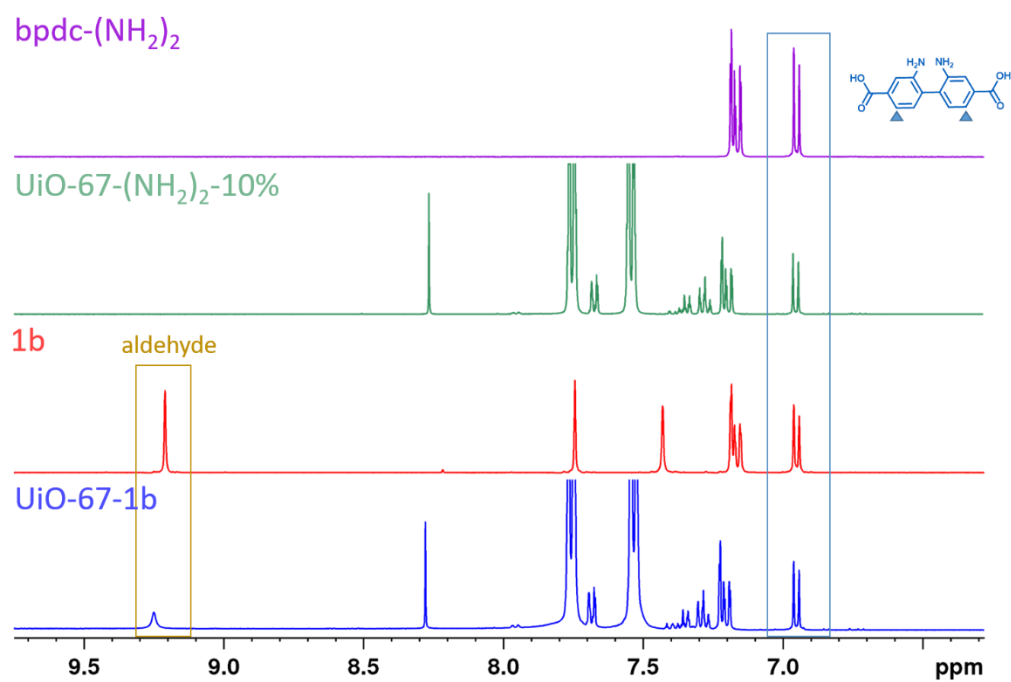
Figure S78. 'Digestion NMR' of UiO-67-(NH₂)₂-10% and UiO-67-**1b** (top two spectra) and the diamino linker (bpdc-(NH₂)₂) and complex **1b** after the digestion treatment.'

Elemental Mapping
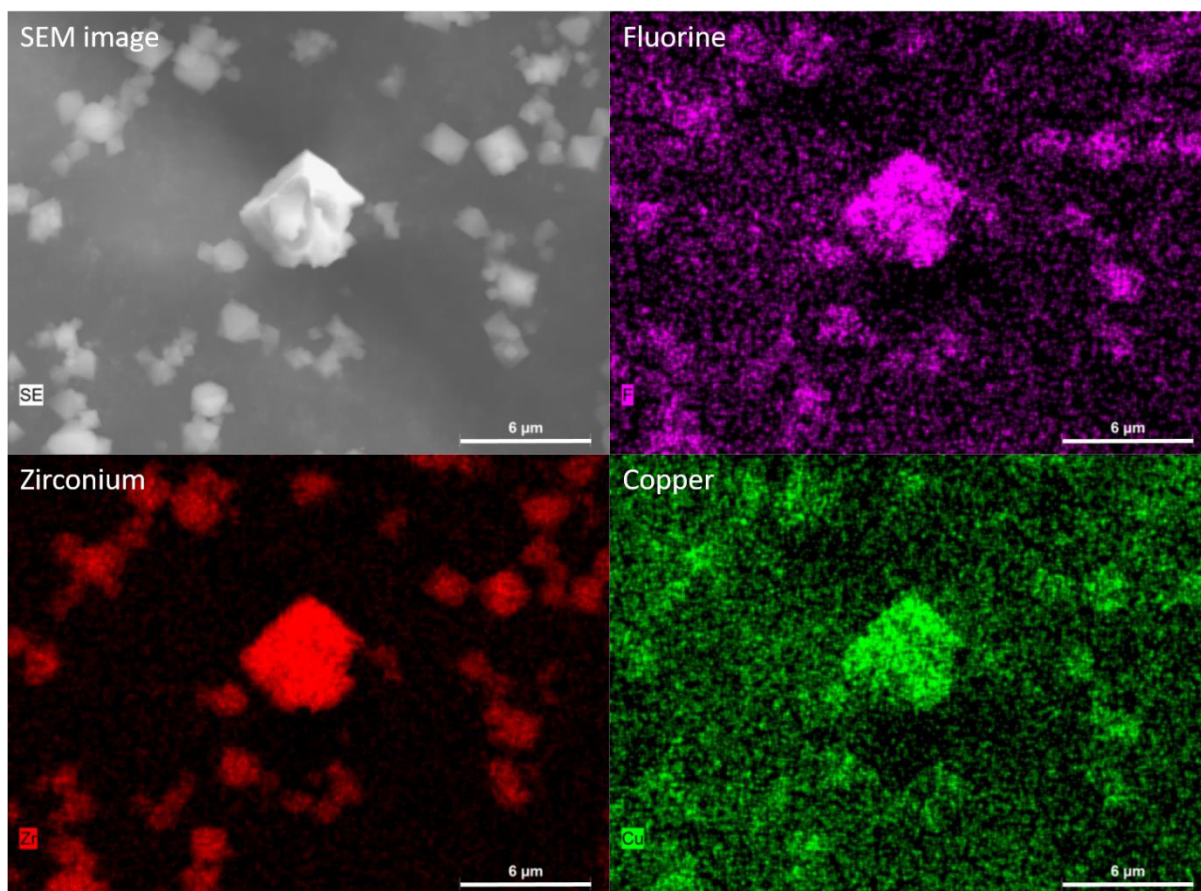
Figure S79. Elemental Mapping showing the distribution of F, Zr and Cu in UiO-67-1b.

EDX

Due to the low copper loading, the error of for the percentage of copper in the functionalised MOF is similar to the percentage itself. By taking the average of three spots, a ratio of copper to zirconium of 1: (0.060 ± 0.003) was obtained. Considering the 1:1 ratio between linker and zirconium in an ideal (defect-free) UiO-67, this value is consistent with the bpdc-$(NH_2)_2$ incorporation found by NMR.

Elemental Analysis

The zirconium copper ratio was verified by elemental analysis and UiO-67-1b was found to contain 22.49 % zirconium and 0.93 % copper. Adjusted for the relative atomic masses, this gives a ratio of zirconium to copper of 1:0.059, which is in excellent agreement with the value obtained from EDX.

TGA
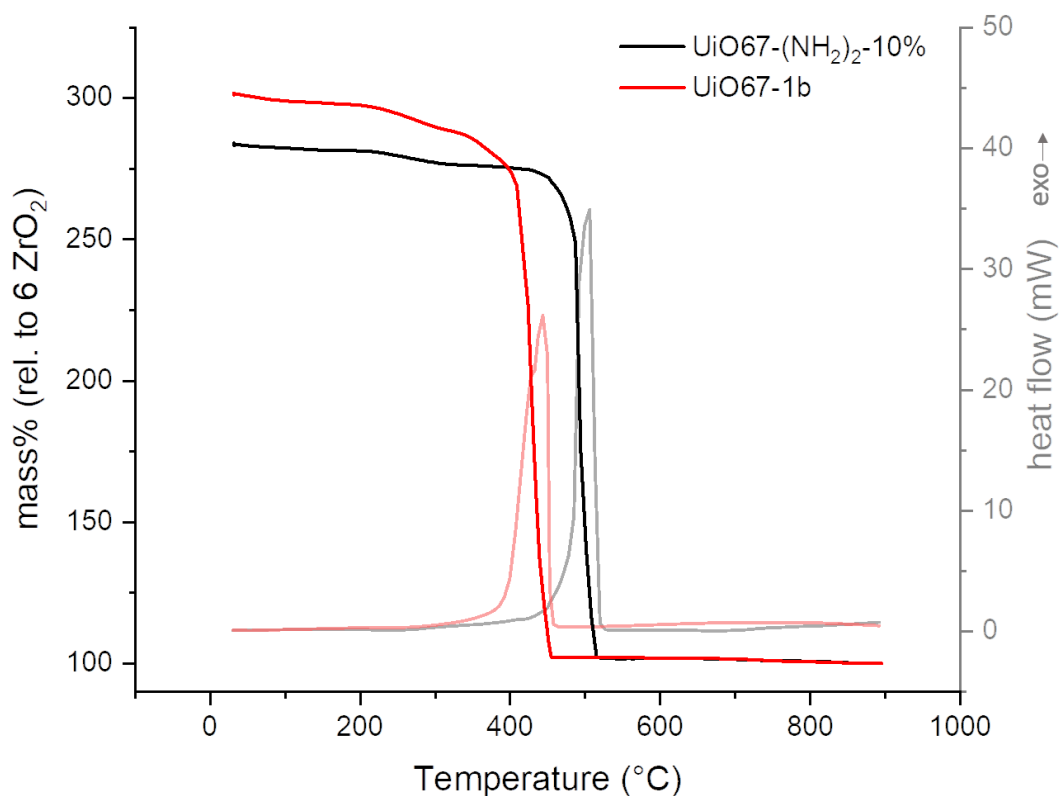
Figure S80. TGA and DSC of the diamino-functionalised MOF (UiO-67-$(NH_2)_2$-10%) and the MOF after incorporation of complex **1b** (UiO-67-1b).

Sources

1 K. T. Hylland, S. Øien-Ødegaard and M. Tilset, *Eur. J. Org. Chem.*, 2020, 4208–4226.

2 K. T. Hylland, S. Øien-Ødegaard, R. H. Heyn and M. Tilset, *Eur. J. Inorg. Chem.*, 2020, 3627–3643.

3 G. M. Sheldrick, *Acta Cryst.*, 2015, **C71**, 3–8.

4 G. M. Sheldrick, *Acta Cryst.*, 2015, **A71**, 3–8.

5 O. V. Dolomanov, L. J. Bourhis, R. J. Gildea, J. a. K. Howard and H. Puschmann, *J. Appl. Crystallogr.*, 2009, **42**, 339–341.

6 F. H. Allen, O. Johnson, G. P. Shields, B. R. Smith and M. Towler, *J. Appl. Crystallogr.*, 2004, **37**, 335–338.

7 A. R. Craze, N. F. Sciortino, M. M. Badbhade, C. J. Kepert, C. E. Marjo and F. Li, *Inorganics*, 2017, **5**, 62.

8 S. Mishra, B. Paital, H. S. Sahoo, S. G. Pati, D. Tripathy and N. B. Debata, *Dalton Trans.*, 2020, **49**, 8850–8854.

9 T. M. Tallon, PhD Thesis, National University of Ireland Maynooth, 2010.

10 Non-Frequency Dimension NMR Analysis Software, https://www.bruker.com/en/products-and-solutions/mr/nmr-software/dynamics-center.html, (accessed July 28, 2021).

11 A. L. Spek, *Acta Cryst.*, 2015, **C71**, 9–18.

12 D. Rosiak, A. Okuniewski and J. Chojnacki, *Polyhedron*, 2018, **146**, 35–41.

13 A. Okuniewski, D. Rosiak, J. Chojnacki and B. Becker, *Polyhedron*, 2015, **90**, 47–57.

14 L. S. Kau, D. J. Spira-Solomon, J. E. Penner-Hahn, K. O. Hodgson and E. I. Solomon, *J. Am. Chem. Soc.*, 1987, **109**, 6433–6442.

15 B. Ravel and M. Newville, *J. Synchrotron Rad.*, 2005, **12**, 537–541.

16 N. Ko, J. Hong, S. Sung, K. E. Cordova, H. J. Park, J. K. Yang and J. Kim, *Dalton Trans.*, 2015, **44**, 2047–2051.

17 K. M. Zwoliński, P. Nowak and M. J. Chmielewski, *Chem. Commun.*, 2015, **51**, 10030–10033.

18 G. Kaur, PhD Thesis, Oslo University, 2020.

Paper II

Enabling a Bioinspired N,N,N- Copper Coordination through Spatial Control in UiO-67: Synthesis and Reactivity towards H_2O and O_2

Isabelle Gerz, Erlend S. Aunan, Knut T. Hylland, Ning Cao, David S. Wragg, Ainara Nova, Mohamed Amedjkouh

Manuscript under preparation

Paper III

Synthesis and Luminescence of Dibenzo[d,f]-1,2-dihydro-[1,3]diazepines

Isabelle Gerz, Rafael Cortez Sgroi Pupo, David S. Wragg, Ainara Nova, Mohamed Amedjkouh

Manuscript under preparation

Paper IV

The Reactivity of Multidentate Schiff Base Ligands Derived from Bi- and Terphenyl Polyamines towards M(II) (M=Ni, Cu, Zn, Cd) and M(III) (M=Co, Y, Lu)

Knut Tormodssønn Hylland, Isabelle Gerz, David S. Wragg, Sigurd Øien-Ødegaard, Mats Tilset

Check for updates

Chemistry
Europe
European Chemical
Societies Publishing

The Reactivity of Multidentate Schiff Base Ligands Derived from Bi- and Terphenyl Polyamines towards M(II) (M=Ni, Cu, Zn, Cd) and M(III) (M=Co, Y, Lu)

Knut Tormodssønn Hylland,*[a, b] Isabelle Gerz,[a, b] David S. Wragg,[a, b]
Sigurd Øien-Ødegaard,[a, b] and Mats Tilset*[a, b]

Multidentate Schiff base ligands derived from a selection of biphenyl- and terphenyl polyamines were synthesized, and their reactivity towards divalent (Ni, Cu, Zn, Cd) and trivalent (Co, Y, Lu) metals was studied by single-crystal X-ray diffraction analysis, NMR spectroscopy, and UV/Vis spectroscopy for the Cu(II) complexes. Large variations in the resulting complexes were observed based on the relative position of the amine substituents in the parent triamines, as well as the electronic properties of the Schiff base ligand itself. Most notably, Schiff base ligands derived from a *m*-terphenyl-2,2′,2″-triamine were found to coordinate in a tetradentate, pentadentate or hexadentate fashion, depending on the size and the valency of the corresponding metal center.

Introduction

Schiff base ligands are popular multidentate ligands in coordination chemistry. Among other things, the popularity arises from the general broad scope of the synthesis of such ligands; a large number of ligands with different denticities can be made from relatively simple precursors.[1] Schiff base complexes of most metals in the periodic table are known,[2] and both Schiff bases and their corresponding metal complexes have found applications within numerous fields, such as catalysis,[3] medicine,[4] supramolecular chemistry[5] and materials science.[6] Of the various Schiff base ligands that are known, tetradentate salen and salen-like ligands are amongst the most studied,[1,3a,7] but ligands with higher denticities are also common.[2,8] Multidentate Schiff base ligands are versatile in the sense that they can stabilize a wide range of coordination geometries and numbers, which makes them suitable ligands for both relatively small metals,[3a,7,9] as well as larger metals.[10] Biphenyl- or terphenyl-2,2′-diamines are attractive starting materials for the synthesis of multidentate Schiff bases, as the 1,4-relation between the amino-groups permits for the formation of a salen-like chelate. Furthermore, the electronic and steric properties of the biphenyl/terphenyl backbone can easily be tuned by standard methods in organic synthesis. Ligands derived from *m*-terphenyls are particularly interesting in coordination chemistry and organometallic chemistry,[11] due to their increased steric bulk compared to the corresponding biphenyls and *p*-terphenyls. In addition, the *m*-terphenyl backbone allows for the installation of three donating moieties in close spatial proximity to each other by functionalization of the positions *ortho* to the $C_{Ar}-C_{Ar}$ bonds (**A**, Figure 1). Although this latter point has been explored to great extent for *m*-terpyridine systems[12] (**B**, Figure 1), relatively few studies have been conducted on tri-*ortho*-substituted *m*-terphenyl ligands.[13]

We recently reported a detailed study on Zn(II) Schiff base complexes derived from biphenyl-2,2′-diamines.[14] Therein, particular focus was devoted to NMR investigations of the metal complexes in solution in the presence or absence of external ligands, such as organic nitrogen-containing bases and Lewis basic solvents (Figure 2a). Several of these complexes were investigated by single-crystal X-ray diffraction as well. In addition to the studies on Zn, Cd complexes of the same ligand systems were investigated.

As a continuation of the work on the Zn complexes in Figure 2a, it was in our interest to investigate Zn complexes with additional Lewis basic groups in the ligand backbone, by

[a] Dr. K. T. Hylland, I. Gerz, Dr. D. S. Wragg, Dr. S. Øien-Ødegaard,
    Prof. Dr. M. Tilset
    Department of Chemistry
    University of Oslo
    P. O. Box 1033 Blindern, 0315 Oslo, Norway
    E-mail: k.t.hylland@smn.uio.no
            mats.tilset@kjemi.uio.no
    http://www.mn.uio.no/kjemi/personer/vit/matst/index.html
[b] Dr. K. T. Hylland, I. Gerz, Dr. D. S. Wragg, Dr. S. Øien-Ødegaard,
    Prof. Dr. M. Tilset
    Centre for Materials Science and Nanotechnology
    University of Oslo
    P.O. Box 1126 Blindern, 0316 Oslo, Norway

X = OH, NH₂, PR₂, etc.
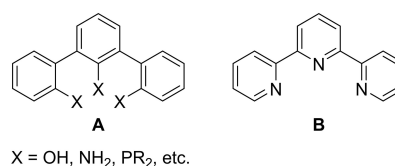
Figure 1. *m*-Terphenyls with donor groups in the positions *ortho* to the $C_{Ar}-C_{Ar}$ bonds (**A**), and *m*-terpyridine (**B**).
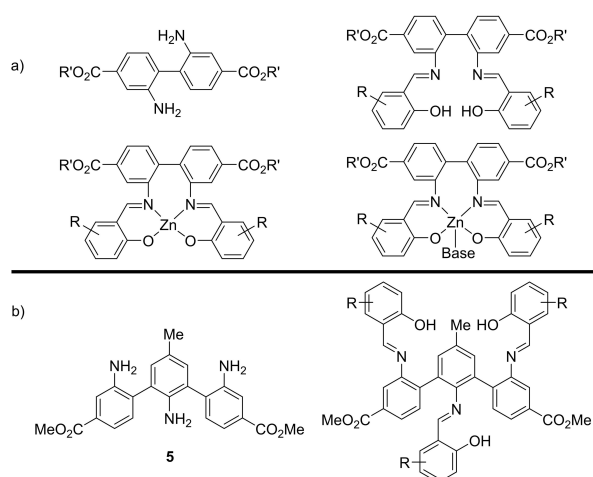
Figure 2. (a) General structure of biphenyl-2,2'-diamines, Schiff base ligands derived from these, and their corresponding Zn complexes that were previously studied by us.[14] (b) *m*-Terphenyl-2,2',2''-triamine **5** and the general structure of its corresponding Schiff base ligands. The reactivity of these ligands towards different metals will be discussed herein.

Scheme 1. Synthesis of Schiff base ligands **1a–d**, **2a–c** and **3** from triamines **5**, **6** and **7**.

employing a *m*-terphenyl-2,2',2''-triamine rather biphenyl-2,2'-diamines as ligand precursors (Figure 2b). Furthermore, metal complexes with pendant Lewis basic groups in the ligand backbone are useful in catalysis,[15] and as building blocks in supramolecular chemistry.[5c,16] The introduction of an additional salicylaldimine group would further make it possible to obtain potential hexadentate Schiff base ligands, for the coordination of larger metals, such as the rare-earth elements. Herein, we report a study of a series of Schiff base ligands, comprising three salicylaldimine groups in the ligand backbone, and their reactivity towards a selection of metals (Cu(II), Zn(II), Cd(II), Co(III), Y(III) and Lu(III)), showing the flexible nature of these ligands. In addition, we present the synthesis and characterization of Ni(II), Cu(II) and Co(III) analogues of the Zn(II) complexes shown in Figure 2a, in order to further demonstrate the versatility of the biphenyl-2,2'-diamine backbone for the synthesis of metal Schiff base complexes.

Results and Discussion

Synthesis of Schiff base ligands 1a–d, 2a–c and 3

In a recent publication we reported the synthesis of biphenyl- and terphenyl triamines using the Suzuki-Miyaura reaction of bromoanilines and an *ortho*-nitro-substituted arylboronic acid as the key step.[17] Some of these triamines (**5**, **6**, and **7**, Scheme 1) were subjected to typical synthesis conditions for formation of Schiff bases giving access to ligands **1a–d**, **2a–c** and **3** (Scheme 1).

The ligands were obtained in good yields and were conveniently purified by recrystallization. Because of the relatively large functional groups in the positions *ortho* to the C_{Ar}—C_{Ar} bonds of *m*-terphenyls **1a–d**, two rotamers were observed in the NMR spectra of these ligands. The extent of this
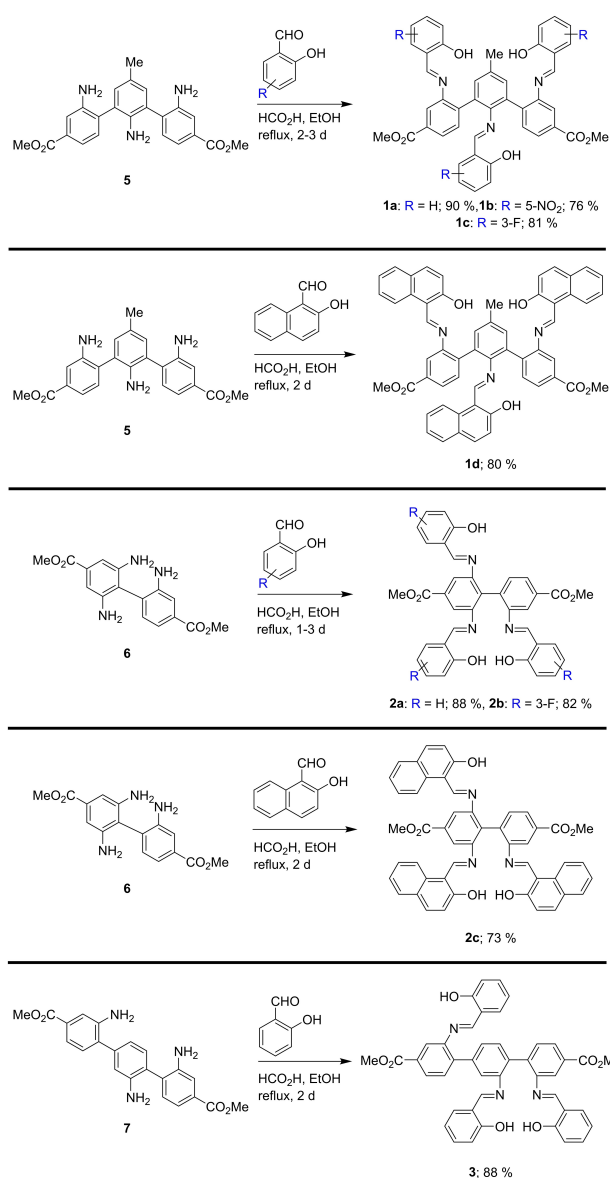
phenomenon was dependent on the exact substitution pattern of the phenolic rings for each ligand and was most pronounced for **1b** and **1d**. As expected for compounds exhibiting rotamers in their ^{1}H NMR spectra,[18] the ^{1}H NMR resonances of the ligands were solvent- and temperature-dependent (see SI). Although Schiff bases derived from aromatic amines often are quite robust towards hydrolytic degradation in the absence of strong acids or bases,[19] it was found that ligand **1b** would undergo partial hydrolysis in [D$_6$]DMSO, and the hydrolytic sensitivity of **1b** is a key aspect of its reactivity towards Cu(II), Zn(II) and Cd(II) (*vide infra*). One of the ligands, **1d**, was analyzed by single-crystal X-ray diffraction analysis (Figure 3). The C_{Ar}—C_{Ar} dihedral angles in the ligand were found to be $-68.4(2)°$ and $-61.8(2)°$, which is comparable to what has been earlier

EurJIC
European Journal of Inorganic Chemistry

Full Papers
doi.org/10.1002/ejic.202100170

Chemistry Europe
European Chemical Societies Publishing
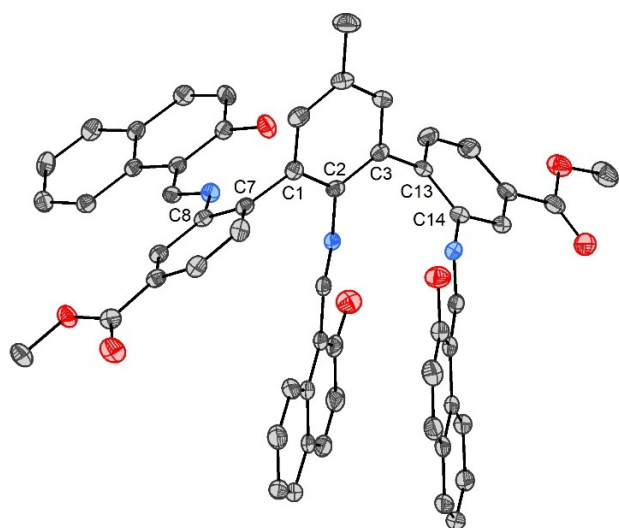
Figure 3. ORTEP plot of **1d** with 50% probability ellipsoids. Hydrogen atoms have been omitted for clarity. Selected angles [°]: C2–C1–C7–C8, −68.4(2), C2–C3–C13–C14, −61.8(2).

reported for sterically encumbered *m*-terphenyls in the literature.[11c,i,17]

Synthesis and NMR studies of Zn complexes 1a-Zn, 1d-Zn, 2a-Zn and 3-Zn

Monometallic Zn(II) complexes of ligands **1a**, **1d**, **2a** and **3** were synthesized by reacting the appropriate ligand with one equivalent of Zn(OAc)$_2$·2H$_2$O in the presence of an excess of NEt$_3$ in MeOH or CH$_2$Cl$_2$/MeOH (Scheme 2).

The complexes were characterized by NMR spectroscopy, MS, elemental analysis, and single-crystal X-ray diffraction analysis (*vide infra*). From NMR studies of complexes **2a**-**Zn** and **3**-**Zn**, the behavior in solution was largely analogous to what has earlier been reported for Zn complexes of biphenyl- and terphenyl-based tetradentate N_2O_2 ligands.[14,17] No evidence was found for the coordination of the third salicylaldimine group to Zn. For complex **1a**-**Zn**, ^{1}H NMR studies were somewhat less straightforward. In strongly Lewis basic solvents ([D$_6$] DMSO, [D$_7$]DMF and [D$_5$]pyridine), the ^{1}H NMR spectrum of the complex was relatively conventional, although modest broadening of some of the ^{1}H NMR resonances was observed at ambient temperature (*vide infra*). The ^{1}H NMR spectrum of **1a**-**Zn** in CDCl$_3$ revealed the presence of two species, which were observed to interconvert by NOESY experiments (see Figure S127–S129, SI). Whereas the ^{1}H NMR resonances corresponding to the major species underwent changes on gradually increasing the concentration of **1a**-**Zn** in CDCl$_3$, the resonances corresponding to the minor species remained practically constant (Figure 4).

For the major species in the ^{1}H NMR spectrum of **1a**-**Zn**, the resonances became more broadened and were moved to lower ppm values at increased concentrations of **1a**-**Zn**, which is in accordance with the formation of a dimeric (or oligomeric)
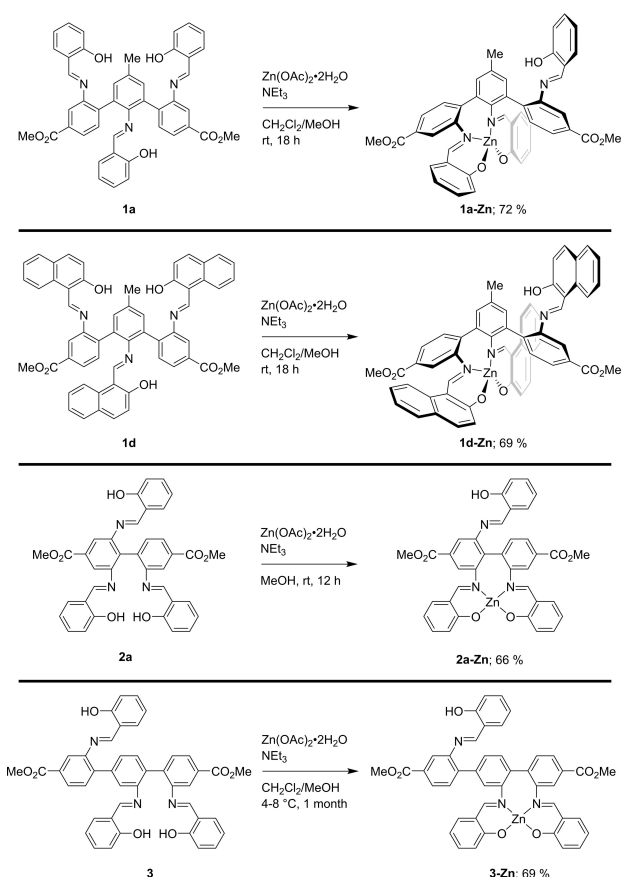
Scheme 2. Synthesis of Zn(II) complexes **1a-Zn**, **1d-Zn**, **2a-Zn** and **3-Zn**.
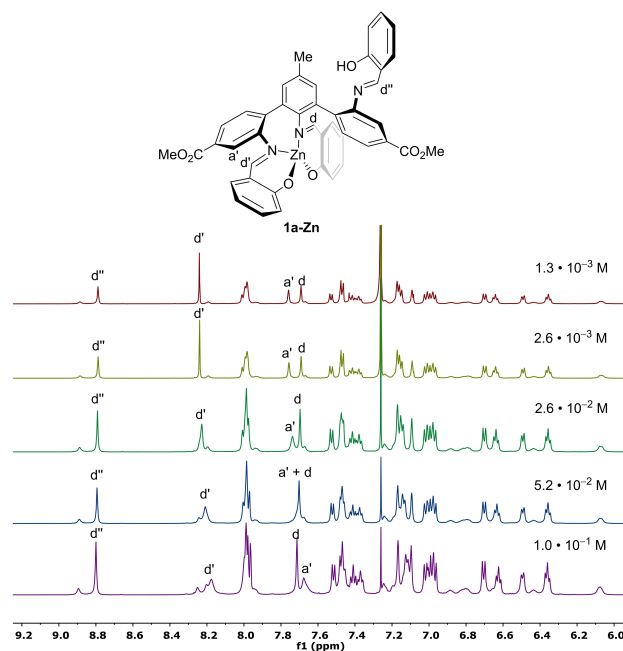
Figure 4. Stacked ^{1}H NMR (600 MHz, CDCl$_3$) spectra of **1a-Zn** with different concentrations of the complex. The complex is depicted as a tetracoordinated monomer for simplicity.

EurJIC
European Journal of Inorganic Chemistry

Full Papers
doi.org/10.1002/ejic.202100170

Chemistry Europe
European Chemical
Societies Publishing

species[20] (**1a-Zn—D**, Scheme 3). The presence of the additional salicylaldimine group in close proximity to the metal center in **1a-Zn** should facilitate coordination of the imine nitrogen to Zn, resulting in a pentacoordinated monomer (**1a-Zn-5**, Scheme 3). The ^{1}H NMR resonances of this species were unaffected by changes in concentration of the complex, as the coordination of the pendant salicylaldimine group is intra-molecular, and not intermolecular like the dimerization process. Hence, **1a-Zn-5** is suggested to be the minor species at any concentration of the complex in CDCl$_3$.

The formation of an N_3O_2-ligated pentacoordinated mono-mer is more likely to take place than the formation of N_3O_3-ligated hexacoordinated species (**1a-Zn-6**), as hexacoordination is very rarely seen in the literature for Zn Schiff base complexes derived from aromatic diamines (e.g. Zn salphen complexes).[21] It should however be noted that octahedral Zn complexes of *reduced* hexadentate N_3O_3 Schiff base ligands are described in
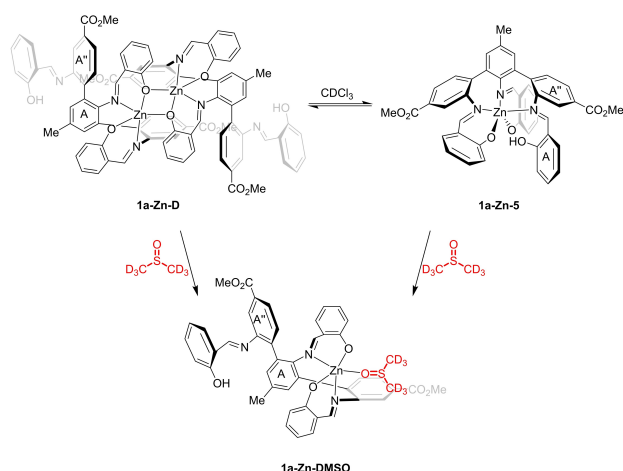
the literature,[22] and that hexacoordinated Zn complexes of tridentate Schiff base ligands are quite common.[23]

The presence of only one species in the ^{1}H NMR spectrum of **1a-Zn** in [D$_6$]DMSO, [D$_7$]DMF and [D$_5$]pyridine may be explained by ligation of a solvent molecule to Zn (Scheme 4).

The ligation of Lewis basic solvent molecules to Zn complexes of tetradentate Schiff base ligands is a characteristic attribute of their coordination chemistry.[5c,24] This ligation would inhibit the interconversions described in Scheme 3, as both the dimerization in **1a-Zn—D** and the coordination of the salicylaldimine group in **1a-Zn-5** depend on an open coordination site at Zn. The absence of a free coordination site at Zn would be expected to restrict the rotation around the C_{Ar}—C_{Ar} bond between rings A and A'' (Scheme 4) to a great extent, although the somewhat broadened ^{1}H NMR resonances of **1a-Zn** in [D$_6$]DMSO, [D$_7$]DMF and [D$_5$]pyridine suggest that the corresponding solvent-ligated complex does not possess a completely static conformation. Also, NOESY experiments of **1a-Zn** in [D$_7$]DMF at different temperatures suggest that several dynamic processes are taking place, as the imine protons H$^{d'}$ and H$^{d''}$ were found to exchange with each other at 27 °C (Scheme 5). Exchange peaks between the same resonances were not observed at −20 °C. For more details see Figure S140 and Figure S141, SI. The fluxional behaviour of **1a-Zn** in [D$_7$]DMF is similar to what has been reported for *m*-terpyridine[25] or pyridine[26] complexes of transition metals (e.g. Re(I) and Pt(IV)) in the literature.

In addition to complex **1a-Zn**, the related complex **1d-Zn** (Scheme 2) was studied by NMR. Complex **1d-Zn** behaved similar to **1a-Zn** in NMR, and two species (**1d-Zn-4** and **1d-Zn-5**) were observed in CDCl$_3$, in a ratio of 1.2:1 at ambient temperature. The interconversion between the two species could be observed in NOESY experiments (see Figure S162, SI), and the process depicted in Scheme 6 is suggested to be operative. Similar observations were made for the complex in C$_6$D$_6$.

The ^{1}H NMR resonances of **1d-Zn** in CDCl$_3$ were concentration-independent and sharp at ambient temperature. The ^{15}N NMR resonances corresponding to the imine nitrogen atoms of **1d-Zn-4** and **1a-Zn-5** in CDCl$_3$ could be obtained from ^{1}H-^{15}N HMBC experiments (Figure 5).

The ^{15}N NMR resonances corresponding to the two non-equivalent imine nitrogen atoms in ligand **1d** were observed at δ −126.9 and δ −119.6 ppm in CDCl$_3$. For **1d-Zn**, the ^{15}N NMR

Scheme 3. Suggested interconversion of complex **1a-Zn** in CDCl$_3$.

Scheme 4. Ligation of DMSO to complex **1a-Zn**. The ligation blocks the two tentative modes of pentacoordination seen for **1a-Zn** in CDCl$_3$, resulting in a more conventional ^{1}H NMR spectrum of the complex in [D$_6$]DMSO than in CDCl$_3$.
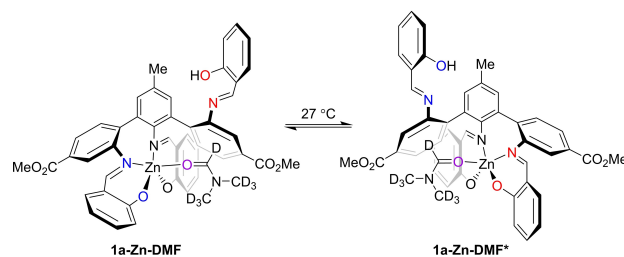
Scheme 5. Interconversion of **1a-Zn—DMF** and **1a-Zn—DMF*** at ambient temperature.
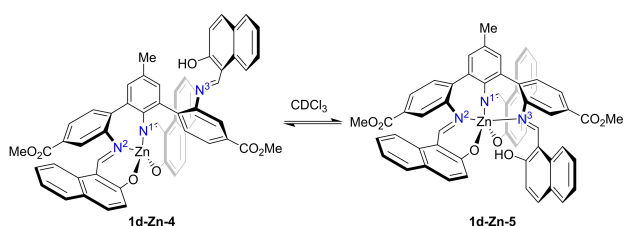
Scheme 6. Suggested dynamic behavior of the naphthol-derived complex **1d-Zn** in CDCl$_3$.
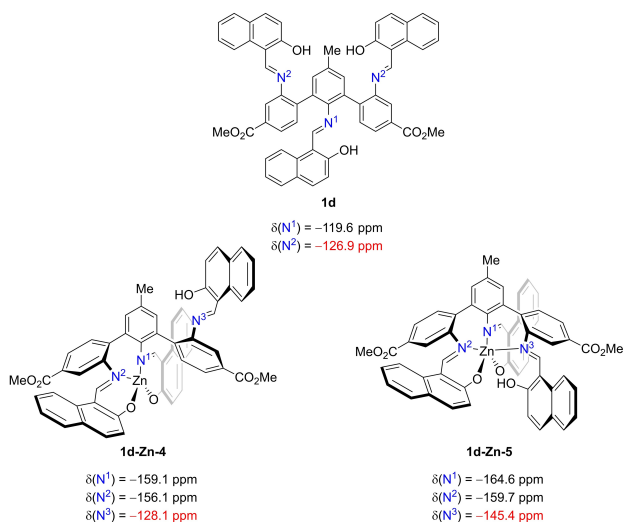
Figure 5. Overview of the ^{15}N NMR resonances found for **1d**, **1d-Zn-4** and **1d-Zn-5** in CDCl$_3$. Although resonances belonging to two different rotamers could be seen in the ^{1}H NMR and ^{13}C NMR spectra of ligand **1d**, their ^{15}N NMR resonances could not be differentiated.

resonances of the imine nitrogen atoms in the major species (**1d-Zn-4**) were found at δ −159.1, δ −156.1 and δ −128.1 for N^1, N^2 and N^3 respectively. The change to lower ppm values for the resonances corresponding to the coordinating imine nitrogen atoms (N^1 and N^2) is in accordance with what is expected when going from an uncoordinated nitrogen to a metal-coordinated nitrogen.[27] The resonance corresponding to the third imine nitrogen (N^3) in **1d-Zn** remained practically unchanged on comparison with the corresponding nitrogen in ligand **1d**, indicating that this nitrogen is not participating in any coordination. For N^3 in **1d-Zn-5** on the other hand, the corresponding ^{15}N NMR resonance was observed at a lower ppm value, δ −145.4, which indicates that N^3 may be participating in coordination to Zn. $\Delta\delta$(N^3) is larger than what would be anticipated if the two different species observed in the ^{1}H NMR spectrum of **1d-Zn** were originating from restricted rotation around the C$_{Ar}$–C$_{Ar}$ bond alone; it would then have been expected that similar differences in the ^{15}N NMR resonances of the two different rotamers of ligand **1d** could be observed, which was not the case.

Crystallographic structure determination of complexes 1a-Zn, 1d-Zn, 2a-Zn and 3-Zn

The four Zn complexes depicted in Scheme 2, **1a-Zn**, **1d-Zn**, **2a-Zn** and **3-Zn** were characterized by single-crystal X-ray diffraction analysis (Figure 6–Figure 9).

Both **1a-Zn** and **2a-Zn** crystallized as dimers, containing two pentacoordinated Zn centers with square pyramidal geometry, as evaluated by their τ_5 values[28] ($\tau_5 = 0.01$ for **1a-Zn**, and $\tau_5 = 0.04$ and 0.07 for **2a-Zn**). Complex **3-Zn** crystallized as the pentacoordinated monomer **3-Zn–MeOH**, with distorted trigonal bipyramidal geometry ($\tau_5 = 0.58$ and 0.65 for the two molecules of the asymmetric unit). For **1a-Zn** and **2a-Zn**, the Zn–μ-O bond distances were similar to what has been reported for a related dimeric Zn complex in literature.[17] The Zn–O-
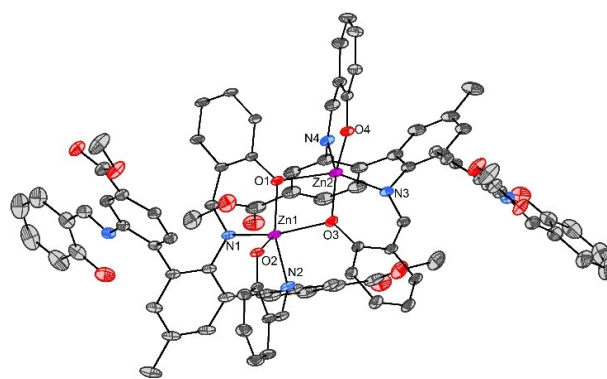
Figure 6. ORTEP plot of **1a-Zn** with 50% probability ellipsoids. Hydrogen atoms have been omitted for clarity. $\tau_5 = 0.01$. Selected bond lengths [Å] and angles [°]: Zn1–N1, 2.1644(18); Zn1–N2, 2.0316(16); Zn1–O1, 1.9592(13); Zn1–O2, 1.9300(15); Zn1–O3, 2.1480(16); N1–Zn1–N2, 87.22(7); N1–Zn1–O1, 88.47(6); N1–Zn1–O2, 108.79(7); N1–Zn1–O3, 147.54(6); N2–Zn1–O1, 148.19(7); N2–Zn1–O2, 94.95(7); N2–Zn1–O3, 92.01(7); O1–Zn1–O2; 116.22(6); O1–Zn1–O3, 75.35(6); O2–Zn1–O3, 103.61(6); Zn1–O1–Zn2, 101.53(6).

Figure 7. ORTEP plot of **1d-Zn** with 50% probability ellipsoids. Hydrogen atoms and non-coordinated solvents of crystallization (benzene and MeOH) have been omitted for clarity. $\tau_4' = 0.70$. Selected bond lengths [Å] and angles [°]: Zn1–N1, 1.9811(15); Zn1–N2, 2.0010(15); Zn1–O1, 1.9068(13); Zn1–O2, 1.9169(13); N1–Zn1–N2, 101.36(6); N1–Zn1–O1, 94.46(6); N1–Zn1–O2, 130.83(6); N2–Zn1–O1, 130.21(6); N2–Zn1–O2, 93.30(6); O1–Zn1–O2, 111.04(6).

EurJIC
European Journal of Inorganic Chemistry

Full Papers
doi.org/10.1002/ejic.202100170

Chemistry Europe
European Chemical Societies Publishing
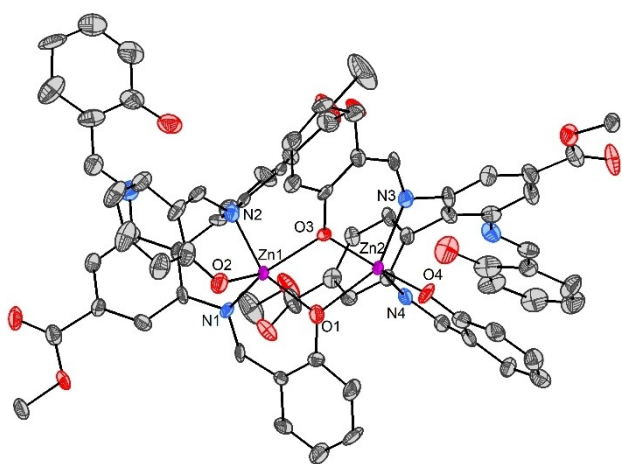
Figure 8. ORTEP plot of **2a**-**Zn** with 50% probability ellipsoids. Hydrogen atoms have been omitted for clarity. $\tau_5 = 0.07$, 0.04. Selected bond lengths [Å] and angles [°]: Zn1–N1, 2.210(9); Zn1–N2, 2.035(10); Zn1–O1, 1.946(8); Zn1–O2, 1.932(8); Zn1–O3, 2.172(7); Zn2–N3, 2.224(10); Zn2–N4, 2.027(9); Zn2–O1, 2.199(8); Zn2–O3, 1.955(7); Zn2–O4, 1.942(8); N1–Zn1–N2, 87.9(3); N1–Zn1–O1, 88.5(3); N1–Zn1–O2, 100.5(4); N1–Zn1–O3, 147.9(3); N2–Zn1–O1, 143.6(4); N2–Zn1–O2, 94.5(4); N2–Zn1–O3, 91.1(3); O1–Zn1–O2, 121.7(3); O1–Zn1–O3, 73.7(3); O2–Zn1–O3, 111.6(3); N3–Zn2–N4, 89.2(4); N3–Zn2–O1, 142.3(3); N3–Zn2–O3, 87.1(3); N3–Zn2–O4, 104.4(4); N4–Zn2–O1, 89.4(3); N4–Zn2–O3, 144.7(4); N4–Zn2–O4, 93.9(4); O1–Zn2–O3, 72.9(3); O1–Zn2–O4, 113.2(3); O3–Zn2–O4, 121.0(3); Zn1–O1–Zn2, 104.5(4); Zn1–O3–Zn2, 105.2(3).
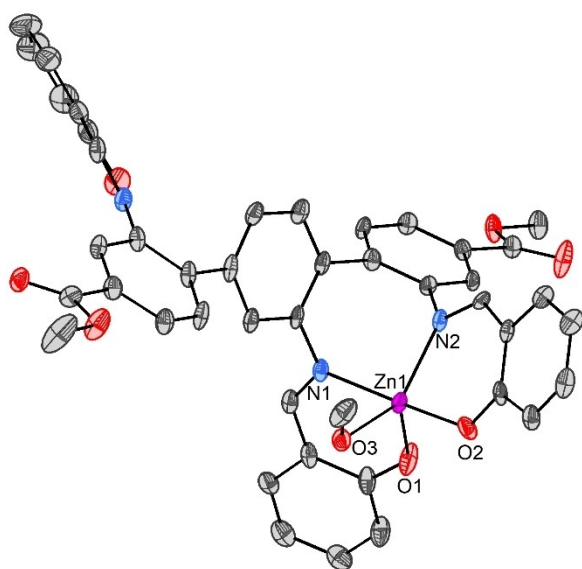
Figure 9. ORTEP plot of **3**−**Zn**−**MeOH** with 50% probability ellipsoids. Only one of the two molecules of the asymmetric unit is displayed, but metric data for both are given below. Hydrogen atoms and CH_2Cl_2 (solvent of crystallization) have been omitted for clarity. $\tau_5 = 0.58$, 0.65. Selected bond lengths [Å] and angles [°]: Zn1–N1, 2.100(3); Zn1–N2, 2.072(3); Zn1–O1, 1.922(3); Zn1–O2, 1.999(2); Zn1–O3, 2.126(3); Zn2–N3, 2.098(3); Zn2–N4, 2.072(3); Zn2–O4, 1.941(2); Zn2–O5, 1.996(3); Zn2–O6, 2.160(2); N1–Zn1–N2, 90.84(11); N1–Zn1–O1, 90.62(11); N1–Zn1–O2, 169.04(11); N1–Zn1–O3, 84.45(10); N2–Zn1–O1, 117.23(12); N2–Zn1–O2, 89.15(11); N2–Zn1–O3, 134.14(11); O1–Zn1–O2, 99.12(12); O1–Zn1–O3, 108.44(12); O2–Zn1–O3, 87.70(10); N3–Zn2–N4, 92.08(11); N3–Zn2–O4, 89.79(11); N3–Zn2–O5, 168.34(10); N3–Zn2–O6, 84.41(10); N4–Zn2–O4, 117.03(11); N4–Zn2–O5, 90.81(11); N4–Zn2–O6, 129.10(10); O4–Zn2–O5, 98.95(10); O4–Zn2–O6, 113.73(10); O5–Zn2–O6, 85.00(9).

(MeOH) bond length for **3-Zn**–**MeOH** (Zn1–O3, 2.126(3) Å) is comparable with reported Zn–O bond lengths in the literature for a EtOH-ligated Zn Schiff base complex,[29] but longer than the Zn–O(MeOH) bond in a MeOH-ligated Zn salphen complex.[30] Although NMR studies suggested the presence of a potential pentacoordinated species, naphthol-derived **1d-Zn** crystallized as a tetracoordinated complex with distorted tetrahedral geometry around Zn, as evaluated by its τ_4' value[31] of 0.70. The distorted geometry and the Zn–N and Zn–O bond lengths are in accordance with observations for related tetracoordinated Zn Schiff base complexes in the literature.[14,32]

Synthesis and characterization of 1a-Co(acac), 1d-Co(acac) and 8-Co(acac)

The ^{1}H NMR spectra of **1a-Zn** and **1d-Zn** in $CDCl_3$ showed the presence of two (interconvertible) species for each complex. To rationalize that this phenomenon was caused by the flexible nature of Zn with respect to ligand substitution reactions, as well as changes in coordination geometries and numbers, the corresponding Co(III) complexes **1a-Co(acac)** and **1d-Co(acac)** were synthesized for comparative NMR studies (Scheme 7). As opposed to Zn(II) complexes, low-spin octahedral Co(III) complexes are known for being kinetically inert, and in the ^{1}H NMR spectra of **1a-Co(acac)** and **1d-Co(acac)** in $CDCl_3$, sharp and well-defined resonances were observed, being in stark contrast to the ^{1}H NMR spectrum of e.g. **1a-Zn** in $CDCl_3$ at comparable concentrations. Furthermore, for the Co(acac) complexes, only one species was observed, while for **1a-Zn** and **1d-Zn**, two
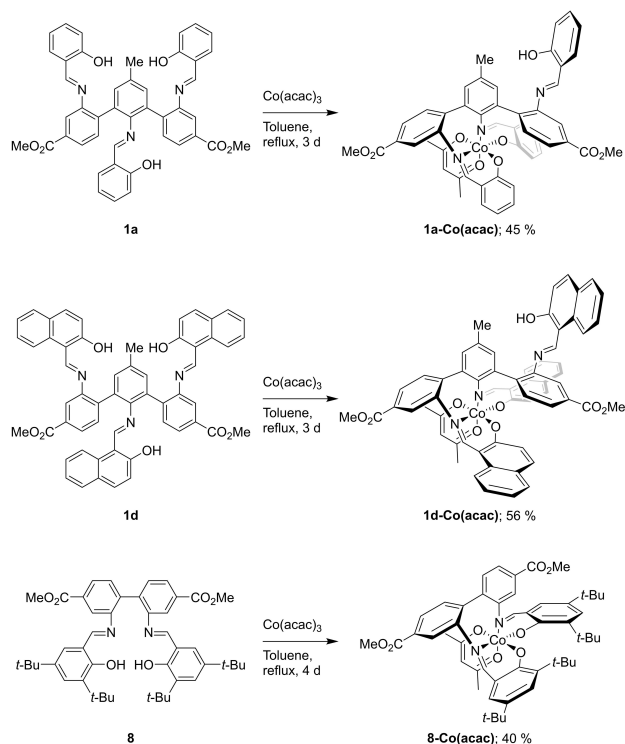
Scheme 7. Synthesis of complexes **1a-Co(acac)**, **1d-Co(acac)**, and **8-Co(acac)**.

EurJIC
European Journal of Inorganic Chemistry

Full Papers
doi.org/10.1002/ejic.202100170

Chemistry Europe
European Chemical
Societies Publishing

species could be observed. This suggest that the accessibility of an open coordination site at the metal center dictates how the ^{1}H NMR spectrum of the corresponding complex will appear.

Complex **1d-Co(acac)** was characterized by single-crystal X-ray diffraction analysis (Figure 10), and crystallized with the expected octahedral geometry around Co. Ligand **1d** acted as a tetradentate N_2O_2 ligand, occupying three of the equatorial and one of the axial sites around Co. The bidentate acac ligand concluded the coordination sphere around Co. Overall, the bond angles and bond lengths in structure of **1d-Co(acac)** were found to be similar to those reported by Shi and Duan for a similar Co(III) complex derived from 1,1′-binaphthalene-2,2′-diamine.[33] In addition to **1a-Co(acac)** and **1d-Co(acac)**, a related complex, **8-Co(acac)**, was synthesized (Scheme 7, lower part). The complex was also crystallographically characterized (see SI), showing very similar geometry around Co as that observed for **1d-Co(acac)**.

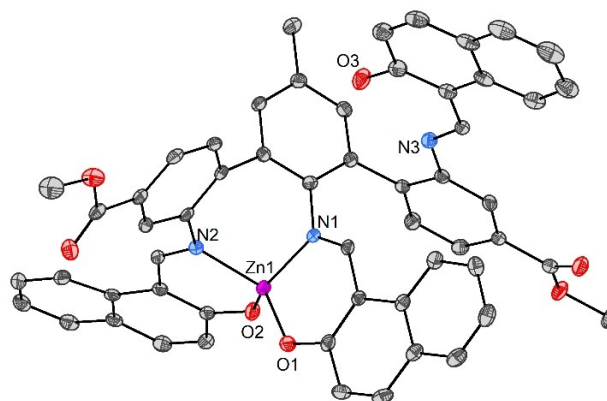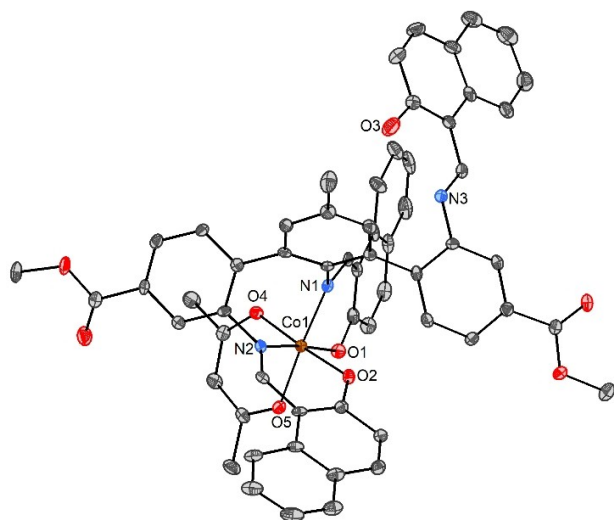**Figure 10.** ORTEP plot of **1d-Co(acac)** with 50 % probability ellipsoids. Hydrogen atoms and non-coordinated solvents of crystallization (benzene and MeCN) have been omitted for clarity. Selected bond lengths [Å] and angles [°]: Co1−N1, 1.925(4); Co1−N2, 1.902(4); Co1−O1, 1.889(3); Co1−O2, 1.871(3); Co1−O4, 1.891(3); Co1−O5, 1.892(3); N1−Co1−N2, 92.46(16); N1−Co1−O1, 92.96(15); N1−Co1−O2, 90.12(15); N1−Co1−O4, 87.50(15); N1−Co1−O5, 175.84(15); N2−Co1−O1, 174.57(16); N2−Co1−O2, 91.82(16); N2−Co1−O4, 92.09(15); N2−Co1−O5, 88.67(15); O1−Co1−O2, 88.60(14); O1−Co1−O4, 87.72(14); O1−Co1−O5, 85.96(14); O2−Co1−O4, 175.50(14); O2−Co1−O5, 85.85(14); O4−Co1−O5, 96.46(14).
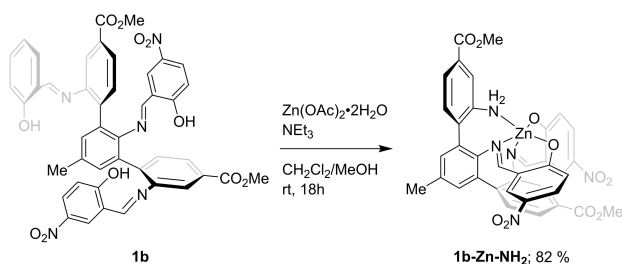
Synthesis and NMR studies of Zn complex 1b-Zn−NH₂

In addition to ligands **1a** and **1d**, the reactivity of the nitro-substituted ligand **1b** towards Zn was studied. Ligand **1b** was found to behave different from **1a** and **1d** when it was reacted with Zn(OAc)$_2$·2H$_2$O in the presence of NEt$_3$ in a solution of CH$_2$Cl$_2$ and MeOH (Scheme 8). For **1b**, only two imine functionalities were intact in the corresponding product **1b-Zn−NH₂**, as the third imine hydrolyzed and left behind an NH$_2$ group. From the single-crystal X-ray diffraction analysis of the complex, the NH$_2$ group was found to coordinate to Zn (*vide infra*). The fluorine-substituted ligand **1c** did not react cleanly with Zn-(OAc)$_2$·2H$_2$O under similar conditions as those described for **1a**, **1b** and **1d**, and a mixture of products was obtained instead (see SI for details).

The partial hydrolysis of imines in complexation of Schiff base ligands is occasionally reported in the literature,[34] leading to metal complexes of mixed amine-imine ligands. NMR characterization of **1b-Zn−NH₂** was mainly conducted in [D$_6$]DMSO, due to the poor solubility of the complex in e.g. CDCl$_3$. Nevertheless, limited ^{1}H NMR studies could be performed in CDCl$_3$ (*vide infra*). In [D$_6$]DMSO, two species were observed. The two species were determined to be interconvertible from NOESY and variable-temperature ^{1}H NMR experiments. From the crystal structure determination of the complex (*vide infra*) it was found that the Zn−NH$_2$ bond (2.177(2) Å) was approximately in the same range as the Zn−μ-O bonds that were found from the single-crystal X-ray diffraction analysis of **1a-Zn** and **2a-Zn**. In addition, the Zn−NH$_2$ bond in **1b-Zn−NH₂** was of similar length as the Zn−O(DMSO) bond in a related Zn complex previously reported by us.[17] As [D$_6$]DMSO is susceptible to break up dimeric pentacoordinated Zn Schiff base complexes and form monomeric pentacoordinated DMSO-ligated complexes, the same may occur for **1b-Zn−NH₂**. However, since the nature of the pentacoordination for the latter is predominantly intramolecular, DMSO ligation would be less favorable compared to dimers where the pentacoordination at Zn is a result of an intermolecular process. This may explain the presence of two interconvertible species in the ^{1}H NMR spectrum of **1b-Zn−NH₂** in [D$_6$]DMSO (Scheme 9), as opposed to e.g. **2a-Zn**, for which only one species could be detected in the ^{1}H NMR spectrum of the complex in [D$_6$]DMSO.

In the ^{1}H NMR spectrum of **1b-Zn−NH₂** in [D$_6$]DMSO, the differences in the resonances of the major species and the corresponding resonances of the minor species were in some

Scheme 8. Synthesis of complex **1b-Zn−NH₂**.
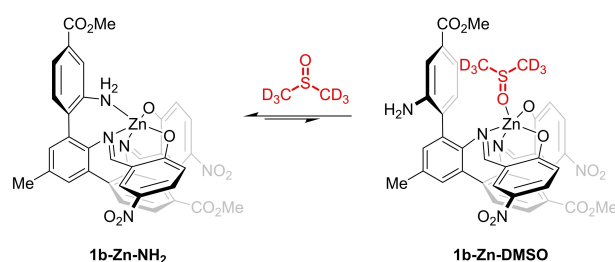
Scheme 9. Proposed partial solvolysis of **1b-Zn−NH₂** in [D$_6$]DMSO.

EurJIC
European Journal of Inorganic Chemistry

Full Papers
doi.org/10.1002/ejic.202100170

**Chemistry
Europe**
European Chemical
Societies Publishing

cases rather large. This was especially evident for the resonances corresponding to the protons of the NH_2-substituted ring, as well as the NH_2 protons (Figure 11). For the major component, the resonances corresponding to the three ring protons $H^{a''}$, $H^{b''}$ and $H^{c''}$ were observed at relatively high ppm values, at δ 7.94–7.96, δ 7.58–7.59 and δ 7.48 respectively, and the resonance corresponding to the NH_2 protons was observed at δ 6.17. In the minor component, the ^1H NMR resonances of the protons of discussion were observed at significantly lower ppm values; δ 7.27, δ 7.00, δ 6.82 and δ 5.16 respectively, being closer to what is expected for an aromatic amine of this kind.[17]

The ^{15}N NMR resonance of the NH_2 nitrogen of the major component was observed at a lower ppm value than the corresponding resonance of the minor component (δ −326.9 and δ −317.2 respectively) (Figure 12). This can be seen as an indication that the major component in $[D_6]DMSO$ actually is the NH_2-coordinated complex depicted to the left in Scheme 9.[27c–d] The ^{15}N NMR resonances of **1b-Zn−NH$_2$** were compared to those of triamine **5**. From ^1H-^{15}N HMBC of **5** in $[D_6]$DMSO, the ^{15}N NMR resonance corresponding to the "outer" NH_2 nitrogen (N^2H_2 in Figure 12) could be assigned. The ppm value was found to be comparable to the corresponding amino nitrogen in the minor species observed for **1b-Zn−NH$_2$**, yet another indication of the coordination of the amino group in the major species.
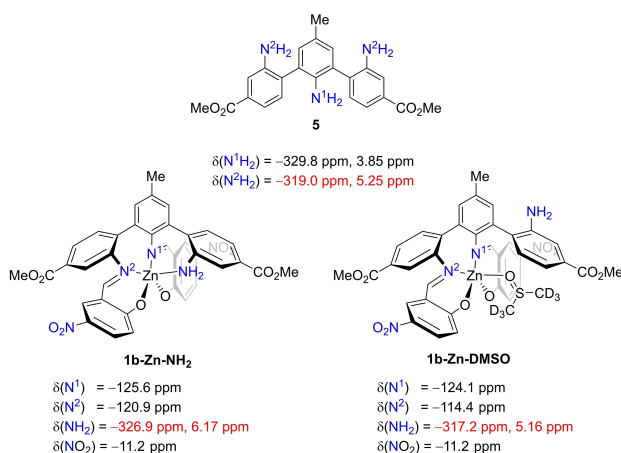
In the ^1H NMR spectrum of **1b-Zn−NH$_2$** in $CDCl_3$, only one species was observed (Figure 13). All the ^1H NMR resonances belonging to the NH_2-substituted ring in **1b-Zn−NH$_2$** were found at relatively high ppm values in $CDCl_3$ (δ 7.82, δ 7.70 and δ 7.51–7.53 for $H^{b''}$, $H^{a''}$ and $H^{c''}$ respectively), similar to what was observed for the major component in $[D_6]DMSO$. This indicates that the pentacoordinated complex might be intact in $CDCl_3$. The resonance corresponding to $H^{a'}$ of **1b-Zn−NH$_2$** in $CDCl_3$ was observed at δ 7.72, which is more upfield than what was reported for the corresponding ^1H NMR resonances of Zn Schiff base complexes derived from biphenyl-2,2′-diamines at approximately the same concentration (typically δ 7.80–7.85 at ca. $2.6 \cdot 10^{-3}$ M).[14] As the chemical shift of this specific resonance was found to be useful for the assignment of coordination numbers of these Zn complexes in $CDCl_3$, the more upfield ^1H NMR resonance of $H^{a'}$ in **1b-Zn−NH$_2$** indicates that Zn is not tetracoordinated, further strengthening the assumption that **1b-Zn−NH$_2$** remains pentacoordinated in $CDCl_3$. The differences observed in the ^1H NMR spectra of **1b-Zn−NH$_2$** as a function of the donating ability of the solvents used, are consistent with those observed for a Ru(II) complex bearing a 6,6′-diamino-2,2′-bipyridine ligand in the literature, where the amino groups were observed to dissociate in CD_3CN but remaining ligated in CD_2Cl_2.[35]

Figure 11. ^1H NMR (600 MHz, $[D_6]$DMSO) spectrum of **1b-Zn−NH$_2$** showing the aromatic region as well as NH_2 protons. Only the assignments that are discussed in the text are shown.

Figure 12. Overview of the ^{15}N NMR resonances found for **5**, **1b-Zn−NH$_2$** and **1b-Zn−DMSO** in $[D_6]$DMSO. Only the ^1H NMR and ^{15}N NMR resonances corresponding to the NH_2 group of the major rotamer of **5** is included.
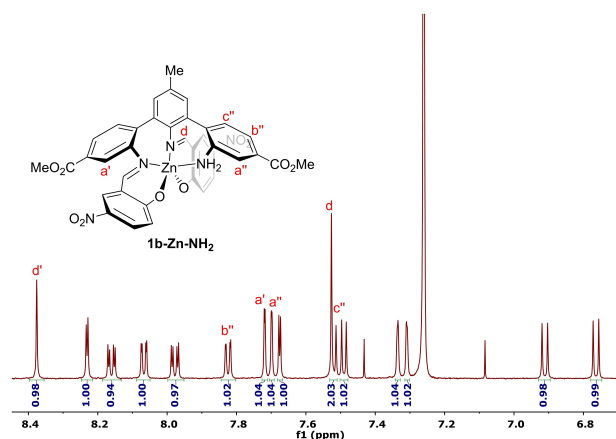
Figure 13. ^1H NMR (600 MHz, $CDCl_3$) spectrum of **1b-Zn−NH$_2$** ($2.6 \cdot 10^{-3}$ M) showing the aromatic region.

Synthesis and NMR studies of Cd complex 1b-Cd−NH₂

In light of the unexpected outcome of the reaction between **1b** and $Zn(OAc)_2 \cdot 2H_2O$, the reactivity of ligand **1b** towards Cd-$(OAc)_2 \cdot 2H_2O$ was investigated (Scheme 10).

The resulting Cd complex was investigated by NMR spectroscopy, in addition to single-crystal X-ray diffraction analysis (*vide infra*), and **1b-Cd−NH₂** was found to crystallize as a dimer, with hexacoordination around both Cd atoms. Analogously to the Zn complex, the ¹H NMR spectrum of **1b-Cd−NH₂** in [D₆]DMSO revealed a mixture of two interconvertible species. At ambient temperature, the ratio between these species was 2:1 in favor the NH₂-coordinated species for **1b-Cd−NH₂**, compared to 6:1 for the Zn complex. The resonance corresponding to the NH₂ protons of the major component showed subtle splitting that could indicate coordination to Cd (Figure 14).
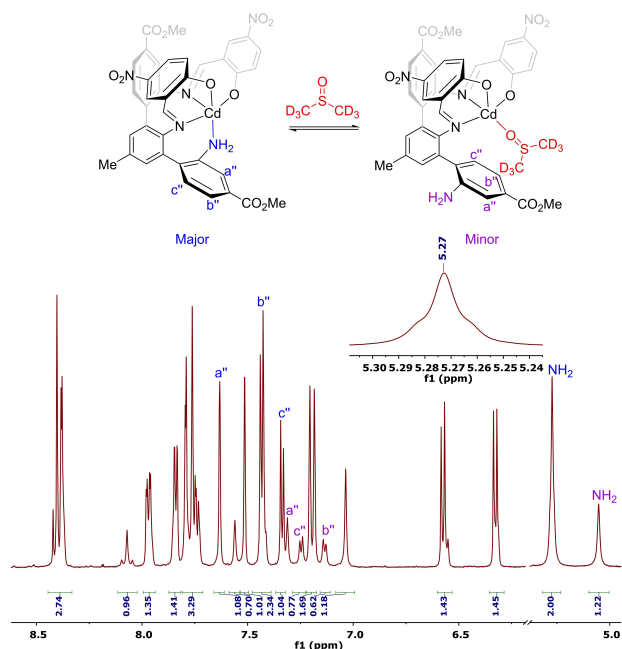
As for **1b-Zn−NH₂**, the largest differences in ppm values for the major and the minor component in [D₆]DMSO were found for the protons of the NH₂-substituted aromatic ring. However, the differences found for **1b-Cd−NH₂** were significantly smaller than what was found for **1b-Zn−NH₂**. For **1b-Cd−NH₂**, $\Delta\delta$ between the major and the minor species was 0.32, 0.29, 0.07 and 0.22 for H$^{a''}$, H$^{b''}$, H$^{c''}$ and NH₂ respectively, whereas $\Delta\delta$ was 0.68, 0.58, 0.66 and 1.01 for **1b-Zn−NH₂**. From these observations, the internal NH₂ coordination in **1b-Cd−NH₂** in [D₆]DMSO seems more labile than that in **1b-Zn−NH₂**, which was further supported by observations from ¹H-¹⁵N HMBC experiments. The ¹⁵N NMR resonances corresponding to the NH₂ nitrogen atoms of the two species were observed at δ −322.8 and δ −318.9 respectively, being closer to each other than what was found for **1b-Zn−NH₂** (Figure 15). This was further illustrated by relatively long Cd−NH₂ bonds in **1b-Cd−NH₂** (2.470(12) Å and 2.418(12) Å) found from the crystal structure determination of the complex (*vide infra*).

The increased lability of the NH₂-coordination in **1b-Cd−NH₂** compared to **1b-Zn−NH₂** was further supported by variable-temperature ¹H NMR experiments performed in [D₆]DMSO. The two NH₂-resonances in Figure 14 had coalesced at 77 °C for **1b-Cd−NH₂**, whereas two distinct resonances still could be observed for **1b-Zn−NH₂** at the same temperature. In addition, the Cd complex was found to undergo significant decomposition when exposed to elevated temperatures in [D₆] DMSO, while the Zn complex showed no signs of degradation. For more details, see Figure S146−S147 (**1b-Zn−NH₂**), and Figure S209−S210 (**1b-Cd−NH₂**), SI. Attempts of synthesizing a Hg(II) complex of ligand **1b** employing the conditions described for the synthesis of **1a-Zn−NH₂** and **1b-Cd−NH₂** did not yield a conclusive outcome.

Scheme 10. Synthesis of Cd complex **1b-Cd−NH₂**.

Figure 14. ¹H NMR (600 MHz, [D₆]DMSO) spectrum of **1b-Cd−NH₂** showing the aromatic region and the amino protons. Only the assignments of the protons discussed in the text are shown. The Cd complexes are depicted as pentacoordinated monomers for simplicity. The insert shows the subtle splitting of the resonance corresponding to the NH₂ protons of the major species.

Figure 15. Overview of the ¹⁵N NMR resonances found for **5**, **1b-Cd−NH₂** and **1b-Cd−DMSO** in [D₆]DMSO. The Cd complexes are depicted as pentacoordinated monomeric species for simplicity. Only the ¹H NMR and ¹⁵N NMR resonances corresponding to the NH₂ group of the major rotamer of **5** is included.

EurJIC
European Journal of Inorganic Chemistry

Full Papers
doi.org/10.1002/ejic.202100170

Chemistry Europe
European Chemical
Societies Publishing

Synthesis and characterization of Ni complex 9-Ni, and Cu complexes 1b-Cu–NH₂, 1a-Cu–NH₂ and 9-Cu.

Whereas Zn(II) and Cd(II) share many similarities in terms of coordination chemistry, Cd(II) is considerably larger than Zn(II). Cu(II) and Ni(II) on the other hand, both have a more similar ionic radius to Zn(II). To investigate Cu(II) and Ni(II) Schiff base
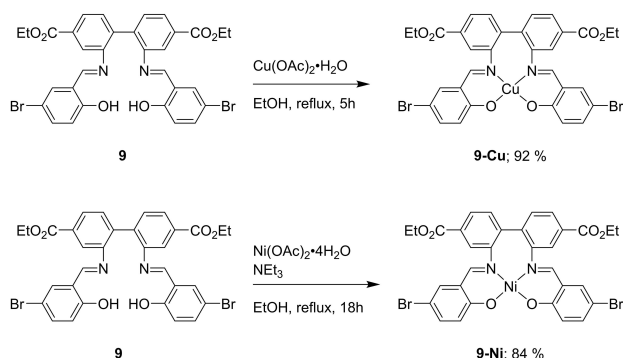
Scheme 11. Synthesis of **9-Cu** and **9-Ni**. The Ni(II) complex is depicted as tetracoordinated monomer for simplicity.
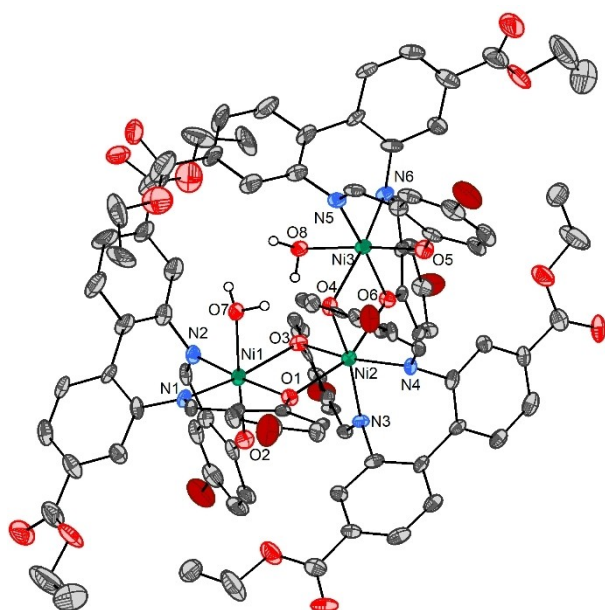
Figure 16. ORTEP plot of **9**–**Ni** with 50% probability ellipsoids. Hydrogen atoms (except those of the water ligands) and non-coordinated, disordered solvent molecules have been omitted for clarity. Selected bond lengths [Å] and angles [°]: Ni1–N1, 2.034(6); Ni1–N2, 2.011(6); Ni1–O1, 2.025(5); Ni1–O2, 1.995(5); Ni1–O3, 2.137(5); Ni1–O7, 2.169(5); Ni2–N3, Ni2–N4, 2.059(6); Ni2–O1, Ni2–O6, 2.144(5); Ni2–O3, Ni2–O4, 2.065(5); N1–Ni1–N2, 92.6(2); N1–Ni1–O1, 93.2(2); N1–Ni1–O2, 95.2(2); N1–Ni1–O3, 167.2(2); N1–Ni1–O7, 84.9(2); N2–Ni1–O1, 174.2(2); N2–Ni1–O2, 89.4(2); N2–Ni1–O3, 92.6(2); N2–Ni1–O7, 95.2(2); O1–Ni1–O2, 90.1(2); O1–Ni1–O3, 81.69(18); O1–Ni1–O7, 85.23(19); O2–Ni1–O3, 96.48(16); O2–Ni1–O7, 175.4(2); O3–Ni1–O7, 83.03(18); Ni1–O3–Ni2, 98.06(19); Ni1–O1–Ni2, 99.14(18); N3–Ni2–N4, 92.3(3); N3–Ni2–O1, N4–Ni2–O6, 82.9(5); N3–Ni2–O3, N4–Ni2–O4, 86.4(2); N3–Ni2–O4, N4–Ni2–O3, 166.3(2); N3–Ni2–O6, N4–Ni2–O1, 112.8(2); O1–Ni2–O3, O4–Ni2–O6, 80.62(18); O1–Ni2–O4, O3–Ni2–O6, 85.03(18); O1–Ni2–O6, 158.1(3); O3–Ni2–O4, 98.0(3).

complexes derived from biphenyl-2,2′-diamines, complexes **9-Cu** and **9-Ni** were prepared (Scheme 11).

The Ni(II) complex was analyzed by MS, elemental analysis and single-crystal X-ray diffraction, in addition to ^{1}H NMR studies in different solvents (CDCl₃, C₆D₆ and [D₆]DMSO). A paramagnetic species was consistently observed, with severe line-broadening of the resonances. Magnetic moment measurement of **9-Ni** in CDCl₃ at 25 °C using Evans method,[36] gave $\mu_B = 2.23$, which is lower than expected for Ni(II) with 2 unpaired electrons ($\mu_B = 2.9$–4.0).[37] This may be indicative of interconversion between different geometries in solution, which is occasionally reported for Ni Schiff base complexes in the literature.[36b,38] Recrystallization of **9-Ni** from benzene gave crystals suitable for single-crystal X-ray diffraction analysis. The complex crystallized as a trimer, with two unique Ni centers, both having distorted octahedral geometry (Figure 16).

For the middle Ni center in **9-Ni** (Ni2), one molecule of the Schiff base ligand was found to coordinate in a $N_2O_2{}^{2-}$ tetradentate fashion, whereas the two other Schiff base ligands in the structure contributed with one bridging oxygen ligand each (O1 and O6 respectively), resulting in the observed hexacoordination around Ni2. For the terminal Ni centers (Ni1 and Ni3), the coordination sphere around each Ni atom was made up from one Schiff base ligand acting as a $N_2O_2{}^{2-}$ tetradentate ligand. The two last coordination sites were occupied by a water ligand, and one bridging oxygen ligand from the Schiff base moiety binding the middle metal center, Ni2. For the two unique Ni centers in the crystal structure, Ni2 was observed to have a more distorted octahedral geometry than Ni1/Ni3.

The synthesis of Cu(II) complex **9-Cu** was carried out according to literature protocols.[38a] The complex was characterized by MS, elemental analysis, UV-Vis (*vide infra*) and single-crystal X-ray diffraction analysis. Single-crystal X-ray diffraction analysis revealed that the Cu complex crystallized as a tetracoordinated monomer even from a mixture of two strongly coordinating solvents, DMSO and MeCN (Figure 17).

For **9-Cu**, a distorted square planar geometry was observed ($\tau_4' = 0.43$). The bond lengths and angles between Cu and the donor atoms of the ligand were similar to those reported in the literature for related Cu(II) complexes.[38a,39] The observed tetracoordination around Cu in **9-Cu** is interesting as it indicates that pentacoordination is less favored for Cu(II) than for Zn(II) in complexes of Schiff base ligands derived from biphenyl- and terphenyl-2,2′-diamines; Zn complexes of this type of ligands readily form DMSO-ligated adducts when recrystallized from DMSO.[14,17] To further investigate these apparent differences between Cu(II) and Zn(II), the reactivity of ligand **1b** towards Cu(II) was studied, as this specific ligand facilitated the formation of a pentacoordinated complex for Zn(II). In addition, the combination of a redox active metal, e.g. Cu, and an amine in proximity can make a catalyst candidate in reactions where both electron and proton transfers are essential.[15b–c,40] The attempted synthesis of **1b-Cu–NH₂** was carried out according to the procedure for **1b-Zn–NH₂** and **1b-Cd–NH₂**. From MS analysis of the product from the reaction of **1b** with Cu-(OAc)₂·H₂O, *m/z* values corresponding to both **1b-Cu–NH₂** and
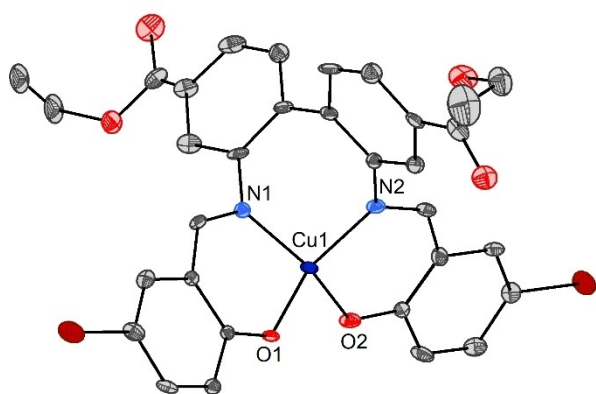
Figure 17. ORTEP plot of **9**−**Cu** with 50% probability ellipsoids. Only one of the two molecules of the asymmetric unit is displayed, but metric data for both are given below. Hydrogen atoms, non-coordinated MeCN (solvent of crystallization) and disorder in one of the ethoxycarbonyl substituents have been omitted for clarity. $\tau_4' = 0.43$, 0.43. Selected bond lengths [Å] and angles [°]: Cu1−N1, 1.952(6); Cu1−N2, 1.951(6); Cu1−O1, 1.896(5); Cu1−O2, 1.897(5); Cu2−N3, 1.955(5); Cu2−N4, 1.950(6); Cu2−O3, 1.886(5); Cu2−O4, 1.900(5); N1−Cu1−N2, 96.8(2); N1−Cu1−O1, 93.7(2); N1−Cu1−O2, 150.4(2); N2−Cu1−O1, 148.1(2); N2−Cu1−O2, 93.5(2); O1−Cu1−O2, 92.1(2); N3−Cu2−N4, 97.0(2); N3−Cu2−O3, 93.7(2); N3−Cu2−O4, 149.8(2); N4−Cu2−O3, 149.9(2); N4−Cu2−O4, 94.8(2); O3−Cu2−O4, 89.8(2).
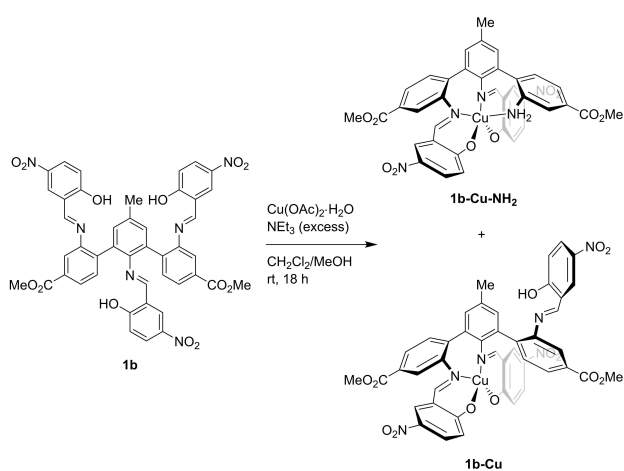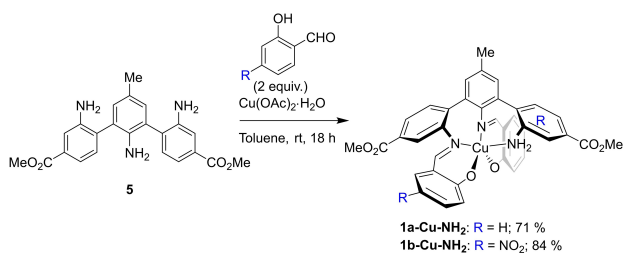
the complex **1b**-**Cu**, with a fully intact ligand, were observed (Scheme 12), indicating that the reactivity of ligand **1b** is highly metal-dependent, even for Cu(II) and Zn(II), which are similarly sized and Lewis acidic.

Whereas the method depicted in Scheme 12 proved unsuccessful for the selective synthesis of **1b**-**Cu**−**NH₂**, the compound as well as the related complex **1a**-**Cu**−**NH₂** could be synthesized directly from triamine **5**, 2 equivalents of the corresponding salicylaldehyde derivative and Cu(OAc)₂·H₂O (Scheme 13).

In addition to single-crystal X-ray diffraction analysis (*vide infra*), **1b**-**Cu**−**NH₂** and **1a**-**Cu**−**NH₂** were characterized by MS, UV/Vis and elemental analysis. The UV-Vis spectra of the two complexes, alongside the previously discussed complex **9**-**Cu** are shown in Figure 18.

The UV/Vis absorption spectra show defined bands at 365 nm, 399 nm and 410 nm for **1b**-**Cu**−**NH₂**, **1a**-**Cu**−**NH₂** and **9**-**Cu** respectively, which could be attributed to ligand-to-metal charge transfer from the phenoxide donors in the ligands to the Cu(II) center, based on observations in the literature concerning related complexes.[41] Of the three complexes, the absorption band of nitro-substituted **1b**-**Cu**−**NH₂** was slightly more blue-shifted and significantly more intense than the corresponding bands for **1a**-**Cu**−**NH₂** and **9**-**Cu**. Similar observations were made by Decinti and co-workers on comparison of a nitro-substituted chiral Cu salen complex with a non-substituted complex.[42] Very intense absorption bands were observed at λ < 300 nm for **1b**-**Cu**−**NH₂**, **1a**-**Cu**−**NH₂** and **9**-**Cu**, which may be attributed to π→π* transitions associated with the ligands. Low-intensity ligand field (d→d) transitions were observed between 651 nm and 687 nm for the three complexes, with the bands associated with **1b**-**Cu**−**NH₂** and **1a**-**Cu**−**NH₂** being more broadened than that of **9**-**Cu** (see insert in Figure 18).

Scheme 12. Attempted synthesis of **1b**-**Cu**−**NH₂**. A mixture of **1b**-**Cu**−**NH₂** and **1b**-**Cu** was obtained.

Scheme 13. Synthesis of **1a**-**Cu**−**NH₂** and **1b**-**Cu**−**NH₂** directly from triamine **5** using a one-pot procedure.
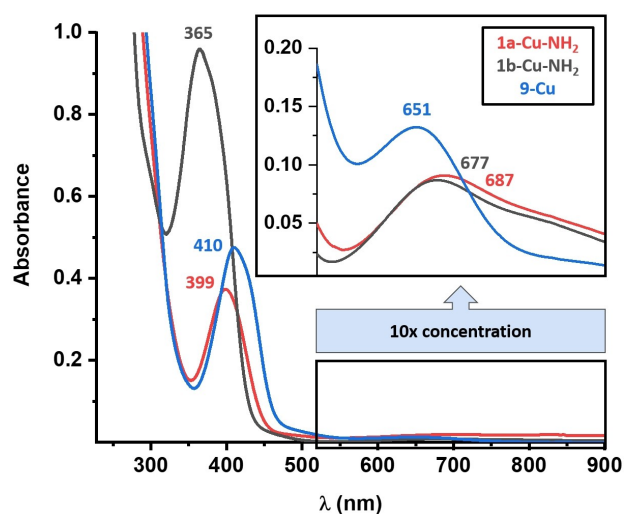
Figure 18. UV/Vis (CH₂Cl₂) spectra of Cu(II) complexes **1b**-**Cu**−**NH₂**, **1a**-**Cu**−**NH₂** and **9**−**Cu** at similar concentrations.

EurJIC
European Journal of Inorganic Chemistry

Full Papers
doi.org/10.1002/ejic.202100170

**Chemistry
Europe**
European Chemical
Societies Publishing

Crystallographic structure determination of 1b-Zn–NH₂, 1b-Cd–NH₂, 1b-Cu–NH₂, and 1a-Cu–NH₂

Complexes **1b-Zn−NH₂**, **1b-Cd−NH₂**, **1b-Cu−NH₂** and **1a-Cu−NH₂** were characterized by single-crystal X-ray diffraction analysis (Figure 19, Figure 20, Figure 21 and Figure 22).

All four complexes crystallized with the NH₂ group coordinating to the metal. Whereas the Zn complex and the two Cu complexes crystallized as pentacoordinated monomers, the Cd complex crystallized as a dimer with distorted octahedral geometries around both Cd atoms. The geometry found for **1b-Cu−NH₂** was distorted trigonal bipyramidal ($\tau_5 = 0.70$), while distorted square pyramidal geometries were found for both **1b-Zn−NH₂** ($\tau_5 = 0.33$) and **1a-Cu−NH₂** ($\tau_5 = 0.25$). The bond distance between Zn and the amino group in **1b-Zn−NH₂** is comparable to literature values for Zn–NH₂ bond distances.[43] In **1b-Cd−NH₂**, the bonds between the Cd atoms and the NH₂ groups (Cd1−N3 and Cd2−N6) are rather long (2.470(12) Å and 2.418(12) Å respectively), and significantly longer than the corresponding Zn−N bond in **1b-Zn−NH₂** (2.177(2) Å), as anticipated from the NMR comparisons of the two complexes (*vide supra*). Similarly, the Cd−μ-O bonds (Cd1−O4, 2.315(10) Å and Cd2−O2, 2.329(10) Å) are considerably longer than the corresponding Zn−O bonds in e.g. dimeric **1a-Zn** (2.1480(16) Å), and of similar length as Cd−μ-O bonds in multinuclear Cd Schiff base complexes reported in the literature.[10b,14,44] Although relatively rare, there are a few reported examples of coordination compounds of Cd where one of the ligands is an aromatic amine, and the observed Cd–NH₂ bond distances in **1b-Cd−NH₂** are in accordance with those reported in literature.[43a–b,45]

Figure 20. ORTEP plot of **1b-Cd−NH₂** with 50% probability ellipsoids. Hydrogen atoms (except for NH₂) and non-coordinated MeOH (solvent of crystallization) have been omitted for clarity. Selected bond lengths [Å] and angles [°]: Cd1−N1, 2.300(11); Cd1−N2, 2.363(13); Cd1−N3, 2.470(12); Cd1−O1, 2.249(11); Cd1−O2, 2.248(9); Cd1−O4, 2.315(10); Cd2−N4, 2.299(12); Cd2−N5, 2.358(12); Cd2−N6, 2.418(12); Cd2−O3, 2.329(10); Cd2−O3, 2.301(10); Cd2−O4, 2.273(9); N1−Cd1−N2, 81.0(4); N1−Cd1−N3, 80.7(4); N1−Cd1−O1, 78.9(4); N1−Cd1−O2; 157.0(4); N1−Cd1−O4, 126.3(4); N2−Cd1−N3, 118.1(4); N2−Cd1−O1, 86.0(4); N2−Cd1−O2, 81.1(4); N2−Cd1−O4, 149.9(4); N3−Cd1−O1, 145.2(4); N3−Cd1−O2, 95.3(4); N3−Cd1−O4, 82.3(4); O1−Cd1−O2, 114.0(4); O1−Cd1−O4, 87.5(4); O2−Cd1−O4, 74.9(3); N4−Cd2−N5, 80.0(4); N4−Cd2−N6, 79.1(4); N4−Cd2−O2, 130.5(4); N4−Cd2−O3, 78.0(4); N4−Cd2−O4, 153.0(4); N5−Cd2−N6, 120.8(4); N5−Cd2−O2, 146.5(4); N5−Cd2−O3, 87.7(4); N5−Cd2−O4, 80.0(4); N6−Cd2−O2, 83.3(4); N6−Cd2−O3, 139.2(4); N6−Cd2−O4, 95.9(4); O2−Cd2−O3, 86.4(4); O2−Cd2−O4, 74.2(3); O3−Cd2−O4, 118.9(3); Cd1−O2−Cd2, 105.6(4); Cd1−O4−Cd2, 105.3(4).

Figure 19. ORTEP plot of **1b-Zn−NH₂** with 50% probability ellipsoids. Hydrogen atoms (except for NH₂) and disorder in the one of the methoxycarbonyl substituents have been omitted for clarity. $\tau_5 = 0.33$. Selected bond lengths [Å] and angles [°]: Zn1−N1, 2.050(2); Zn1−N2, 2.205(2); Zn1−N3, 2.177(2); Zn1−O1, 1.9896(12); Zn1−O2, 1.9833(17); N1−Zn1−N2, 85.00(8); N1−Zn1−N3, 89.18(8); N1−Zn1−O1, 90.91(8); N1−Zn1−O2, 170.51(8); N2−Zn1−N3, 114.97(8); N2−Zn1−O1, 93.93(8); N2−Zn1−O2, 89.55(7); N3−Zn1−O1, 150.98(8); N3−Zn1−O2, 86.08(8); O1−Zn1−O2, 97.22(7).

Figure 21. ORTEP plot of **1b-Cu−NH₂** with 50% probability ellipsoids. Hydrogen atoms (except for NH₂) have been omitted for clarity. $\tau_5 = 0.70$. Selected bond lengths [Å] and angles [°]: Cu1−N1, 1.933(3); Cu1−N2, 2.041(3); Cu1−N3, 2.299(3); Cu1−O1, 1.986(2); Cu1−O2, 1.903(2); N1−Cu1−N2, 91.95(11); N1−Cu1−N3, 86.83(11); N1−Cu1−O1, 92.02(11); N1−Cu1−O2, 172.46(12); N2−Cu1−N3, 114.29(11); N2−Cu1−O1, 130.68(11); N2−Cu1−O2, 91.23(11); N3−Cu1−O1, 115.00(10); N3−Cu1−O2, 85.64(10); O1−Cu1−O2, 91.08(10).

EurJIC
European Journal of Inorganic Chemistry

Full Papers
doi.org/10.1002/ejic.202100170

**Chemistry
Europe**
European Chemical
Societies Publishing
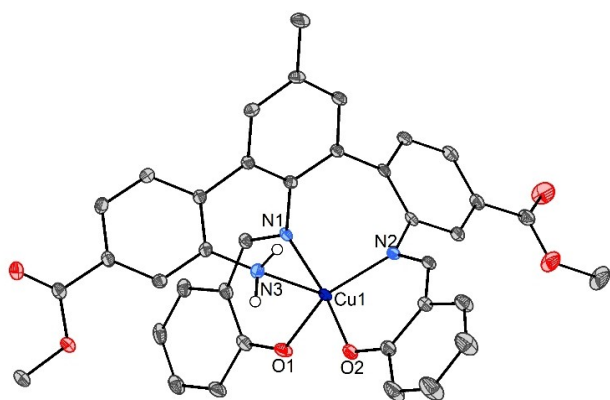
Figure 22. ORTEP plot of **1a-Cu−NH₂** with 50% probability ellipsoids. Hydrogen atoms (except for NH₂) and non-coordinated EtOH (solvent of crystallization) have been omitted for clarity. $\tau_5 = 0.25$. Selected bond lengths [Å] and angles [°]: Cu1−N1, 1.9618(15); Cu1−N2, 1.9818(14); Cu1−N3, 2.4795(15); Cu1−O1, 1.9154(13); Cu1−O2, 1.9205(13); N1−Cu1−N2, 94.41(6); N1−Cu1−N3, 77.57(6); N1−Cu1−O1, 94.51(6); N1−Cu1−O2, 165.87(6); N2−Cu1−N3, 112.16(6); N2−Cu1−O1, 150.95(6); N2−Cu1−O2, 91.85(6); N3−Cu1−O1, 96.75(6); N3−Cu1−O2, 88.34(6); O1−Cu1−O2, 86.03(6).

On comparison of **1b-Zn−NH₂** and **1b-Cu−NH₂**, a significantly longer metal-NH₂ bond was found for **1b-Cu−NH₂** (Cu1−N3, 2.299(3) Å) than for **1b-Zn−NH₂** (Zn1−N3, 2.177(2) Å). This may be attributed to weaker axial ligation for the d^9 Cu(II) center, compared to the d^{10} Zn(II) center.[46] This observation is consistent with literature reports, comparing Cu(II) complexes of pentadentate N_3O_2 ligands derived from bis(3-aminopopyl) amines and salicylaldehyde derivatives with their Zn(II) homologues.[41a,47] The elongated Cu−NH₂ bond found in **1b-Cu−NH₂** is also in agreement with general observations concerning the bond lengths in crystal structures of pentacoordinated Cu(II) complexes, where one of the Cu-ligand bonds often is significantly longer than the others.[48] Comparing the nitro-substituted complex **1b-Cu−NH₂** with its unsubstituted analog **1a-Cu−NH₂**, the large influence of the relatively peripheral nitro groups became evident. Nitro-substituted **1b-Cu−NH₂** crystallized with distorted trigonal bipyramidal geometry, while **1a-Cu−NH₂** crystallized with distorted square pyramidal geometry. The Cu−NH₂ bond was significantly longer for **1a-Cu−NH₂** (Cu1−N3, 2.4795(15) Å) than for **1b-Cu−NH₂** (Cu1−N3, 2.299(3) Å). Furthermore, the two other Cu−N bonds and the two Cu−O bonds were closer to each other in values for **1a-Cu−NH₂** than for **1b-Cu−NH₂**.

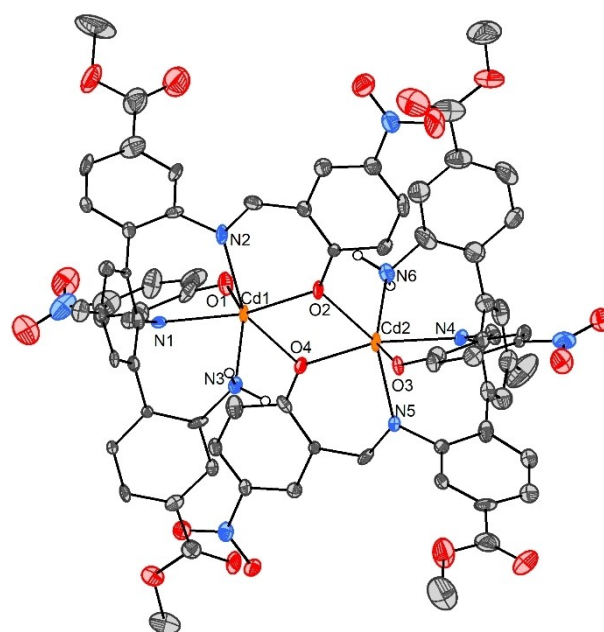imine nitrogen of the third salicylaldimine group could participate in coordination to the metal center, hence **1a** and **1d** would partially function as pentadentate $N_3O_2{}^{2-}$ ligands. To investigate whether e.g. **1d** could act as a hexadentate $N_3O_3{}^{3-}$ ligand, its reactivity towards Lu(III) was studied. The metal was chosen on basis of being trivalent and relatively large,[49] thus facilitating high coordination numbers as well as flexible coordination geometries,[50] which may be needed in order to accommodate ligand **1d**. In addition, Lu(III) possess the d^0 configuration, which renders the metal diamagnetic and suitable for conventional NMR studies, comparable to those of e.g. ligand **1d** and Zn complex **1d-Zn**. Reacting **1d** with Lu(NO₃)₃·xH₂O lead to the successful formation of complex **1d-Lu** (Scheme 14).

Complex **1d-Lu** was characterized by NMR, MS, elemental analysis and single-crystal X-ray diffraction analysis. Combined ¹H, ¹³C and ¹⁵N NMR studies in different solvents suggested that **1d** coordinated in a hexadentate fashion to Lu, acting as an $N_3O_3{}^{3-}$ ligand.[51] This was most evident in the ¹H NMR spectrum of the complex, as no resonances that could be attributed to naphtholic protons were observed. Furthermore, imine coordination to Lu was rationalized from ¹H-¹⁵N HMBC experiments, where small coordination shifts $(\Delta\delta(N^1) = 18.0$ ppm, and $\Delta\delta(N^2) = 2.8$ ppm, see Figure 27 for numbering scheme) were found for the imine nitrogen atoms in [D₆]DMSO. As opposed to what is commonly observed for coordination of metals to nitrogen atoms in ¹⁵N NMR, the resonances corresponding to imine nitrogen atoms of **1d-Lu** were moved to higher ppm values on comparison with those of **1d**, indicating a rather weak interaction.[27b] Crystals suitable for single-crystal X-ray diffraction analysis of the complex were obtained from a DMSO/EtOH mixture, and it was found that the complex crystallized as the heptacoordinated complex **1d-Lu−DMSO** (Figure 23). A related heptacoordinated complex **1d-Lu−MeOH** (Figure 24) was obtained from recrystallization of **1d-Lu** from a CDCl₃/MeOH mixture.

Both Lu complexes crystallized with geometries best described as intermediate between capped octahedral and pentagonal bipyramidal. The bond lengths between Lu and the heteroatoms within the hexadentate ligand were similar for both complexes, with Lu−N and Lu−O bond lengths in the range of 2.350(3)−2.472(3) Å and 2.178(3)−2.200(3) Å respectively for **1d-Lu−DMSO**, and 2.362(16)−2.486(16) Å and 2.146(15)−2.193(13) Å respectively for **1d-Lu−MeOH**. In addition, the bond lengths were similar to what has been reported

Exploring 1d as a hexadentate ligand: Synthesis, single-crystal X-ray diffraction analysis and NMR studies of 1d-Lu

From the studies of Co(III) complexes **1a-Co(acac)** and **1d-Co(acac)**, it was observed that in case of rather small Co(III), potentially hexadentate ligands **1a** and **1d** would act as tetradentate $N_2O_2{}^{2-}$ ligands, leaving the third salicylaldimine group uncoordinated. From the NMR studies of Zn complexes **1a-Zn** and **1d-Zn**, however, there were indications that the

Scheme 14. Synthesis of **1d-Lu**. The product is depicted as a hexacoordinated complex for simplicity, although the complex is probably heptacoordinated, bearing an additional water ligand.

EurJIC
European Journal of Inorganic Chemistry

Full Papers
doi.org/10.1002/ejic.202100170

Chemistry Europe
European Chemical Societies Publishing
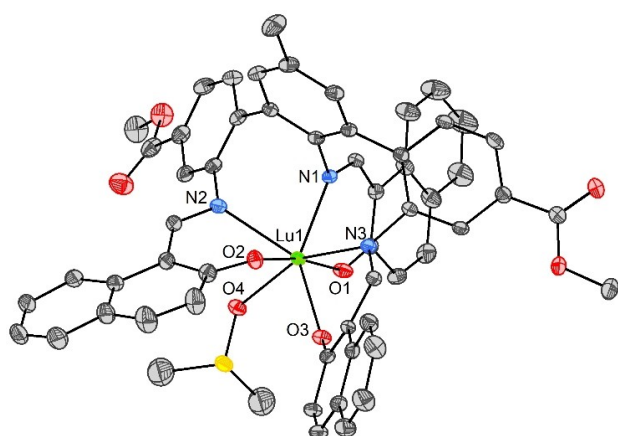
Figure 23. ORTEP plot of **1d-Lu−DMSO** with 50% probability ellipsoids. Hydrogen atoms and two non-coordinated molecules of DMSO (solvent of crystallization) have been omitted for clarity. Selected bond lengths [Å] and angles [°]: Lu1−N1, 2.350(3); Lu1−N2, 2.472(3); Lu1−N3, 2.445(3); Lu1−O1, 2.178(3); Lu1−O2, 2.200(3); Lu1−O3, 2.193(3); Lu1−O4, 2.268(3); N1−Lu1−N2, 76.50(10); N1−Lu1−N3, 78.42(10); N1−Lu1−O1, 73.61(10); N1−Lu1−O2, 114.68(10); N1−Lu1−O3, 143.30(10); N1−Lu1−O4, 127.83(10); N2−Lu1−N3, 128.00(10); N2−Lu1−O1, 115.15(10); N2−Lu1−O2, 71.61(10); N2−Lu1−O3, 140.17(10); N2−Lu1−O4, 71.33(10); N3−Lu1−O1, 100.00(10); N3−Lu1−O2, 78.91(10); N3−Lu1−O3, 74.90(10); N3−Lu1−O4, 153.02(10); O1−Lu1−O2, 170.95(10); O1−Lu1−O3, 86.65(10); O1−Lu1−O4, 84.24(10); O2−Lu1−O3, 84.39(10); O2−Lu1−O4, 92.74(10); O3−Lu1−O4, 78.80(10).
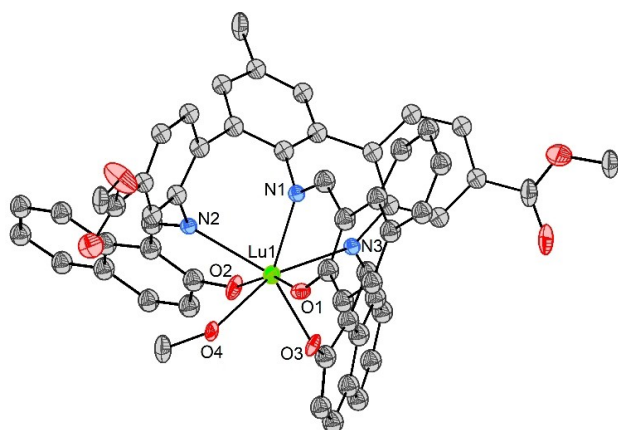
Figure 24. ORTEP plot of **1d-Lu−MeOH** with 50% probability ellipsoids. Hydrogen atoms have been omitted for clarity. The OH proton of the MeOH ligand could not be detected in the crystal structure. Selected bond lengths [Å] and angles [°]: Lu1−N1, 2.362(16); Lu1−N2, 2.477(17); Lu1−N3, 2.486(16); Lu1−O1, 2.165(14); Lu1−O2, 2.146(15); Lu1−O3, 2.193(13); Lu1−O4, 2.296(14); N1−Lu1−N2, 77.8(6); N1−Lu1−N3, 72.1(5); N1−Lu1−O1, 74.7(5); N1−Lu1−O2, 126.0(6); N1−Lu1−O3, 135.0(6); N1−Lu1−O4, 126.7(6); N2−Lu1−N3, 124.5(5); N2−Lu1−O1, 113.7(5); N2−Lu1−O2, 71.6(5); N2−Lu1−O3, 146.5(5); N2−Lu1−O4, 75.1(5); N3−Lu1−O1, 101.8(5); N3−Lu1−O2, 90.1(6); N3−Lu1−O3, 72.3(5); N3−Lu1−O4, 157.8(5); O1−Lu1−O2, 158.9(5); O1−Lu1−O3, 86.7(5); O1−Lu1−O4, 75.7(5); O2−Lu1−O3, 80.4(5); O2−Lu1−O4, 86.7(6); O3−Lu1−O4, 85.5(5).

in the literature for Lu−N and Lu−O bond lengths in Schiff base complexes of heptacoordinated Lu.[10g,52] The Lu−O(solvent) bond distances are in accordance with literature values for Lu−O(DMSO) and Lu−O(MeOH) bond lengths.[53]

The ^{1}H NMR spectrum of **1d-Lu** was found to be highly solvent-dependent. At ambient temperature in [D$_6$]DMSO and [D$_7$]DMF, the ^{1}H NMR resonances of each of the two methoxycarbonyl-substituted moieties in the complex were time-averaged (ring systems A′ in Figure 25), and the resonances of ring systems A′ and A integrated in a 2:1 ratio. Several of the ^{1}H and ^{13}C NMR resonances were broadened in [D$_6$]DMSO at ambient temperature, most notably the resonance corresponding to H$^{e′}$ (Figure 25). A gradual sharpening of the broadened resonances in the ^{1}H NMR spectrum of **1d-Lu** was observed on elevated temperatures in [D$_6$]DMSO (Figure 25).

The very broadened nature of the resonance corresponding to H$^{e′}$ at ambient temperature indicated dynamic behavior of the complex in [D$_6$]DMSO. For low-temperature ^{1}H NMR studies, [D$_7$]DMF was used, in which the complex had a similar ^{1}H NMR spectrum to that in [D$_6$]DMSO at ambient temperature. The ^{1}H NMR spectra of **1d-Lu** in the temperature range between 27 °C and −53 °C are shown in Figure 26.

On decreasing the temperature, the resonance corresponding to H$^{e′}$ gradually decoalesced into two new resonances (H$^{e′1}$ and H$^{e′2}$) (see Figure 26). Notably, a relatively large separation in chemical shifts for the resonances corresponding to H$^{e′1}$ and H$^{e′2}$ (δ 5.26 and δ 6.89) was observed, indicating that one of the methoxycarbonyl-substituted ring systems (A′ in Figure 26) must be significantly more shielded than the other. Because of the dynamic behavior of **1d-Lu** in [D$_6$]DMSO and [D$_7$]DMF, attention was turned to the coordination number of the complex in solution. Whereas ligand **1d** itself is hexadentate, Lu complexes usually possess coordination numbers of seven, eight or nine.[50,54] As both [D$_6$]DMSO and [D$_7$]DMF are strongly coordinating solvents, it is reasonable to assume that at least one solvent molecule is ligated to the Lu center in both solvents, as it is commonly seen in the coordination chemistry of rare earth metals.[55] In addition, solvent-ligation was already
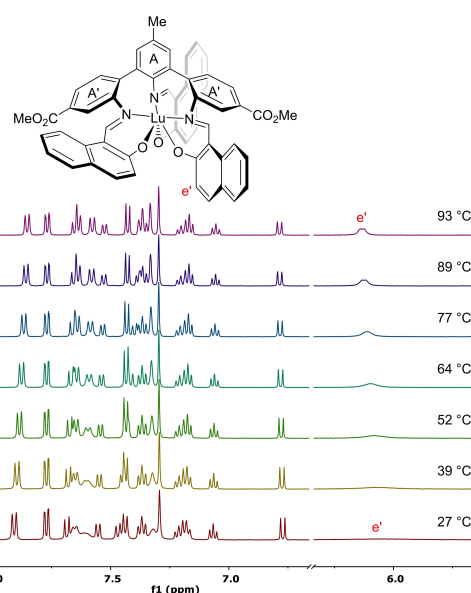
Figure 25. ^{1}H NMR of **1d-Lu** (500 MHz, [D$_6$]DMSO) at increasing temperatures (bottom to top). Only selected regions of the ^{1}H NMR spectra are shown.

EurJIC
European Journal of Inorganic Chemistry

Full Papers
doi.org/10.1002/ejic.202100170

**Chemistry
Europe**
European Chemical
Societies Publishing
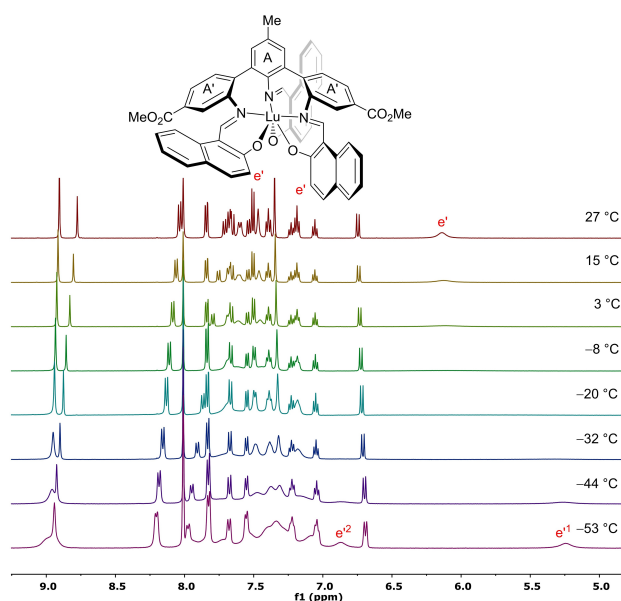
Figure 26. ^{1}H NMR of **1d-Lu** (500 MHz, [D$_7$]DMF) at increasing temperatures (bottom to top). Only the region between δ 5.0 and 9.25 is shown.

Scheme 15. Synthesis of **1b-Lu**. The product is depicted as a hexacoordinated complex for simplicity.

Scheme 16. Reactivity of ligand **1d** towards La(NO$_3$)$_3$·6H$_2$O and Y-(NO$_3$)$_3$·6H$_2$O.

observed from the crystallographic characterization of **1d-Lu−DMSO** and **1d-Lu−MeOH** (*vide supra*). Hepta-, octa- and nonacoordinated metal complexes are known to be stereochemically non-rigid,[56] which rationalize the dynamic behavior of **1d-Lu** in [D$_6$]DMSO and [D$_7$]DMF.[57] The combined structural and NMR-based investigations suggest that **1d-Lu** contains (at least) one labile monodentate ligand, which in combination with the high relative Lewis acidity of Lu(III),[58] makes it an interesting candidate for various applications, e.g. as a polymerization catalyst.[59] As **1d** acts a hexadentate $N_3O_3^{3-}$ ligand, the formation of monomeric complexes of Lu(III), as well as other rare earth metals (*vide infra*), should be favored compared to tetradentate $N_2O_2^{2-}$ salen-type ligands,[60] which occasionally give rise to dimeric complexes with rare earth metals,[59c] or homoleptic ML$_2$- or M$_2$L$_3$-type complexes.[10h,s,59b] However, it should be noted that dimer formation for rare earth metal complexes of e.g. heptadentate Schiff base ligands has been reported in the literature.[61]

As the nitro-substituted ligand **1b** was found to react in a different manner with Zn(OAc)$_2$·2H$_2$O than e.g. **1d**, the reactivity of **1b** towards Lu(NO$_3$)$_3$·xH$_2$O was studied. Although a pure product could not be obtained, the ^{1}H NMR spectrum of the obtained product indicates that the ligand acts as an $N_3O_3^{3-}$ ligand towards Lu(III) (Scheme 15). This result shows again that the reactivity of ligand **1b** is highly metal-dependent, as already observed for Cu(II), Zn(II) and Cd(II).

A preliminary investigation of the reactivity of ligand **1d** towards larger rare-earth metals (Y(III) and La(III)) (Scheme 16) did not yield any fully conclusive results.

Complex **1d-Y** was obtained in good yields, and was characterized by NMR, as well as elemental analysis of its DMSO-ligated adduct **1d-Y−DMSO**. The complex was found to undergo demetallation during MS measurements, and attempts
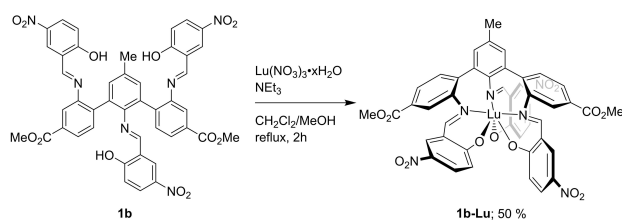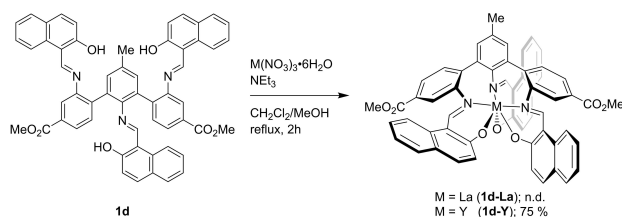
to obtain crystals for single-crystal X-ray diffraction analysis lead to crystal formation of the demetallated species, **1d** (which accordingly *could* be characterized by single-crystal X-ray diffraction analysis, *vide supra*). The ^{1}H NMR spectra of **1d-Y** in [D$_6$]DMSO and CDCl$_3$ were very similar to those of **1d-Lu**. Hence they will not be discussed in detail, but it should be noted that the ^{1}H NMR and ^{13}C NMR resonances of the Y(III) complex were less broadened than those of the Lu(III) complex in [D$_6$]DMSO at ambient temperature, while the opposite was observed in CDCl$_3$ (see Figure S256–S258, SI). The attempted synthesis of **1d-La** did not yield a clear outcome, and a complex mixture of different species was obtained instead (see Figure S259, SI). The unsuccessful attempt of synthesizing **1d-La** might be attributed to the considerably larger size of La(III) compared to Y(III) and Lu(III),[49] and issues concerning the successful coordination of early lanthanoids, the middle lanthanoids (having similar ionic radii as Y(III)) and the late lanthanoids to the same ligand system are occasionally reported in the literature.[62] The use of more reactive starting materials (e.g. the corresponding rare-earth bis(trimethylsilyl)amide compounds[63]) would perhaps lead to the successful synthesis of complexes of **1d** with the early lanthanoids, and this topic deserves further investigations.

Conclusion

Herein, the reactivity of new polydentate Schiff base ligands towards different metals was presented. For the reactions of Zn(OAc)$_2$·2H$_2$O and Schiff bases derived from a substituted 2,6,2′-triaminobiphenyl or a linear 2,2′,2″-triamino-*p*-terphenyl, the obtained complexes were similar to those Zn complexes that are commonly obtained from Schiff bases derived from 2,2′-diaminobiphenyl. For the reactions of Zn(OAc)$_2$·2H$_2$O and the hexadentate Schiff bases derived from a substituted 2,2′,2″-

EurJIC
European Journal of Inorganic Chemistry

Full Papers
doi.org/10.1002/ejic.202100170

Chemistry Europe
European Chemical
Societies Publishing

triamino-*m*-terphenyl and either salicylaldehyde or 2-hydroxy-1-naphthaldehyde, the obtained complexes were found to exist as either tetracoordinated monomeric complexes, or pentacoordinated monomeric or dimeric/oligomeric species in solution, as observed by NMR spectroscopy. For a related hexadentate ligand obtained from the condensation of the same 2,2′,2″-triamino-*m*-terphenyl and 5-nitrosalicylaldehyde, a pentadentate, NH_2-containing ligand was formed upon reaction with $Zn(OAc)_2 \cdot 2H_2O$ and $Cd(OAc)_2 \cdot 2H_2O$, and complexes containing a labile metal-NH_2 bond were isolated as the sole products. When the same reaction was carried out using $Cu(OAc)_2 \cdot H_2O$, a mixture of different products were obtained instead, most notably an NH_2-containing pentacoordinated complex as well as a tetracoordinated complex, analogous to those that were obtained for Zn using ligands derived from less electron poor salicylaldehydes. The pentacoordinated complex could be synthesized selectively by reacting the 2,2′,2″-triamino-*m*-terphenyl with 2 equivalents of 5-nitrosalicylaldehyde in the presence of $Cu(OAc)_2 \cdot H_2O$. The method was successfully extended to salicylaldehyde, yielding another pentacoordinated Cu complex. Finally, one of the *m*-terphenyl ligands that acted as tetradentate/pentadentate ligand towards divalent and relatively small Zn(II), was found to act as a hexadentate ligand towards larger and trivalent Lu(III) and Y(III). The results presented herein highlight the versatility of the triamine-*m*-terphenyl backbone and its Schiff base ligands, creating metal complexes with easily tunable properties. Further studies should focus on the application of the complexes in various catalytic settings, as well as broadening the scope of the synthesis of rare earth metal complexes.

Experimental Section

Triamines 5–7,[17] and Schiff base ligands 8–9[14] were synthesized as described elsewhere. THF (unstabilized), MeCN and CH_2Cl_2 were dried using an MB SPS-800 solvent purifier system from MBraun. Toluene was dried using 3 Å molecular sieves. Hexanes and ethyl acetate were distilled before use. Other chemicals and solvents were used as received from commercial sources. TLC was performed using Merck 60 F254 plates. Flash chromatography was performed using silica gel from Merck (60, 0.040–0.063 mm). NMR spectroscopy was performed using Bruker Avance DPX300, AVII400, AVIIIHD400, DRX500, AVI600, AVII600 or AVIIHD800 operating at 300 MHz (^{1}H NMR), or 400 MHz (^{1}H NMR), 376 MHz (^{19}F NMR), 101 MHz (^{13}C NMR), or 500 MHz (^{1}H NMR), or 600 MHz (^{1}H NMR) and 151 MHz (^{13}C NMR), or 800 MHz (^{1}H NMR) and 201 MHz (^{13}C NMR) respectively. All spectra were recorded at room temperature unless otherwise mentioned. The temperature of the variable temperature NMR experiments was measured indirectly by correlation of the observed probe temperature to independently measured temperatures (or extrapolated temperatures for the temperatures above the boiling point of methanol) using a Delta OHM HD9214 thermometer fitted into a NMR tube containing CD_3OD/CH_3OH. Because of this, small deviations in the exact temperature cannot be excluded. ^{1}H NMR and ^{13}C NMR spectra have been referenced relative to the residual solvent signals, and the peaks are numbered according to Figure 27. Chemical shifts in ^{19}F NMR have been referenced to $CFCl_3$ by using C_6F_6 (−164.9 ppm with respect to $CFCl_3$ at 0 ppm) as an internal standard, and are proton decoupled. Chemical shifts in ^{15}N NMR have been calibrated against CH_3NO_2 as
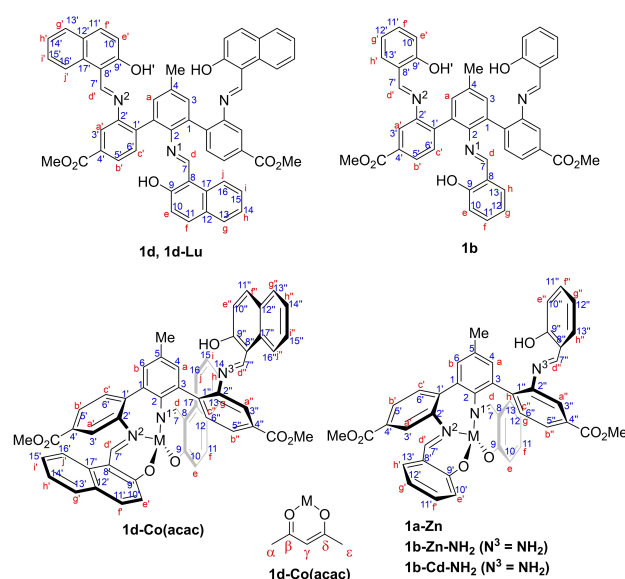
Figure 27. Numbering scheme used for reporting the NMR data. Roman letters = protons, numbers = carbons. Greek letters = protons and carbons. For **1b-Zn−NH₂** and **1b-Cd−NH₂**, imine nitrogen N^3 is not present, instead an NH_2 group is present. For complex **1b-Cd**, the imine nitrogen N^3 is present, although this species was only observed in MS.

an external standard (0.0 ppm). All ^{15}N NMR chemical shifts were obtained and assigned using ^{1}H–^{15}N HMBC experiments. The peaks in the ^{1}H NMR and ^{13}C NMR spectra were assigned using various 2D experiments (NOESY, COSY, TOCSY, HSQC, HMBC and HETCOR). MS (ESI) was recorded on a Bruker maXis II ETD spectrometer. All melting points are uncorrected and were obtained with a Stuart SMP10 melting point apparatus. UV/Vis measurements were performed on a Specord 200 Plus instrument. Elemental analysis was performed by Mikroanalytisches Laboratorium Kolbe, Oberhausen, Germany. Single-crystal diffraction data were acquired on a Bruker D8 Venture equipped with a Photon 100 CMOS area detector, and using Mo Kα radiation (λ = 0.71073 Å) from an Incoatec iμS microsource. Data reduction was performed with the Bruker Apex3 Suite, the structures were solved with ShelXT[64] and refined with ShelXL.[65] Olex2 was used as user interface.[66] The cif files were edited with enCIFer v. 1.4.[67] Disordered solvent molecules in the structures of **1a-Zn**, **1b-Zn−NH₂**, **1b-Cu−NH₂** and **1d-Lu−MeOH** were removed using the SQUEEZE algorithm.[68] Molecular graphics were produced with Diamond v. 4.6.2. Full details of the data collection, structure solution and refinement for each compound are contained in the cif files. The data are summarized in Table S1–Table S15, SI.

Experimental and analytical data for a selection of compounds described within the text are presented here, data for all compounds can be found in the SI.

1b. A suspension of triamine 5 (0.408 g, 1.01 mmol, 1.0 equiv.), 5-nitrosalicylaldehyde (0.555 g, 3.31 mmol, 3.3 equiv.) and HCO_2H (10 drops) in EtOH (10 mL) was heated at reflux temperature for 3 days. After cooling to rt, the precipitated solids were filtered off, and washed with EtOH. **1b** was obtained as orange crystals after recrystallization from MeCN. Yield: 0.656 g, 0.770 mmol, 76%. M.p. 170–172 °C; ^{1}H NMR (800 MHz, $CDCl_3$, major rotamer): δ = 13.30 (s, 2H, OH′), 12.78 (s, 1H, OH), 8.53 (s, 2H, H^d), 8.25 (d, $^3J_{H,H}$ = 9.1 Hz, 2H, H$^{f'}$), 8.19 (s, 2H, H$^{h'}$), 8.11 (d, $^3J_{H,H}$ = 7.8 Hz, 2H, H$^{b'}$), 8.04 (m, 1H, H^f), 7.88 (s, 2H, H^a), 7.71–7.72 (m, 3H, H^d + H^c), 7.40 (s, 1H, H^h), 7.27 (s, 2H, H^a), 7.03 (d, $^3J_{H,H}$ = 9.1 Hz, 2H, H^e), 6.71 (d, $^3J_{H,H}$ = 9.1 Hz, 1H, H^e),

EurJIC
European Journal of Inorganic Chemistry

Full Papers
doi.org/10.1002/ejic.202100170

Chemistry Europe
European Chemical Societies Publishing

3.95 (s, 6H, CO$_2$CH_3), 2.49 ppm (s, 3H, Ar—CH_3); ^{13}C NMR (201 MHz, CDCl$_3$, major rotamer): δ = 165.9 (C^9), 165.8 (CO$_2$CH$_3$), 165.6 (C^9), 164.6 (C^7), 161.3 (C^7), 144.8 (C^2), 141.9 (C^2), 140.2 (C^{12}), 139.8 (C^{12}), 139.4 (C^1), 137.3 (C^4), 131.9 (C^3), 131.5 (C^6), 131.4 (C^1), 131.2 (C^4), 129.2 (C^5), 128.8 (C^{11}), 128.6 (C^{11}), 128.5 (C^{13}), 127.6 (C^{13}), 118.8 (C^3), 118.1 (C^{10} + C^{10}), 118.0 (C^8), 117.1 (C^8), 52.5 (CO$_2$CH$_3$), 21.1 ppm (Ar—CH$_3$); ^{15}N{^{1}H} NMR (600 MHz, CDCl$_3$): δ = −13.2 (NO$_2$), −85.6 ppm (CH=N^1 + CH=N^2); LRMS (ESI): m/z (%): 875.191 (100) [M + Na]$^+$; HRMS (ESI): m/z calcd for C$_{44}$H$_{32}$N$_6$O$_{13}$ + Na: 875.1920 [M + Na]$^+$; found: 875.1921; elemental analysis calcd (%) for C$_{44}$H$_{32}$N$_6$O$_{13}$: C 61.97, H 3.78, N 9.86; found: C 62.02, H 3.76, N 9.83.

For ^{1}H NMR and ^{13}C NMR data of the minor rotamer of **1b** in CDCl$_3$, see SI. Additional NMR data in C$_6$D$_6$ are also presented in the SI.

1d. A suspension of triamine **5** (0.412 g, 1.02 mmol, 1.0 equiv.), 2-hydroxy-1-naphthaldehyde (0.582 g, 3.38 mmol, 3.3 equiv.) and HCO$_2$H (10 drops) in EtOH (10 mL) was heated at reflux temperature for 2 days. After cooling to rt, the precipitated solids were filtered off, and washed with EtOH. **1d** was obtained as golden yellow crystals after recrystallization from 10% benzene in MeCN. Yield: 0.708 g, 0.815 mmol, 80%. M.p. 266–267 °C; ^{1}H NMR (600 MHz, [D$_6$]DMSO, major rotamer): δ = 14.73 (s, 2H, OH'), 13.63 (s, 1H, OH), 9.28 (s, 2H, H^d'), 8.50 (s, 1H, H^d), 8.08–8.13 (m, 4H, H^a' + H^j), 7.97 (d, $^3J_{H,H}$ = 7.9 Hz, 2H, H^b'), 7.86 (d, $^3J_{H,H}$ = 9.1 Hz, 2H, H^f), 7.80 (d, $^3J_{H,H}$ = 7.9 Hz, 2H, H^c), 7.68 (d, $^3J_{H,H}$ = 7.9 Hz, 2H, H^g), 7.57 (d, $^3J_{H,H}$ = 9.0 Hz, 1H, H^f), 7.45 (d, $^3J_{H,H}$ = 8.0 Hz, 1H, H^g), 7.39 (s, 2H, H^a), 7.30–7.33 (m, 2H, H^i'), 7.23–7.26 (m, 2H, H^h'), 6.98–7.02 (m, 3H, H^h + H^e'), 6.82–6.84 (m, 1H, H^i), 6.59 (d, $^3J_{H,H}$ = 8.5 Hz, 1H, H^j), 6.55 (d, $^3J_{H,H}$ = 9.0 Hz, 1H, H^e), 3.83 (s, 6H, CO$_2$CH_3), 2.48 ppm (s, 3H, Ar—CH_3); ^{13}C NMR (151 MHz, [D$_6$]DMSO, major rotamer): δ = 167.2 (C^9), 165.7 (CO$_2$CH$_3$), 163.1 (C^9), 161.5 (C^7), 157.6 (C^7), 144.1 (C^2), 142.8 (C^2), 138.3 (C^1), 136.5 (C^{11}), 135.7 (C^4), 135.2 (C^{11}), 132.6 (C^{17}), 131.6 (C^{17}), 131.5 (C^6), 131.3 (C^3), 131.2 (C^1), 130.5 (C^4), 128.7 (C^{13}), 128.5 (C^{13}), 127.7 (C^{15}), 127.2 (C^{15}), 126.9 (C^5), 126.8 (C^{12}), 126.6 (C^{12}), 123.4 (C^{14}), 123.0 (C^{14}), 120.7 (C^{10}), 120.4 (C^{16}), 119.2 (C^{10}), 119.1 (C^3), 117.8 (C^{16}), 109.1 (C^8), 107.8 (C^8), 52.3 (CO$_2$CH$_3$), 20.5 ppm (Ar—CH$_3$); ^{15}N{^{1}H} NMR (600 MHz, [D$_6$]DMSO): δ = −115.0 ppm (CH=N^2), −136.0 ppm (CH=N^1); LRMS (ESI): m/z (%): 890.284 (100) [M + Na]$^+$; HRMS (ESI): m/z calcd for C$_{56}$H$_{41}$N$_3$O$_7$ + Na: 890.2837 [M + Na]$^+$; found: 890.2841; elemental analysis calcd (%) for C$_{56}$H$_{41}$N$_3$O$_7$: C 77.49, H 4.76, N 4.84; found: C 77.48, H 4.76, N 4.83.

For ^{1}H NMR and ^{13}C NMR data of the minor rotamer of **1d** in [D$_6$]DMSO, see SI. Additional NMR data in different solvents and at different temperatures are also presented in the SI. Crystals of **1d** suitable for single-crystal X-ray diffraction analysis were obtained from vapor diffusion of EtOH into a DMSO solution of the Y complex **1d-Y**. Crystal and refinement data are given in Table S1, SI.

1a-Zn. Ligand **1a** (0.356 g, 0.495 mmol, 1.0 equiv.) was dissolved in CH$_2$Cl$_2$ (2 mL). NEt$_3$ (0.35 mL, 2.5 mmol, 5.0 equiv.) was added, followed by a solution of Zn(OAc)$_2$·2H$_2$O (0.113 g, 0.513 mmol, 1.0 equiv.) in MeOH (10 mL). A solid started to precipitate within few minutes, and the resulting pale yellow suspension was stirred at rt for 18 h. The solids were then filtered off and washed with MeOH. **1a-Zn** was obtained as pale yellow crystals after recrystallization from MeCN. Yield: 0.277 g, 0.355 mmol, 72%. M.p. 213–215 °C; ^{1}H NMR (600 MHz, [D$_6$]DMSO): δ = 12.38 (s, 1H, OH), 9.00 (s, 1H, H^d''), 8.18 (s, 1H, H^d'), 7.93 (s, 1H, H^a''), 7.89 (dd, $^3J_{H,H}$ = 8.0 Hz, $^4J_{H,H}$ = 1.7 Hz, 1H, H^b'), 7.73 (s, 1H, H^h''), 7.71 (dd, $^3J_{H,H}$ = 8.0 Hz, $^4J_{H,H}$ = 1.6 Hz, 1H, H^b''), 7.63 (s, H^d), 7.59–7.60 (m, 2H, H^a' + H^c'), 7.51 (d, $^3J_{H,H}$ = 7.5 Hz, 1H, H^c''), 7.41 (s, 1H, H^f'), 7.21–7.24 (m, 2H, H^f + H^h'), 7.19 (s, 1H, H^a), 7.12 (s, 1H, H^b), 7.05 (ddd, $^3J_{H,H}$ = 8.5 Hz, $^3J_{H,H}$ = 6.8 Hz, $^4J_{H,H}$ = 1.6 Hz, 1H, H^f), 6.98 (s, 1H, H^g''), 6.93 (s, 1H, H^e''), 6.78 (d, $^3J_{H,H}$ = 6.8 Hz, 1H, H^e'), 6.54 (s, 1H, H^h), 6.44–6.46 (m, 2H, H^e + H^g), 6.20 (s, 1H, H^g), 3.86 (s, 3H, CO$_2$CH_3'), 3.84 (s, 3H, CO$_2$CH''$_3$), 2.30 ppm (s, 3H, Ar—CH_3); ^{13}C NMR (201 MHz, [D$_6$]DMSO): δ = 173.0 (C^7), 171.3 (C^9),

171.1 (C^9), 168.4 (C^7), 165.6 (C'O$_2$CH$_3$), 165.5 (C''O$_2$CH$_3$), 164.3 (C^7''), 160.1 (C^9''), 148.1 (C^2), 147.2 (C^2''), 144.1 (C^2), 138.7 (C^1''), 137.7 (C^1'), 136.2 (C^{13}), 135.5 (C^{13}), 135.1 (C^5), 134.8 (C^{11}), 134.6 (C^{11}), 133.6 (C^{11}''), 133.0 (C^{13}''), 132.7 (C^1 or C^3), 132.3 (C^4 + C^1 or C^3), 132.0 (C^6''), 131.0 (C^6), 130.6 (C^6''), 129.9 (C^4''), 129.7 (C^4''), 126.8 (C^5''), 126.6 (C^5), 123.2 (C^3), 122.8 (C^{10}), 122.2 (C^{10}), 119.4 (C^8''), 119.1 (C^8' + C^{12}''), 118.9 (C^3''), 117.8 (C^8), 116.5 (C^{10}''), 113.1 C^{12}), 112.9 (C^{12}), 52.2 (CO$_2$C'H$_3$ or CO$_2$C''H$_3$), 52.1 (CO$_2$C'H$_3$ or CO$_2$C''H$_3$), 20.2 ppm (Ar—CH$_3$). Several of the ^{1}H and ^{13}C NMR resonances were broadened. ^{15}N{^{1}H} NMR (600 MHz, [D$_6$]DMSO): δ = −89.0 (CH=N^3), −123.4 (CH=N^2–Zn), −131.8 ppm (CH=N^1–Zn); LRMS (ESI): m/z (%): 802.150 (100) [M + Na]$^+$; HRMS (ESI): m/z calcd for C$_{44}$H$_{33}$N$_3$O$_7$Zn + Na: 802.1502 [M + Na]$^+$; found: 802.1501; elemental analysis calcd (%) for C$_{44}$H$_{33}$N$_3$O$_7$Zn: C 67.66, H 4.26, N 5.38, Zn 8.37; found: C 67.48, H 4.24, N 5.35, Zn 8.32.

For additional NMR data for **1a-Zn** in different solvents and at different temperatures, see SI. Crystals of **1a-Zn** suitable for single-crystal X-ray diffraction analysis were obtained by slow evaporation of a solution of the complex in THF. Crystal and refinement data are given in Table S2, SI.

1b-Zn−NH$_2$. Ligand **1b** (0.434 g, 0.508 mmol, 1.0 equiv.) was dissolved in CH$_2$Cl$_2$ (10 mL). NEt$_3$ (0.35 mL, 2.5 mmol, 4.9 equiv.) was added, and the originally yellow solution quickly turned red-brown. A solution of Zn(OAc)$_2$·2H$_2$O (0.114 g, 0.522 mmol, 1.0 equiv.) in MeOH (10 mL) was then added, and a pale yellow precipitate formed within 30 min of stirring at rt. The resulting suspension was stirred for a total reaction time of 18 h at rt. Additional MeOH (10 mL) was added, and the reaction mixture was stirred for a few minutes before the product was filtered off and washed with MeOH, furnishing **1b-Zn−NH$_2$** as a pale yellow solid. Yield: 0.320 g, 0.418 mmol, 82%. M.p. > 310 °C; ^{1}H NMR (600 MHz, [D$_6$]DMSO): δ = 8.69 (s, 1H, H^d'), 8.51 (d, $^4J_{H,H}$ = 3.1 Hz, 1H, H^h'), 8.11 (dd, $^3J_{H,H}$ = 9.5 Hz, $^4J_{H,H}$ = 3.1 Hz, 1H, H^f'), 7.94–7.96 (m, 2H, H^a'' + H^b'), 7.90–7.91 (m, 2H, H^d + H^h), 7.87 (dd, $^3J_{H,H}$ = 9.5 Hz, $^4J_{H,H}$ = 3.1 Hz, 1H, H^f), 7.67 (d, $^4J_{H,H}$ = 1.7 Hz, 1H, H^a'), 7.58–7.59 (m, 2H, H^b'' + H^c'), 7.48 (d, $^3J_{H,H}$ = 7.9 Hz, 1H, H^c''), 7.37 (d, $^4J_{H,H}$ = 1.5 Hz, 1H, H^a), 7.34 (d, $^4J_{H,H}$ = 1.2 Hz, 1H, H^b), 6.79 (d, $^3J_{H,H}$ = 9.5 Hz, 1H, H^e'), 6.53 (d, $^3J_{H,H}$ = 9.5 Hz, 1H, H^e), 6.17 (broadened s, 2H, NH$_2$), 3.81 (s, 3H, CO$_2$CH'$_3$), 3.78 (s, 3H, CO$_2$CH''$_3$), 2.43 ppm (s, 3H, Ar—CH_3); ^{13}C NMR (151 MHz, [D$_6$]DMSO): δ = 176.1 (C^9), 176.0 (C^9), 173.4 (C^7), 168.7 (C^7), 165.8 (C''O$_2$CH$_3$), 165.3 (C'O$_2$CH$_3$), 149.0 (C^2), 140.7 (C^2''), 140.6 (C^2), 136.8 (C^1'), 136.6 (C^5), 134.9 (C^{13}), 134.3 (C^{12}), 134.1 (C^{12}), 133.1 (C^{13}), 131.4 (C^6), 131.0 (C^4 + C^6''), 130.8 (C^3), 130.7 (C^4), 130.6 (C^1''), 130.5 (C^3 + C^6), 129.7 (C^4''), 129.1 (C^{11}), 129.0 (C^{11}), 127.7 (C^5), 124.9 (C^3), 123.6 (C^{10}), 123.4 (C^{10}), 123.0 (C^5''), 121.5 (C^3'), 118.3 (C^8), 117.1 (C^8), 52.3 (CO$_2$C'H$_3$), 52.1 (CO$_2$C''H$_3$), 20.5 ppm (Ar—CH$_3$); ^{15}N{^{1}H} NMR (600 MHz, [D$_6$]DMSO): δ = −11.2 (2 × NO$_2$), −120.9 (CH=N^2–Zn), −125.6 (CH=N^1–Zn), −326.9 ppm (|$^1J_{N,H}$| = 72 Hz, NH$_2$); LRMS (ESI): m/z (%): 788.094 (100) [M + Na]$^+$; HRMS (ESI): m/z calcd for C$_{37}$H$_{27}$N$_5$O$_{10}$Zn + Na: 788.0942 [M + Na]$^+$; found: 788.0945; elemental analysis calcd (%) for C$_{37}$H$_{27}$N$_5$O$_{10}$Zn: C 57.94, H 3.55, N 9.13, Zn 8.52; found: C 57.75, H 3.51, N 9.09, Zn 8.49.

For NMR data of the minor species of **1b-Zn−NH$_2$** in [D$_6$]DMSO (**1b-Zn-DMSO**), see SI. Additional NMR data in different solvents and at different temperatures are also presented in the SI. Crystals of **1b-Zn−NH$_2$** suitable for single-crystal X-ray diffraction analysis were obtained by performing the abovementioned procedure under more diluted conditions (CH$_2$Cl$_2$ (20 mL) and MeOH (20 mL) were used), and without any stirring, furnishing **1b-Zn−NH$_2$** as yellow crystals during the course of 1 day. The product obtained by this crystallization method had an identical ^{1}H NMR spectrum to the product obtained from the abovementioned method. Crystal and refinement data are given in Table S7, SI.

EurJIC
European Journal of Inorganic Chemistry

Full Papers
doi.org/10.1002/ejic.202100170

Chemistry Europe
European Chemical Societies Publishing

1b-Cd−NH₂. The Cd complex was prepared analogously to **1b-Zn−NH₂**, by employing **1b** (0.433 g, 0.508 mmol, 1.0 equiv.), Cd-(OAc)₂·2H₂O (0.134 g, 0.505 mmol, 1.0 equiv.), NEt₃ (0.35 mL, 2.5 mmol, 4.9 equiv.), CH₂Cl₂ (10 mL) and MeOH (10 + 10 mL). **1b-Cd−NH₂** was obtained as a yellow solid. Yield: 0.325 g, 0.400 mmol, 79%. M.p. > 310 °C; ¹H NMR (600 MHz, [D₆]DMSO): δ = 8.37–8.42 (m, 2H, Hᵈ′ + Hʰ), 7.96–7.98 (m, 1H, Hᶠ), 7.83–7.85 (m, 1H, Hᵇ), 7.73–7.80 (m, 3H, Hᵈ + Hᶠ + Hʰ), 7.63 (s, 1H, Hᵃ′), 7.51 (s, 1H, Hᵃ), 7.43–7.44 (m, 2H, Hᶜ + Hᵇ′), 7.31–7.34 (m, 1H, Hᶜ′), 7.20 (s, 1H, Hᵃ), 7.18 (s, 1H, Hᵇ), 6.55–6.58 (m, 1H, Hᵉ), 6.32–6.34 (m, 1H, Hᵉ), 5.27 (m, 2H, NH₂), 3.83 (s, 3H, CO₂CH′₃), 3.78 (s, 3H, CO₂CH′₃), 2.37 ppm (s, 3H, Ar–CH₃); ¹³C NMR (151 MHz, [D₆]DMSO): δ = 177.8 (C⁹), 177.6 (C⁹), 171.2 (C⁷), 170.9 (C⁷), 166.2 (C″O₂CH₃), 165.6 (C′O₂CH₃), 150.5 (C²), 143.6 (C²), 142.3 (C²″), 137.4 (C¹′), 135.4 (C⁵ + C¹³), 134.1 (C¹³), 133.0 (C¹²), 132.4 (C¹²), 132.3 (C¹″), 131.8 (C¹), 131.0 (C⁶′), 131.0 (C⁴), 130.7 (C⁶″), 130.3 (C⁶), 130.2 (C³), 130.1 (C⁴′), 129.2 (C⁴″), 128.09 (C¹¹), 128.02 (C¹¹), 126.5 (C⁵), 124.14 (C¹⁰), 123.6 (C¹⁰), 123.59 (C³′), 120.8 (C⁵″), 120.1 (C³″), 119.3 (t, ³J_{C,Cd} = 18.7 Hz, C⁸), 118.0 (t, ³J_{C,Cd} = 22.3 Hz, C⁸), 52.3 (CO₂C′H₃), 52.0 (CO₂C″H₃), 20.4 ppm (Ar–CH₃). Several of the ¹H and ¹³C NMR resonances were broadened. ¹⁵N{¹H} NMR (600 MHz, [D₆]DMSO): δ = −11.4 (2 × NO₂), −97.8 (CH=N²–Cd), −112.6 (CH=N¹–Cd), −322.7 ppm (|¹J_{N,H}| = 77 Hz, NH₂); LRMS (ESI, positive mode): m/z (%): 838.069 (14) [M + Na]⁺; HRMS (ESI): m/z calcd for C₃₇H₂₇¹¹⁰CdN₅O₁₀ + Na: 834.0680 [M + Na]⁺; found: 834.0677; LRMS (ESI, negative mode): m/z (%): 702.184 (< 10), 814.072 (29) [**1b-Cd−NH₂**−H]⁻, 850.048 (100) [**1b-Cd−NH₂** + Cl]⁻, 963.084 (< 10) [**1b-Cd**−H]⁻; HRMS (ESI, negative mode): m/z calcd for C₃₇H₂₆¹¹⁰CdN₅O₁₀: 810.0715 [**1b-Cd−NH₂**−H]⁻; found: 810.0710; m/z calcd for C₃₇H₂₇¹¹⁰CdN₅O₁₀ + Cl: 846.0482 [**1b-Cd−NH₂** + Cl]⁻, found: 846.0475; m/z calcd for C₄₄H₂₉¹¹⁰CdN₆O₁₃: 959.0828 [**1b-Cd**−H]⁻, found: 959.0821; elemental analysis calcd (%) for C₃₇H₂₇N₅O₁₀Cd: C 54.59, H 3.34, N 8.60, Cd 13.81; found: C 54.41, H 3.27, N 8.55, Cd 13.76.

Complex **1b-Cd** was only observed by MS. For NMR data of the minor species of **1b-Cd−NH₂** in [D₆]DMSO (**1b-Cd−DMSO**), see SI. Additional NMR data in different solvents and at different temperatures are also presented in the SI. Crystals of **1b-Cd−NH₂** suitable for single-crystal X-ray diffraction analysis were obtained by slow diffusion of MeOH into a solution of the complex in DMSO. Alternatively, crystals could obtained by performing the abovementioned procedure under more diluted conditions (CH₂Cl₂ (20 mL) and MeOH (20 mL) were used), and without any stirring, furnishing **1b-Cd−NH₂** as yellow crystals during the course of 1 day. The product obtained by this method had an identical ¹H NMR spectrum to the product obtained from the abovementioned method. Crystal and refinement data are given in Table S8, SI.

1b-Cu−NH₂. Triamine **5** (0.200 g, 0.493 mmol, 1.0 equiv.), Cu-(OAc)₂·H₂O (0.098 g, 0.49 mmol, 1.0 equiv.) and 5-nitrosalicylaldehyde (0.165 mg, 0.987 mmol, 2.0 equiv.) were stirred in toluene (2 mL) overnight. The product was isolated by gravity filtration, washed with toluene (2 × 1 mL) and then dried in a vacuum oven at 70 °C over night, yielding the product as a bright green solid. Yield: 0.315 g, 0.412 mmol, 84%. UV/Vis (CH₂Cl₂): λ_max (ε) = 259 (62000), 365 (36000), 677 nm (327 mol⁻¹ dm³ cm⁻³); LRMS (ESI): m/z (%): 787.095 (100) [M + Na]⁺; HRMS (ESI): m/z calcd for C₃₇H₂₇CuN₅O₁₀ + Na: 787.0946 [M + Na]⁺; found: 787.0947; elemental analysis calcd (%) for C₃₇H₂₇CuN₅O₁₀: C 58.08, H 3.56, N 9.15, Cu 8.30; found: C 57.67, H 3.59, N 9.17, Cu 8.24.

Recrystallization by vapor diffusion of methanol into a solution of **1b-Cu−NH₂** in DMSO yielded crystals suitable for single-crystal X-ray diffraction analysis. Crystal and refinement data are given in Table S11, SI.

1d-Co(acac). Ligand **1d** (0.431 g, 0.496 mmol, 1.0 equiv.) and Co-(acac)₃ (0.177 g, 0.496 mmol, 1.0 equiv.) were dissolved in toluene (10 mL), and the dark green-brown solution was heated at reflux temperature under Ar for 3 days. After cooling to rt, the reaction mixture was diluted with CH₂Cl₂ (50 mL), and evaporated to dryness under reduced pressure. Purification by flash chromatography (95% CH₂Cl₂/5% EtOAc), followed by recrystallization from MeCN/benzene (5:1) gave **1d-Co(acac)** as dark green crystals. Yield: 0.290 g, 0.283 mmol, 57%. ¹H NMR (600 MHz, CDCl₃): δ = 14.53 (d, ⁴J_{H,H} = 2.1 Hz, 1H, OH), 9.19 (d, ⁴J_{H,H} = 2.1 Hz, 1H, Hᵈ′), 8.10 (dd, ³J_{H,H} = 8.1 Hz, ⁴J_{H,H} = 1.6 Hz, 1H, Hᵇ), 8.02 (d, ³J_{H,H} = 8.5 Hz, 1H, Hʲ′), 7.99 (s, 1H, Hᵈ), 7.97 (d, ³J_{H,H} = 8.1 Hz, 1H, Hᶜ′), 7.85–7.87 (m, 2H, Hᵇ″ + Hᶠ′), 7.76–7.78 (m, 2H, Hᵃ′ + Hᵍ″), 7.70 (d, ³J_{H,H} = 8.5 Hz, 1H, Hʲ), 7.68 (d, ³J_{H,H} = 8.1 Hz, 1H, Hᶜ), 7.65–7.67 (m, 3H, Hᶠ + Hᵍ′ + Hᵃ″), 7.59 (d, ³J_{H,H} = 9.2 Hz, 1H, Hᵉ), 7.55 (ddd, ³J_{H,H} = 8.5 Hz, ³J_{H,H} = 6.7 Hz, ⁴J_{H,H} = 1.0 Hz, 1H, Hⁱ″), 7.39–7.42 (m, 3H, Hᵍ + Hⁱ′ + Hʰ″), 7.35–7.37 (m, 2H, Hᵈ + Hᶠ), 7.19–7.22 (m, 2H, Hᵉ + Hʰ′), 7.11–7.13 (m, 2H, Hʲ + Hᵉ″), 7.08 (m, 2H, Hᵃ + Hᵇ), 6.87–6.89 (m, 1H, Hʰ), 6.53 (ddd, ³J_{H,H} = 8.2 Hz, ³J_{H,H} = 7.3 Hz, ⁴J_{H,H} = 1.1 Hz, 1H, Hⁱ), 5.31 (s, 1H, Hʲ′), 3.95 (s, 3H, CO₂CH′₃), 3.86 (s, 3H, CO₂CH″₃), 2.33 (s, 3H, Ar–CH₃), 2.01 (s, 3H, Hᵅ), 1.11 ppm (s, 3H, Hᵋ); ¹³C NMR (151 MHz, CDCl₃): δ = 189.3 (Cᵝ), 187.3 (Cᵟ), 168.7 (C⁹), 167.3 (C⁹), 166.6 (C⁹″), 166.4 (C″O₂CH₃), 166.3 (C′O₂CH₃), 164.1 (C⁷), 161.7 (C⁷), 156.6 (C⁷″), 149.8 (C²), 146.5 (C²), 145.6 (C²″), 140.8 (C¹′), 138.6 (C¹″), 137.1 (C⁵), 136.1 (C¹¹″), 135.7 (C³), 135.4 (C¹¹), 135.3 (C¹¹′), 134.9 (C¹), 134.2 (C¹⁷), 133.6 (C¹⁷), 133.07 (C⁴ or C⁶), 133.04 (C⁶″), 132.9 (C¹⁷″), 132.1 (C⁴ or C⁶), 131.0 (C⁶′), 130.3 (C⁴″), 130.0 (C⁴′), 129.2 (C¹³″), 128.9 (C¹³), 128.5 (C¹³), 128.4 (C⁵′), 128.0 (C¹⁵″), 127.53 (C¹²″), 127.51 (C¹⁵), 127.24 (C⁵″), 127.17 (C¹⁵), 126.5 (C¹²), 126.1 (C¹⁰), 125.9 (C¹²), 124.6 (C¹⁰ + C³′), 123.8 (C¹⁴′), 122.3 (C¹⁴), 121.6 (C¹⁴), 120.8 (C¹⁰′), 119.8 (C¹⁶′), 119.1 (C¹⁶), 118.3 (C¹⁶), 117.6 (C³″), 113.4 (C⁸), 111.7 (C⁸′), 109.5 (C⁸″), 96.9 (Cᵞ), 52.4 (CO₂C′H₃), 52.1 (CO₂C″H₃), 26.5 (Cᵅ), 25.2 (Cᵋ), 21.0 ppm (Ar–CH₃); ¹⁵N{¹H} NMR (600 MHz, CDCl₃): δ = −125.6 (CH=N³), −214.6 (CH=N²–Co), −226.9 ppm (CH=N¹–Co); LRMS (ESI): m/z (%): 1046.245 (100) [M + Na]⁺; HRMS (ESI): m/z calcd for C₆₁H₄₆CoN₃O₉ + Na: 1046.2458 [M + Na]⁺; found: 1046.2451; elemental analysis calcd (%) for C₆₁H₄₆CoN₃O₉: C 71.55, H 4.53, N 4.10, Co 5.76; found: C 71.37, H 4.53, N 4.09, Co 5.73.

Crystals of **1d-Co(acac)** suitable for single-crystal X-ray diffraction analysis were obtained by vapor diffusion of MeCN into a solution of the complex in benzene. Crystal and refinement data are given in Table S6, SI.

1d-Lu. Ligand **1d** (0.219 g, 0.252 mmol, 1.0 equiv.) was dissolved in CH₂Cl₂ (5 mL). NEt₃ (0.30 mL, 2.2 mmol, 8.8 equiv.) was added, followed by a solution of Lu(NO₃)₃·xH₂O (0.117 g, 0.259 mmol, 1.0 equiv., assuming x = 5) in MeOH (10 mL). The reaction mixture was stirred at reflux temperature for 2 hours, and a yellow precipitate gradually formed. After cooling to rt, the precipitated solids were filtered off, washed with MeOH, and dried in an oven at 100 °C for 1 day, furnishing **1d-Lu** as a yellow solid. Yield: 0.216 g, 0.208 mmol, 82%. ¹H NMR (600 MHz, [D₆]DMSO): δ = 8.68 (s, 2H, Hᵈ′), 8.49 (s, 1H, Hᵈ), 7.91 (d, ³J_{H,H} = 8.6 Hz, 2H, Hʲ′), 7.77 (dd, ³J_{H,H} = 7.9 Hz, ⁴J_{H,H} = 1.6 Hz, 2H, Hᵇ), 7.68 (d, ³J_{H,H} = 9.1 Hz, 1H, Hᶠ), 7.61–7.64 (m, 4H, Hᶠ + Hᵍ), 7.55 (d, ³J_{H,H} = 7.3 Hz, 1H, Hᵍ), 7.47 (d, ³J_{H,H} = 8.7 Hz, 1H, Hʲ), 7.44 (d, ³J_{H,H} = 7.9 Hz, 2H, Hᶜ), 7.35–7.38 (m, 2H, Hⁱ), 7.29–7.32 (m, 4H, Hᵃ + Hᵃ′), 7.17–7.22 (m, 3H, Hⁱ + Hʰ′), 7.05–7.08 (m, 1H, Hʰ), 6.77 (d, ³J_{H,H} = 9.1 Hz, 1H, Hᵉ), 6.05 (s (d expected), 2H, Hᵉ), 3.72 (s, 6H, CO₂CH₃), 2.37 ppm (s, 3H, Ar–CH₃); ¹³C NMR (151 MHz, [D₆]DMSO): δ = 169.5 (C⁹), 168.6 (C⁹′), 165.5 (CO₂CH₃), 164.9 (C⁷), 164.4 (C⁷), 153.5 (C²), 143.5 (C²), 137.6 (C¹′), 136.4 (C¹¹), 136.1 (C⁴), 135.6 (C¹¹′), 134.62 (C¹⁷), 134.61 (C¹⁷), 133.1 (C¹), 131.0 (C⁶), 130.1 (C³), 130.0 (C⁴′), 128.7 (C¹³ + C¹³′), 127.5 (C¹⁵), 127.4 (C¹⁵), 126.1 (C⁵′), 125.4 (C¹²), 125.3 (C¹²), 125.0 (C¹⁰), 124.5 (C³′), 121.6 (C¹⁴ + C¹⁴′), 119.6 (C¹⁶), 118.2 (C¹⁶), 114.1 (C⁸), 110.3 (C⁸), 52.2 (CO₂CH₃), 20.5 ppm (Ar–CH₃). Several of the ¹H and ¹³C NMR resonances were broadened. The resonance corresponding to C⁸′ could only be detected indirectly by HMBC experiments (600 MHz). The resonance corresponding to C¹⁰′ was not observed at ambient temperature, but could be observed at 90 °C (δ 123.9; 125 MHz). ¹⁵N{¹H} NMR (600 MHz, [D₆]DMSO): δ =

EurJIC
European Journal of Inorganic Chemistry

Full Papers
doi.org/10.1002/ejic.202100170

Chemistry Europe
European Chemical Societies Publishing

−112.2 (CH=N²-Lu), −118.0 ppm (CH=N¹−Lu); LRMS (ESI): m/z (%): 890.284 (20) [**1d** + Na]⁺, 1062.201 (100) [M + Na]⁺; HRMS (ESI): m/z calcd for $C_{56}H_{38}LuN_3O_7 + Na$: 1062.2010 [$M$ + Na]⁺; found: 1062.2013; elemental analysis calcd (%) for $C_{56}H_{38}N_3O_7Lu$: C 64.68, H 3.68, N 4.04, Lu 16.83; found: C 63.59, H 3.92, N 4.16, Lu 16.49.

For additional NMR data for **1d-Lu** in different solvents and at different temperatures, see SI. For a discussion of the NMR characterization of **1d-Lu** in CDCl₃, see SI. **1d-Lu** was crystallographically characterized as **1d-Lu−DMSO** and **1d-Lu−MeOH**. Crystals of **1d-Lu−DMSO** suitable for single-crystal X-ray diffraction analysis were obtained by slow diffusion of EtOH into a solution of **1d-Lu** in DMSO. Crystal and refinement data are given in Table S12, SI. Crystals of **1d-Lu−MeOH** were obtained by slow diffusion of MeOH into a solution of **1d-Lu** in CDCl₃. Crystal and refinement data are given in Table S13, SI. A low carbon content was observed in the elemental analysis of **1d-Lu**. The low carbon content may be explained by the presence of one water ligand in the complex, although it is difficult to prove its presence unambiguously. For more info on potential water-ligation in **1d-Lu**, see SI.

Deposition Numbers 2021584 (for **8-Co(acac)**), 2021585 (for **9-Cu**), 2021586 (for **9-Ni**), 2021587 (for **2a-Zn**), 2021588 (for **1a-Zn**), 2021589 (for **3-Zn−MeOH**), 2021590 (for **1b-Zn−NH₂**), 2021591 (for **1b-Cd−NH₂**), 2054568 (for **1d-Zn**), 2054771 (for **1d-Co(acac)**), 2054854 (for **1b-Cu−NH₂**), 2053903 (for **1a-Cu−NH₂**), 2054825 (for **1d**), 2054856 (for **1d-Lu−DMSO**), and 2054826 (for **1d-Lu−MeOH**) contain the supplementary crystallographic data for this paper. These data are provided free of charge by the joint Cambridge Crystallographic Data Centre and Fachinformationszentrum Karlsruhe Access Structures service www.ccdc.cam.ac.uk/structures.

Acknowledgements

Conflict of Interest

The authors declare no conflict of interest.

Keywords: Cadmium · Copper · Rare earth metals · Schiff base ligands · Zinc

[1] R. Hernández-Molina, A. Mederos, in *Comprehensive Coordination Chemistry II* (Eds.: J. A. McCleverty, T. J. Meyer), Pergamon, Oxford, **2003**, pp. 411–446.

[2] X. Liu, J.-R. Hamon, *Coord. Chem. Rev.* **2019**, *389*, 94–118.

[3] a) P. G. Cozzi, *Chem. Soc. Rev.* **2004**, *33*, 410–421; b) K. Matsumoto, B. Saito, T. Katsuki, *Chem. Commun.* **2007**, 3619–3627; c) X. Wu, C. Chen, Z. Guo, M. North, A. C. Whitwood, *ACS Catal.* **2019**, *9*, 1895–1906; d) X. Liu, C. Manzur, N. Novoa, S. Celedón, D. Carrillo, J.-R. Hamon, *Coord. Chem. Rev.* **2018**, *357*, 144–172.

[4] a) A. Erxleben, *Inorg. Chim. Acta* **2018**, *472*, 40–57; b) J. C. Pessoa, I. Correia, *Coord. Chem. Rev.* **2019**, *388*, 227–247; c) N. Kumar, Roopa, V. Bhalla, M. Kumar, *Coord. Chem. Rev.* **2021**, *427*, 213550; d) M. T. Kaczmarek, M. Zabiszak, M. Nowak, R. Jastrzab, *Coord. Chem. Rev.* **2018**, *370*, 42–54.

[5] a) A. W. Kleij, M. Kuil, D. M. Tooke, M. Lutz, A. L. Spek, J. N. H. Reek, *Chem. Eur. J.* **2005**, *11*, 4743–4750; b) S. H. A. M. Leenders, R. Gramage-Doria, B. de Bruin, J. N. H. Reek, *Chem. Soc. Rev.* **2015**, *44*, 433–448; c) A. W. Kleij, *Dalton Trans.* **2009**, 4635–4639.

[6] a) C. Freire, M. Nunes, C. Pereira, D. M. Fernandes, A. F. Peixoto, M. Rocha, *Coord. Chem. Rev.* **2019**, *394*, 104–134; b) J. L. Segura, M. J. Mancheño, F. Zamora, *Chem. Soc. Rev.* **2016**, *45*, 5635–5671; c) J. Zhang, L. Xu, W.-Y. Wong, *Coord. Chem. Rev.* **2018**, *355*, 180–198.

[7] C.-M. Che, J.-S. Huang, *Coord. Chem. Rev.* **2003**, *242*, 97–113.

[8] a) P. A. Vigato, S. Tamburini, *Coord. Chem. Rev.* **2004**, *248*, 1717–2128; b) S. Yamada, *Coord. Chem. Rev.* **1999**, *190–192*, 537–555; c) W. Radecka-Paryzek, V. Patroniak, J. Lisowski, *Coord. Chem. Rev.* **2005**, *249*, 2156–2175; d) P. A. Vigato, V. Peruzzo, S. Tamburini, *Coord. Chem. Rev.* **2012**, *256*, 953–1114.

[9] a) K. Bernardo, S. Leppard, A. Robert, G. Commenges, F. Dahan, B. Meunier, *Inorg. Chem.* **1996**, *35*, 387–396; b) A. Mrutu, A. C. Lane, J. M. Drewett, S. D. Yourstone, C. L. Barnes, C. M. Halsey, J. W. Cooley, J. R. Walensky, *Polyhedron* **2013**, *54*, 300–308; c) J. Rich, M. Rodríguez, I. Romero, X. Fontrodona, P. W. N. M. van Leeuwen, Z. Freixa, X. Sala, A. Poater, M. Solà, *Eur. J. Inorg. Chem.* **2013**, 1213–1224.

[10] a) A. Sahraei, H. Kargar, M. Hakimi, M. N. Tahir, *J. Mol. Struct.* **2017**, *1149*, 576–584; b) P. D. Frischmann, M. J. MacLachlan, *Chem. Commun.* **2007**, 4480–4482; c) J. Parr, A. T. Ross, A. M. Z. Slawin, *J. Chem. Soc. Dalton Trans.* **1996**, 1509–1512; d) J. Hamblin, L. J. Childs, N. W. Alcock, M. J. Hannon, *J. Chem. Soc. Dalton Trans.* **2002**, 164–169; e) E. C. Alyea, A. Malek, A. E. Vougioukas, *Can. J. Chem.* **1982**, *60*, 667–672; f) D. J. Berg, S. J. Rettig, C. Orvig, *J. Am. Chem. Soc.* **1991**, *113*, 2528–2532; g) J. K. Molloy, C. Philouze, L. Fedele, D. Imbert, O. Jarjayes, F. Thomas, *Dalton Trans.* **2018**, *47*, 10742–10751; h) E. E. Hardy, K. M. Wyss, R. J. Keller, J. D. Gorden, A. E. V. Gorden, *Dalton Trans.* **2018**, *47*, 1337–1346; i) W.-K. Wong, H. Liang, J. Guo, W.-Y. Wong, W.-K. Lo, K.-F. Li, K.-W. Cheah, Z. Zhou, W.-T. Wong, *Eur. J. Inorg. Chem.* **2004**, 829–836; j) D. Lionetti, V. W. Day, J. D. Blakemore, *Dalton Trans.* **2017**, *46*, 11779–11789; k) B. E. Klamm, C. J. Windorff, C. Celis-Barros, M. L. Marsh, D. S. Meeker, T. E. Albrecht-Schmitt, *Inorg. Chem.* **2018**, *57*, 15389–15398; l) S. T. Tsantis, A. Lagou-Rekka, K. F. Konidaris, C. P. Raptopoulou, V. Bekiari, V. Psycharis, S. P. Perlepes, *Dalton Trans.* **2019**, *48*, 15668–15678; m) B. E. Klamm, C. J. Windorff, M. L. Marsh, D. S. Meeker, T. E. Albrecht-Schmitt, *Chem. Commun.* **2018**, *54*, 8634–8636; n) B. E. Klamm, C. J. Windorff, C. Celis-Barros, M. J. Beltran-Leiva, J. M. Sperling, T. E. Albrecht-Schönzart, *Inorg. Chem.* **2020**, *59*, 18035–18047; o) T. Radoske, R. Kloditz, S. Fichter, J. März, P. Kaden, M. Patzschke, M. Schmidt, T. Stumpf, O. Walter, A. Ikeda-Ohno, *Dalton Trans.* **2020**, *49*, 17559–17570; p) T. Radoske, J. März, M. Patzschke, P. Kaden, O. Walter, M. Schmidt, T. Stumpf, *Chem. Eur. J.* **2020**, *26*, 16853–16859; q) F. Gao, F.-L. Yang, G.-Z. Zhu, Y. Zhao, *Dalton Trans.* **2015**, *44*, 20232–20241; r) H.-H. Chen, D.-F. Wu, Y.-Y. Duan, L. Li, Y.-J. Wang, X.-M. Zhang, J.-Z. Cui, H.-L. Gao, *New J. Chem.* **2020**, *44*, 2561–2570; s) E. E. Hardy, K. M. Wyss, J. D. Gorden, I. R. Ariyarathna, E. Miliordos, A. E. V. Gorden, *Chem. Commun.* **2017**, *53*, 11984–11987.

[11] a) M. Niemeyer, P. P. Power, *Inorg. Chem.* **1996**, *35*, 7264–7272; b) J. A. C. Clyburne, N. McMullen, *Coord. Chem. Rev.* **2000**, *210*, 73–99; c) M. Olaru, J. Beckmann, C. I. Raţ, *Organometallics* **2014**, *33*, 3012–3020; d) M. A. Boreen, B. F. Parker, S. Hohloch, B. A. Skeel, J. Arnold, *Dalton Trans.* **2018**, *47*, 96–104; e) T. Wiedemann, G. Voit, A. Tchernook, P. Roesle, I. Göttker-Schnetmann, S. Mecking, *J. Am. Chem. Soc.* **2014**, *136*, 2078–2085; f) R. C. Smith, J. D. Protasiewicz, *Organometallics* **2004**, *23*, 4215–4222; g) R. C. Smith, C. R. Bodner, M. J. Earl, N. C. Sears, N. E. Hill, L. M. Bishop, N. Sizemore, D. T. Hehemann, J. J. Bohn, J. D. Protasiewicz, *J. Organomet. Chem.* **2005**, *690*, 477–481; h) B. R. Barnett, C. C. Mokhtarzadeh, J. S. Figueroa, P. Lummis, S. Wang, J. Gavenonis, N. Schüwer, T. D. Tilley, J. N. Boynton, P. P. Power, T. B. Ditri, N. Weidemann, D. W. Agnew,

P. W. Smith, A. E. Carpenter, J. K. Pratt, N. D. Mendelson, J. D. Queen, in *Inorganic Syntheses* (Ed.: P. P. Power), **2018**, pp. 85–122; i) A. S. Crossman, A. T. Larson, J. X. Shi, S. M. Krajewski, E. S. Akturk, M. P. Marshak, *J. Org. Chem.* **2019**, *84*, 7434–7442; j) E. J. Hopkins, S. M. Krajewski, A. S. Crossman, F. D. R. Maharaj, L. T. Schwanz, M. P. Marshak, *Eur. J. Inorg. Chem.* **2020**, 1951–1959.

[12] C. Wei, Y. He, X. Shi, Z. Song, *Coord. Chem. Rev.* **2019**, *385*, 1–19.

[13] a) A. Kayal, A. F. Ducruet, S. C. Lee, *Inorg. Chem.* **2000**, *39*, 3696–3704; b) G. A. Edouard, P. Kelley, D. E. Herbert, T. Agapie, *Organometallics* **2015**, *34*, 5254–5277.

[14] K. T. Hylland, S. Øien-Ødegaard, R. H. Heyn, M. Tilset, *Eur. J. Inorg. Chem.* **2020**, 3627–3643.

[15] a) X.-B. Lu, W.-M. Ren, G.-P. Wu, *Acc. Chem. Res.* **2012**, *45*, 1721–1735; b) M. H. Rønne, D. Cho, M. R. Madsen, J. B. Jakobsen, S. Eom, É. Escoudé, H. C. D. Hammershøj, D. U. Nielsen, S. U. Pedersen, M.-H. Baik, T. Skrydstrup, K. Daasbjerg, *J. Am. Chem. Soc.* **2020**, *142*, 4265–4275; c) M. R. Madsen, J. B. Jakobsen, M. H. Rønne, H. Liang, H. C. D. Hammershøj, P. Nørby, S. U. Pedersen, T. Skrydstrup, K. Daasbjerg, *Organometallics* **2020**, *39*, 1480–1490.

[16] a) M. Marcos, A. Omenat, J. Barberá, F. Durán, J. L. Serrano, *J. Mater. Chem.* **2004**, *14*, 3321–3327; b) C. J. Whiteoak, G. Salassa, A. W. Kleij, *Chem. Soc. Rev.* **2012**, *41*, 622–631; c) Y. Sunatsuki, Y. Motoda, N. Matsumoto, *Coord. Chem. Rev.* **2002**, *226*, 199–209.

[17] K. T. Hylland, S. Øien-Ødegaard, M. Tilset, *Eur. J. Org. Chem.* **2020**, 4208–4226.

[18] a) D. X. Hu, P. Grice, S. V. Ley, *J. Org. Chem.* **2012**, *77*, 5198–5202; b) R. A. Al-Horani, U. R. Desai, *Tetrahedron* **2012**, *68*, 2027–2040.

[19] A. Bruylants, E. F.-D. Medicis, in *Carbon-Nitrogen Double Bonds (1970)* (Ed.: S. Patai), John Wiley & Sons Ltd., Great Britain, **1970**, pp. 465–504.

[20] G. Consiglio, S. Failla, P. Finocchiaro, I. P. Oliveri, S. D. Bella, *Dalton Trans.* **2012**, *41*, 387–395.

[21] a) S. J. Wezenberg, G. A. Metselaar, E. C. Escudero-Adán, J. Benet-Buchholz, A. W. Kleij, *Inorg. Chim. Acta* **2009**, *362*, 1053–1057; b) F. Castro-Gómez, G. Salassa, A. W. Kleij, C. Bo, *Chem. Eur. J.* **2013**, *19*, 6289–6298; c) W. Lamine, S. Boughdiri, L. Christ, C. Morell, H. Chermette, *J. Comput. Chem.* **2019**, *40*, 717–725.

[22] a) O. Schlager, K. Wieghardt, H. Grondey, A. Rufinska, B. Nuber, *Inorg. Chem.* **1995**, *34*, 6440–6448; b) A. Sokolowski, J. Müller, T. Weyhermüller, R. Schnepf, P. Hildebrandt, K. Hildenbrand, E. Bothe, K. Wieghardt, *J. Am. Chem. Soc.* **1997**, *119*, 8889–8900; c) K. P. Wainwright, *Coord. Chem. Rev.* **1997**, *166*, 35–90.

[23] a) B. Samanta, J. Chakraborty, S. Shit, S. R. Batten, P. Jensen, J. D. Masuda, S. Mitra, *Inorg. Chim. Acta* **2007**, *360*, 2471–2484; b) S. Basak, S. Sen, S. Banerjee, S. Mitra, G. Rosair, M. T. G. Rodriguez, *Polyhedron* **2007**, *26*, 5104–5112; c) M. Orio, C. Philouze, O. Jarjayes, F. Neese, F. Thomas, *Inorg. Chem.* **2010**, *49*, 646–658; d) G. Consiglio, S. Failla, P. Finocchiaro, I. P. Oliveri, S. Di Bella, *Inorg. Chem.* **2012**, *51*, 8409–8418.

[24] a) G. Forte, I. P. Oliveri, G. Consiglio, S. Failla, S. Di Bella, *Dalton Trans.* **2017**, *46*, 4571–4581; b) G. Consiglio, I. P. Oliveri, S. Failla, S. Di Bella, *Molecules* **2019**, *24*, 2514.

[25] a) E. W. Abel, N. J. Long, K. G. Orrell, A. G. Osborne, H. M. Pain, V. Šik, *J. Chem. Soc. Chem. Commun.* **1992**, 303–304; b) E. R. Civitello, P. S. Dragovich, T. B. Karpishin, S. G. Novick, G. Bierach, J. F. O'Connell, T. D. Westmoreland, *Inorg. Chem.* **1993**, *32*, 237–241.

[26] a) K. G. Orrell, in *Annu. Rep. NMR Spectrosc., Vol. 37* (Ed.: G. A. Webb), Academic Press, **1999**, pp. 1–74; b) K. G. Orrell, A. G. Osborne, J. O. Prince, V. Šik, D. K. Vellianitis, *Eur. J. Inorg. Chem.* **2000**, 383–391; c) M. L. Creber, K. G. Orrell, A. G. Osborne, V. Šik, M. B. Hursthouse, M. E. Light, *Polyhedron* **2001**, *20*, 1973–1982.

[27] a) L. Pazderski, *Magn. Reson. Chem.* **2008**, *46*, S3-S15; b) R. Kleinmaier, S. Arenz, A. Karim, A.-C. C. Carlsson, M. Erdélyi, *Magn. Reson. Chem.* **2013**, *51*, 46–53; c) J. Jaźwiński, *J. Mol. Struct.* **2005**, *750*, 7–17; d) D. Niedzielska, T. Pawlak, A. Wojtczak, L. Pazderski, E. Szlyk, *Polyhedron* **2015**, *92*, 41–51.

[28] A. W. Addison, T. N. Rao, J. Reedijk, J. van Rijn, G. C. Verschoor, *J. Chem. Soc. Dalton Trans.* **1984**, 1349–1356.

[29] J. A. Connor, M. Charlton, D. C. Cupertino, A. Lienke, M. McPartlin, I. J. Scowen, P. A. Tasker, *J. Chem. Soc. Dalton Trans.* **1996**, 2835–2838.

[30] A. W. Kleij, M. Kuil, M. Lutz, D. M. Tooke, A. L. Spek, P. C. J. Kamer, P. W. N. M. van Leeuwen, J. N. H. Reek, *Inorg. Chim. Acta* **2006**, *359*, 1807–1814.

[31] a) A. Okuniewski, D. Rosiak, J. Chojnacki, B. Becker, *Polyhedron* **2015**, *90*, 47–57; b) D. Rosiak, A. Okuniewski, J. Chojnacki, *Polyhedron* **2018**, *146*, 35–41.

[32] E. C. Constable, G. Zhang, C. E. Housecroft, M. Neuburger, J. A. Zampese, *Inorg. Chim. Acta* **2010**, *363*, 4207–4213.

[33] M. Shi, W.-L. Duan, *Appl. Organomet. Chem.* **2003**, *17*, 175–180.

[34] a) S. G. Telfer, T. Sato, T. Harada, R. Kuroda, J. Lefebvre, D. B. Leznoff, *Inorg. Chem.* **2004**, *43*, 6168–6176; b) J.-M. Xiao, W. Zhang, *Inorg. Chem. Commun.* **2009**, *12*, 1175–1178; c) P. Liu, X.-J. Feng, R. He, *Tetrahedron* **2010**, *66*, 631–636.

[35] D. DiMondo, M. E. Thibault, J. Britten, M. Schlaf, *Organometallics* **2013**, *32*, 6541–6554.

[36] a) D. F. Evans, *J. Chem. Soc.* **1959**, 2003–2005; b) K. De Buysser, G. G. Herman, E. Bruneel, S. Hoste, I. Van Driessche, *Chem. Phys.* **2005**, *315*, 286–292.

[37] A. B. P. Lever, *Inorg. Chem.* **1965**, *4*, 763–764.

[38] a) S. Mariko, S. Hisako, M. Yukie, F. Yutaka, *Bull. Chem. Soc. Jpn.* **2009**, *82*, 1266–1273; b) S. Mukhopadhyay, D. Mandal, D. Ghosh, I. Goldberg, M. Chaudhury, *Inorg. Chem.* **2003**, *42*, 8439–8445.

[39] T. P. Cheeseman, D. Hall, T. N. Waters, *J. Chem. Soc. A* **1966**, 1396–1406.

[40] a) J. B. Jakobsen, M. H. Rønne, K. Daasbjerg, T. Skrydstrup, *Angew. Chem. Int. Ed.* **2021**, *60*, 9174–9179; b) N. W. Kinzel, C. Werlé, W. Leitner, *Angew. Chem. Int. Ed.*, DOI: doi.org/10.1002/anie.202006988.

[41] a) M. Franks, A. Gadzhieva, L. Ghandhi, D. Murrell, A. J. Blake, E. S. Davies, W. Lewis, F. Moro, J. McMaster, M. Schröder, *Inorg. Chem.* **2013**, *52*, 660–670; b) A. K. Nairn, S. J. Archibald, R. Bhalla, B. C. Gilbert, E. J. MacLean, S. J. Teat, P. H. Walton, *Dalton Trans.* **2006**, 172–176; c) E. Bill, J. Müller, T. Weyhermüller, K. Wieghardt, *Inorg. Chem.* **1999**, *38*, 5795–5802; d) F. Thomas, O. Jarjayes, C. Duboc, C. Philouze, E. Saint-Aman, J.-L. Pierre, *Dalton Trans.* **2004**, 2662–2669.

[42] S. Zolezzi, A. Decinti, E. Spodine, *Polyhedron* **1999**, *18*, 897–904.

[43] a) M. K. Paira, J. Dinda, T. H. Lu, A. R. Paital, C. Sinha, *Polyhedron* **2007**, *26*, 4131–4140; b) V. Lozovan, V. Ch Kravtsov, E. B. Coropceanu, P. Rotaru, A. V. Siminel, M. S. Fonari, *Inorg. Chim. Acta* **2019**, *491*, 42–51; c) M. Martínez Belmonte, E. C. Escudero-Adán, E. Martin, A. W. Kleij, *Dalton Trans.* **2012**, *41*, 5193–5200.

[44] a) W.-K. Lo, W.-K. Wong, W.-Y. Wong, J. Guo, *Eur. J. Inorg. Chem.* **2005**, 3950–3954; b) P. D. Frischmann, G. A. Facey, P. Y. Ghi, A. J. Gallant, D. L. Bryce, F. Lelj, M. J. MacLachlan, *J. Am. Chem. Soc.* **2010**, *132*, 3893–3908.

[45] Q. Shi, L. Xu, J. Ji, Y. Li, R. Wang, Z. Zhou, R. Cao, M. Hong, A. S. C. Chan, *Inorg. Chem. Commun.* **2004**, *7*, 1254–1257.

[46] a) D. Reinen, C. Friebel, *Inorg. Chem.* **1984**, *23*, 791–798; b) I. B. Bersuker, *Chem. Rev.* **2001**, *101*, 1067–1114.

[47] a) N. Charef, F. Sebti, L. Arrar, M. Djarmouni, N. Boussoualim, A. Baghiani, S. Khennouf, A. Ourari, M. A. AlDamen, M. S. Mubarak, D. G. Peters, *Polyhedron* **2015**, *85*, 450–456; b) M. A. AlDamen, N. Charef, H. K. Juwhari, K. Sweidan, M. S. Mubarak, D. G. Peters, *J. Chem. Crystallogr.* **2016**, *46*, 411–420.

[48] a) M. A. Halcrow, *Chem. Soc. Rev.* **2013**, *42*, 1784–1795; b) B. Murphy, B. Hathaway, *Coord. Chem. Rev.* **2003**, *243*, 237–262.

[49] R. Shannon, *Acta Crystallogr. Sect. A* **1976**, *32*, 751–767.

[50] J.-C. G. Bünzli, *J. Coord. Chem.* **2014**, *67*, 3706–3733.

[51] Orvig and co-workers reported that the reactions between potentially heptadentate Schiff base ligands (H_3L) and $Ln(NO_3)_3 \cdot xH_2O$ yielded nonacoordinated $Ln(H_3L)(NO_3)_3$ complexes where the ligands in fact acted as neutral tridentate O_3 ligands, rather than heptadentate $N_4O_3{}^{3-}$ ligands. By using the corresponding chloride salts they obtained complexes of the type Ln(L) with the ligands being heptadentate. A. Smith, S. J. Rettig, C. Orvig, *Inorg. Chem.* **1988**, *27*, 3929–3934.

[52] a) Y. Yao, H.-Y. Yin, Y. Ning, J. Wang, Y.-S. Meng, X. Huang, W. Zhang, L. Kang, J.-L. Zhang, *Inorg. Chem.* **2019**, *58*, 1806–1814; b) K. Masatoshi, Y. Toshiro, *Chem. Lett.* **1999**, *28*, 137–138.

[53] a) J. Harrowfield, M. Ogden, A. White, *Aust. J. Chem.* **1991**, *44*, 1237–1247; b) L. Semenova, B. Skelton, A. White, *Aust. J. Chem.* **1996**, *49*, 997–1004; c) A. Abbasi, E. Damian Risberg, L. Eriksson, J. Mink, I. Persson, M. Sandström, Y. V. Sidorov, M. Y. Skripkin, A.-S. Ullström, *Inorg. Chem.* **2007**, *46*, 7731–7741; d) Z. Asfari, E. J. Chan, J. M. Harrowfield, B. W. Skelton, A. N. Sobolev, P. Thuéry, A. H. White, *Aust. J. Chem.* **2020**, *73*, 447–454; e) M. E. Minyaev, I. E. Nifant'ev, A. N. Tavtorkin, S. y A. Korchagina, S. S. Zeynalova, I.-v. Ananyev, A. V. Churakov, *Acta Crystallogr. Sect. C* **2017**, *73*, 820–827; f) J.-i. Setsune, K. Watanabe, *J. Porphyrins Phthalocyanines* **2012**, *16*, 508–517.

[54] L. G. Nielsen, A. K. R. Junker, T. J. Sørensen, *Dalton Trans.* **2018**, *47*, 10360–10376.

[55] W. Zhou, D. McKearney, D. B. Leznoff, *Chem. Eur. J.* **2020**, *26*, 1027–1031.

[56] a) J. P. Jesson, E. L. Muetterties, in *Dynamic Nuclear Magnetic Resonance Spectroscopy* (Eds.: L. M. Jackman, F. A. Cotton), Academic Press, **1975**, pp. 253–316; b) U. Casellato, S. Tamburini, P. Tomasin, P. A. Vigato, S.

Aime, M. Botta, *Inorg. Chem.* **1999**, *38*, 2906–2916; c) V. Peruzzo, A. Lanza, F. Nestola, P. A. Vigato, S. Tamburini, *Inorg. Chim. Acta* **2014**, *416*, 226–234; d) J. Kotek, V. Kubíček, P. Hermann, I. Lukeš, in *The Chemistry of Contrast Agents in Medical Magnetic Resonance Imaging*, 2nd. ed. (Eds.: A. Merbach, L. Helm, É. Tóth), John Wiley & Sons, Ltd, Great Britain, **2013**, pp. 83–155; e) J.-P. Costes, A. Dupuis, G. Commenges, S. Lagrave, J.-P. Laurent, *Inorg. Chim. Acta* **1999**, *285*, 49–54.

[57] For additional NMR studies of **1d-Lu** in a non-donating solvent (CDCl$_3$), see SI.

[58] B. L. Ramirez, P. Sharma, R. J. Eisenhart, L. Gagliardi, C. C. Lu, *Chem. Sci.* **2019**, *10*, 3375–3384.

[59] For examples of Schiff base complexes of rare earth metals as polymerization catalysts: a) C. Bakewell, T.-P.-A. Cao, N. Long, X. F. Le Goff, A. Auffrant, C. K. Williams, *J. Am. Chem. Soc.* **2012**, *134*, 20577–20580; b) A. Decortes, R. M. Haak, C. Martín, M. M. Belmonte, E. Martin, J. Benet-Buchholz, A. W. Kleij, *Macromolecules* **2015**, *48*, 8197–8207; c) W. Gu, P. Xu, Y. Wang, Y. Yao, D. Yuan, Q. Shen, *Organometallics* **2015**, *34*, 2907–2916; d) C.-H. Ho, H.-J. Chuang, P.-H. Lin, B.-T. Ko, *J. Polym. Sci. Part A* **2017**, *55*, 321–328; e) R. Xu, L. Hua, X. Li, Y. Yao, X. Leng, Y. Chen, *Dalton Trans.* **2019**, *48*, 10565–10573.

[60] S. Tanase, S. Sottini, V. Marvaud, E. J. J. Groenen, L.-M. Chamoreau, *Eur. J. Inorg. Chem.* **2010**, 3478–3483.

[61] L.-W. Yang, S. Liu, E. Wong, S. J. Rettig, C. Orvig, *Inorg. Chem.* **1995**, *34*, 2164–2178.

[62] a) C.-P. Wong, G. Bisset, in *Inorganic Syntheses* (Ed.: S. L. Holt Jr.), **1984**, pp. 156–162; b) W. Xie, M. J. Heeg, P. G. Wang, *Inorg. Chem.* **1999**, *38*,

2541–2543; c) H. He, W.-K. Wong, J. Guo, K.-F. Li, W.-Y. Wong, W.-K. Lo, K.-W. Cheah, *Inorg. Chim. Acta* **2004**, *357*, 4379–4388; d) S. Tamburini, S. Sitran, V. Peruzzo, P. A. Vigato, *Eur. J. Inorg. Chem.* **2009**, 155–167.

[63] For examples of the utilization of Ln[N(TMS)$_2$]$_3$ as starting materials for the synthesis of Ln Schiff base complexes: a) S. A. Schuetz, V. W. Day, R. D. Sommer, A. L. Rheingold, J. A. Belot, *Inorg. Chem.* **2001**, *40*, 5292–5295; b) S. A. Schuetz, C. M. Silvernail, C. D. Incarvito, A. L. Rheingold, J. L. Clark, V. W. Day, J. A. Belot, *Inorg. Chem.* **2004**, *43*, 6203–6214; c) F. Han, Q. Teng, Y. Zhang, Y. Wang, Q. Shen, *Inorg. Chem.* **2011**, *50*, 2634–2643; d) W. Lv, Y. Wang, B. Wu, Y. Yao, Q. Shen, *Z. Anorg. Allg. Chem.* **2012**, *638*, 1167–1172; e) W. Ren, L. Chen, N. Zhao, Q. Wang, G. Hou, G. Zi, *J. Organomet. Chem.* **2014**, *758*, 65–72.

[64] G. M. Sheldrick, *Acta Crystallogr. Sect. A* **2015**, *71*, 3–8.

[65] G. M. Sheldrick, *Acta Crystallogr. Sect. C* **2015**, *71*, 3–8.

[66] O. V. Dolomanov, L. J. Bourhis, R. J. Gildea, J. A. K. Howard, H. Puschmann, *J. Appl. Crystallogr.* **2009**, *42*, 339–341.

[67] F. H. Allen, O. Johnson, G. P. Shields, B. R. Smith, M. Towler, *J. Appl. Crystallogr.* **2004**, *37*, 335–338.

[68] A. Spek, *Acta Crystallogr. Sect. C* **2015**, *71*, 9–18.